A PROBABILITY-BASED NUMERICAL METHOD FOR ESTIMATING EFFECTIVE DIFFUSION COEFFICIENT IN CONCRETE

A Dissertation

Presented to the Faculty of the Graduate School

of Cornell University

in Partial Fulfillment of the Requirements for the Degree of

Doctor of Philosophy

by

Riza Secer Orkun Keskin

August 2008

A PROBABILITY-BASED NUMERICAL METHOD FOR ESTIMATING EFFECTIVE DIFFUSION COEFFICIENT IN CONCRETE

Riza Secer Orkun Keskin, Ph.D.

Cornell University 2008

Reinforced concrete is a common structural material since it is strong, durable and relatively cheap. Of the various deterioration mechanisms of reinforced concrete structures, chloride-induced corrosion of steel reinforcement is of great importance since numerous reinforced concrete structures are exposed to chloride sources [129]. ASCE 2005 Report Card estimates a cost of $9.4 billion a year for 20 years to eliminate deficiencies of 590,750 bridges in the United States, almost half of which are reinforced concrete. A 1998 survey states that 9% of the reinforced concrete bridges in the United States are structurally deficient, primarily due to corrosion of steel reinforcement [196]. Accurate lifetime predictions are of great use for developing efficient strategies to handle the corrosion damage. Since chloride ingress is a transport phenomenon, it is necessary to have an accurate representation of concrete at microscale to obtain adequate lifetime predictions of reinforced concrete structures.

Diffusion, convection, migration and permeation are transport mechanisms in reinforced concrete structures. Chloride ingress into concrete usually occurs by either diffusion or diffusion coupled with another transport mechanism. Diffusion is of interest to this research, since it is the most dominant chloride transport mechanism.

Our objective is to predict service life of reinforced concrete structures. We focus on the estimation of effective diffusion coefficient since it is closely related to the rate of chloride diffusion through concrete. A probability-based numerical method is developed for estimating the effective diffusion coefficient of

chloride in concrete. The method has two essential steps. First, virtual concrete specimens are constructed. Each specimen is modeled as a three-phase material consisting of (i) aggregate, (ii) cement paste, and (iii) interfacial transition zones. The algorithm constructing virtual specimens places virtual aggregates at random locations. The aggregates are ellipses of random aspect ratios with noisy boundaries defined by beta translation fields. Second, properties of Itô process are used to estimate the effective diffusion coefficients in virtual specimens and the chloride concentration at arbitrary points of specimens. All numerical results are limited to 2D mortar specimens.

BIOGRAPHICAL SKETCH

Riza Secer Orkun Keskin was born on May 23, 1977 in Ankara, Turkey. He received a Bachelor of Science degree in Civil Engineering from Middle East Technical University in January 2000. Under the supervision of Prof. Guney Ozcebe, he studied behavior of brick infilled reinforced concrete frames strengthened by CFRP reinforcement, and received a Master of Science degree in Civil Engineering from Middle East Technical University in July 2002. In 2003, he was hired as a structural engineer by a Turkish company for a marina construction in Aqaba, Jordan. In September 2003, he got a scholarship from the Higher Education Council of Turkey for pursuing a Doctor of Philosophy degree in Civil Engineering at Cornell University. He joined Cornell University in January 2004, and received a Master of Science degree in Civil Engineering in September 2006. Under the supervision of Prof. Mircea Grigoriu, he studied stochastic methods for solving partial differential equations, particularly chloride diffusion equation in concrete, and received the Doctor of Philosophy degree in Civil Engineering from Cornell University in June 2008.

His research interests are deterioration mechanisms of reinforced concrete structures and applications of stochastic methods in civil engineering.

To my family,

ACKNOWLEDGEMENTS

I would like to thank Technical University of Yildiz and the Higher Education Council of Turkey for providing me financial support. None of this would have been possible without their support.

This is a great opportunity to express my respect and appreciation to the chairman of my committee, Professor Mircea Grigoriu. I would like to sincerely thank him for his guidance, patience and support throughout my five years at Cornell. His contribution to this dissertation is invaluable.

I would like to thank the other members of my committee, Professor Kenneth Hover and Professor Gennady Samorodnitsky, for their helpful comments and revisions.

I could never have finished this research without the support of my family and my girlfriend Selcen. Special thanks go to my parents. This dissertation is especially dedicated to my grandmother, who was taken under intensive care the day I defended this dissertation. Rest in peace grandmother.

I would like to thank also my friends, Ibrahim Erdem, Umut Can, Cagdas Kafali, Demirhan Kobat, Yesim Soyer and Cagla Aydin, for their social support throughout my five years in Ithaca.

This research was conducted using the resources of the Cornell University Center for Advanced Computing, which receives funding from Cornell University, New York State, the National Science Foundation, and other leading public agencies, foundations, and corporations.

TABLE OF CONTENTS

LIST OF TABLES

LIST OF FIGURES

CHAPTER 1

INTRODUCTION

1.1 Introduction

Reinforced concrete is the most common structural material, since it is strong, durable and relatively cheap. It is a composite material consisting of concrete and steel. While steel reinforcement increases structural performance, concrete protects steel reinforcement from environmental attacks. Concrete is a random heterogeneous material consisting of aggregate held together by a hardened cement paste.

The durability of a reinforced concrete structure is the capacity of its constituents, *i.e.*, concrete and steel, to maintain their physical characteristics and mechanical performances at satisfactory levels of safety and serviceability [38]. Strength-based criteria are insufficient for the design of reinforced concrete structures since these structures deteriorate in time. In recent years, research focused on the mechanism of deterioration of reinforced concrete structures to develop durability-based design criteria. Current building codes specify durability-based design criteria as well as strength-based design criteria [110].

Reinforced concrete structures are likely to be subjected to various adverse conditions, *e.g.*, chemical attacks and freeze-thaw cycles. Of the various deterioration mechanisms of reinforced concrete structures, chloride-induced corrosion of steel reinforcement bars is of great importance since numerous reinforced concrete structures are exposed to chloride sources, *e.g.*, de-icing salts or marine environment [129]. Direct cost of corrosion in highway bridges (includ-

ing all types), *i.e.*, cost of maintenance, repair and rehabilitation, was estimated as $8.29 billion annually [196]. Indirect costs due to traffic delays and lost productivity were estimated to be more than ten times the direct cost [196]. A recent study, ASCE 2005 Report Card, estimates a cost of $9.4 billion a year for 20 years to eliminate deficiencies of 590,750 bridges in the United States, almost half of which are reinforced concrete. A 1998 survey states that 9% of the reinforced concrete bridges in the United States are structurally deficient, primarily due to corrosion of steel reinforcement [196]. Accurate lifetime predictions are of great use for developing efficient strategies to handle the corrosion damage. Since chloride ingress is a transport phenomenon, it is necessary to have an accurate representation of concrete at microscale to obtain adequate lifetime predictions of reinforced concrete structures.

Concrete has a high alkali internal environment encouraging the development of a passive (oxide) film around steel reinforcement bars. The alkalinity of concrete is reduced, as more chloride penetrates concrete. When chloride concentration in a vicinity of a steel bar reaches a critical value, the passive film protecting the bar is damaged. Provided that there is adequate oxygen and moisture in the environment, corrosion of the bars initiates leading to cracking, spalling or delamination of the concrete cover since the volume of the corrosion products are several times larger than the volume of the steel lost by corrosion. A secondary effect is reduction in load-carrying capacity of the steel bars, due to loss of cross-sectional area at locations where corrosion takes place. In summary, the concrete cover acts as both a physical and a chemical barrier protecting the steel reinforcement in the case of chloride ingress through a reinforced concrete structure.

Chloride within concrete may exist in the state of either free or bound. The free chloride is responsible for the initiation of corrosion of steel reinforcement. Chloride ingress occurs through pores in the cement paste, mainly capillary pores, therefore the properties of the pore structure have a major effect on the quality of concrete cover as a physical barrier against chloride ingress. On the other hand, solid phases of cement paste have the ability of binding chloride, thus behaving as a chemical barrier against chloride ingress.

There are mainly four groups of chloride transport mechanisms observed in reinforced concrete structures: (i) permeation, (ii) migration, (iii) convection, and (iv) diffusion. For instance, chloride ingress into partially saturated concrete occurs by a coupled mechanism of diffusion and convection, whereas it is the diffusion that dominates the chloride ingress into fully saturated concrete, unless there exists a high pressure head. Diffusion is of interest to this research, since it is the most dominant chloride transport mechanism. Chloride diffusion through concrete is usually described by Fick's law [42].

A critical parameter for evaluating the resistance of concrete to chloride diffusion is the effective diffusion coefficient, which provides information on the rate of chloride diffusion through concrete specimens. The effective diffusion coefficient of chloride in concrete can be obtained experimentally, numerically or analytically, and depends on specimen size.

Diffusion- and electrical-based methods are commonly used to find experimentally the effective diffusion coefficients in concrete specimens. Diffusion experiments can be performed under either steady-state or non-steady-state conditions. Since diffusion experiments are time-consuming, electrical methods have been developed. The advantage of electrical methods over diffusion ex-

periments is that the duration of experiment can be reduced significantly due to the accelerated chloride ingress caused by application of an electrical potential. An alternative method to accelerate chloride ingress into a test specimen is to apply a hydraulic pressure, but the method is infrequently used. It is important to note that chloride diffusion coefficients obtained through different methods are not directly comparable mainly due to the differences in the hypotheses behind the methods [170].

There are few numerical methods developed for estimating the effective diffusion coefficient of chloride in concrete. A well known method is a multi-scale microstructural model developed by Garboczi and Bentz [63]. The model is based on random walks executed in a computational concrete volume, in which aggregate particles and interfacial transition zones are represented by spheres and thin shells surrounding those spheres, respectively.

There are also analytical and empirical models, usually developed using an effective medium theory [67] or a composite model [187], for estimating the effective diffusion coefficient of chloride in concrete. Since chloride diffusion through concrete depends on many parameters, it is difficult to calculate the effective diffusion coefficient from simple equations.

1.2 Objective

The objective of this research is to develop a method for predicting service life of reinforced concrete structures. Service life of a reinforced concrete structure relates to the effective diffusion coefficient of chloride in the concrete since

it is a measure of the resistance of concrete to chloride diffusion. A probability-based numerical method is developed for estimating the effective diffusion coefficient of chloride in concrete. The method has two essential steps.

First, virtual concrete specimens are constructed. A concrete specimen is modeled as a three-phase material consisting of (i) aggregate particles with zero diffusivity, (ii) bulk cement paste with a constant chloride diffusion coefficient, and (iii) interfacial transition zones around aggregate particles in which the chloride diffusion coefficient increases as the aggregate surface is approached. The algorithm constructing virtual concrete specimens places virtual aggregates at random locations. The aggregates are ellipses of random aspect ratios with noisy boundaries defined by beta translation fields. Virtual specimens are constructed in 2D using volume fraction statistics obtained from 3D specimens. This is an approximation and has been used to reduce calculations.

Second, properties of Itô process are used to estimate the effective diffusion coefficients in virtual specimens and the chloride concentration at arbitrary points of specimens. A probabilistic method in [80] for estimating the effective diffusion coefficient of chloride in a virtual concrete specimen is adopted. The effective diffusion coefficient of the virtual concrete specimen is the diffusion coefficient of a virtual homogeneous specimen.

The proposed method is general but is only applied to estimate the effective diffusion coefficients of chloride in 2D virtual mortar specimens and the chloride concentration at arbitrary points of these specimens. We limit calculations to this type of specimens for two reasons. First, computation time is much smaller for 2D specimens than for 3D specimens. Second, effective properties of mortar can be used to construct large virtual concrete specimens.

1.3 Outline

Concrete and chloride diffusion in concrete is covered in Chapter 2. The proposed method, the algorithm generating virtual specimens and the application of the proposed method are presented in Chapters 3, 4 and 5, respectively. The content of each chapter is briefly summarized below.

Chapter 2 consists of two parts. In the first part, the fundamentals and microstructural features of concrete with regard to its transport properties are reviewed. In the second part, chloride diffusion in concrete is discussed.

Chapter 3 presents the proposed method for estimating the effective diffusion coefficient of chloride in a random heterogeneous medium. It starts with a review of numerical methods for solving partial differential equations. Then the essentials of the method chosen for solving the transport equation, a partial differential equation, are given. Two examples considering steady-state and transient-state diffusion are presented. The probabilistic method in [80] is used to estimate the effective diffusion coefficient of chloride in a deterministic/random heterogenous medium. Two examples considering a deterministic and a random diffusivity field are presented.

Chapter 4 presents the algorithm developed for generating virtual 2D mortar/concrete specimens. First, the algorithm for generating virtual 2D aggregate particles, second, the algorithm for placing the virtual particles into a given container, is presented. Three examples are given to illustrate the features of the developed algorithm.

Chapter 5 starts with a review of the most common methods for obtaining

the effective diffusion coefficient of chloride in cement paste, mortar or concrete. Then the parameters of the chloride diffusivity random field model are calibrated to experiments by using the output of the proposed method. The resulting parameter values are used in all subsequent calculations. The calibrated version of the method is used to calculate effective diffusion coefficients in several virtual specimens and these coefficients are compared with experimental results. Also, chloride concentration is estimated at arbitrary points of virtual specimens and the resulting estimates are compared with experimental results. All numerical results are for 2D mortar specimens.

Chapter 6 presents the conclusions of the study and proposes future work related to the study.

CHAPTER 2

CHLORIDE DIFFUSION IN CONCRETE

2.1 Introduction

Concrete has been widely used as a construction material throughout the world due to its various advantages, *e.g.*, strength, durability and cost. It is usually used with steel reinforcement, resulting in a strong and durable composite material, referred to as *reinforced concrete*. While steel reinforcement increases structural performance, concrete protects steel reinforcement from environmental attacks. There have been numerous reinforced concrete structures built in aggressive environments, and most of them are still standing in spite of the severe environmental conditions.

Chemrouk and Attari [38] defined the durability of a reinforced concrete structure as the ability of its constituents, *i.e.*, concrete and steel, to keep their physical characteristics and mechanical performances at satisfactory levels of safety and serviceability. Then the durability of the structure is provided mainly by the concrete since the steel reinforcement is protected by the concrete.

Reinforced concrete structures may deteriorate due to external and/or internal factors, *e.g.*, chemical attacks and freezing-thawing cycles. Of the various deterioration mechanisms observed in reinforced concrete structures, chloride-induced corrosion of steel reinforcement bars is of great importance since numerous reinforced concrete structures are exposed to chloride sources, *e.g.*, deicing salts or marine environment [129]. In the case of chloride ingress through a reinforced concrete structure, the concrete cover acts as both a physical and a

chemical barrier protecting the steel reinforcement. The fundamentals of concrete are reviewed briefly in Section 2.2, and chloride diffusion in concrete is discussed within the rest of the chapter.

2.2 Concrete

Concrete is a heterogeneous medium consisting of aggregate held together by a hardened cement paste. The basic cementitious constituent of concrete is Portland cement. Modern concrete mixtures contain one or a few supplementary cementitious materials, formerly referred to as *mineral admixtures*, as well as Portland cement. A brief review of the constituents of concrete is given below. Detailed discussions on them can be found elsewhere [29, 109, 115, 116, 127, 128, 146].

Portland cement is a hydraulic material composed of crystalline minerals, such as oxides of calcium, silicon, aluminium and iron. The four main minerals found in the Portland cement are tricalcium silicate (alite), dicalcium silicate (belite), tricalcium aluminate and tetracalcium aluminoferrite. *Supplementary cementitious materials* are either byproducts of industrial processes or natural materials that may or may not be further processed. Typical examples of supplementary cementitious materials are fly ash, ground granulated blast furnace slag, silica fume and natural pozzolans such as metakaolin and calcined shale or clay. The use of supplementary cementitious materials allows concrete manufacturers to meet certain requirements on the workability, durability and strength of concrete. There are also *chemical admixtures*, the major types of which are accelerators, retarders, air-entrainers, plasticizers (water-reducing), super-

plasticizers and corrosion inhibitors, used for enhancing certain properties of concrete.

Water is required for the chemical reactions which produce *cement paste*. Drinking water can be used safely for manufacturing cement pastes. Non-potable water can also be used, but necessary tests should be carried out prior to the manufacturing process. The quality of the resulting cement paste will be low if harmful ingredients, contamination, silt, or oil, exist in the water.

Aggregates are granular materials such as sand, gravel, or crushed stone. Formerly, aggregate had been referred to as the filler material of concrete, which reduces the cost since it is cheaper than cement. Actually, it is an essential constituent of concrete, affecting the strength and durability of concrete significantly as well as reducing the cost.

2.2.1 Cement Paste

When Portland cement and water are mixed, the mixture first sets, and then hardens through a series of chemical reactions, called *hydration*, between water and minerals found in the cement. Two important parameters related to the hydration process are *heat of hydration* and *degree of hydration*. The former is a measure of released energy -hydration is an exothermic process- during the hydration reactions, and the latter is the fraction of the cement particles that have fully hydrated.

2.2.1.1 Hydration of Portland Cement

The hydration of Portland cement is a complicated process, the details of which can be found elsewhere [29, 56, 69, 109, 146]. Two mechanisms observed in the hydration process of Portland cements are through-solution hydration and topochemical (or solid-state) hydration [109]. The dissolution of anhydrous cement compounds into their ionic constituents, which then form hydrates in the solution, and the eventual precipitation of these hydrates from this supersaturated solution is called the *through-solution hydration mechanism*. On the other hand, the *topochemical (or solid-state) hydration mechanism* consists of the reactions taking place on the surface of anhydrous cement compounds.

The hydration starts on the surface of a cement particle, and then extends towards the interior gradually. As time proceeds, a solid shell of hydrates forms around the cement particle. The water in contact with the unhydrated part of the cement particle either reacts with it or dissolves a portion of it. The supersaturated solution diffuses out towards capillary pores through very small pores of the solid shell. The hydrates precipitate from the supersaturated solution in air- or water-filled pores that are large enough to allow nucleation of a new solid phase. The details of the hydration of individual phases can be found elsewhere [29, 56, 69, 109, 146].

The rate of the hydration reactions can be studied by examining the rate of heat evolution during the hydration process [29, 146]. Just after mixing, the highest rate of heat evolution is observed. However, the duration of this peak is relatively short. The period following this peak, referred to as *induction* or *dormant period*, lasts about 3 hours [146]. The mixture starts to gain stiffness, and loses its workability during the induction period, so the duration of the

induction period determines the time limit for placing concrete. The induction period ends with an increase in the rate of heat evolution. Setting occurs during this increase. The second peak in the rate of heat evolution is observed at around the tenth hour for ordinary Portland cements hydrated at 20° [29]. It depends on the type of cement whether the third peak occurs or not. The hydration may continue for a very long time, but the rate of the reactions decreases in time. A rate of heat evolution curve during hydration of a typical Portland cement is plotted in Figure 2.1.

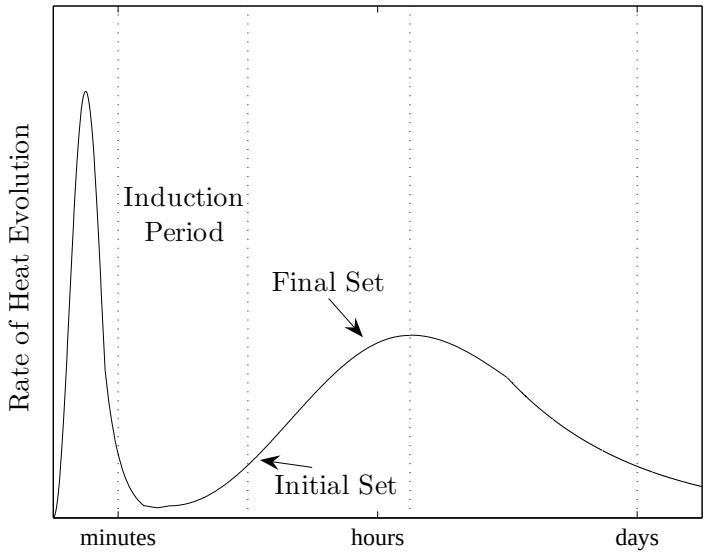

Figure 2.1: A Rate of Heat Evolution Curve During the Hydration of PC

2.2.1.2 Solid Phases of Cement Paste

As the hydration takes place, the hydration products develop gradually, forming finely structured porous solids called *cement gel*. There are four principal solid phases, which can be resolved by scanning electron microscope (SEM), in a hydrated cement paste [109]:

- Calcium-silicate-hydrate (C-S-H) constitutes 50% to 60% of the volume of the solid phases in a completely hydrated cement paste, so it is the most important solid phase. C-S-H has a morphology varying from poorly crystalline fibers to a reticular network.

Figure 2.2: A SEM Image by Stutzman [160]

- The proportion of calcium hydroxide (CH), referred to as *portlandite*, in the solid phases is 20% to 25%. Unlike C-S-H, it has a well-defined stoichiometry. It exists in the form of massive hexagonal crystals.
- Calcium sulfoaluminates make up 15% to 20% of the volume of the solid phases in a hydrated cement paste. In the early stages of the hydration, the formation of trisulfate hydrate, referred to as *ettringite*, in the form of needle-shaped prismatic crystals is observed.
- Unhydrated cement, in the form of partially hydrated cement particles, are typically present in a hydrated cement paste. The amount of unhydrated

cement depends on the cement particle size distribution and the degree of hydration.

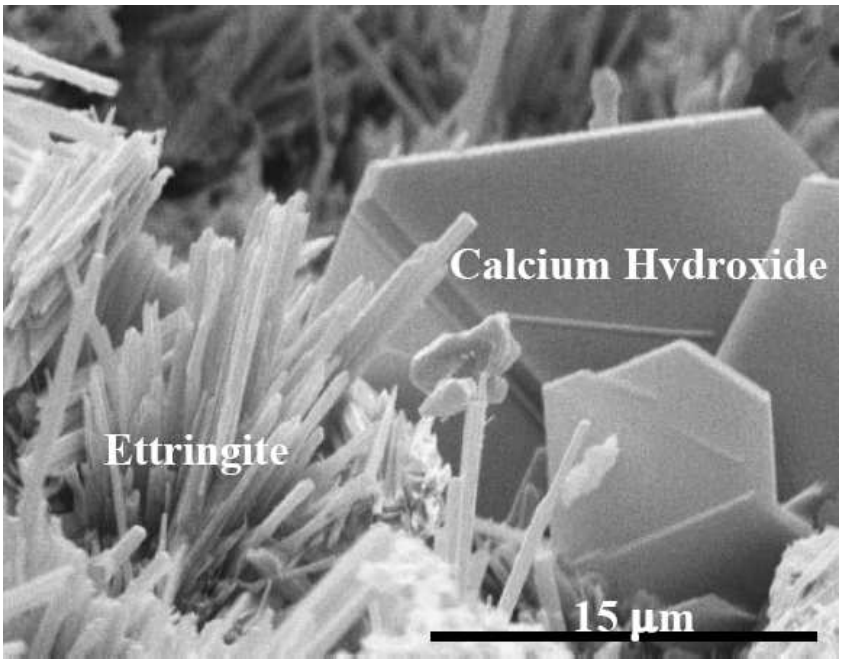

Figure 2.3: Another SEM Image by Stutzman [160]

2.2.1.3 Voids in Cement Paste

There exist several types of voids in a hydrated cement paste [109]:

- *Capillary pores* (see Section 2.2.1.5) are the void space left from initially water filled space that is consumed as the hydration proceeds.
- *Gel pores* (see Section 2.2.1.5) are the void space in the cement gel remaining from the solid hydration products. The volume fraction of gel pores in the total cement gel is almost constant (∼27-28%).
- Air voids can be either *entrapped* during mixing or *entrained* purposely by means of an air entraining agent. The primary objective of air entrain-

ment is to provide resistance to freeze-thaw damage. It also improves the workability of concrete. However, too much entrained air may reduce the strength of concrete. The size of entrained air bubbles ranges from 0.01 mm to 1 mm. On the other hand, entrapped air voids are relatively large, 1 mm to 10 mm or more, and usually have irregular shapes rather than being spherical. The volume fraction of entrapped air in concrete is usually 1-2 %.

2.2.1.4 Water in Cement Paste

Besides the solid phases and the air voids, there exists water in a hydrated cement paste. In addition to vapor in the empty or partially water-filled voids, water exists in a hydrated cement paste in the following forms [109]:

- *Capillary water* is the water that exists in the capillary pores. The removal of the water held by capillary tension in the small capillaries may cause shrinkage.
- *Adsorbed water* is the water physically held on the surfaces of the solid phases of cement pastes. The removal of the adsorbed water causes drying shrinkage.
- *Interlayer water* is the water that exists in the gel pores. The loss of the gel water causes the C-S-H structure to shrink.
- *Chemically combined water*, also known as *hydrate water* or *bound water*, is the water which is part of the hydration products.

2.2.1.5 Capillary Porosity and Gel/Space Ratio

Two important parameters characterizing the pore structure in a hydrated cement paste are *capillary porosity* and *gel/space ratio*. Based on the observed facts, complete hydration of 1 g of cement is considered below for studying the relationship of capillary porosity and gel/space ratio with degree of hydration α and water-to-cement ratio w/c [115, 116].

The volume of 1 g of cement is equal to 0.32 ml since the density of unhydrated cement is 3.15 g/ml. The mass of chemically combined water depends on cement composition. If it is assumed as 0.25 g, the mass of the solid hydration products is 1.25 g (1 g cement + 0.25 g water). Then the volume of the solid hydration products is 0.48 ml since the density of solid hydration products is observed to be 2.6 g/ml. If it was a simple combination of cement and water, it would have a density of 2.72 g/ml, therefore the resulting hydrated product is less dense than the simple combination of cement and water. The solid hydration products occupy 73% of the volume of the cement gel, then the volume of the cement gel is 0.66 ml, and the volume and mass of the gel water are 0.18 ml and 0.18 g, respectively. Hence, the density of the gel, including gel pores, is 2.17 g/ml since its mass and volume are 1.43 g (1 g of cement + 0.25 g of bound water + 0.18 g of gel water) and 0.66 ml, respectively. Since the volumes of the cement paste and the cement gel are 0.75 ml (0.32 ml cement + 0.43 ml water) and 0.66 ml, respectively, capillary pores occupy a volume of 0.09 ml, corresponding to a capillary porosity of 12%.

Based on the complete hydration of 1 g of cement, a general relationship for capillary porosity can be derived. Let m_c denote the mass of cement. Then the mass and volume of water are $m_c(w/c)$, and the volume of cement is $0.32m_c$.

The total volume of resulting paste is then $m_c(0.32 + w/c)$. The volume of hydrated and saturated gel is $0.66\alpha m_c$, where αm_c is the mass of cement that has hydrated. The mass and volume of remaining unhydrated cement are $(1-\alpha)m_c$ and $0.32(1-\alpha)m_c$, respectively. Then the volume of remaining empty or water-filled capillary pore space is $m_c(0.32+w/c)-0.66\alpha m_c-0.32(1-\alpha)m_c = m_c(w/c-0.34\alpha)$, so the capillary porosity is

$$\text{Capillary Porosity} = \frac{w/c - 0.34\alpha}{0.32 + w/c}. \tag{2.1}$$

Gel/space ratio is the ratio of the volume of hydrated gel to the space available for gel development, *i.e.*, the volume of gel and the capillary pore volume. Based on the complete hydration of 1 g of cement, a general relationship for gel/space ratio can be derived. The volume of hydrated and saturated gel is $0.66\alpha m_c$, and the volume of remaining empty or water-filled capillary pore space is $m_c(w/c-0.34\alpha)$. Then the gel/space ratio is

$$\text{Gel/Space Ratio} = \frac{0.66\alpha m_c}{m_c(w/c-0.34\alpha)+0.66\alpha m_c} = \frac{0.66\alpha}{w/c+0.32\alpha}. \tag{2.2}$$

For a given w/c ratio, capillary porosity and gel/space ratio as a function of degree of hydration is plotted in Figure 2.4 and Figure 2.7, respectively. Similarly, for a given degree of hydration, capillary porosity and gel/space ratio as a function of w/c ratio is plotted in Figure 2.5 and Figure 2.8, respectively. In Figure 2.6 and Figure 2.9, the relationship of capillary porosity and gel/space ratio with degree of hydration and w/c ratio is illustrated, respectively.

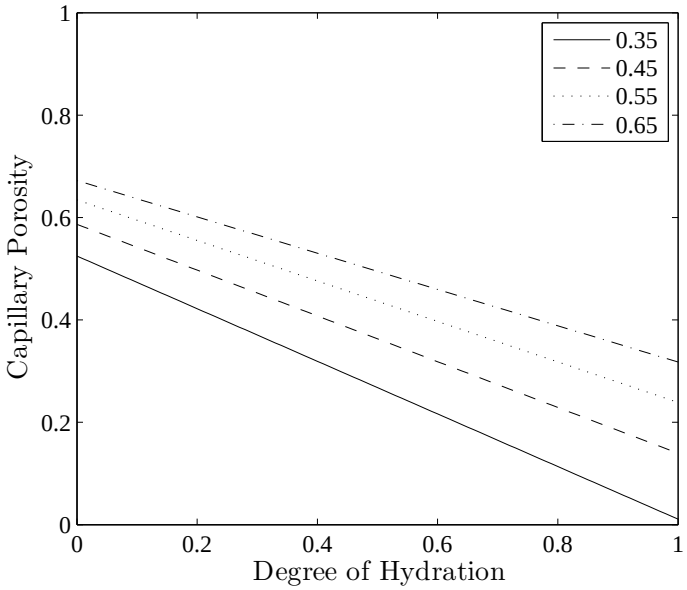

Figure 2.4: Capillary Porosity vs. α for $w/c = 0.35, 0.45, 0.55, 0.65$

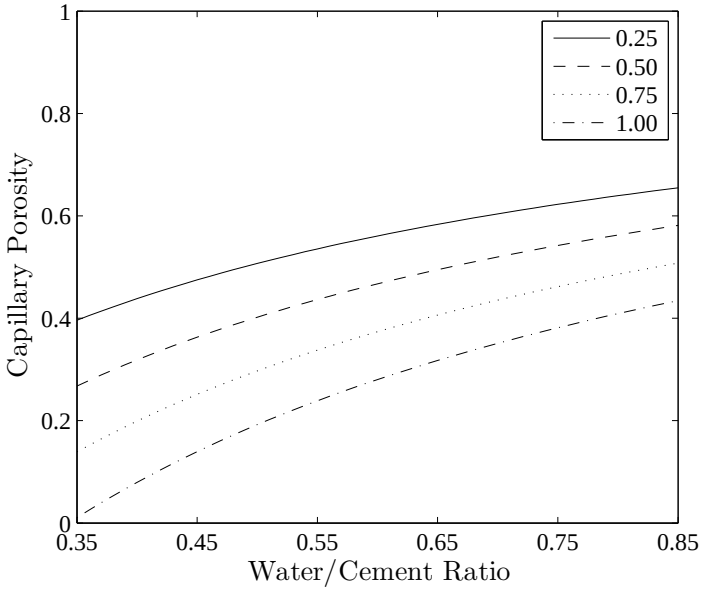

Figure 2.5: Capillary Porosity vs. w/c for $\alpha = 0.25, 0.50, 0.75, 1.00$

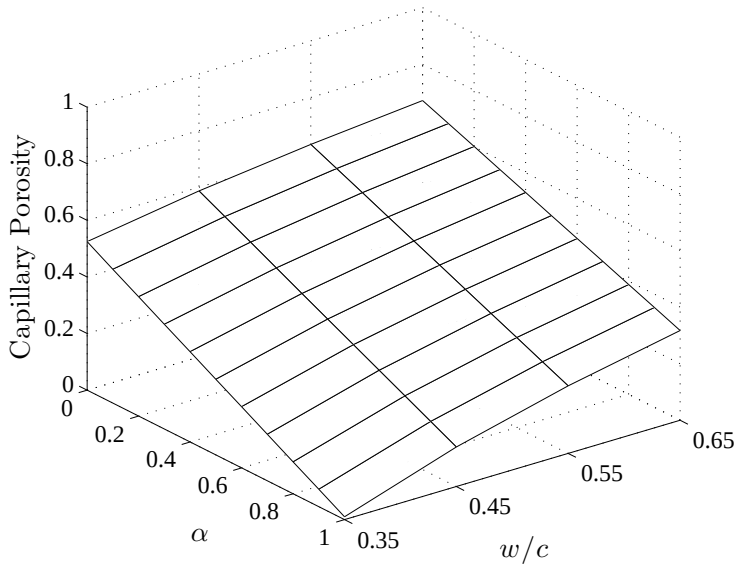

Figure 2.6: Capillary Porosity vs. α and w/c

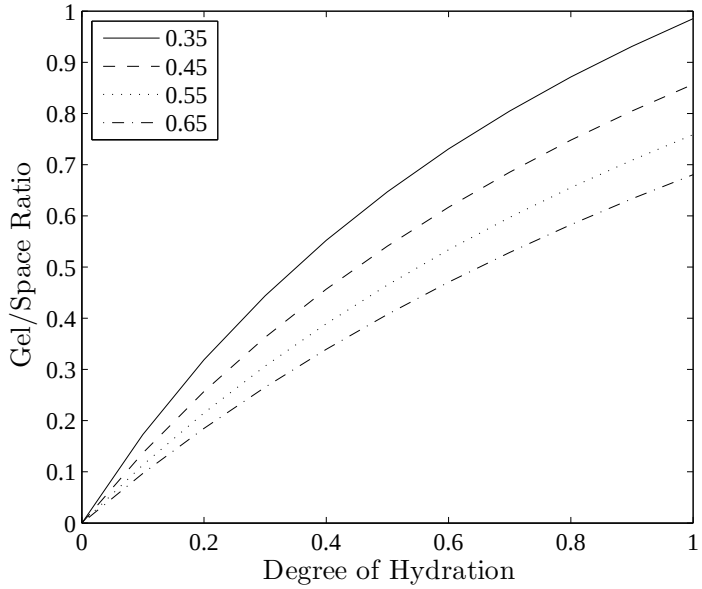

Figure 2.7: Gel/Space Ratio vs. α for $w/c = 0.35, 0.45, 0.55, 0.65$

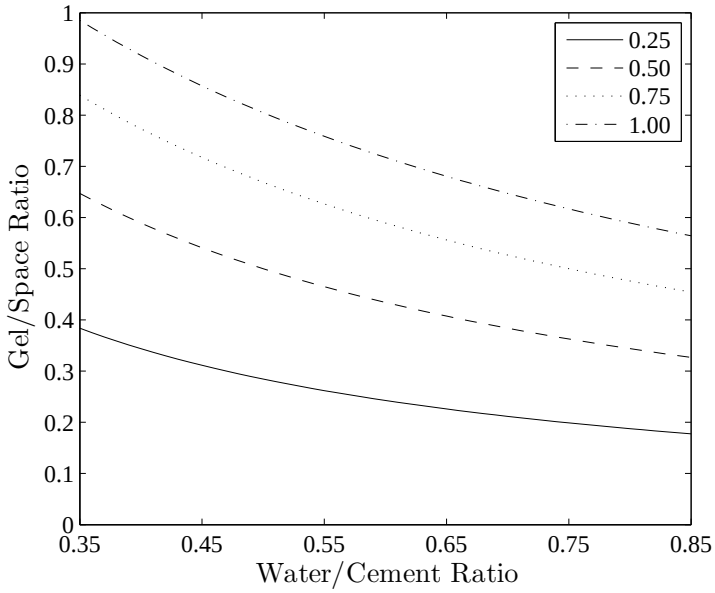

Figure 2.8: Gel/Space Ratio vs. w/c for $\alpha = 0.25, 0.50, 0.75, 1.00$

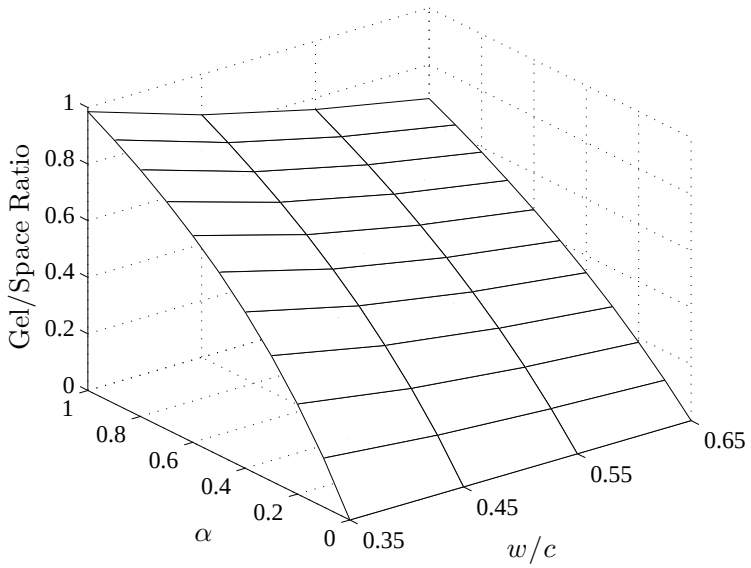

Figure 2.9: Gel/Space Ratio vs. α and w/c

Capillary porosity and gel/space ratio are functions of w/c ratio, degree of hydration and degree of compaction. It can be clearly observed in Figure 2.4 through Figure 2.9 that: (i) with increasing degree of hydration, capillary porosity decreases, while gel/space ratio increases, and (ii) with increasing w/c ratio, capillary porosity increases, while gel/space ratio decreases. That is, a cement paste with a high w/c ratio requires a high degree of hydration to achieve a high gel/space ratio, while a cement paste with a low w/c ratio requires a moderate degree of hydration to achieve a high gel/space ratio. In order to obtain a dense cement paste, cement particles should be brought as close as possible by a low w/c ratio and a high degree of compaction, and maximum degree of hydration should be promoted leading to a high gel/space ratio and a low capillary porosity.

Table 2.1: Curing Period for Capillary Pores to Become Segmented [131]

w/c Ratio by Mass	Degree of Hydration	Curing Period Required
0.40	0.50	3 days
0.45	0.60	7 days
0.50	0.70	14 days
0.60	0.92	6 months
0.70	1.00	1 year
> 0.70	1.00	Impossible

Degree of hydration is a function of time, available moisture and temperature, therefore curing period and conditions are of great importance. With continuing hydration, cement gel grows blocking capillary pores. A suitable combination of w/c ratio and a moist curing period is needed to obtain capillary pores interconnected by gel pores. Powers *et al.* [131] measured the approximate

moist curing periods required to block capillary pores with cement gel so as to produce impermeable cement pastes. As can be seen in Table 2.1, it would not be possible to block capillary pores with cement gel for w/c ratios greater than 0.7, even complete hydration of cement is achieved.

During hydration of cement, specific surface area of solid phases increases enormously ($\sim$700 times) resulting in adsorption of a large amount of water on the solid surfaces. If it is a closed system, *i.e.*, there is no water in or out, free water in the system is consumed by the hydration reactions until too little is left to saturate the solid surfaces, therefore the relative humidity decreases. This phenomenon is referred to as *self-desiccation* [115, 116, 124]. Hydration, which is significantly retarded when relative humidity drops below 80% [130], continues as along as there is moisture in the pores surrounding the cement gel. For complete cement gel formation, a w/c ratio of 0.42 is required if the system is closed. Even though complete hydration is achieved, there will be still voids present in the resulting cement paste. A w/c ratio of 0.36 with a water supply from an external source results in minimum voids, but hydration will be incomplete without external water. On the other hand, for w/c ratios less than 0.36, hydration cannot be completed even under water cure.

Temperature has a significant effect on the development of the pore structure of a cement paste, since it affects the rate of the hydration reactions. In the early life of concrete (during first two hours), higher temperature results in a more porous cement gel. The increased rate of hydration causes retardation of the subsequent hydration and non-uniformly distributed cement gel because there is not enough time for the hydration products to diffuse far away from the cement particles and for a uniform precipitation at the increased rate of hydra-

tion [115]. Detailed discussions on curing conditions and curing duration can be found elsewhere [115, 116, 124].

Chloride ingress into concrete occurs through the pores in the cement paste. Since capillary pores are much larger than gel pores, chloride ingress occurs mainly through the capillary pores. Thus the characteristics of the capillary pore structure is of paramount importance with regard to the resistance of concrete to chloride ingress. Based on the discussions above and studies conducted by numerous researchers (see Appendix A), it is concluded that:

- The resistance of concrete to chloride ingress increases as the w/c ratio decreases [43, 45, 46, 47, 82, 87, 88, 103, 126, 154, 189, 193].
- The resistance of concrete to chloride ingress increases with the degree of hydration [175, 185].
- Increasing the curing time and/or improving the curing method increases the degree of hydration [40, 47, 50, 185], thus the resistance of concrete to chloride ingress. Rapid drying stops the hydration process earlier resulting in a coarser pore structure, thus leads to a reduced resistance to chloride ingress [185]. Elevated curing temperatures also reduce the resistance of concrete to chloride ingress [30, 46].

2.2.2 Aggregate

Aggregate occupies 60 to 75 percent of the total volume of concrete. It affects the strength and durability of concrete significantly. Concrete has a higher volume stability than the corresponding neat cement paste does because aggregate

restrains the drying shrinkage that cement paste could undergo [29, 115, 116]. An increase in the aggregate content from 65 to 75 percent may decrease creep by 10% [115, 116]. Aggregate having inadequate strength limits the strength of concrete [115, 116]. If there exist impurities and/or contaminants in the aggregate, the strength and durability of concrete may suffer [115, 116]. A well-known fact about aggregate is that it reduces the cost since it is cheaper than cement and constitutes a major part of concrete. Extensive discussions on the physical and chemical properties of aggregates can be found elsewhere [7, 109, 115, 116, 127, 171, 172, 173].

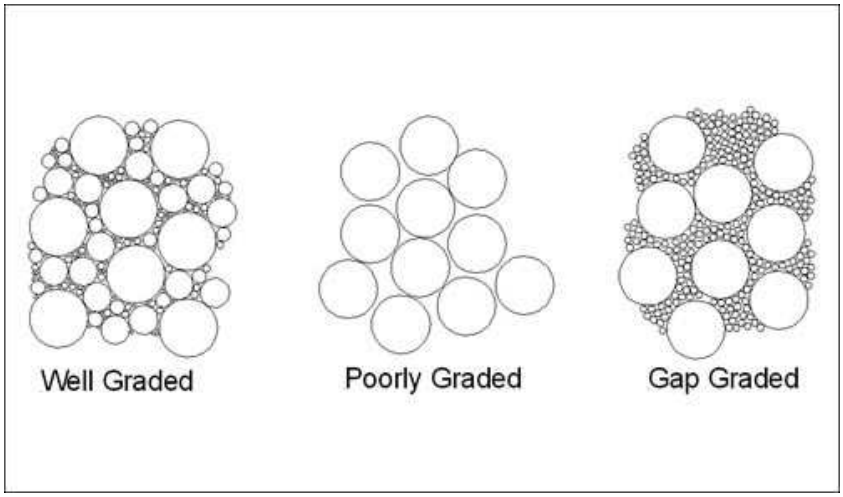

Figure 2.10: Schematical Representation of Different Gradings

There are several ways to classify aggregates. The one used in the design of mixtures is the classification according to the size, which divides the aggregates into coarse and fine aggregates. *Coarse aggregate* is defined such that the smallest particle size is 4.75 mm. *Fine aggregate* has a size range from 150 μm to 4.75 mm. *Particle size distribution*, also known as *grading*, is an important parameter affecting the quality of concrete. Well-graded combinations of coarse and fine aggregates are proposed by American Society for Testing and Materials [3].

In the early stages of the hydration of a cement paste, only the physical properties of aggregate are of importance if there are no impurities and contaminants present within the aggregate particles. Particle size distribution, particle shape and texture are the factors that affect the structure of the cement paste surrounding the aggregate particles.

The components of some of the aggregate particles may react with some of the compounds present in the cement paste after several years. The most detrimental reaction between aggregate particles and cement paste is known as *aggregate-alkali reaction*, which produces a gel that may cause cracking of concrete by swelling due to the water absorbed by the gel.

2.2.3 Microstructure of Concrete

A better understanding of the transport properties of concrete can be achieved by studying its microstructure. Concrete is considered as a three-phase material -cement paste, aggregate and transition zone between cement paste and aggregate- at microscale.

There exist various techniques, which can be divided into two main categories as indirect and direct [146, 147], developed to study the microstructure of composite materials. Thermogravimetry (TG), X-ray diffraction (XRD) and mercury intrusion porosimetry (MIP) are examples of indirect techniques. TG and XRD are used for determining the amounts of certain phases, while MIP is used for determining the pore size distribution. On the other hand, direct techniques like scanning electron microscope (SEM) using back-scattered-electron (BSE) imaging provide information on the arrangement of various phases.

Scrivener [146] discussed the development of cement paste microstructure extensively, and stated that the microstructure of a cement paste depends on:

- the composition of cement,
- the cement particle size distribution,
- the degree of hydration,
- and the w/c ratio.

2.2.3.1 Microstructure of Cement Paste

The transport properties of cement paste depends strongly upon the amount, distribution and connectivity of pores, primarily capillary pores. Initially, there exist only water and unhydrated cement. As the hydration proceeds, the unhydrated cement and the free water are consumed, producing solid hydration products, thus reducing the amount of capillary pores (Figure 2.11). With the increasing amount of the solid hydration products, the amount of gel pores also increases, but its proportion in the cement gel remains almost constant ($\sim$27-28%).

The application of percolation theory to cement pastes provides a better understanding of the microstructural development of cement pastes. Initially, capillary pores form a continuous network, while solid phases are discontinuous [19, 63, 180]. As the hydration takes place, cement gels start to form, and then grow gradually in a random manner. At some point, referred to as *initial set* (Figure 2.1), the cement gels begin to form a weak skeletal framework. The point at which the skeleton becomes fully established is referred to as *final set*

(Figure 2.1). Beyond the final set, the cement gel still continues to grow filling in the framework, referred to as *hardening*.

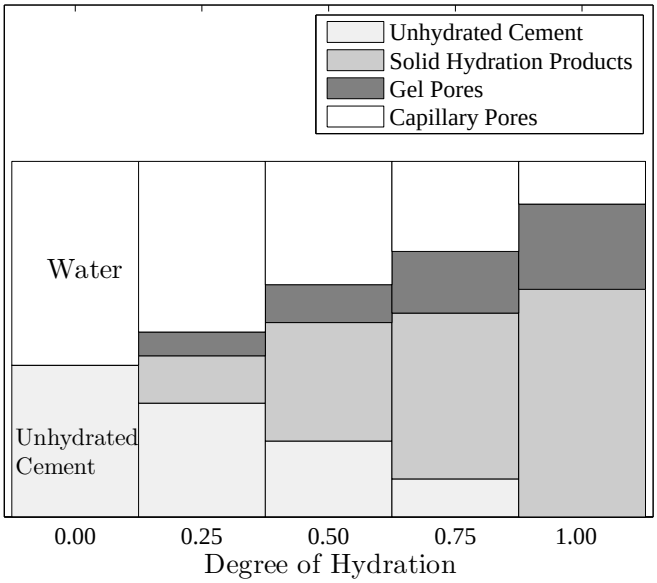

Figure 2.11: Volume Changes of Pores and Hydration Products

On the other hand, the volume and size of the capillary pores decrease, and their connectivity diminishes gradually. Depending on the w/c ratio and the degree of hydration, the capillary pores may be blocked at some point, resulting in isolated capillary pores. The capillary porosity at which the capillary pores are blocked with the cement gel is called *de-percolation threshold* [180] or *capillary porosity percolation threshold* [19, 63]. Since chloride ingress into concrete occurs mainly through capillary pores, the connectivity of capillary pores affects the rate of chloride ingress significantly. As more capillary pores are isolated, the rate of chloride ingress is reduced.

A widely used experimental method to study the pore structure in a cement paste is MIP, which is performed by putting a cement paste specimen in a chamber, evacuating the chamber and filling it with mercury, and then applying a

gradually increasing pressure on the mercury surrounding the cement paste specimen [40]. If the pore network is continuous, mercury can pass through the pore necks and penetrate the bulk volume. If it is not, mercury can intrude into the specimen volume by breaking through the pore walls. A measure of the connecting pore necks of a continuous system or a breakthrough pressure in a discontinuous system can be obtained by monitoring the applied pressures and the corresponding mercury intrusion volumes [40]. A measure of total porosity can also be obtained by means of MIP, that is, by dividing the volume of the mercury intruded at the maximum applied pressure by the bulk volume of the unintruded specimen [40]. *Threshold pore width*, also known as *percolation pore width* or *critical pore width*, is defined as the pore width corresponding to the highest rate of mercury intrusion per change in pressure. MIP may not detect true pore size distribution since mercury may not pass through the narrowest pores. If there exist too small or too isolated pores to be intruded by mercury, it will measure a porosity lower than the actual one.

Cook and Hover [40] used MIP technique to analyze 92 cement paste specimens having w/c ratios ranging from 0.3 to 0.7 at curing times from 1 day to 56 days, and drew the following conclusions:

- Longer curing times and higher w/c ratios result in higher degrees of hydration.
- Longer curing times and lower w/c ratios result in lower porosity and lower threshold pore width values.
- Considering the investigated specimens, lowering the w/c ratio by 0.1 is a more effective method to minimize the threshold pore width and the total MIP porosity than doubling the curing time.

Tortuosity and constrictivity affect the rate of chloride ingress as well as the connectivity of pores. *Tortuosity* is the ratio of the effective travel distance through the pores to the shortest straight flow path, and *constrictivity* is a measure of variations in cross-sectional area of pores (Figure 2.12). They are determined by indirect methods since they cannot be measured directly [150].

Figure 2.12: Schematical View of Tortuosity and Constrictivity [150]

Supplementary cementitious materials alters a pore structure significantly, therefore affects the resistance of concrete to chloride ingress. Streicher and Alexander [154] compared Portland cement mixes with 70% Portland cement + 30% fly ash mixes, and reported that the fly ash mixes yielded a better resistance to chloride ingress. Dhir *et al.* [47, 48, 50] observed that the resistance of concrete to chloride ingress increases with the fly ash content, and that the resistances of air-cured and water-cured concrete specimens approach each other with the increase in their fly ash contents. Yang *et al.* [189, 192] examined a number of concrete specimens containing fly ash and slag, and obtained similar

results. It is worthy to note that the pore structure of a fly ash concrete, which does not necessarily have a lower total porosity than a Portland cement concrete does, has a more discontinuous and tortuous pore network due to the ongoing pozzolanic reactions within the existing pores [47]. Tang and Nilsson [167], and Jensen *et al.* [87, 88] found out that high strength concrete blended with silica fume has a significantly better resistance to chloride ingress than Portland cement concrete does.

2.2.3.2 Interfacial Transition Zone (ITZ)

There exist a zone around an aggregate particle in concrete, referred to as *interfacial transition zone* (ITZ), in which the microstructure of cement paste differs from the microstructure of bulk cement paste (Figure 2.13). It is characterized by a relatively high porosity (Figure 2.14) and coarser pores compared to the ones far away from the aggregate surface. Although the boundary of an ITZ is not definite, it can be thought as a thin shell surrounding the aggregate particle and having a thickness up to 50 μm [15, 123, 146, 147, 149]. The existence of ITZ is attributed primarily to the so-called *wall-effect* [15, 58, 123, 147, 149].

The presence of aggregate disturbs the initial packing characteristics of cement particles, resulting in a looser packing of the cement particles in the immediate vicinity of the aggregate particles. In other words, a gradient of w/c ratio, where w/c ratio decreases with increasing distance from aggregate, develops in the immediate vicinity of each aggregate particle due to the constraints imposed by the surface of an aggregate particle, *i.e.*, wall-effect [15, 58, 123, 147]. The gradient of w/c ratio around an aggregate particle results in a gradient of porosity around the aggregate particle (Figure 2.14).

In addition to the wall-effect, *bleeding*, the accumulation of water beneath aggregate particles during the vibration of fresh concrete, contributes to the formation of ITZs by causing heterogeneity in the w/c ratio gradients around the aggregate particles [15, 26, 37, 123].

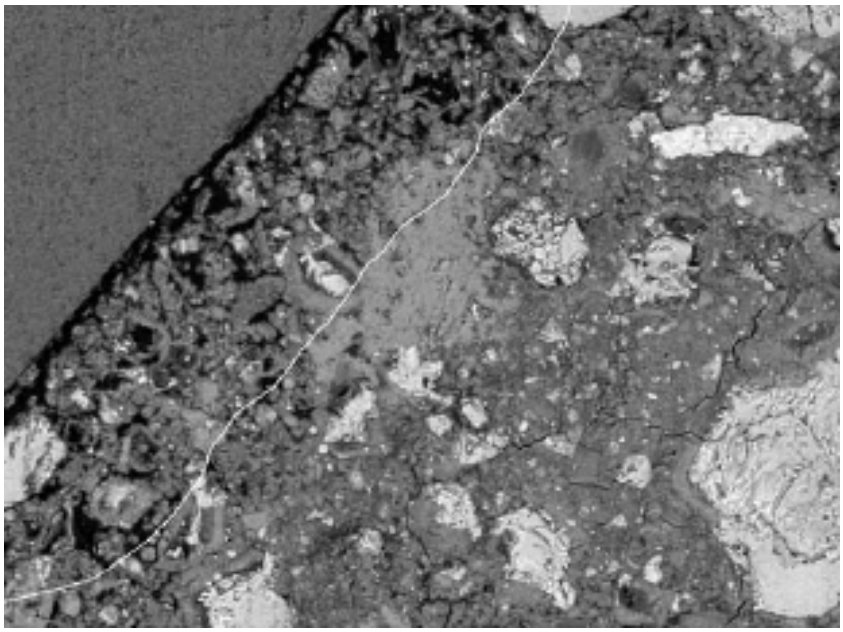

Figure 2.13: ITZ Between Aggregate and Cement Paste [184]

Two common methods for studying ITZ are to use BSE image analysis on polished sections of concrete and to conduct MIP measurements. SEM observations allow to determine porosity, unhydrated cement content and fraction of hydration products as functions of distance to an aggregate surface. However, it is not possible to obtain three-dimensional pore size distribution since the images are two-dimensional. MIP measurements, on the other hand, provide information about pore size distribution. MIP analyses on concrete specimens allow to study the connectivity of ITZs as a function of aggregate volume fraction and particle size distribution.

Laskar *et al.* [99] studied two types of concrete samples that could be used

in MIP analyses: (i) mortar containing coarse aggregate, and (ii) mortar without coarse aggregate. Both types of samples were taken from the same concrete specimen by drilling cores. The cores were crushed, and then the chunks suitable for MIP analyses were selected from the crushed cores. It was observed that mortar containing coarse aggregate was more porous than mortar without coarse aggregate, probably due to the existence of ITZ. Kumar and Bhattacharjee [97] also compared two types of concrete samples that could be used for MIP analyses: (i) concrete chunk samples obtained by crushing large-sized cores, 75 mm in diameter and 100 mm in height, drilled from concrete beams of dimensions $100 \times 200 \times 1000$ mm, and (ii) small cores, 25 mm in diameter and 15-25 mm in height, drilled from the same concrete beams at randomly chosen locations. Although both types of samples yielded similar results, Kumar and Bhattacharjee [97] suggested to use small cores for MIP analyses since they exhibited a lower sample-to-sample variation. It was also suggested that the number of concrete samples used in MIP analyses should be at least six, in order to achieve a reasonable accuracy [97, 99].

Ollivier *et al.* [123] described the microstructure of concrete in terms of its porous microstructure by reviewing two types of studies -SEM using BSE imaging and MIP- carried out to analyze the porosity of its cement paste fraction. The porosity gradients detected in the immediate vicinity of aggregate particles by SEM observations, like the ones shown in Figure 2.14, were accepted as an evidence for the existence of the wall-effect [123]. By reviewing SEM observations and MIP tests, Ollivier *et al.* [123] concluded that (i) the porosity is higher in the ITZ than in the bulk, and (ii) the pores in the ITZ are coarser than the ones in the bulk.

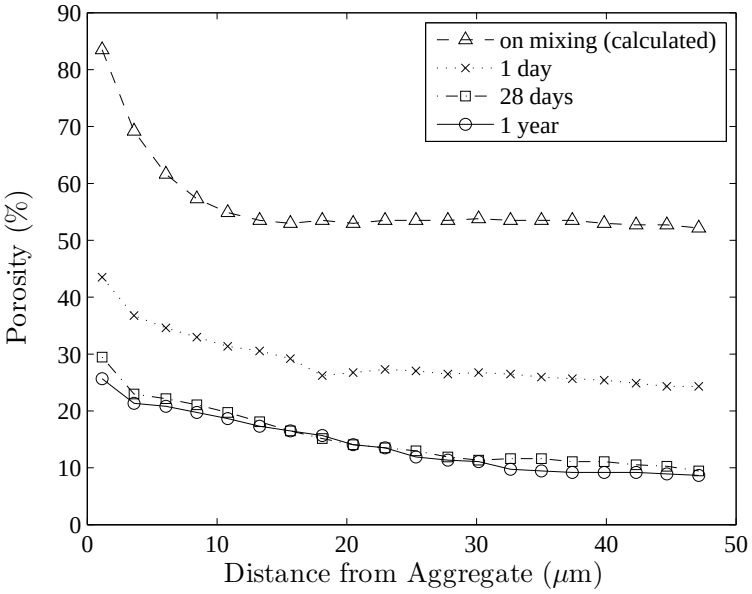

Figure 2.14: Average Porosity in ITZ [149]

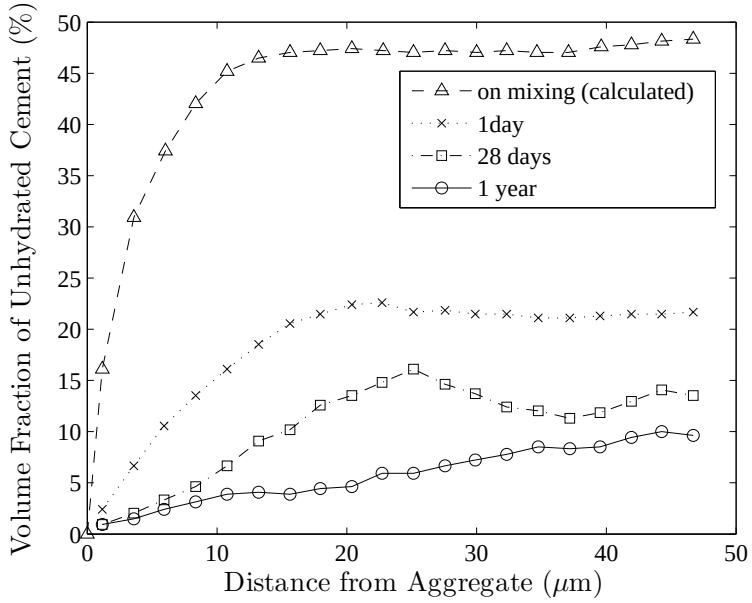

Figure 2.15: Volume Fraction of Unhydrated Cement in ITZ [149]

Scrivener *et al.* [149] studied ITZ in concrete specimens by examining 100 BSE images chosen randomly for each specimen. The fractions of the unhydrated cement and the hydration products, and the porosity were investigated by using 30 bands of about 3 μm width around the aggregate particles. The initial distribution of the unhydrated cement back-calculated from the distribution of the unhydrated cement at one day shows that the wall-effect is effective in a zone of 15 μm adjacent to the aggregate surfaces (Figure 2.15), which is a value close to the average cement particle diameter. There exist small cement particles in the immediate vicinity of the aggregate particles, while larger cement particles are far away from the aggregate particles due to the wall-effect. The width of the zone with a reduced amount of unhydrated cement increases with the age of concrete (Figure 2.15) because small cement particles in the immediate vicinity of the aggregate particles may hydrate completely, while larger cement particles far away from the aggregate has always a greater unhydrated fraction than the small ones do [149].

Ollivier *et al.* [123] and Scrivener *et al.* [149] described the microstructure of concrete also in terms of the progress of hydration. Two major solid hydration products, C-S-H and CH, dominate the microstructural development of concrete. Initially, the concentration of silicate ions, which have relatively low mobility, is low resulting in the deposition of C-S-H around the cement particles, while the concentration of calcium ions, which have relatively high mobility, is high resulting in the deposition of CH in the open pores. Large areas filled with water in the immediate vicinity of the aggregate particles due to the wall-effect, as shown in Figure 2.14 and Figure 2.15, leads to the deposition of more CH in the ITZ compared to the amount of CH in the bulk cement paste (Figure 2.16). Although the ITZ contains more CH than the bulk cement paste does, the

CH deposits in the ITZ are local rather than forming a continuous layer [149]. The distribution of other hydration products -predominantly C-S-H- detected by Scrivener *et al.* [149] is shown in Figure 2.17. As shown in Figure 2.14, even though the rate of change of porosity in the ITZ as a function of distance from aggregate surface decreases with the age of concrete, a porosity gradient can be still observed at an age of one year. The connectivity of the pores in the ITZ can be seen in Figure 2.18, an image of concrete intruded with Wood's metal. Therefore, it can be concluded that ITZ might facilitate transport of chloride through concrete due to the relatively high porosity and the connectivity of pores in the ITZ.

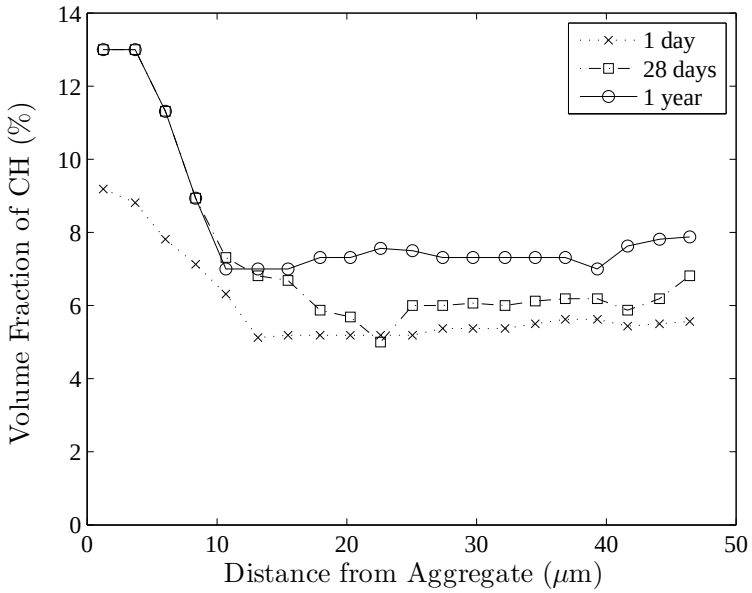

Figure 2.16: Average Distribution of CH in ITZ [149]

Wong and Buenfeld [84, 184, 186] proposed an effective method called Euclidean Distance Mapping (EDM) to analyze the microstructural characteristics of ITZ. The method employs distance transformation to convert a binary image composed of background and foreground pixels into a greyscale image,

where each pixel has a brightness value equal to its linear distance to the nearest background pixel. Then the porosity distribution at any distance from an aggregate surface is obtained by converting the brightness values into the actual distance values. Wong and Buenfeld [184] used this method to examine the microstructural features of ITZ within an ordinary Portland cement concrete with a w/c ratio of 0.4. The porosity and the volume fraction of unhydrated cement as a function of distance from the aggregate surface observed by Wong and Buenfeld [184] is similar to the ones shown in Figure 2.14 and Figure 2.15, respectively. Based on the analyses of BSE images, Wong and Buenfeld [184] detected three types of ITZ as: (i) very porous with a sharp porosity gradient, (ii) denser with large amounts of CH deposited on the aggregate surface, and (iii) a mixture of both.

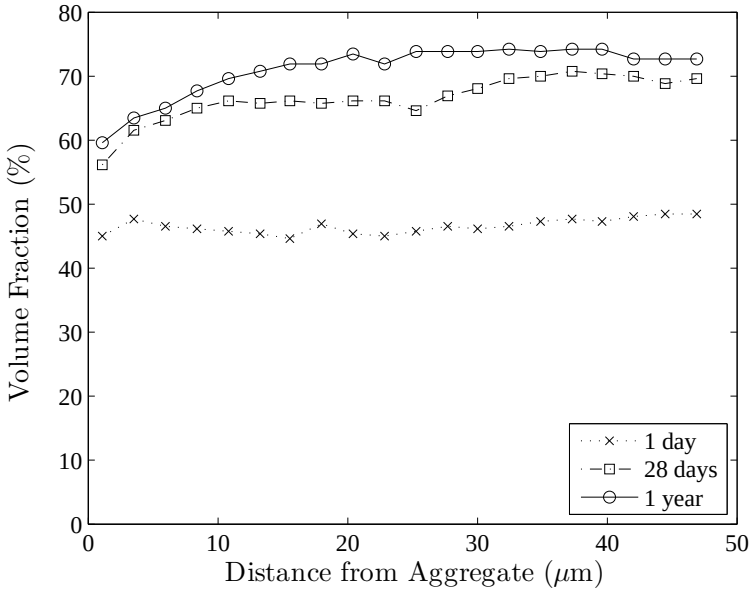

Figure 2.17: Average Distribution of Other Hydration Products [149]

The microstructure of an ITZ can be altered in mainly two ways [123]: (i) adding particles finer than Portland cement particles in order to obtain a dense

packing in the immediate vicinity of aggregate particles, and (ii) modifying the hydration process.

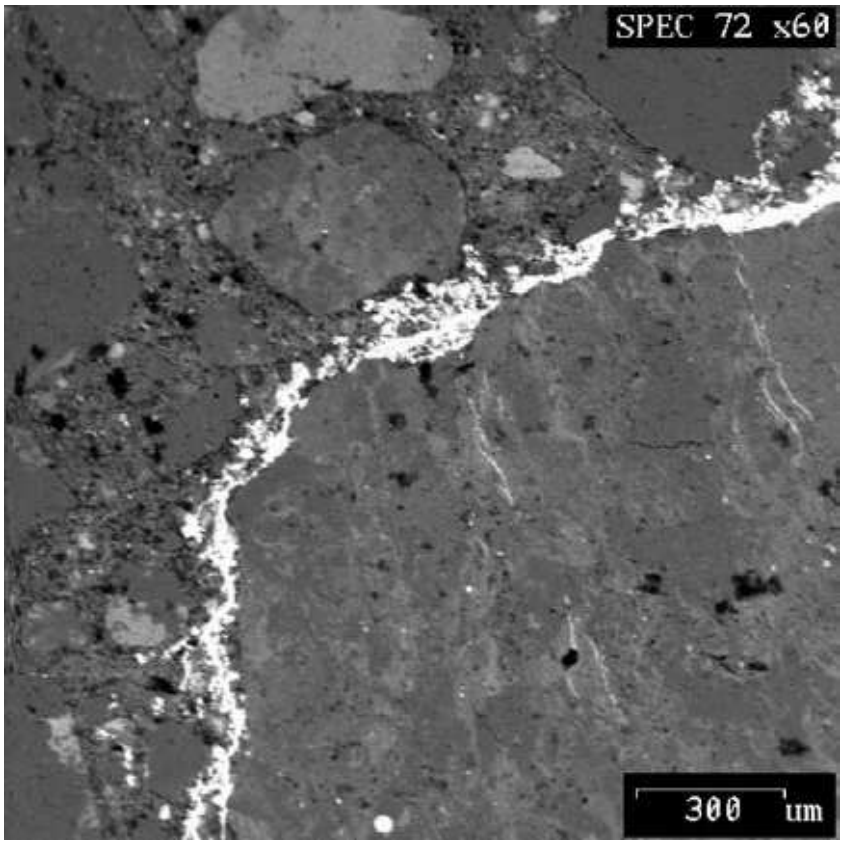

Figure 2.18: Concrete Intruded with Wood's Metal [149]

Supplementary cementitious materials modify the characteristics of ITZs. For instance, the use of silica fume results in a dense packing, thus a reduced porosity, in the immediate vicinity of aggregate particles because (i) silica fume particles fill large voids within an ITZ since they are finer than cement particles, and (ii) they reduce the porosity by producing extra C-S-H by reacting with CH [26]. Goldman and Bentur [73] performed a series of experiments to separate the filler effects and the pozzolanic effects of silica fume on ITZs by replacing silica fume with a non-reactive filler material called carbon black. It was found that the use of silica fume lowers the porosity in the immediate vicinity of the ag-

gregate particles, independent of its pozzolanic effect. This effect of silica fume was considered as a proof of the existence of the wall-effect [73, 123]. Scrivener *et al.* [148] also reported that silica fume leads to a dense packing in the immediate vicinity of the aggregate particles due to its smaller size compared to cement particles.

Chemical reactions between aggregate and cement paste may also affect the microstructure of an ITZ [123, 171, 173]. A beneficial type of such reactions is the one between the calcareous aggregate and the ordinary cement paste. This reaction is limited to the ITZs since the mobility of carbonate ions is low [123].

The thickness of ITZ is related to the range of cement particle size as well as w/c ratio. Ollivier *et al.* [123] had results showing that the thickness of ITZ equals to the mean diameter of cement particles, while Bentz and Garboczi [20] found that it is equal to the median cement particle diameter. On the other hand, Hu and Stroeven [86] pointed out that it depends on the evaluation parameter of interest.

In summary, there exist transition zones of thickness up to 50 μm between aggregate and cement paste, therefore concrete is considered as a three-phase material at microscale. Such zones result from the effect of aggregate particles on the initial packing of cement particles in the immediate vicinity of the aggregate particles. A transition zone is characterized by a relatively high porosity and coarser pores than the ones far away from the aggregate surface. It is important to note that the gradients of porosity, unhydrated cement and solid hydration products in transition zones get less pronounced as the age of concrete increases, due to the ongoing hydration reactions. In conclusion, ITZ is the weakest component of concrete with regard to its resistance to chloride ingress.

2.2.3.3 Simulation of Microstructure

As an alternative to experimental methods, several researchers have developed computer simulation models to help understand the structure of cement paste and/or concrete at microscale. Garbozci and Bentz [61] defined a material model as a theoretical construction that can estimate the structure and the properties of a material quantitatively. The mathematical language used to construct a material model may be in various forms, *e.g.*, a set of deterministic empirical equations obtained from experimental data and a set of differential equations with coefficients obtained from experimental data. A computer simulation returns numerical results for physical quantities of interest by executing the prescribed computer algorithms on numerically or analytically represented system [61].

Garbozci and Bentz [60] developed a computer simulation model, known as the NIST model, to simulate the microstructural development of a cement paste. Portland cement was considered to be composed entirely of C_3S in the original version, but the model was then modified to consider all major phases [16]. Cement particles are represented by circles (or spheres) in a 2D (or 3D) domain of pixels, where each pixel is assigned to a single phase such as water-filled pore space or cement, with periodic boundary conditions. The model executes an iteration of several simple growth rules, which are based more on the physical mechanism of microstructural development than on the chemical mechanism. Each cycle of iteration consists of three steps: dissolution, diffusion and reaction. In the dissolution step, some of the cement pixels in contact with a water-filled pore space pixel start random walks according to a given probability law. For each dissolved cement pixel, extra diffusing pixels are added at random

positions in order to take into account the CH formation and the volume expansion due to the C-S-H formation. The dissolved pixels execute random walks throughout the pore space during the diffusion/reaction steps. When a C-S-H pixel encounters a cement surface or a C-S-H pixel previously stuck to a cement surface, it reacts and sticks to this surface. On the other hand, a diffusing CH pixel can either nucleate at its present location with a nonzero probability, which decreases exponentially as the number of diffusing CH pixels decreases, or stick to a surface of CH cluster if it encounters one of them. Aggregate is assumed to be nonreactive.

Garbozci and Bentz [60] observed that the distributions of porosity, C_3S, CH and C-S-H in the ITZ simulated by the NIST model have a similar trend with the distributions in real concrete, like the ones shown in Figure 2.14 through Figure 2.17, respectively. Bentz and Garbozci [19] studied the effects of w/c ratio and degree of hydration on the evolution of pore structure using the NIST model, and observed a capillary porosity percolation threshold of approximately 18% for the cement pastes simulated from cement particles having only four different sizes. Bentz *et al.* [23] used the NIST model with additional rules to simulate the effects of supplementary cementitious materials, *e.g.*, silica fume and fly ash, and lightweight absorptive aggregate or cement clinker in place of normal weight aggregate on the microstructural development of ITZ, and compared the numerical results with experimental measurements [26]. It was observed that the fine pozzolanic materials, particularly silica fume, improve the physical properties of ITZ microstructure by filling large voids in the immediate vicinity of aggregate particles and producing more C-S-H as a result of their pozzolanic reactions with CH [23, 26]. It was also observed that the use of lightweight absorptive aggregate or cement clinker in place of normal weight aggregate en-

hances the physical properties of ITZ microstructure due to the rearrangement of the cement particles around aggregate particles as a result of water absorption by the lightweight absorptive aggregate or the cement clinker [23].

Bentz [16] improved the NIST model to a three-dimensional cement hydration model, referred to as CEMHYD3D, that considers all major phases. Furthermore, it determines the heat of hydration and the volume reduction resulting from the hydration reactions, and adjusts the densities of C-S-H, ettringite and iron hydroxide to model the experimental data better. In the previous model, all diffusing species have to be reacted before a new dissolution step is started, but CEMHYD3D allows diffusing species to remain in the solution from one step to the next [17]. The reaction rules for each diffusing species can be found elsewhere [16, 17]. CEMHYD3D allows hydration products to grow with a random morphology, but it attempts to make ettringite grow into needle-shaped structures. Bentz [17] showed that the model can predict the hydration kinetics behavior of a cement type with various w/c ratios once a calibration is performed at a single w/c ratio, provided that the cement particle size distribution and the phase distribution of the cement are known. Of the three major sources of error in numerical models -statistical fluctuation, finite size and digital resolution-, Garboczi and Bentz [66] identified the digital resolution as the most important one for their model. Based on a visual comparison of two-dimensional images and a numerical comparison of normalized correlation functions, Bentz [18] reported a good agreement between the microstructures of real and simulated cement pastes. Garboczi and Bentz [66] obtained a capillary porosity percolation threshold of 20-22% with realistic cement particle size distributions by using CEMHYD3D. Bentz *et al.* [21] studied the effect of cement particle size distribution on setting time, heat release during hydration, capillary porosity

connectivity, shrinkage, relative humidity evolution, microstructure of ITZ and chloride diffusivity by using CEMHYD3D. Bentz *et al.* [25] studied the role of silica fume in reducing the diffusivity of tritiated water and chloride in cement pastes, and compared the simulated values obtained by CEMHYD3D with the experimental values. Rémond *et al.* [134, 135] used CEMHYD3D to study the microstructural evolution of cement pastes containing fly ash.

Breugel [177, 178, 179] developed a computer-based cement hydration model, called HYMOSTRUC, to study the microstructural characteristics of cement pastes. In this model, cement particles are represented by spheres placed randomly in a three-dimensional domain. These spheres grow gradually simulating the hydration of cement particles, where it is assumed that particles of the same size hydrate at the same rate. The growing spheres become more and more connected with the continuing hydration, and a porous microstructure is formed eventually. Ye *et al.* [194] simulated two cement pastes with w/c ratios of 0.3 and 0.4 by using the HYMOSTRUC. Then they analyzed the simulated microstructures by using a serial sectioning method, which scans the simulated microstructures from three orthogonal directions layer by layer. Geometrical and topological characteristics of the simulated microstructures were derived by performing calculations on these layers consisting of pixels representing solid or pore phases. The trend of solid phase development obtained by the HYMOSTRUC was similar to the one obtained by the NIST model. However, capillary porosity percolation threshold calculated by the HYMOSTRUC was less than that obtained by the NIST model. The difference results from the different digital resolutions used by the two methods and the different principles employed by the two methods to simulate the hydration process [194].

Gao and Stroeven [58] developed a model, called the *non-placement model*, to simulate the effect of cement particle packing in the vicinity of an aggregate particle. The model assumes that a particle arch structure may be formed near the aggregate surface such that no cement particles can be placed between the aggregate surface and the arch, so that there may occur relatively large spaces near the aggregate surface. Cement particles with random sizes are placed at random locations, and a particle arch will be formed if certain conditions, *e.g.*, the stability of the arch structure, are met.

Stroeven and Stroeven [155, 157, 158, 159] analyzed the characteristics of ITZ by using the Software Package for the Assessment of Compositional Evolution (SPACE), which simulates the production process of composite materials based on a dynamic concept that imitates the production stage of materials. The software models the hydration process of a single cement particle, represented by a sphere, by employing a growth model consisting of two subsequent stages, the details of which can be found elsewhere [157, 158]. The hydration rate is controlled by a phase-boundary mechanism and a diffusion mechanism in the first and second stages, respectively. The wall-effect was simulated for different w/c ratios by using the SPACE, and it was observed that the volume fraction of cement particles decreases as the aggregate surface is approached, which is an evidence for the wall-effect.

2.3 Chloride Diffusion in Concrete

Reinforced concrete structures may deteriorate due to various environmental factors, *e.g.*, chemical attacks and freeze-thawing cycles. Of such factors,

chloride ingress into concrete is of interest to this research, since chloride-induced corrosion of steel reinforcement bars is one of the main causes of deterioration of reinforced concrete structures built in chloride environments.

High alkali environment within concrete encourages the development of a passive (oxide) film around steel reinforcement bars, which protects them against corrosion. As more chloride penetrates concrete, the alkalinity of concrete is reduced. When chloride concentration in a vicinity of a steel bar reaches a critical value, referred to as *chloride threshold value*, the passive film protecting the bar is damaged. Provided that there is adequate oxygen and moisture in the environment, corrosion of the bars initiates leading to cracking, spalling or delamination of the concrete cover since the volume of the corrosion products are several times (2 to 6 times) larger than the volume of the steel lost by corrosion. A secondary effect is reduction in load-carrying capacity of the steel bars, due to loss of cross-sectional area at locations where corrosion takes place.

The sources of chlorides to which reinforced concrete structures are exposed are divided into two main groups [129]:

- Chlorides present in the constituents of concrete, *e.g.*, salty aggregate, salty mixing water and admixtures containing chlorides.
- Chlorides from environmental sources, *e.g.*, seawater, sea spray, de-icing salts and salty groundwater.

There are mainly four groups of chloride transport mechanisms observed in concrete [129]: (i) permeation, (ii) migration, (iii) convection, and (iv) diffusion. Of the four main mechanisms, diffusion is of interest to this research, since it is the most dominant chloride transport mechanism.

Permeation is the movement of water through concrete driven by a hydraulic pressure gradient [129]. The movement is always towards the regions with lower hydraulic pressure. If there exist any chlorides in the permeating water, they are also carried into concrete within the water. Permeability coefficient of a cement paste is determined by the size and the connectivity of pores in the cement paste [109]. As the degree of hydration increases, the porosity of the cement paste decreases, and so does the permeability coefficient. The relationship between the permeability coefficient and the degree of hydration is strong at the beginning of the hydration process. As the large pores are consumed by the hydration products, and the connections between the pores become tortuous, the relationship weakens. Also, a high w/c ratio, especially at a low degree of hydration, results in a high permeability coefficient. In general, the permeability of natural aggregate is lower than the permeability of cement pastes.

Migration is the movement of chloride ions under the influence of an electrical field [129]. Chloride ions always migrate towards the anode. The migration mechanism is exploited in various test methods, which is discussed extensively in Chapter 5, to measure the resistance of cement paste or concrete specimens to chloride ingress.

Convection is the transport of chlorides carried within the water driven by a moisture gradient [129]. Water always moves towards regions with lower moisture content. In partially saturated concrete structures, chloride ingress occurs by convection coupled with diffusion [8, 120]. For example, when a concrete structure is exposed to drying-wetting cycles, *e.g.*, a marine structure under tidal conditions, water will penetrate into the dry regions of concrete carrying chlorides within itself. It is important to note that chloride remains in the structure

when water evaporates. A discussion on chloride accumulation in concrete during alternating wetting-drying cycles can be found elsewhere [115, 116].

Diffusion is the movement of chlorides driven by the chloride concentration gradient. For instance, if a concrete structure is fully submerged in seawater, it is the diffusion that dominates the chloride ingress, unless there is a high pressure head. Chloride diffusion through concrete is usually considered as a Fickean diffusion [8, 129]. The mathematical representation of the Fickean diffusion is given below.

2.3.1 Fick's Law of Diffusion

Fick's diffusion theory assumes that the transport of chloride through a unit area of a section per unit time is proportional to the chloride concentration gradient measured normal to this section. Let $H \subset \mathbb{R}^d$ be a bounded subset containing a heterogeneous medium (*e.g.*, concrete) with a deterministic diffusivity field $D(\boldsymbol{x}) > 0$, $\boldsymbol{x} \in H$. Then Fick's first general law of diffusion [42] states that

$$J_{x_k}(\boldsymbol{x}, t) = -D(\boldsymbol{x}) \frac{\partial C(\boldsymbol{x}, t)}{\partial x_k}, \quad k = 1, \ldots, d, \quad \boldsymbol{x} \in H, \tag{2.3}$$

where $J_{x_k}(\boldsymbol{x}, t)$ and $C(\boldsymbol{x}, t)$ are the chloride flux in the x_k-axis and the chloride concentration at position $\boldsymbol{x}$ and time t, respectively. The negative sign in Eq. 2.3 shows that the diffusion occurs towards the direction along which chloride concentration decreases, that is, the tendency of chloride transport is to diminish the chloride concentration gradient. The mass conservation law requires that the change in the chloride concentration per unit time is equal to the change in

the chloride flux per unit length [42], that is,

$$\frac{\partial C(\boldsymbol{x},t)}{\partial t}+\sum_{k=1}^{d}\frac{\partial J_{x_k}(\boldsymbol{x},t)}{\partial x_k}=0,\quad \boldsymbol{x}\in H,\quad t\geq 0. \tag{2.4}$$

Fick's second general law of diffusion [42] can be obtained by replacing $J_{x_k}(\boldsymbol{x},t)$ in Eq. 2.4 with Eq. 2.3 such that

$$\frac{\partial C(\boldsymbol{x},t)}{\partial t}=\sum_{k=1}^{d}\frac{\partial D(\boldsymbol{x})}{\partial x_k}\frac{\partial C(\boldsymbol{x},t)}{\partial x_k}+D(\boldsymbol{x})\Delta C(\boldsymbol{x},t),\quad \boldsymbol{x}\in H,\quad t\geq 0, \tag{2.5}$$

where $\Delta=\sum_{k=1}^{d}\partial^2/\partial x_k^2$ is the Laplace operator. The chloride concentration at position $\boldsymbol{x}\in H$ and time $t\geq 0$ is completely defined when the initial and boundary conditions are imposed to Eq. 2.5. The methods for solving Eq. 2.5 are discussed in Chapter 3.

2.3.2 Fick's Law of Diffusion with Chloride Binding

Chloride within concrete may exist in the state of either free or bound. The one dissolved in pore solution is called *free chloride*, whereas the one chemically bound to aluminate hydrates forming *Friedel's salt* or physically bound to cement hydrates (adsorbed by C-S-H) are called *bound chloride*. Only the free chloride is responsible for the initiation of corrosion of steel reinforcement since it is the one capable of reducing the alkalinity of concrete. Chloride binding reduces the rate of chloride diffusion through concrete. It is important to note that some of the bound chloride can be released in time due to various factors, *e.g.*, the level of alkalinity and the temperature, resulting in an increase in the free chloride concentration, which in turn increases the risk for corrosion of steel reinforcement [105, 129, 169].

Chloride binding mechanism is affected by many parameters such as composition of pore solution, chloride concentration in pore solution, type of cement, use of supplementary cementitious material(s), type of coexisting cation, type of aggregate and temperature [44, 48, 98, 103, 169, 174]. Delagrave *et al.* [44] reported that using $CaCl_2$ in an experiment instead of NaCl, as well as the use of a saturated lime ($CaOH_2$) solution instead of an alkaline (NaOH + KOH) solution, increases the amount of bound chloride. It was found that chloride binding capacity depends strongly upon the amount of cement gel regardless of the w/c ratio [44, 169]. Larsen [98] showed that the capacity decreases significantly with increasing temperature, and is also reduced in the presence of aggregate.

The relationship between the free and bound chloride concentrations at a given temperature is usually described by chloride binding isotherms. Even though numerous researchers have shown that this relationship is non-linear [44, 72, 105, 169], it has often been assumed as linear for simplicity [111]. The widely used non-linear chloride binding isotherms are Langmuir and Freundlich isotherms, which are said to be good at low and high chloride concentrations, are given by

$$\frac{\partial C_b}{\partial C_f} = \frac{c_\alpha}{(1 + c_\beta C_f)^2}, \tag{2.6}$$

$$\frac{\partial C_b}{\partial C_f} = c_\alpha c_\beta C_f^{c_\beta - 1}, \tag{2.7}$$

respectively [169]. Here, C_f and C_b are the free and bound chloride concentrations, respectively, and, c_α and c_β are empirical constants [169].

Considering the chloride binding effect, Fick's second law can be written as

$$\frac{\partial C_t(\boldsymbol{x}, t)}{\partial t} = \frac{\partial}{\partial \boldsymbol{x}} \left(D(\boldsymbol{x}) \frac{\partial C_f(\boldsymbol{x}, t)}{\partial \boldsymbol{x}} \right), \quad \boldsymbol{x} \in H, \quad t \geq 0, \tag{2.8}$$

where C_t and C_f are the total chloride concentration in per m^3 of concrete and

the free chloride concentration in per m^3 of pore solution, respectively [105]. Since the units of C_t and C_f are different, Eq. 2.8 needs to be rewritten. The relationship between the total, free and bound chloride concentrations is

$$C_t = C_b + w_e C_f, \tag{2.9}$$

where w_e is the evaporable water content of concrete (m^3 evaporable water/m^3 concrete). By applying mass conservation to Eq. 2.9 and then substituting into Eq. 2.8, the modified equation can be written as

$$\frac{\partial C_f(\boldsymbol{x},t)}{\partial t} = \frac{\partial}{\partial \boldsymbol{x}}\left(\tilde{D}(\boldsymbol{x})\frac{\partial C_f(\boldsymbol{x},t)}{\partial \boldsymbol{x}}\right), \quad \boldsymbol{x} \in H, \quad t \geq 0, \tag{2.10}$$

where

$$\tilde{D}(\boldsymbol{x}) = \frac{D(\boldsymbol{x})}{w_e + \frac{\partial C_b}{\partial C_f}}. \tag{2.11}$$

2.4 Parameters Affecting Chloride Diffusivity

Chloride diffusivity in concrete depends on many parameters. Since chloride diffusion occurs mainly through capillary pores in the cement paste [59], the properties of the pore structure have a major effect on the rate of chloride diffusion. The presence of aggregate has two opposite effects on the chloride diffusivity in concrete such that it promotes the resistance of concrete to chloride diffusion by increasing tortuosity and diluting cement paste, while ITZs around the aggregate particles facilitates chloride diffusion through concrete. Furthermore, the interactions -ion/solid interactions, ion/ion interactions and ion/solvent interactions- affect the rate of chloride diffusion. Temperature affects the chloride diffusivity in concrete by both altering the chloride binding capacity and influencing the activation energy of the diffusion process.

2.4.1 Pore Structure

The pore structure in a cement paste consists of capillary pores and gel pores. Since capillary pores are much larger than gel pores, chloride diffusion in concrete occurs mainly through capillary pores. Then capillary porosity, connectivity of capillary pores and threshold pore diameter are of paramount importance with regard to the resistance of concrete to chloride diffusion. The parameters affecting a capillary pore structure, also reviewed briefly below, are discussed in Section 2.2.1.5 and Section 2.2.3.

The resistance of concrete to chloride diffusion increases with decreasing capillary porosity, which is a function of w/c ratio and degree of hydration (Eq. 2.1), that is, capillary porosity increases with w/c ratio, while it decreases as degree of hydration increases (Figure 2.6). Therefore the resistance of concrete to chloride diffusion increases with degree of hydration, while it decreases as w/c ratio increases. Degree of hydration is a function of time, available moisture and temperature, then curing conditions and curing period affect the resistance of concrete to chloride diffusion significantly. Increasing the curing period and/or improving the curing method increase the resistance of concrete to chloride diffusion since they increase degree of hydration [40, 47, 50, 185].

The application of the percolation theory to cement pastes, which explains the development of pore structure, is discussed in Section 2.2.3.1. As the hydration takes place, *i.e.*, degree of hydration increases, capillary pores are blocked with cement gel diminishing the connectivity of capillary pores, which increases the resistance of concrete to chloride diffusion. However, it may not be possible to block all capillary pores with cement gel for high w/c ratios (Table 2.1).

Halamickova *et al.* [82] reported that threshold pore width decreases with the ongoing hydration and it is larger for a mortar specimen than the one for the corresponding neat cement paste specimen. A linear relationship between the threshold pore width and the resistance of concrete to chloride diffusion has been found by various researchers [82, 185, 190].

Supplementary cementitious materials modify pore structures significantly. Streicher and Alexander [154], Dhir *et al.* [47, 48, 50] and Yang *et al.* [189, 192] studied the effect of fly ash and slag on the resistance of concrete to chloride ingress, and found that the resistance increases with the use of fly ash or slag. Dhir *et al.* [47, 48, 50] observed that the chloride diffusion coefficients in both air and moist cured concrete approach each other with increasing fly ash content. It was reported that the use of fly ash also improves the chloride binding capacity of concrete probably due to an increase in more active regions available for binding reactions [47]. It is worthy to note that the pore structure of a fly ash concrete, which does not necessarily have a lower total porosity than an ordinary concrete does, has a more discontinuous and tortuous pore network due to the ongoing pozzolanic reactions within the existing pores [47]. Tang and Nilsson [167], and Jensen *et al.* [87, 88] found out that high strength concrete blended with silica fume has a significantly better resistance to chloride ingress than ordinary concrete does.

2.4.2 Presence of Aggregate

The presence of aggregate causes the existence of interfacial transition zones (ITZ) around the aggregate particles. It is discussed in Section 2.2.3.2 that the

microstructure of ITZ differs from the microstructure of bulk cement paste in an ordinary concrete such that the ITZ has a more porous microstructure and coarser pores than the bulk cement paste does. If there were no ITZ, concrete would certainly have a lower chloride diffusivity than its cement paste fraction, since aggregate particles, unless they are porous, behave as physical barriers against diffusing chloride ions by increasing tortuosity and diluting cement paste. The effect of ITZ on the diffusivity fo chloride in concrete depends on the connectivity of ITZs and how different the microstructures of ITZ and bulk cement paste are [24].

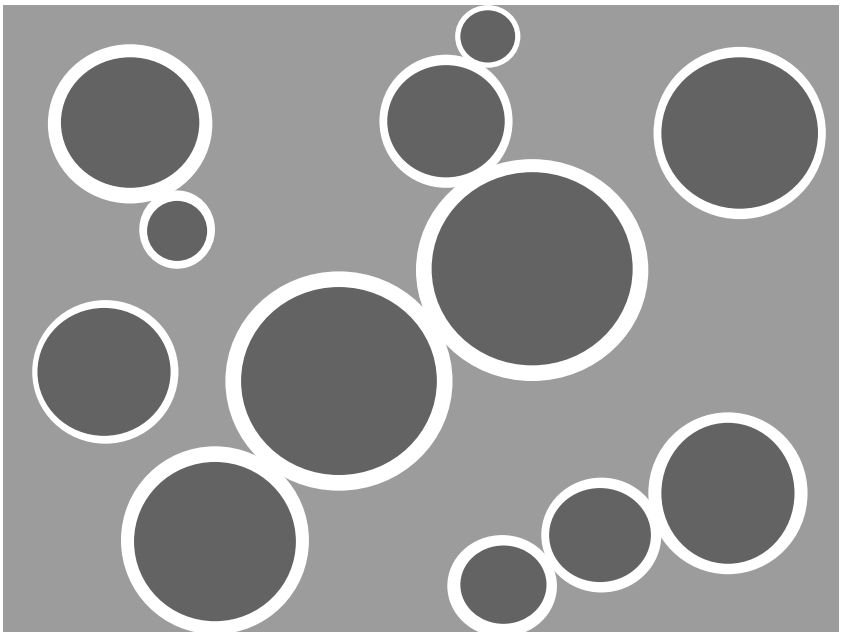

Figure 2.19: Schematical Connectivity of ITZs (represented by white area)

The connectivity of ITZs is a function of volume fraction of aggregate. Winslow *et al.* [183] conducted pore structure analyses on a series of mortar specimens having different sand contents, but a constant w/c ratio of 0.4, by using the MIP technique. A significant difference was observed between the cumulative mercury intrusion curves for sand volume fractions of 45% and 49%,

thus it was concluded that the mortar specimen having a sand volume fraction of 49% had a continuous path, consisting of ITZs, that percolates the specimen.

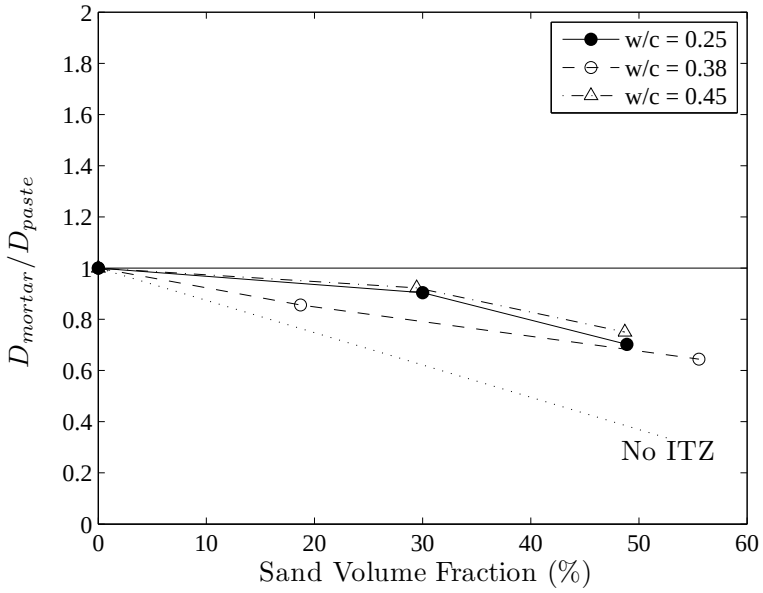

Figure 2.20: Evolution of Diffusivity against Sand Volume Fraction [43]

Delagrave *et al.* [43] and Yang *et al.* [191, 193] studied the effect of ITZ on the chloride diffusivity in mortar. The ratio of the diffusion coefficients in mortar specimens to the ones in the corresponding neat cement pastes, obtained by Delagrave *et al.* [43], is plotted as a function of sand volume fraction in Figure 2.20. The dotted line in Figure 2.20, calculated by Garboczi [68], is the conductivity ratio of mortar to neat cement paste, where there is no ITZ, that is, it represents the effects of tortuosity and dilution.

It can be observed in Figure 2.20 that, for mortar specimens tested by Delagrave *et al.* [43], even though the transport coefficient of cement paste fraction of mortar increases with sand volume fraction probably due to the increased connectivity of ITZs, the reduction in the transport coefficient due to the effects of tortuosity and dilution dominates the overall behavior, resulting in a trans-

port coefficient in mortar lower than the coefficient in the corresponding neat cement paste. Using the numerical model developed by Bourdette *et al.* [27], Delagrave *et al.* [43] found that almost all ITZs in the specimens having sand volume fractions 50% and 57% were connected. Therefore, a continuous path of ITZs percolating a specimen might not be sufficient for the transport coefficient to be higher than the coefficient in the corresponding neat cement paste. Yang *et al.* [191, 193] obtained results similar to those of Delagrave *et al.* [43].

On the other hand, Halamickova *et al.* [82] observed that the chloride diffusion coefficients in mortar specimens, which have almost the same degree of hydration and the same w/c ratio, increase with the volume fraction of sand. The chloride diffusion coefficients in concrete specimens measured by Zhang and Gjørv [197] were higher than the ones in mortar specimens with the same w/c ratio of 0.5. Based on the experiments on mortar specimens with varying sand fractions and a constant w/c ratio of 0.45, Caré [31] observed both cases, that is, an aggregate particle size distribution resulted in a lower chloride diffusivity than the one in the neat cement paste specimen, while the other two distributions caused a higher value. Therefore, the effect of ITZ on the chloride diffusivity in mortar/concrete depends on not only the connectivity of ITZs, but also the ratio of the chloride diffusivity in the ITZ to the diffusivity in the bulk cement paste. Based on their simulations on computational concrete volumes, Garboczi *et al.* [68, 145] concluded that how much the chloride diffusivity in concrete is affected by ITZ is determined by the the ratio of the chloride diffusivity in the ITZ to the one in the bulk cement paste.

In conclusion, there are two opposite effects of the presence of aggregate competing with each other [31, 43, 63, 102, 193]:

- The presence of aggregate tends to reduce the chloride diffusivity in concrete by increasing the tortuosity, which makes diffusing chloride ions travel along longer paths, combined with a volumetric dilution effect.
- The connectivity of ITZs tends to increase the chloride diffusivity in concrete by forming a continuous path along which chloride ions can travel faster. The effect of ITZ depends on the ratio of the chloride diffusivity in the ITZ to that in the bulk cement paste.

An important property of aggregate that may affect the chloride diffusivity in concrete is aggregate porosity. Price *et al.* [132] studied the effects of aggregate porosity on the chloride diffusivity in concrete by testing a series of concrete specimens manufactured from various cement types and natural aggregate with varying water absorption capacities. It was observed that the increase in the chloride diffusivity due to the use of high absorption aggregate in place of low absorption aggregate at a fixed w/c ratio was higher than the increase due to a change in w/c ratio from 0.4 to 0.5. The probable reason for the increase due to the use of high absorption aggregate is continuous pores existing within the aggregate particles that would provide relatively short paths for chloride ions to travel along.

2.4.3 Surface Interactions and Characteristics of Solution

From an electrochemical point of view, chloride transport in concrete is affected by various interactions such as ion/solid interactions, ion/ion interactions and ion/solvent interactions, therefore, the ionic diffusivity depends on the ionic concentration in the pore solution [199, 201].

An *electrical double layer*, a common phenomenon to all solid-electrolytic solution systems, forms on the capillary pore walls of the concrete whose pores are filled up with a chloride containing electrolyte solution [103, 199]. Surface potential, determined by the adsorbed ions, decreases along the direction away from the pore wall according to the properties of pore solution. The repulsion/attraction forces between the electrical double layer and the ions present in the pore solution influence the movement of the ions. For a given capillary pore size, a minimum concentration is required for the ions to diffuse in. In other words, for a given concentration, the ions can only diffuse in the capillary pores over a certain size. Zhang and Gjørv [199] considered this effect of electrical double layer as one of the possible reasons of the increase in the resistance of concrete to chloride ingress due to the use of silica fume and/or blast furnace slag.

Page *et al.* [118, 195] suggested that the surface interactions between pore walls and pore solution may influence the rate of chloride diffusion in cement pastes by observing the differences between the activation energies for chloride diffusion in cement pastes and in simple aqueous electrolytes. In order to examine the effect of surface interactions on the rate of chloride diffusion, a series of experiments was conducted to measure the chloride and oxygen diffusivities in cement paste specimens [32, 118, 195]. The reason for selecting oxygen was that it has a similar diffusion coefficient to that of chloride in infinitely dilute solutions, and that it is not affected by surface interactions since it is a neutral molecule. It was observed that the ratio of oxygen to chloride diffusion coefficients increases as the w/c ratio decreases, which supports their suggestion that the surface interactions affects the rate of chloride diffusion in cement pastes [32, 118, 195].

Another type of interaction in pore solutions is the one between the ions present in the solutions. During a diffusion process in an electrolytic solution, the faster ions slow down and the slower ions accelerate due to the conservation of electroneutrality [103, 139]. Hence, the rate of chloride diffusion is affected by *ion/ion interaction* in order to preserve the local electroneutrality at any point in the pore solution of concrete. This interaction results in retardation of drift velocity of the chloride ions [103, 139, 199]. The effect of ion/ion interaction gets more pronounced as the concentration in pore solution increases since the distances between the ions decrease [103, 139]. Another interaction decreasing the ionic mobility is ion/solvent interaction, which is the tendency of ions moving in a solution to drag numerous solvent molecules with them [139].

The chemical potential of a diffusing species, driven by the gradient of its chemical potential, in an electrolytic solution needs a correction factor, referred to as *activity coefficient*, which is equal to unity for an infinite dilute solution [103, 139, 199], so the diffusion coefficient of the diffusing species depends on its activity coefficient for the solution in which it diffuses. In electrolytic solutions, ionic interaction is responsible for the decrease in the chemical potential of the diffusing species, thus the decrease in its diffusion coefficient [103, 139, 199]. Therefore, the chloride diffusion coefficient in concrete decreases as the concentration in the pore solution of concrete increases, due to the effect of ionic interaction. Zhang [201] noted that the various interaction mechanisms affecting the chloride diffusivity lose their sensitivities to the chloride concentration level with the increasing chloride concentration.

2.4.4 Temperature

Temperature has two main effects on the chloride diffusivity in concrete [88, 187]. First, it alters the chloride binding capacity of cement paste fraction, as explained in Section 2.3.2. Second, it increases the frequency of thermal vibrations of the chloride ions. The second effect can be taken into account by Arrhenius equation given as

$$D_{T_c} = D_{T_r} \exp\left[\frac{U_{\text{act}}}{R}\left(\frac{1}{T_r} - \frac{1}{T_c}\right)\right], \tag{2.12}$$

where T_c and T_r are the current and reference absolute temperatures, respectively, D_{T_c} is the chloride diffusivity at temperature T_c, D_{T_r} is the known chloride diffusivity at temperature T_r, U_{act} is the activation energy of the diffusion process and R is the universal gas constant. The rate of chloride diffusion increases with temperature [87, 88, 141, 187].

2.5 Summary

Reinforced concrete is the most common structural material throughout the world since it is strong, durable and relatively cheap. Of the deterioration mechanisms of reinforced concrete structures, chloride ingress into concrete is of interest to this research, since numerous reinforced concrete structures suffer from chloride-induced corrosion of steel reinforcement. The resistance of a reinforced concrete structure to chloride ingress is provided by the concrete, which behaves as a physical and a chemical barrier protecting the steel reinforcement. Modern concrete is made of Portland cement, supplementary cementitious material(s),

water and aggregate. Chemical admixtures are sometimes used to enhance certain properties of concrete.

Concrete is a random heterogeneous material. It is usually considered as a three-phase material -cement paste, aggregate and transition zones between cement paste and aggregate particles- at microscale. Studying the microstructure of concrete provides a better understanding of its transport properties. Researches on the microstructure of concrete revealed that there may exist a zone up to 50 μm around an aggregate particle, in which the microstructure of cement paste differs from the microstructure far away from the aggregate surface. Such a zone, referred to as interfacial transition zone (ITZ), around an aggregate particle has a relatively high porosity and coarser pores than the ones far away from the aggregate surface. The primary reason of ITZ formation is wall-effect, the effect of aggregate particles on the initial packing of cement particles in the immediate vicinity of aggregate particles.

The two main chloride sources are the constituents of concrete, *e.g.*, salty aggregate particles and salty mixing water, and the environmental sources such as seawater or de-icing salts. Steel reinforcement is protected against corrosion by a passive film encouraged by the high alkali environment within concrete. When the chloride concentration in the near vicinity of steel reinforcement bars exceeds a certain value, the passive film is removed, and the corrosion of steel reinforcement bars initiates, provided that there is enough oxygen and moisture. Therefore, the resistance of concrete to chloride ingress is of great importance to the durability of a reinforced concrete structure.

Of the four main types of chloride transport mechanisms -permeation, migration, convection and diffusion- observed in concrete, diffusion is of interest

to this research, since it is the most dominant mechanism. Chloride diffusion in concrete is usually described by Fick's laws of diffusion. Chloride exists in concrete as either free or bound. Only the free chloride can initiate the corrosion of steel reinforcement bars since it is the one capable of reaching the bars. Therefore, chloride binding capacity is of great importance with regard to the rate of chloride ingress. The relationship between the free and bound chloride is represented by either a linear isotherm or a non-linear isotherm, *e.g.*, Langmuir or Freundlich.

Chloride diffusion in concrete is affected by many factors. Since diffusion takes place mainly through capillary pores in the cement paste, the parameters characterizing a pore structure such as capillary porosity, connectivity of capillary pores, threshold pore width, tortuosity and constrictivity, and the parameters affecting the development of a pore structure, such as w/c ratio, degree of hydration, volume fraction of aggregate, and curing conditions, influence the resistance of concrete to chloride diffusion. The presence of aggregate has two opposite effects on the rate of chloride diffusion such that the connectivity of ITZs tends to increase the rate of chloride diffusion by forming a continuous path along which chlorides can travel faster, while the presence of aggregate tends to reduce the rate of chloride diffusion by increasing the tortuosity, which makes chloride ions travel along longer paths, combined with a volumetric dilution effect. The effect of ITZ on the chloride diffusivity in concrete depends on the ratio of the chloride diffusivity in the ITZ to that in the bulk cement paste. The use of porous aggregate particles results in a significant increase in the rate of chloride diffusion. The formation of electrical double layers, ion/ion interactions and ion/solvent interactions decrease the rate of chloride diffusion in concrete, implying that the chloride diffusivity in concrete depends on the ionic

concentration in its pore solution. Temperature increases the rate of chloride diffusion within concrete by affecting both the chloride binding capacity of cement paste and the activation energy of the chloride diffusion process.

CHAPTER 3

LOCAL SOLUTION METHOD

3.1 Introduction

A large number of reinforced concrete structures is exposed to chlorides, which may initiate corrosion of reinforcing steel bars in a structure, thus endanger the serviceability of the structure, due to several reasons, *e.g.*, marine environment or de-icing salts [129]. Of the four main chloride ingress mechanisms in concrete, *i.e.*, diffusion, permeation, migration, and convection, chloride transport by diffusion is studied in this research. Diffusion of chlorides in concrete has been considered as a Fickean diffusion process [8, 129].

Fick's law of diffusion that describes chloride diffusion within a bounded subset $H \subset \mathbb{R}^d$ containing a heterogeneous medium (*e.g.*, concrete) with a deterministic chloride diffusivity field $D(\boldsymbol{x}) > 0$, $\boldsymbol{x} \in H$, is given in Section 2.3.1 as

$$\frac{\partial C(\boldsymbol{x},t)}{\partial t} = \sum_{k=1}^{d} \frac{\partial D(\boldsymbol{x})}{\partial x_k} \frac{\partial C(\boldsymbol{x},t)}{\partial x_k} + D(\boldsymbol{x}) \Delta C(\boldsymbol{x},t), \quad \boldsymbol{x} \in H, \quad t \geq 0, \tag{2.5}$$

where $C(\boldsymbol{x},t)$ is the chloride concentration at position $\boldsymbol{x}$ and time t, and $\Delta = \sum_{k=1}^{d} \partial^2/\partial x_k^2$ is the Laplace operator. If there exists an additional chloride source within concrete, *e.g.*, salty aggregates, an additional term associated with this source is added to the right-hand-side of Eq. 2.5. Then the chloride concentration at position $\boldsymbol{x} \in H$ and time $t \geq 0$ is defined by

$$\frac{\partial C(\boldsymbol{x},t)}{\partial t} = \sum_{k=1}^{d} \frac{\partial D(\boldsymbol{x})}{\partial x_k} \frac{\partial C(\boldsymbol{x},t)}{\partial x_k} + D(\boldsymbol{x}) \Delta C(\boldsymbol{x},t) + \gamma(\boldsymbol{x},t) \tag{3.1}$$

with the initial and boundary conditions

$$C(\boldsymbol{x}, 0) = \eta(\boldsymbol{x}), \quad \boldsymbol{x} \in H, \tag{3.2}$$

$$C(\boldsymbol{x}, t) = \xi(\boldsymbol{x}, t), \quad \boldsymbol{x} \in \partial H, \quad t > 0, \tag{3.3}$$

respectively, where $\gamma(\boldsymbol{x}, t)$ represents the chloride flux at $(\boldsymbol{x}, t) \in H \times [0, \infty)$ associated with the additional chloride source, η and ξ are $\mathbb{R}$-valued prescribed functions, and ∂H denotes the boundary of H.

If $\gamma(\boldsymbol{x}, t) = \gamma(\boldsymbol{x})$ is time-invariant and Eq. 3.1 admits a steady-state solution $C(\boldsymbol{x}) = \lim_{t\to\infty} C(\boldsymbol{x}, t)$, then $C(\boldsymbol{x})$ is defined by

$$\sum_{k=1}^{d} \frac{\partial D(\boldsymbol{x})}{\partial x_k} \frac{\partial C(\boldsymbol{x})}{\partial x_k} + D(\boldsymbol{x}) \Delta C(\boldsymbol{x}) = -\gamma(\boldsymbol{x}), \quad \boldsymbol{x} \in H, \tag{3.4}$$

with the boundary condition

$$C(\boldsymbol{x}) = \xi(\boldsymbol{x}), \quad \boldsymbol{x} \in \partial H. \tag{3.5}$$

Boundary conditions can be of the Dirichlet and/or Neumann type. Eqs. 3.3 and 3.5 are the Dirichlet type of boundary conditions. In case of mixed boundary conditions, Dirichlet and Neumann boundary conditions on ∂H_d and ∂H_n, respectively, where $\partial H_d \cup \partial H_n = \partial H$ and $\partial H_d \cap \partial H_n = \emptyset$, are given by

$$C(\boldsymbol{x}, t) = \xi_d(\boldsymbol{x}, t), \quad \boldsymbol{x} \in \partial H_d, \quad t > 0, \tag{3.6a}$$

$$\nabla C(\boldsymbol{x}, t) \cdot \boldsymbol{u}(\boldsymbol{x}, t) = \xi_n(\boldsymbol{x}, t), \quad \boldsymbol{x} \in \partial H_n, \quad t > 0, \tag{3.6b}$$

for time-dependent case, where $\boldsymbol{u}$ and ξ_d, ξ_n are $\mathbb{R}^d$- and $\mathbb{R}$-valued prescribed functions, respectively, and ∇ is the gradient operator. For time-independent case, they are given as

$$C(\boldsymbol{x}) = \xi_d(\boldsymbol{x}), \quad \boldsymbol{x} \in \partial H_d, \tag{3.7a}$$

$$\nabla C(\boldsymbol{x}) \cdot \boldsymbol{u}(\boldsymbol{x}) = \xi_n(\boldsymbol{x}), \quad \boldsymbol{x} \in \partial H_n. \tag{3.7b}$$

Concrete specimens modeled in this research have either surfaces subjected to a chloride field or sealed surfaces. A surface subjected to a chloride field is described as the Dirichlet type boundary since the chloride concentration on this boundary is known. On the other hand, the chloride concentration at a sealed surface is not known, but the gradient of chloride concentration normal to this surface is assumed to be zero. Therefore, the sealed surfaces are described as the Neumann type boundaries.

One of the main objectives of this research is to calculate the chloride concentration at one or a few points in a concrete specimen, *e.g.*, at location of steel bars. Since it is not possible to solve Eqs. 3.1 and 3.4 analytically except for few simple cases, numerical methods have been used to solve these equations approximately. Two types of methods can be used to achieve this objective:

- Global methods, *e.g.*, finite element and finite difference methods.
- Local methods, *e.g.*, fixed and floating random walk methods.

Classical global methods are reviewed briefly below since detailed discussions can be found elsewhere. Then a review of local methods is given. Next, the essentials of the local method used in this study are given, and the application of the local method is illustrated.

3.2 Global Methods

The methods which give a field solution, *i.e.*, a solution over the entire domain of interest, are classified as global methods. The solution returned by

global methods is always an approximation to the exact solution because of the discretization of space and time domains. Two well-known classical global methods are finite element method (FEM) and finite difference method (FDM).

3.2.1 Finite Element Method (FEM)

FEM discretizes the domain of interest into small pieces called *finite elements*, a particular arrangement of which is called a *mesh*. A collection of finite elements assembled to each other at points called *nodes* is a *finite element structure*.

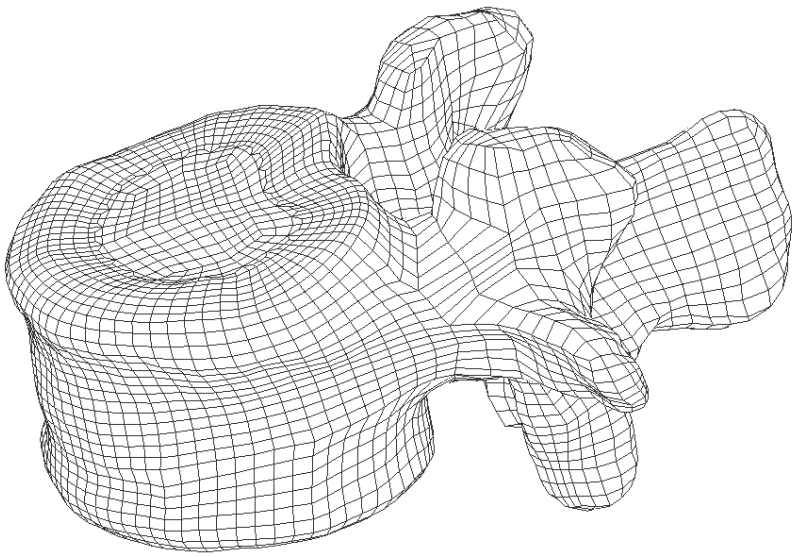

Figure 3.1: FE Structure of an Arbitrarily Shaped Body

Chloride concentration within a finite element is allowed to have a simple spatial variation, generally described by polynomials. For a steady-state solution, a system of algebraic equations is derived according to a prescribed mesh. The system of equations can be solved for values of chloride concentration at nodes by imposing boundary conditions. Chloride concentration over a finite

element is completely described by the nodal values of chloride concentration combined with the presumed variation of chloride concentration within the element, so that the chloride concentration field over the entire domain is approximated element by element. The accuracy of the approximation depends on the quality and the number of finite elements.

If chloride concentration depends on time, a similar approach is used but a time integration scheme is implemented. For a time-dependent solution, initial conditions should be imposed in addition to boundary conditions. For instance, Martín-Pérez *et al.* [104] proposed a 2D finite element formulation for solving transport of chlorides, moisture, oxygen and heat convection through concrete, which is a coupled boundary-initial value problem describing the corrosion of steel reinforcement in concrete.

FEM has been widely used in engineering analyses because of its advantages over the other methods [41]. First, it can be applied to any field problem. Second, it has no restrictions on geometrical properties, boundary conditions or loading. Third, material properties can be changed from one element to another or within an element. Fourth, it allows to have different grades of mesh at different regions that enables the use of finer mesh at critical regions. In addition to those, it can also be used in parallel computing [161]. On the other hand, it requires relatively complex computer codes or commercial softwares. Furthermore, a stability problem may arise unless the space and time domains are discretized properly.

3.2.2 Finite Difference Method (FDM)

FDM replaces derivatives of the unknown functions in governing differential equations with finite difference approximations [14, 36]. The domain of interest is treated as a grid of discrete points called *nodes*.

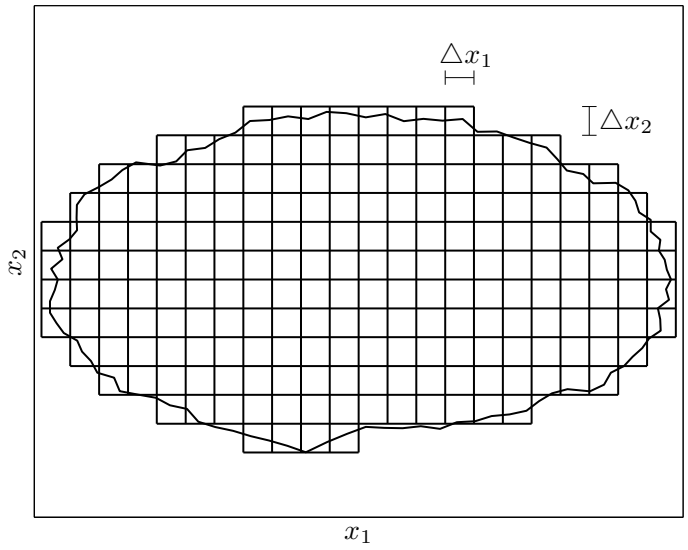

Figure 3.2: FD Representation of an Arbitrarily Shaped Domain

After H is transformed into a grid of nodes (Figure 3.2), finite difference approximations based on this grid are substituted for the partial derivatives of chloride concentration in Eqs. 3.1 and 3.4. Then a system of algebraic equations is derived, where the unknowns are the chloride concentrations at nodes. The nodal values of chloride concentration are obtained by solving the system of equations for the given initial and boundary conditions. Grid spacing and type of finite difference approximation, *e.g.*, forward difference, central difference, *etc.*, affect the accuracy of the approximation significantly.

The finite difference representation of Eq. 3.1 at an arbitrary node $\boldsymbol{x} \in H \subset$

$\mathbb{R}^2$ and time $t > 0$ is

$$\begin{aligned}\frac{C(\boldsymbol{x}, t+\triangle t) - C(\boldsymbol{x}, t)}{\triangle t} &= \frac{\partial D(\boldsymbol{x})}{\partial x_1}\frac{C(x_1+h, x_2, t) - C(x_1-h, x_2, t)}{2h} \\ &+ \frac{\partial D(\boldsymbol{x})}{\partial x_2}\frac{C(x_1, x_2+h, t) - C(x_1, x_2-h, t)}{2h} \\ &+ D(\boldsymbol{x})\frac{C(x_1+h, x_2, t) - 2C(\boldsymbol{x}, t) + C(x_1-h, x_2, t)}{h^2} \\ &+ D(\boldsymbol{x})\frac{C(x_1, x_2+h, t) - 2C(\boldsymbol{x}, t) + C(x_1, x_2-h, t)}{h^2} \\ &+ \gamma(\boldsymbol{x}, t) \end{aligned} \tag{3.8}$$

for the mesh in Figure 3.2 with grid spacing $\triangle x_1 = \triangle x_2 = h > 0$.

Similarly, the finite difference representation of Eq. 3.4 at an arbitrary node $\boldsymbol{x} \in H \subset \mathbb{R}^2$ is

$$\begin{aligned}&\frac{\partial D(\boldsymbol{x})}{\partial x_1}\frac{C(x_1+h, x_2) - C(x_1-h, x_2)}{2h} + \frac{\partial D(\boldsymbol{x})}{\partial x_2}\frac{C(x_1, x_2+h) - C(x_1, x_2-h)}{2h} \\ &+ D(\boldsymbol{x})\frac{C(x_1+h, x_2) - 2C(\boldsymbol{x}) + C(x_1-h, x_2)}{h^2} \\ &+ D(\boldsymbol{x})\frac{C(x_1, x_2+h) - 2C(\boldsymbol{x}) + C(x_1, x_2-h)}{h^2} = -\gamma(\boldsymbol{x}). \end{aligned} \tag{3.9}$$

A notable difficulty with the implementation of FDM relates to boundary conditions since the nodes of the meshed version of H may not belong to ∂H unless H is a rectangular domain. Moreover, there might be stability issues if grid spacing and time increment are not chosen properly.

3.3 Local Methods

Global methods provide approximate field solutions. However, it is not worthy to use a global method if only a particular region of H is of interest. In such

a case, local methods are more efficient than global methods since they are able to provide solutions only at points of interest.

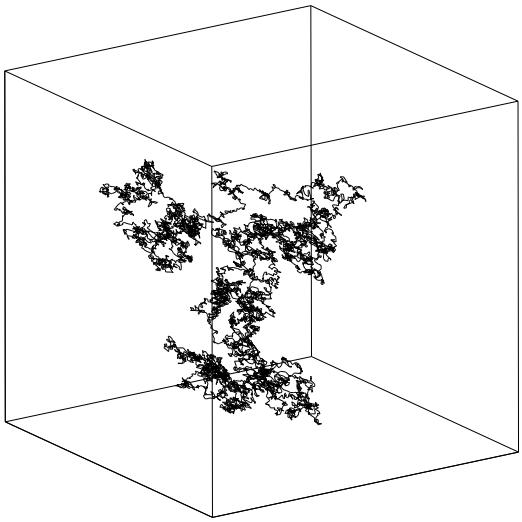

Figure 3.3: A Random Walk in Three Dimensions

Local methods generally employ Monte Carlo simulations for obtaining a solution. The primary component of Monte Carlo algorithms is *random walk*. In the simplest sense, a random walk is composed of successive steps, each of which is taken in a random direction (Figure 3.3). The steps of a random walk is a sequence of independent and identically distributed random variables. For example, the path traced by a molecule while it travels in a fluid can be thought of as a random walk.

The general idea of Monte Carlo algorithms is the following. Random walks are started at a point where the solution is needed. The walks are terminated at either space or time boundaries. The exit points are recorded for each random walk. The solution can be obtained by using these exit points.

Two types of random walk methods are reviewed. The first has a fixed step size and its paths belong to a preset graph. The second has varying step size and paths. Then the random walk method used in this study is presented.

For simplicity, a homogeneous medium in 2D with the Dirichlet boundary conditions is considered in the review of random walk methods. Let $H^* \subset \mathbb{R}^2$ be a bounded subset containing a homogeneous medium with a deterministic chloride diffusivity field $D^* > 0$ and ∂H^* denote the boundary of H^*. Since D^* is constant over H^*, the partial derivatives of the chloride diffusivity field in Eqs. 3.1 and 3.4 vanish.

3.3.1 Fixed Random Walk Method

The classical random walk moves on a grid of nodes similar to that used in a FDM, so it has a fixed step size and its paths belong to a preset graph, and is called *fixed random walk*. The Monte Carlo algorithm employing fixed random walks is based on a finite difference representation of the partial differential equation of interest, like the one given in Eq. 3.8 or Eq. 3.9 by the FDM [81, 92, 136].

Let chloride concentration over H^* be dependent on time and $\gamma(\boldsymbol{x}, t) = 0$, $\boldsymbol{x} \in H^*, t \geq 0$. Then the finite difference representation of chloride concentration at an arbitrary node $\boldsymbol{x} \in H^*$ and time $t + \triangle t > 0$ is given by

$$\begin{aligned} C(\boldsymbol{x}, t + \triangle t) = \frac{D^* \triangle t}{h^2} & [C(x_1 + h, x_2, t) + C(x_1 - h, x_2, t) \\ & + C(x_1, x_2 + h, t) + C(x_1, x_2 - h, t)] \\ & + \left(1 - 4\frac{D^* \triangle t}{h^2}\right) C(\boldsymbol{x}, t), \end{aligned} \tag{3.10}$$

where the initial and boundary conditions are

$$C(\boldsymbol{x}, 0) = \eta(\boldsymbol{x}), \quad \boldsymbol{x} \in H^*, \tag{3.11}$$

$$C(\boldsymbol{x}, t) = \xi(\boldsymbol{x}, t), \quad \boldsymbol{x} \in \partial H^*, \quad t > 0, \tag{3.12}$$

respectively. If $D^* \triangle t / h^2$ is set to $1/4$, the last term in Eq. 3.10 vanishes. Then Eq. 3.10 can be interpreted such that a random walk at node $\boldsymbol{x}$ has an equal probability of stepping to one of the four neighboring nodes during a time $\triangle t$.

Suppose that the chloride concentration at node $\boldsymbol{x}_0 \in H^*$ and time $t_0 > 0$ is needed. The following Monte Carlo algorithm can be used to estimate the chloride concentration at $(\boldsymbol{x}_0, t_0)$. A random walk is started at $(\boldsymbol{x}_0, t_0)$, and moves to one of the neighboring nodes according to the value of a random number drawn from a uniform distribution on (0,1). At each step, time proceeds backwards by an amount of $\triangle t$ (see Eq. 3.23 in Section 3.3.4.2). The walk is terminated when either it arrives at a boundary node $\boldsymbol{x}_\xi \in \partial H^*$ at $t > 0$ or $t = 0$ before it reaches ∂H^*. If the walk is terminated at a boundary node $\boldsymbol{x}_\xi$, the chloride concentration at $\boldsymbol{x}_\xi$ is recorded as $C(\boldsymbol{x}_0, t_0, \omega) = \xi(\boldsymbol{x}_\xi, t_\xi)$, $\omega = 1, \ldots, n_s$, where n_s is the number of random walk samples and $t_\xi > 0$ is the time that the random walk arrives at $\boldsymbol{x}_\xi$. If the walk is terminated when $t = 0$, it is still at an interior node $\boldsymbol{x}_\eta \in H^*$ and the initial chloride concentration at $\boldsymbol{x}_\eta$ is recorded as $C(\boldsymbol{x}_0, t_0, \omega) = \eta(\boldsymbol{x}_\eta)$. After n_s random walks are executed, the chloride concentration at $(\boldsymbol{x}_0, t_0)$ is estimated by

$$\hat{C}(\boldsymbol{x}_0, t_0) = \frac{1}{n_s} \sum_{\omega=1}^{n_s} C(\boldsymbol{x}_0, t_0, \omega). \tag{3.13}$$

If chloride concentration over H^* is time-invariant and $\gamma(\boldsymbol{x}) \neq 0$, $\boldsymbol{x} \in H^*$, the

finite difference representation of $C(\boldsymbol{x})$ is

$$C(\boldsymbol{x}) = \frac{1}{4}\, C(x_1 + h, x_2) + \frac{1}{4} C(x_1 - h, x_2) + \frac{1}{4} C(x_1, x_2 + h) + \frac{1}{4} C(x_1, x_2 - h) + \frac{h^2 \gamma(\boldsymbol{x})}{4D^*}, \tag{3.14}$$

where the boundary condition is

$$C(\boldsymbol{x}) = \xi(\boldsymbol{x}), \quad \boldsymbol{x} \in \partial H^*. \tag{3.15}$$

Then the chloride concentration at node $\boldsymbol{x}_0 \in H^*$ can be estimated by starting n_s random walks at $\boldsymbol{x}_0$. To take into account the contribution of $\gamma(\boldsymbol{x})$, $C(\boldsymbol{x}_0, \omega)$ is set to zero at start and updated as

$$C(\boldsymbol{x}_0, \omega) = C(\boldsymbol{x}_0, \omega) + \frac{h^2 \gamma(\boldsymbol{x})}{4D^*}, \quad \boldsymbol{x} \in H^*, \quad \omega = 1, \ldots, n_s, \tag{3.16}$$

at each step. A random walk is terminated when it arrives at a boundary node $\boldsymbol{x}_\xi \in \partial H^*$ and $C(\boldsymbol{x}_0, \omega)$ is updated as $C(\boldsymbol{x}_0, \omega) = C(\boldsymbol{x}_0, \omega) + \xi(\boldsymbol{x}_\xi)$. After n_s random walks are executed, the chloride concentration at $\boldsymbol{x}_0$ is estimated by

$$\hat{C}(\boldsymbol{x}_0) = \frac{1}{n_s} \sum_{\omega=1}^{n_s} C(\boldsymbol{x}_0, \omega). \tag{3.17}$$

As $n_s \uparrow \infty$, $\hat{C}(\boldsymbol{x}_0, t_0)$ and $\hat{C}(\boldsymbol{x}_0)$ converge to the exact solutions of finite difference representations of $C(\boldsymbol{x}, t)$ and $C(\boldsymbol{x})$ at $(\boldsymbol{x}_0, t_0)$ and $\boldsymbol{x}_0$, respectively [81]. Since the fixed random walk method is based on the finite difference representations used in the FDM, it has the same disadvantage as the FDM, that is, some difficulties may arise from boundary conditions in case of a non-rectangular domain.

If the diffusivity field is space-variant, *i.e.*, the domain of interest contains a heterogeneous medium, the probability of a random walk's moving from a node to the neighboring nodes are not necessarily equal anymore. The probability of

moving to a neighboring node depends on the diffusivity gradient along that direction.

3.3.2 Exodus Method

The *exodus method* is a modified version of the fixed random walk method [52, 136, 137, 138]. Similar to the fixed random walk method, it operates on the nodes of the meshed version of H^*.

Let chloride concentration over H^* be time-invariant, $\gamma(\boldsymbol{x}) = 0$, $\boldsymbol{x} \in H^*$, and $C(\boldsymbol{x}) = \xi(\boldsymbol{x})$, $\boldsymbol{x} \in \partial H^*$. Then the chloride concentration at an arbitrary node $\boldsymbol{x} \in H^*$ can be given in the form

$$C(\boldsymbol{x}) = \sum_{i=1}^{n_b} P(\boldsymbol{x} \rightarrow \boldsymbol{x}_{\xi,i}) \xi(\boldsymbol{x}_{\xi,i}), \quad \boldsymbol{x}_{\xi,i} \in \partial H^*, \tag{3.18}$$

where $P(\boldsymbol{x} \rightarrow \boldsymbol{x}_{\xi,i})$ is the transition probability, defined as the probability that a random walk starting at $\boldsymbol{x}$ ends at a boundary node $\boldsymbol{x}_{\xi,i}$, and n_b is the number of the boundary nodes except the corner nodes, since a random walk executed on the nodes has to pass through a boundary node, where it will be stopped, in order to arrive a corner node. The exodus method approximates the transition probabilities in Eq. 3.18.

Suppose that the chloride concentration at node $\boldsymbol{x}_0 \in H^*$ is needed. For this purpose, a large number of walks is started at $\boldsymbol{x}_0$. At each iteration step, the walks that are not at boundary nodes are dispatched to the neighboring nodes in proportions equal to the random walk probabilities used in the fixed random walk method, which are equal to $1/4$ in this particular case. The iteration is carried out until a predetermined fraction of walks arrives at boundary nodes.

Then the transition probabilities are approximated as

$$\hat{P}(\boldsymbol{x}_0 \rightarrow \boldsymbol{x}_{\xi,i}) = \frac{n_\xi(i)}{n_s}, \tag{3.19}$$

where $n_\xi(i)$ is the number of walks ended at $\boldsymbol{x}_{\xi,i}$ and n_s is the number of walks started at $\boldsymbol{x}_0$. If $n_s \uparrow \infty$, $h \downarrow 0$, and all walks were allowed to arrive at a boundary node, the solution would be exact [136, 138]. It is important to note that the walks employed by the exodus method are not random walks like the ones employed by the fixed random walk method, therefore no pseudo-random number generator is needed in the exodus method.

In case that $\gamma(\boldsymbol{x}) \neq 0$, $\boldsymbol{x} \in H^*$, transient probabilities are needed in addition to transition probabilities. Transient probability $P(\boldsymbol{x} \xrightarrow{\boldsymbol{x}_k} \partial H^*)$ is defined as the probability that a random walk starting at $\boldsymbol{x} \in H^*$ passes through a node $\boldsymbol{x}_k \in H^*$, $k = 1, \ldots, n_i$, on its way to ∂H^*, where n_i is the number of interior nodes. Then Eq. 3.18 becomes

$$C(\boldsymbol{x}) = \sum_{j=1}^{n_b} P(\boldsymbol{x} \rightarrow \boldsymbol{x}_{\xi,j}) \xi(\boldsymbol{x}_{\xi,j}) + \sum_{k=1}^{n_i} P(\boldsymbol{x} \xrightarrow{\boldsymbol{x}_k} \partial H^*) \frac{h^2 \gamma(\boldsymbol{x})}{4D^*}. \tag{3.20}$$

More information on transient probabilities can be found in [136].

The advantages of the exodus method over the fixed random walk method is: (i) the former is computationally more efficient than the latter since it does not require any pseudo-random number generator, and (ii) the former is more accurate than the latter. Since the exodus method is similar to the fixed random walk method such that it also operates on the nodes of the meshed version of H^*, the difficulties related to the boundary conditions in case of a non-rectangular domain is valid also for the exodus method.

If the diffusivity field is space-variant, the proportions of walks dispatched to the neighboring nodes are not necessarily equal anymore.

3.3.3 Floating Random Walk Method

Contrary to the fixed random walk method, step sizes and random walk paths are not fixed in the *floating random walk method*, also known as *sphere walk method*. The solution given by the floating random walk method is based on the Green function and the mean value property [78, 81, 136]. It is worthy to note that this method works only for space-invariant diffusivity fields, *i.e.*, homogenous media.

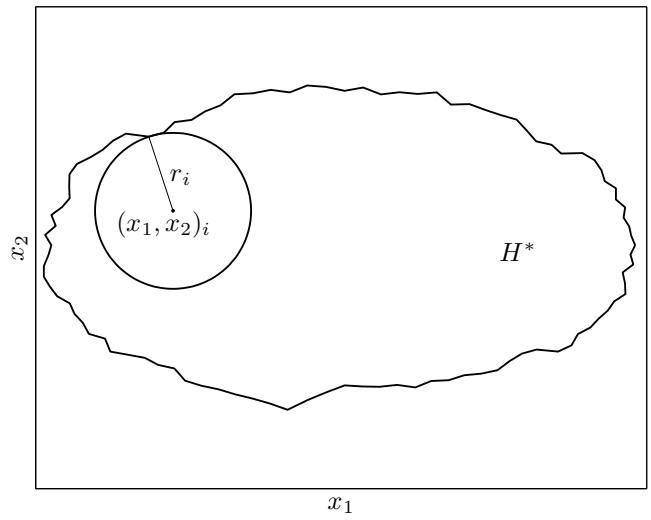

Figure 3.4: Floating Random Walk at i-th Step

Let chloride concentration over H^* be dependent on time and $\gamma(\boldsymbol{x}, t) = 0$, $\boldsymbol{x} \in H^*$, $t \geq 0$. Suppose that the chloride concentration at $(\boldsymbol{x}_0, t_0)$, $\boldsymbol{x}_0 \in H^*$, $t_0 > 0$, is needed. A random walk is started at point $\boldsymbol{x}_0$ and time t_0. At each step, a circle is constructed, where its center is located at the random walk's position and its radius is equal to the shortest distance between the random walk's position and ∂H^* (Figure 3.4). The size of the next step is set equal to the radius of the circle. Two random numbers are generated to determine the orientation

of the next step and the time to be elapsed during this step. Each angle has an equal probability. The discussion about determination of elapsed time is available in [81]. The rest is similar to the fixed random walk method. If the random walk reaches ∂H^* at time $t = t_\xi > 0$, $C(\boldsymbol{x}_0, t_0, \omega) = \xi(\boldsymbol{x}_\xi, t_\xi)$. If it is still in the interior of H^* at time $t = 0$, $C(\boldsymbol{x}_0, t_0, \omega) = \eta(\boldsymbol{x}_\eta)$. The chloride concentration at $(\boldsymbol{x}_0, t_0)$ is estimated by Eq. 3.13 after executing n_s random walks.

If chloride concentration over H^* is time-invariant, only one random number, which determines the orientation of step, is drawn at each step. Suppose that $\gamma(\boldsymbol{x}) = 0$ and the chloride concentration at $\boldsymbol{x}_0$ is needed. Random walks are started at $\boldsymbol{x}_0$. At each step, they move with a step size equal to the shortest distance between the random walk's position and ∂H^*. When a random walk reaches ∂H^*, the chloride concentration is recorded, *i.e.*, $C(\boldsymbol{x}_0, \omega) = \xi(\boldsymbol{x}_\xi)$. The chloride concentration at $\boldsymbol{x}_0$ is estimated by Eq. 3.17 after executing n_s random walks. As $n_s \uparrow \infty$, $\hat{C}(\boldsymbol{x}_0)$ converges to $C(\boldsymbol{x}_0)$ [81].

As the random walks approach the boundaries, step sizes become too small which results in a significant increase in computation time. It is usual to set a stopping rule, *e.g.*, a random walk is stopped if the distance distance between the random walk's position and ∂H^* is less than a certain value.

3.3.4 Random Walk Method (RWM)

Since one of the main objectives of this research is to calculate chloride concentration at a particular region of a concrete structure, local solution methods has been of interest instead of global methods. Grigoriu [76, 77] proposed a method for solving the heat conduction, Poisson and Laplace equations lo-

cally, which can also be used for solving chloride diffusion problems. The advantage of this method is that there is no need to discretize the domain as required, *e.g.*, by FEM or FDM. Moreover, the computer algorithm based on this method is simple to construct, always stable, accurate and ideal for parallel computing [76]. The method, denoted as RWM hereinafter, is based on an extension of a random walk method and smooth approximations of diffusivity field [76, 77, 78].

The essentials of RWM, that is, Brownian motion and Itô process, are reviewed briefly below. Then basic steps of derivation of RWM are given for both time-dependent and time-invariant cases. Details of derivations can be found in [78, 122]. Before the application of the method is illustrated, it is explained how to deal with a random diffusivity field.

3.3.4.1 Brownian Motion

The $\mathbb{R}^d$-valued Brownian motion $\boldsymbol{B}(t)$, $t \geq 0$, consists of d independent real valued Brownian motions B_i, $i = 1, \ldots, d$. It is a stochastic process with the following properties:

- $\boldsymbol{B}$ can start at any point $\boldsymbol{x} \in \mathbb{R}^d$, *i.e.*, $\boldsymbol{B}(0) = \boldsymbol{x}$.
- The increment $\boldsymbol{B}(t_2) - \boldsymbol{B}(t_1)$ of $\boldsymbol{B}$ in an arbitrary time interval (t_1, t_2), $t_2 > t_1$, is a d-dimensional Gaussian vector with mean zero and covariance matrix $\boldsymbol{i}(t_2 - t_1)$, where $\boldsymbol{i}$ is the (d, d)-identity matrix. The process has stationary increments because the properties of the increments of $\boldsymbol{B}$ depend upon only the duration of the time interval, *i.e.*, $t_2 - t_1$.

- The increments $\boldsymbol{B}(t_4) - \boldsymbol{B}(t_3)$ and $\boldsymbol{B}(t_2) - \boldsymbol{B}(t_1)$, $t_4 > t_3 \geq t_2 > t_1$, of $\boldsymbol{B}$ are independent random vectors. Hence, $\boldsymbol{B}$ has stationary and independent increments.
- The Brownian motion samples are continuous and nondifferentiable everywhere. The lack of differentiability is due to the rapid oscillations of the Brownian motion samples.

3.3.4.2 The Itô Process

Assume that diffusivity field $D(\boldsymbol{x}) > 0$ has continuous first order partial derivatives with respect to $\boldsymbol{x} \in H$ and set $\boldsymbol{a}(\boldsymbol{x})$ and $\boldsymbol{b}(\boldsymbol{x})$ for all $\boldsymbol{x} \in H$ as

$$a_k(\boldsymbol{x}) = \frac{\partial D(\boldsymbol{x})}{\partial x_k}, \quad k = 1, \ldots, d, \tag{3.21}$$

$$\boldsymbol{b}(\boldsymbol{x}) = \sqrt{2D(\boldsymbol{x})}\boldsymbol{i}, \tag{3.22}$$

where the elements of the $(d, 1)$ and (d, d) matrices $\boldsymbol{a}$ and $\boldsymbol{b}$ are real-valued functions. Let $\tilde{\boldsymbol{X}} = (\boldsymbol{X}, X_{d+1})$ be an $\mathbb{R}^{d+1}$-valued stochastic process defined by the stochastic differential equation

$$d\boldsymbol{X}(\tau) = \boldsymbol{a}(\boldsymbol{X}(\tau))d\tau + \boldsymbol{b}(\boldsymbol{X}(\tau))d\boldsymbol{B}(\tau), \quad \tau \geq 0, \tag{3.23a}$$

$$dX_{d+1}(\tau) = -d\tau. \tag{3.23b}$$

The matrices $\boldsymbol{a}$ and $\boldsymbol{b}$ are called drift and diffusion coefficients, respectively. The process is driven by Brownian motion whose magnitude is controlled by the diffusion coefficient. If the drift and diffusion are relatively smooth functions satisfying the so-called Lipschtz conditions, the solution of Eq. 3.23 exists and is unique [78]. This solution is based on the Riemann and the Itô integrals

$\int_0^t \boldsymbol{a}(\boldsymbol{X}(\tau))d\tau$ and $\int_0^t \boldsymbol{b}(\boldsymbol{X}(\tau))d\boldsymbol{B}(\tau)$, respectively (Eq. 3.24). The process $\tilde{\boldsymbol{X}}$, referred to as Itô process, is a semimartingale with continuous samples.

$$\tilde{\boldsymbol{X}}(t) = \begin{bmatrix} \boldsymbol{X}(0) + \int_0^t \boldsymbol{a}(\boldsymbol{X}(\tau))d\tau + \int_0^t \boldsymbol{b}(\boldsymbol{X}(\tau))d\boldsymbol{B}(\tau) \\ X_{d+1}(0) - \int_0^t d\tau \end{bmatrix}. \tag{3.24}$$

3.3.4.3 Transient-State Diffusion

If chloride concentration over H is time-dependent, the Itô process $\tilde{\boldsymbol{X}}$, defined by Eq. 3.23, is used to obtain the local solution at $(\boldsymbol{x}, t)$, $\boldsymbol{x} \in H$, $t > 0$, where $\tilde{\boldsymbol{X}}(0) = (\boldsymbol{x}, t)$. Let $\tilde{\mathcal{A}}$ be the generator function of $\tilde{\boldsymbol{X}}$ defined by

$$\tilde{\mathcal{A}}\left[g(\boldsymbol{x}, t)\right] = \lim_{\tau \downarrow 0} \frac{E\left[g(\tilde{\boldsymbol{X}}(\tau))\right] - g(\boldsymbol{x}, t)}{\tau}, \tag{3.25}$$

where g is a real-valued function defined on $\mathbb{R}^{d+1}$ with continuous second order partial derivatives and continuous first order partial derivative with respect to $\boldsymbol{x} \in H$ and $\tau \geq 0$, respectively. The expectation of the Itô formula applied to the function $g(\tilde{\boldsymbol{X}}(\tau))$ is

$$\begin{aligned} E\left[g(\tilde{\boldsymbol{X}}(\tau))\right] - g(\boldsymbol{x}, t) = E\Bigg[\int_0^\tau \left(\sum_{i=1}^d \frac{\partial g(\tilde{\boldsymbol{X}}(\varpi))}{\partial x_i} a_i(\boldsymbol{X}(\varpi)) - \frac{\partial g(\tilde{\boldsymbol{X}}(\varpi))}{\partial x_{d+1}}\right) d\varpi \\ + \frac{1}{2}\sum_{i,j=1}^d \int_0^\tau \left(\boldsymbol{b}(\boldsymbol{X}(\varpi))\boldsymbol{b}(\boldsymbol{X}(\varpi))^T\right)_{ij} \frac{\partial^2 g(\tilde{\boldsymbol{X}}(\varpi))}{\partial x_i \partial x_j} d\varpi\Bigg]. \end{aligned} \tag{3.26}$$

The term under the expectation on the right-hand-side of Eq. 3.26 divided by a small $\tau > 0$ can be approximated by

$$\begin{aligned} &\sum_{i=1}^d \frac{\partial g(\tilde{\boldsymbol{X}}(\theta(\omega)\tau, \omega))}{\partial x_i} a_i(\boldsymbol{X}(\theta(\omega)\tau, \omega)) - \frac{\partial g(\tilde{\boldsymbol{X}}(\theta(\omega)\tau, \omega))}{\partial x_{d+1}} \\ &+ \frac{1}{2}\sum_{i,j=1}^d \left(\boldsymbol{b}(\boldsymbol{X}(\theta(\omega)\tau, \omega))\boldsymbol{b}(\boldsymbol{X}(\theta(\omega)\tau, \omega))^T\right)_{ij} \frac{\partial^2 g(\tilde{\boldsymbol{X}}(\theta(\omega)\tau, \omega))}{\partial x_i \partial x_j} \end{aligned} \tag{3.27}$$

for each $\omega \in \Omega$, where $\theta(\omega) \in [0, 1]$. The limit of Eq. 3.27 as $\tau \downarrow 0$ is deterministic because

- $\boldsymbol{a}$ and $\boldsymbol{b}$ are bounded functions,
- $\tilde{\boldsymbol{X}}$ has continuous sample paths,
- and g has continuous second order partial derivatives and continuous first order partial derivative with respect to $\boldsymbol{x}$ and τ, respectively,

so that the generator function $\tilde{\mathcal{A}}$ defined by Eq. 3.25 is

$$\tilde{\mathcal{A}} = -\frac{\partial}{\partial x_{d+1}} + \sum_{i=1}^{d} a_i \frac{\partial}{\partial x_i} + \frac{1}{2} \sum_{i,j=1}^{d} \left(\boldsymbol{b}\boldsymbol{b}^T\right)_{ij} \frac{\partial^2}{\partial x_i \partial x_j}, \tag{3.28}$$

which coincides with the differential operator of Eq. 3.1 if the drift and diffusion coefficients are defined by Eqs. 3.21 and 3.22, respectively. Then Eq. 3.26 becomes

$$E\left[g(\tilde{\boldsymbol{X}}(\tau))\right] - g(\boldsymbol{x}, t) = E\left[\int_0^\tau \tilde{\mathcal{A}}\left[g(\tilde{\boldsymbol{X}}(\varpi))\right] d\varpi\right]. \tag{3.29}$$

Let

$$\tilde{T} = \inf\{\tau > 0 : \tilde{\boldsymbol{X}}(\tau) \notin H \times (0, t)\} \tag{3.30}$$

be an $\mathcal{F}_t = \sigma(\boldsymbol{B}(\tau) : 0 \leq \tau \leq t)$-stopping time, that is, the time at which $\tilde{\boldsymbol{X}}$ exits $H \times (0, t)$ for the first time, and $\tilde{\boldsymbol{X}}^{\tilde{T}}$ be the process $\tilde{\boldsymbol{X}}$ stopped at $\tilde{T}$. It can be shown that $\tilde{\boldsymbol{X}}^{\tilde{T}}$ is also a semimartingale, so that Eq. 3.28 is applicable to the function $g(\tilde{\boldsymbol{X}}^{\tilde{T}})$ [78]. Applying Eq. 3.28 to the function $g(\tilde{\boldsymbol{X}}^{\tilde{T}})$ gives

$$E\left[g(\tilde{\boldsymbol{X}}^{\tilde{T}}(\tau))\right] - g(\boldsymbol{x}, t) = E\left[\int_0^\tau \tilde{\mathcal{A}}\left[g(\tilde{\boldsymbol{X}}^{\tilde{T}}(\varpi))\right] d\varpi\right]. \tag{3.31}$$

By definition of $\tilde{\boldsymbol{X}}^{\tilde{T}}$, $\tilde{\boldsymbol{X}}^{\tilde{T}}(\tau)$ can be replaced with $\tilde{\boldsymbol{X}}(\tilde{T} \wedge \tau)$. Then Eq. 3.31 becomes

$$g(\boldsymbol{x}, t) = E\left[g(\tilde{\boldsymbol{X}}(\tilde{T}))\right] - E\left[\int_0^{\tilde{T}} \tilde{\mathcal{A}}\left[g(\tilde{\boldsymbol{X}}(\varpi))\right] d\varpi\right] \tag{3.32}$$

for $\tau \geq \tilde{T}$.

If the function g is replaced with the solution C of Eq. 3.1 with the initial and boundary conditions in Eqs. 3.2 and 3.3, respectively, Eq. 3.32 becomes

$$C(\boldsymbol{x}, t) = E\left[C(\tilde{\boldsymbol{X}}(\tilde{T}))\right] - E\left[\int_0^{\tilde{T}} \tilde{\mathcal{A}}\left[C(\tilde{\boldsymbol{X}}(\varpi))\right] d\varpi\right]. \tag{3.33}$$

Then the local solution of Eq. 3.1 is given by

$$\begin{aligned} C(\boldsymbol{x}, t) &= E\left[C(\tilde{\boldsymbol{X}}(\tilde{T}))\right] + E\left[\int_0^{\tilde{T}} \gamma(\tilde{\boldsymbol{X}}(\varpi)) d\varpi\right] \\ &= E\left[\eta(\boldsymbol{X}(t)) \,\middle|\, \tilde{T} = t\right] P\left(\tilde{T} = t\right) + E\left[\xi(\tilde{\boldsymbol{X}}(t - \tilde{T})) \,\middle|\, \tilde{T} < t\right] P\left(\tilde{T} < t\right) \\ &\quad + E\left[\int_0^{\tilde{T}} \gamma(\tilde{\boldsymbol{X}}(\varpi)) d\varpi\right], \end{aligned} \tag{3.34}$$

since $\tilde{\boldsymbol{X}}(\varpi) \in H \times (0, t)$ for $\varpi < \tilde{T}$ and $\tilde{\boldsymbol{X}}(\varpi)$ is on the boundary of $H \times (0, t)$ for $\varpi = \tilde{T}$, so that $\tilde{\mathcal{A}}[C(\tilde{\boldsymbol{X}}(\varpi))] = -\gamma(\tilde{\boldsymbol{X}}(\varpi))$ and

$$C(\tilde{\boldsymbol{X}}(\tilde{T})) = \begin{cases} \xi(\tilde{\boldsymbol{X}}(t - \tilde{T})) & \text{if } \tilde{T} < t \\ \eta(\boldsymbol{X}(t)) & \text{if } \tilde{T} = t \end{cases}. \tag{3.35}$$

In general, the expectations in Eq. 3.34 can not be calculated analytically. Instead, they are estimated from samples of $\tilde{\boldsymbol{X}}$ generated by Monte Carlo simulation. The local solution in Eq. 3.34 can be estimated by

$$\begin{aligned} \hat{C}(\boldsymbol{x}, t) &= \frac{n'_s}{n_s}\left[\frac{1}{n'_s}\sum_{\omega'=1}^{n'_s} \eta(\boldsymbol{X}(t, \omega'))\right] + \frac{n''_s}{n_s}\left[\frac{1}{n''_s}\sum_{\omega''=1}^{n''_s} \xi(\tilde{\boldsymbol{X}}(t - \tilde{T}(\omega''), \omega''))\right] \\ &\quad + \frac{1}{n_s}\sum_{\omega=1}^{n_s}\int_0^{\tilde{T}(\omega)} \gamma(\tilde{\boldsymbol{X}}(\varpi, \omega)) d\varpi, \end{aligned} \tag{3.36}$$

where $\tilde{\boldsymbol{X}}(\cdot,\omega)$ and $\tilde{T}(\omega), \omega = 1,\ldots,n_s$ are samples of $\tilde{\boldsymbol{X}}$ and $\tilde{T}$, respectively, $n_s = n_s' + n_s''$ denotes the number of independent samples of $\tilde{\boldsymbol{X}}$, and, n_s' and n_s'' are the number of samples of $\tilde{\boldsymbol{X}}$ that exit $H \times (0,t)$ through H and ∂H, respectively. The accuracy of the estimate given by Eq. 3.36 depends on

- the sample size, n_s,
- the time step used to generate sample paths of the Itô process, $\triangle\tau$,
- the accuracy of the recurrence formula used for generating samples of the Itô process.

The simplest way of generating the samples of an Itô process is to use finite difference approximation. The recurrence formula given by

$$\boldsymbol{X}(\tau+\triangle\tau) \simeq \boldsymbol{X}(\tau) + \boldsymbol{a}(\boldsymbol{X}(\tau))\triangle\tau + \boldsymbol{b}(\boldsymbol{X}(\tau))\triangle\boldsymbol{B}(\tau) \tag{3.37}$$

is known as *Euler's scheme*. The Euler's scheme converges strongly with order 0.5 [93]. More advanced schemes can be used if a higher order of convergence is required. A scheme with a higher order of convergence compared to Euler's scheme is *Milstein's scheme*, which converges strongly with order 1.0 [93]. It has an additional term on the right side of Eq. 3.37 such that

$$\begin{aligned} X_k(\tau+\triangle\tau) \simeq X_k(\tau) + a_k(X_k(\tau))\triangle\tau + b_{k,k}(X_k(\tau))\triangle B_k(\tau) \\ + \sum_{j_1,j_2=1}^{2} \mathcal{L}^{j_1} b_{k,j_2}(X_k(\tau))\mathcal{I}_{j_1,j_2}, \quad k=1,2, \end{aligned} \tag{3.38}$$

where

$$\mathcal{L}^j = \sum_{p=1}^{2} b_{p,j}\frac{\partial}{\partial x_p}, \quad j=1,2, \tag{3.39}$$

and

$$\mathcal{I}_{j_1,j_2} = \int_{\tau}^{\tau+\triangle\tau} \int_{\tau}^{\varpi} dB_{j_1} dB_{j_2}$$
$$= \begin{cases} \frac{1}{2}\left[(\triangle B_k(\tau))^2 - \triangle\tau\right], & \text{for } j_1 = j_2 \\ 0, & \text{for } j_1 \neq j_2 \end{cases}, \quad j_1, j_2 = 1, 2, \tag{3.40}$$

since $B_1(\tau)$ and $B_2(\tau)$ are independent. Then Eq. 3.38 becomes

$$X_k(\tau + \triangle\tau) \simeq X_k(\tau) + a_k(X_k(\tau))\triangle\tau + b_{k,k}(X_k(\tau))\triangle B_k(\tau)$$
$$+ \frac{1}{2} b_{k,k}(X_k(\tau)) \frac{\partial b_{k,k}(X_k(\tau))}{\partial x_k} \left[(\triangle B_k(\tau))^2 - \triangle\tau\right] \tag{3.41}$$

since $b_{i_1,i_2}(X_k(\tau)) = 0$, $i_1 \neq i_2$, $\tau \geq 0$. Discussions on more advanced numerical schemes can be found in [93].

3.3.4.4 Steady-State Diffusion

If C is time-invariant, the Itô process $\boldsymbol{X}$, defined by Eq. 3.23a, with the initial condition $\boldsymbol{X}(0) = \boldsymbol{x} \in H$, is used instead of $\tilde{\boldsymbol{X}}$. Let $\mathcal{A}$ be the generator function of $\boldsymbol{X}$ defined by

$$\mathcal{A}\left[g(\boldsymbol{x})\right] = \lim_{\tau \downarrow 0} \frac{E\left[g(\boldsymbol{X}(\tau))\right] - g(\boldsymbol{x})}{\tau}, \tag{3.42}$$

where g is a real-valued function defined on $\mathbb{R}^d$ with continuous second order partial derivatives with respect to $\boldsymbol{x} \in H$. The expectation of the Itô formula applied to the function $g(\boldsymbol{X}(\tau))$ is

$$E\left[g(\boldsymbol{X}(\tau))\right] - g(\boldsymbol{x}) = E\left[\sum_{i=1}^{d} \int_0^{\tau} \frac{\partial g(\boldsymbol{X}(\varpi))}{\partial x_i} a_i(\boldsymbol{X}(\varpi)) d\varpi \right.$$
$$\left. + \frac{1}{2} \sum_{i,j=1}^{d} \int_0^{\tau} \left(\boldsymbol{b}(\boldsymbol{X}(\varpi))\boldsymbol{b}(\boldsymbol{X}(\varpi))^T\right)_{ij} \frac{\partial^2 g(\boldsymbol{X}(\varpi))}{\partial x_i \partial x_j} d\varpi \right]. \tag{3.43}$$

The term under the expectation on the right-hand-side of Eq. 3.43 divided by a small $\tau > 0$ can be approximated by

$$\sum_{i=1}^{d} \frac{\partial g(\boldsymbol{X}(\theta(\omega)\tau, \omega))}{\partial x_i} a_i(\boldsymbol{X}(\theta(\omega)\tau, \omega)) + \frac{1}{2} \sum_{i,j=1}^{d} \left(\boldsymbol{b}(\boldsymbol{X}(\theta(\omega)\tau, \omega))\boldsymbol{b}(\boldsymbol{X}(\theta(\omega)\tau, \omega))^T\right)_{ij} \frac{\partial^2 g(\boldsymbol{X}(\theta(\omega)\tau, \omega))}{\partial x_i \partial x_j} \tag{3.44}$$

for each $\omega \in \Omega$ where $\theta(\omega) \in [0, 1]$. The limit of Eq. 3.44 as $\tau \downarrow 0$ is deterministic because

- $\boldsymbol{a}$ and $\boldsymbol{b}$ are bounded functions,
- $\boldsymbol{X}$ has continuous sample paths,
- and g has continuous second order partial derivatives with respect to $\boldsymbol{x}$,

so that the generator function $\mathcal{A}$ defined by Eq. 3.42 is

$$\mathcal{A} = \sum_{i=1}^{d} a_i \frac{\partial}{\partial x_i} + \frac{1}{2} \sum_{i,j=1}^{d} \left(\boldsymbol{b}\boldsymbol{b}^T\right)_{ij} \frac{\partial^2}{\partial x_i \partial x_j}, \tag{3.45}$$

which coincides with the differential operator of Eq. 3.4 if the drift and diffusion coefficients are defined by Eqs. 3.21 and 3.22, respectively. Then Eq. 3.43 becomes

$$E\left[g(\boldsymbol{X}(\tau))\right] - g(\boldsymbol{x}) = E\left[\int_0^\tau \mathcal{A}\left[g(\boldsymbol{X}(\varpi))\right] d\varpi\right]. \tag{3.46}$$

Let

$$T = \inf\{\tau > 0 : \boldsymbol{X}(\tau) \notin H)\} \tag{3.47}$$

be an $\mathcal{F}_t = \sigma(\boldsymbol{B}(\tau) : 0 \leq \tau \leq t)$-stopping time, that is, the time at which the process $\boldsymbol{X}$ exits H for the first time. It can be shown that Eq. 3.46 holds with T in place of τ [78], so that Eq. 3.46 becomes

$$E\left[g(\boldsymbol{X}(T))\right] - g(\boldsymbol{x}) = E\left[\int_0^T \mathcal{A}\left[g(\boldsymbol{X}(\varpi))\right] d\varpi\right]. \tag{3.48}$$

If the function g is replaced with the solution C of Eq. 3.4 with the boundary condition in Eq. 3.5, the local solution of Eq. 3.4 is obtained as

$$C(\boldsymbol{x}) = E\left[\xi(\boldsymbol{X}(T))\right] + E\left[\int_0^T \gamma(\boldsymbol{X}(\varpi))d\varpi\right] \tag{3.49}$$

since $\boldsymbol{X}(\varpi) \in H$ for $\varpi < T$ and $\boldsymbol{X}(\varpi) \in \partial H$ for $\varpi = T$, so that $C(\boldsymbol{X}(T)) = \xi(\boldsymbol{X}(T))$ and $\mathcal{A}[C(\boldsymbol{X}(\varpi))] = -\gamma(\boldsymbol{X}(\varpi))$.

The expectations in Eq. 3.49 can be estimated from samples of $\boldsymbol{X}$ generated by Monte Carlo simulation, so the local solution in Eq. 3.49 can be estimated by

$$\hat{C}(\boldsymbol{x}) = \frac{1}{n_s}\sum_{\omega=1}^{n_s} \xi(\boldsymbol{X}(T(\omega),\omega)) + \frac{1}{n_s}\sum_{\omega=1}^{n_s}\int_0^{T(\omega)} \gamma(\boldsymbol{X}(\varpi,\omega))d\varpi, \tag{3.50}$$

where $\boldsymbol{X}(\cdot,\omega)$ and $T(\omega)$, $\omega = 1,\ldots,n_s$, are samples of $\boldsymbol{X}$ and T, respectively.

3.4 Random Diffusivity Fields

If the domain of interest contains a random diffusivity field instead of a deterministic one, the solutions of Eqs. 3.1 and 3.4 will be random variables, and can be obtained by using one of the solution methods given above, either global or local, in three steps:

(i) The solution of partial differential equation is calculated for a sample of diffusivity field $D(\cdot,\omega)$.

(ii) The first step is repeated for a collection of samples of diffusivity field $\{D(\cdot,\omega)\}$.

(iii) The statistics of the solution are estimated by using the results obtained in the second step.

3.5 Examples

Two examples, a 1D-specimen with a deterministic diffusivity field under steady-state conditions and a 2D-specimen with a random diffusivity field under transient-state conditions, are given below to illustrate the application of the RWM. In the third example, two numerical schemes, the Euler's and Milstein's schemes, are compared.

3.5.1 1D Steady-State Diffusion

Consider a rod of unit length with the deterministic diffusivity field defined by

$$D(x) = 2 + \sin(10\pi x), \quad x \in [0, 1]. \tag{3.51}$$

The concentration $C(x)$ satisfies the partial differential equation

$$\frac{dD(x)}{dx}\frac{dC(x)}{dx} + D(x)\frac{d^2C(x)}{dx^2} = 0, \quad x \in [0, 1] \tag{3.52}$$

with the boundary conditions given as $C(0) = 0$ and $C(1) = 1$. The objective is to estimate $C(x)$ at $x = 0.3, 0.5$ and 0.7 by using the RWM.

The local solution of Eq. 3.52 is given by Eq. 3.49 as $C(x) = P(X(T) = 1)$, *i.e.*, it is equal to the probability that the $\mathbb{R}$-valued Itô process X defined by

$$dX(\tau) = a(X(\tau))d\tau + b(X(\tau))dB(\tau), \quad \tau \geq 0, \quad X(0) = x \in (0, 1), \tag{3.53}$$

exists through the boundary $x = 1$ for the first time, where T is the stopping time defined by Eq.3.47, $a(x)$ and $b(x)$ are defined by Eqs. 3.21 and 3.22, respectively,

so

$$a(x) = 10\pi \cos(10\pi x), \tag{3.54}$$

$$b(x) = \sqrt{4 + 2\sin(10\pi x)}. \tag{3.55}$$

Table 3.1: Comparison of Results

x	BVP Solver $\hat{C}(x)$	RWM $\hat{C}(x)$	Rel. Err. (%)
0.3	0.2666	0.2725	+2.2
0.5	0.4666	0.4779	+2.4
0.7	0.6666	0.6607	-0.9

Estimates of $C(x)$ based on 10000 samples, generated by using the Euler's scheme with a time increment of 0.0001, for $x = 0.3, 0.5$ and 0.7 are shown in Table 3.1. Also, the solution of Eq. 3.52 obtained by using the MATLAB's boundary-value-problem (BVP) solver and the error in $\hat{C}(x)$ obtained by using the RWM relative to the results by the BVP solver are shown in Table 3.1.

3.5.2 2D Transient-State Diffusion

Consider a unit square, $H = (0,1) \times (0,1)$, with a random diffusivity field defined by

$$D(\boldsymbol{x}) = 0.1 + 0.9Z(\boldsymbol{x}), \quad \boldsymbol{x} \in H, \tag{3.56}$$

where Z is a beta translation field taking values in $[0,1]$ with shape parameters equal to 2. Samples of Z can be obtained by

$$Z(\boldsymbol{x}, \omega) = F_Z^{-1} \circ \Phi(Y(\boldsymbol{x}, \omega)), \quad \omega = 1, \ldots, n_d, \tag{3.57}$$

where n_d is the number of samples of diffusivity field, F_Z denotes a beta distribution on the unit interval with shape parameters equal to 2, and Y is a zero mean, unit variance, stationary Gaussian field with marginal distribution Φ and covariance function $c(\varphi) = \exp(-\varphi)$, where φ denotes the distance between two points.

The concentration $C(\boldsymbol{x}, t)$, $\boldsymbol{x} \in H$, $t \geq 0$, satisfies the partial differential equation

$$\frac{\partial C(\boldsymbol{x}, t)}{\partial t} = \sum_{p=1}^{2} \frac{\partial D(\boldsymbol{x})}{\partial x_p} \frac{\partial C(\boldsymbol{x}, t)}{\partial x_p} + D(\boldsymbol{x}) \Delta C(\boldsymbol{x}, t), \tag{3.58}$$

where $C(\boldsymbol{x}, t) = 1$, $\boldsymbol{x} \in \partial H$, $t \geq 0$, and $C(\boldsymbol{x}, 0) = 0$, $\boldsymbol{x} \in H$. The objective is to estimate the statistics of chloride concentration at the center of the specimen at time $t = 0.1$ by using the RWM.

The following Monte Carlo algorithm has been used to analyze the specimen:

1. Generate samples of D by using the following procedure:

   - Generate samples of Y by using its spectral representation (Section 5.3.1.2, [78]) as follows:
     - Take a bounded rectangle M centered at the origin of $\mathbb{R}^2$ with cutoff frequencies ν_k^*, that is, $M = \times_{k=1}^{2} [-\nu_k^*, \nu_k^*]$.
     - Partition M into rectangles M_r, $r = 1, \ldots, n_r$, of size $\triangle \nu_k$.
     - Generate samples of independent Gaussian variables, $G_{r,1}$ and $G_{r,2}$, with zero mean and variance

$$E[G_{r,1}^2] = E[G_{r,2}^2] = \int_{M_r} s(\boldsymbol{\nu}) d\boldsymbol{\nu} \approx s(\boldsymbol{\nu}_r) \prod_{k=1}^{2} \Delta \nu_k, \tag{3.59}$$

where $s(\boldsymbol{\nu})$ is the spectral density function derived as

$$s(\boldsymbol{\nu}) = \frac{1}{2\pi} \frac{1}{(\nu_1^2 + \nu_2^2 + 1)^{3/2}} \tag{3.60}$$

and $\boldsymbol{\nu}_r = (\nu_{r,1}, \nu_{r,2})$ denotes the center of M_r.

– Calculate $Y(\boldsymbol{x}, \omega)$, $\omega = 1, \ldots, n_d$, using

$$Y(\boldsymbol{x}, \omega) = \sum_{r=1}^{n_r} \left[G_{r,1} \cos(\boldsymbol{\nu}_r \cdot \boldsymbol{x}) + G_{r,2} \sin(\boldsymbol{\nu}_r \cdot \boldsymbol{x}) \right]. \tag{3.61}$$

- Obtain $Z(\boldsymbol{x}, \omega)$ by introducing $Y(\boldsymbol{x}, \omega)$ into Eq. 3.57 for each ω.
- Obtain $D(\boldsymbol{x}, \omega)$ by introducing $Z(\boldsymbol{x}, \omega)$ into Eq. 3.56 for each ω.

2. For each $D(\boldsymbol{x}, \omega)$, calculate the corresponding chloride concentration $C(\boldsymbol{x}, \omega)$ by using the RWM and the FDM.
3. Estimate the statistics of $C(\boldsymbol{x}, t)$ and compare the results.

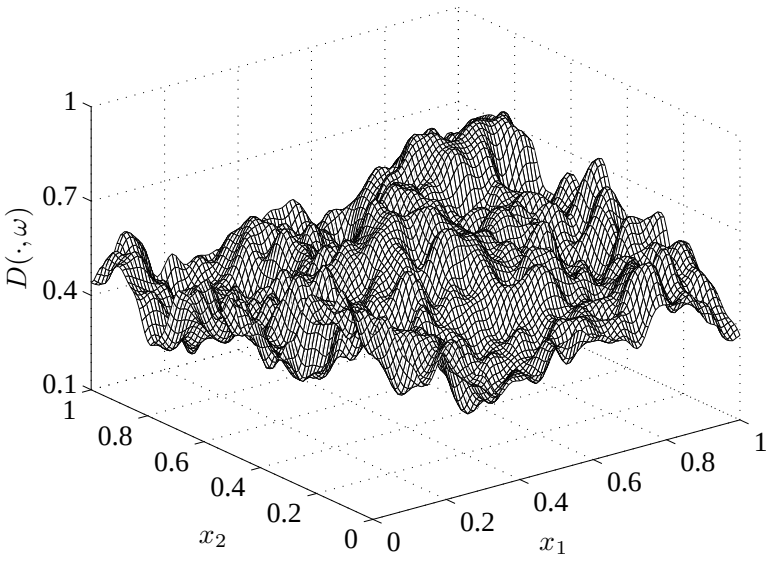

Figure 3.5: A Sample of Diffusivity Field

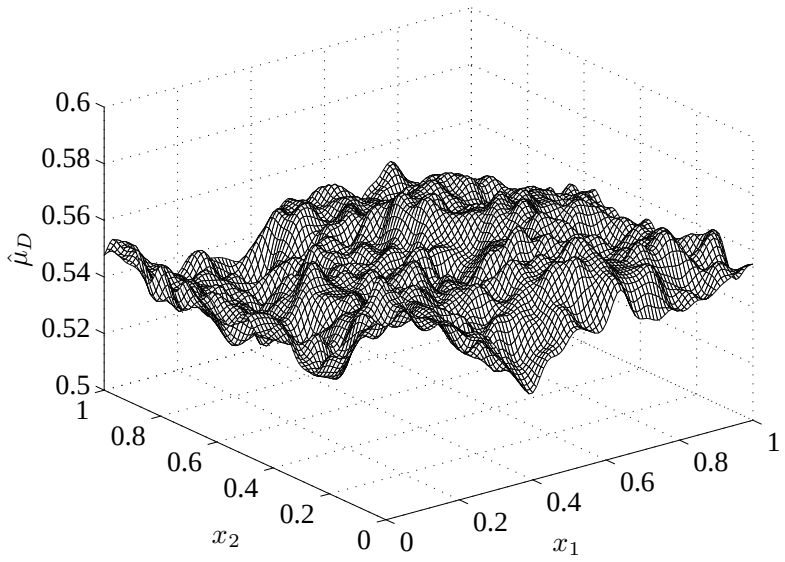

Figure 3.6: Estimate of Mean of D

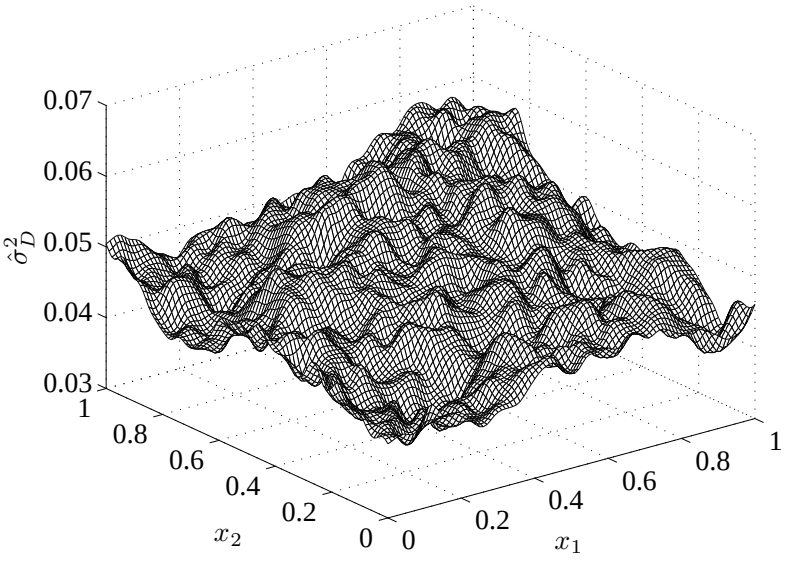

Figure 3.7: Estimate of Variance of D

A sample of diffusivity field is shown in Figure 3.5. The exact mean and variance of D are 0.55 and 0.0405, respectively. Estimates of mean and variance of D based on 100 samples are plotted in Figure 3.6 and Figure 3.7, respectively. Cutoff frequency ν_k^* and step size $\Delta\nu_k$, $k = 1, 2$, are 100 and 1, respectively.

The local solution of Eq. 3.58, given by Eq. 3.34, is $C(\boldsymbol{x}, t) = P(\tilde{T} < t)$, *i.e.*, it is equal to the probability that the $\mathbb{R}^3$-valued Itô process $\tilde{\boldsymbol{X}} = (\boldsymbol{X}, X_3)$ defined by

$$d\boldsymbol{X}(\tau) = \boldsymbol{a}(\boldsymbol{X}(\tau))d\tau + \boldsymbol{b}(\boldsymbol{X}(\tau))d\boldsymbol{B}(\tau), \quad \tau \in (0, t), \tag{3.62a}$$

$$dX_3(\tau) = -d\tau, \tag{3.62b}$$

exists through the boundary ∂H for the first time before $\tau = t$, where $\boldsymbol{a}$ and $\boldsymbol{b}$ are defined by Eqs. 3.21 and 3.22, respectively, and $\tilde{\boldsymbol{X}}(0) = (\boldsymbol{x}, t)$.

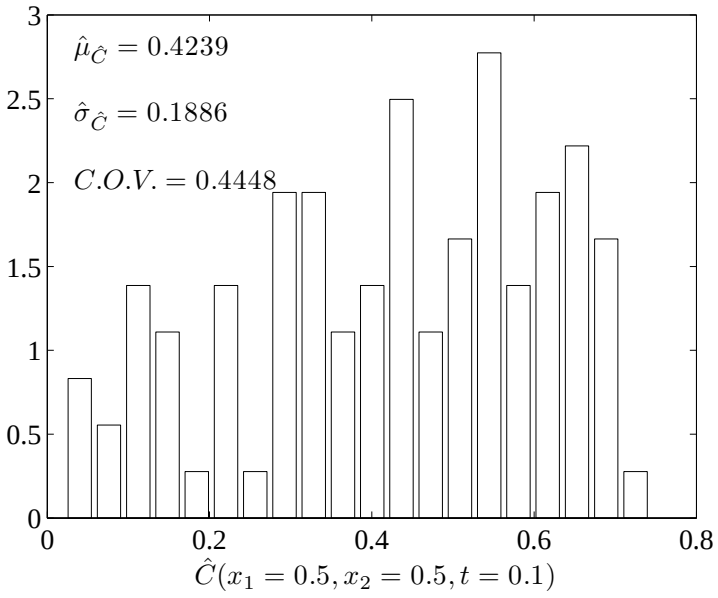

Figure 3.8: Histogram of $\hat{C}$ by the RWM ($n_s = 1000$)

For each sample of diffusivity field, the corresponding chloride concentration at the center of the specimen at time $t = 0.1$ has been calculated based on

1000 samples of $\tilde{\boldsymbol{X}}$ generated by using the Euler's scheme with a time increment of 10^{-5}. Histogram of $\hat{C}(x_1 = 0.5, x_2 = 0.5, t = 0.1)$ obtained by using the RWM is plotted in Figure 3.8. Resulting estimates of mean and standard deviation of $\hat{C}(x_1 = 0.5, x_2 = 0.5, t = 0.1)$ are 0.4239 and 0.1886, respectively.

For comparison, Eq. 3.58 has been solved by using the FDM in which forward difference scheme in time domain and central difference scheme in space domain have been used (Eq. 3.8). Grid spacing and time increment are set as $h = 0.01$ and $\triangle t = 10^{-5}$, respectively, since finer meshes result in the same solution. Histogram of $\hat{C}$ obtained by using the FDM is plotted in Figure 3.9. Resulting estimates of mean and standard deviation of $\hat{C}(x_1 = 0.5, x_2 = 0.5, t = 0.1)$ are 0.4267 and 0.1877, respectively. Relative error in $\hat{C}(\cdot, \omega)$ is calculated as

$$\epsilon_{\text{rel}}(\omega) = \frac{|\hat{C}_{\text{RWM}}(\cdot, \omega) - \hat{C}_{\text{FDM}}(\cdot, \omega)|}{\hat{C}_{\text{FDM}}(\cdot, \omega)} \times 100, \quad \omega = 1, \ldots, n_d, \tag{3.63}$$

where $\hat{C}_{\text{RWM}}$ and $\hat{C}_{\text{FDM}}$ are the estimates obtained by the RWM and FDM, respectively. Relative error for each sample of diffusivity field is shown in Figure 3.10. Relative errors are mostly less than 10%. In case that relative errors are more than 10%, the values of $\hat{C}$ are very low, *i.e.*, close to zero.

Increasing the number of samples of $\tilde{\boldsymbol{X}}$ ten times, while the time increment is the same, *i.e.*, $n_s = 10000$ and $\triangle\tau = 10^{-5}$, reduces the relative errors. Histogram of $\hat{C}(x_1 = 0.5, x_2 = 0.5, t = 0.1)$ is plotted in Figure 3.11. Resulting estimates of mean and standard deviation of $\hat{C}(x_1 = 0.5, x_2 = 0.5, t = 0.1)$ are 0.4239 and 0.1872, respectively. Relative errors are less than 5% for 98 samples, while they are less than 9% for the remaining 2 samples (Figure 3.12).

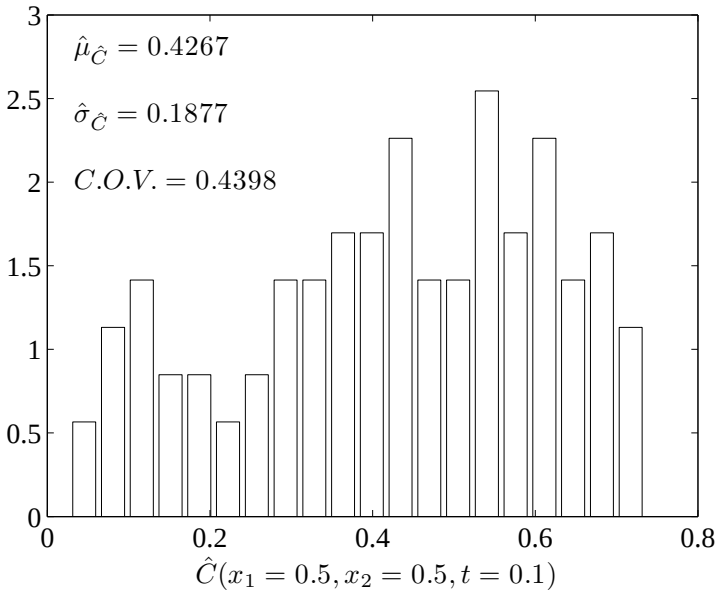

Figure 3.9: Histogram of $\hat{C}$ by the FDM

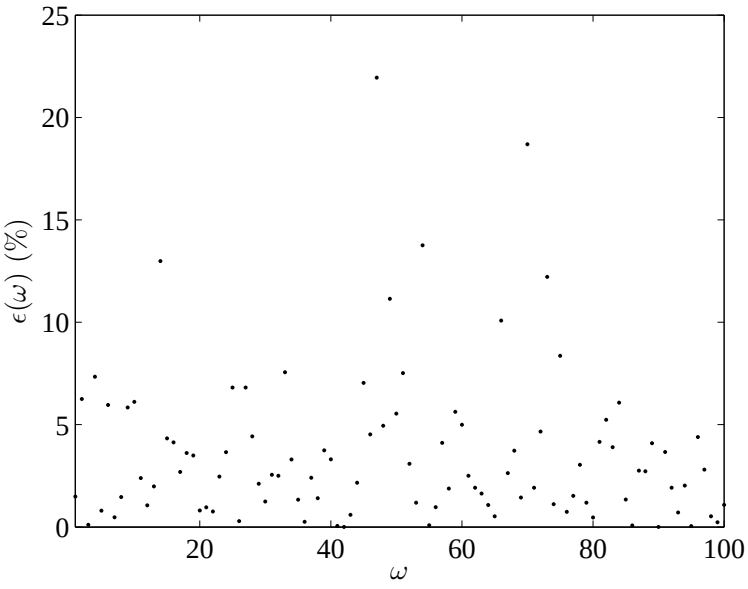

Figure 3.10: Relative Error ($n_s = 1000$)

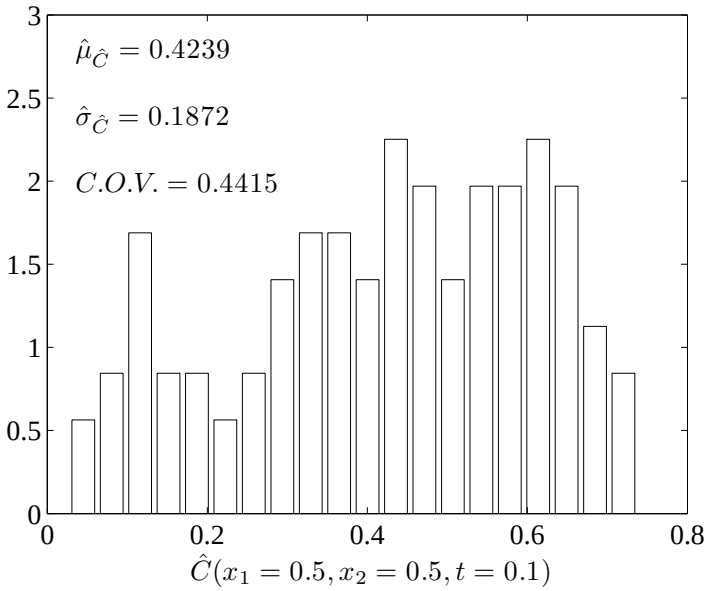

Figure 3.11: Histogram of $\hat{C}$ by the RWM ($n_s = 10000$)

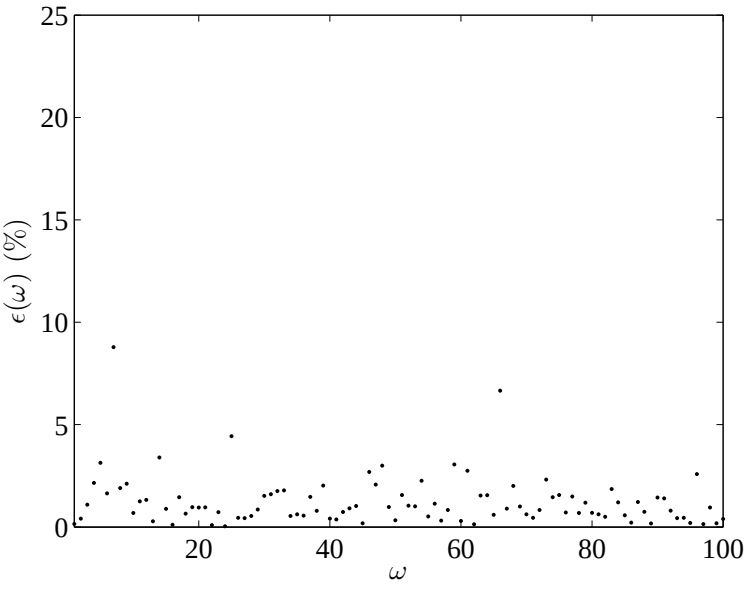

Figure 3.12: Relative Error ($n_s = 10000$)

3.5.3 The Euler Scheme vs. The Milstein Scheme

Let $X(\tau)$, $\tau \geq 0$, be an $\mathbb{R}$-valued Itô process defined by

$$dX(\tau) = a(X(\tau))d\tau + b(X(\tau))dB(\tau), \quad X(0) = x \in \mathbb{R}, \tag{3.64}$$

where $a(x) = 3x$ and $b(x) = 2x$. The exact solution of Eq. 3.64 is

$$X(\tau) = X(0)\exp\left(\tau + 2B(\tau)\right). \tag{3.65}$$

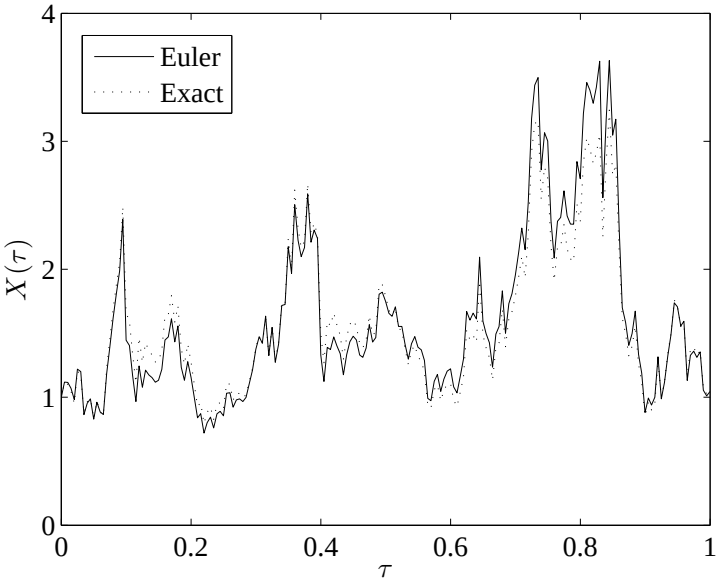

Figure 3.13: A Sample of $X(\tau)$ with the Euler approximation

A sample of $X(\tau)$, $\tau \in [0, 1]$, with the Euler and Milstein approximations are plotted in Figure 3.13 and Figure 3.14, respectively. Relative error in $\hat{X}(\tau)$ is calculated as

$$\epsilon_{\text{rel}}(\tau) = \frac{|\hat{X}(\tau) - X(\tau)|}{X(\tau)} \times 100, \tag{3.66}$$

where $\hat{X}(\tau)$, $\tau \in [0, 1]$, is an approximation of $X(\tau)$, $\tau \in [0, 1]$, obtained by either the Euler or Milstein scheme.

As expected, the Milstein approximation is better than the Euler approximation for the same time increment $\triangle\tau = 0.005$. Maximum relative errors are 18.7% and 7.1% for the Euler and the Milstein approximations, respectively. If $\triangle\tau$ is reduced to 0.001, maximum relative errors decreases to 5.7% and 1.1%, respectively.

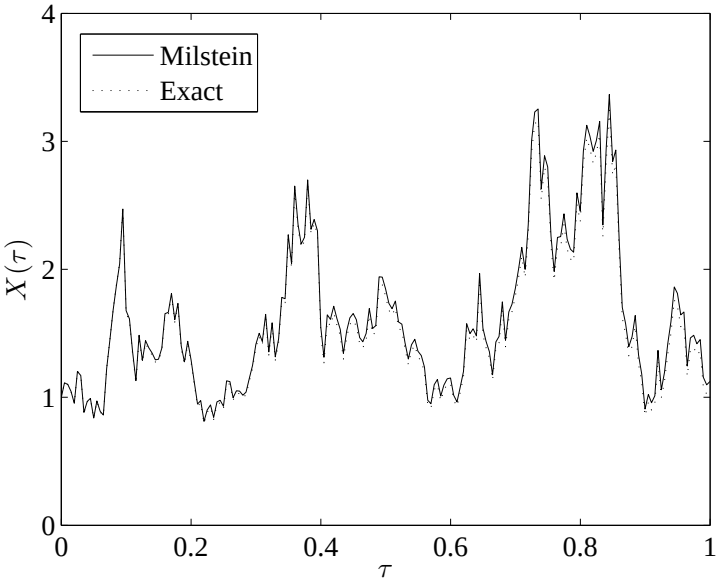

Figure 3.14: A Sample of $X(\tau)$ with the Milstein approximation

3.6 Effective Diffusivity

Let $D(\boldsymbol{x}) > 0$, $\boldsymbol{x} \in H$, $H \subset \mathbb{R}^d$, be a deterministic or random function defining the chloride diffusivity of a heterogeneous material specimen and let D^* be the chloride diffusivity of a homogeneous material specimen with the same geometry. Let J_{heter} and J_{homog} be the amount of chloride passing through the heterogeneous and homogeneous specimens, respectively. Then the effective diffusion coefficient D_{eff} is the value of D^* for which J_{homog} is equal to J_{heter}. D_{eff}

is a number and a random variable for deterministic and random heterogeneous materials, respectively.

3.6.1 Effective Diffusivity by the RWM

One of the objectives of this study is to propose a method to estimate the effective diffusion coefficient of chloride in a concrete specimen. For this purpose, a method based on the RWM given in Section 3.3.4 is chosen [75, 78, 80]. The advantage of this method is its applicability to random heterogeneous media with arbitrary number of phases and geometry. Derivation of the method, presented by Grigoriu and Papoulia [80], is reviewed briefly below.

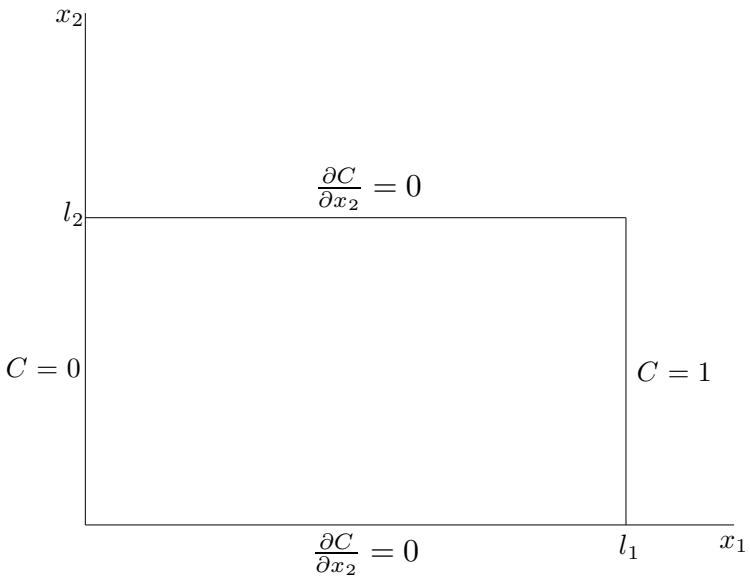

Figure 3.15: A 2D Heterogeneous Material Specimen

Consider a 2D rectangular specimen $H = (0, l_1) \times (0, l_2)$, $l_1 > 0$, $l_2 > 0$, with a deterministic chloride diffusivity field $D(\boldsymbol{x}) > 0$, $\boldsymbol{x} \in H$. Suppose that it is subjected to a unit chloride concentration field (Figure 3.15). The chloride

concentration $C(\boldsymbol{x})$, $\boldsymbol{x} \in H$, satisfies the partial differential equation

$$\sum_{p=1}^{2} \frac{\partial D(\boldsymbol{x})}{\partial x_p} \frac{\partial C(\boldsymbol{x})}{\partial x_p} + D(\boldsymbol{x}) \Delta C(\boldsymbol{x}) = 0, \tag{3.67}$$

with the Dirichlet boundary conditions

$$C(0, x_2) = 0 \quad \text{and} \quad C(l_1, x_2) = 1, \quad x_2 \in (0, l_2), \tag{3.68}$$

and the Neumann boundary conditions

$$\frac{\partial C(\boldsymbol{x})}{\partial x_2} = 0, \quad \boldsymbol{x} \in (0, l_1) \times \{0\} \quad \text{and} \quad \boldsymbol{x} \in (0, l_1) \times \{l_2\}. \tag{3.69}$$

The amount of chloride passing through the specimen in Figure 3.15 is

$$J_{\text{heter}} = \int_{x_1 \times (0, l_2)} D(\boldsymbol{x}) \frac{\partial C(\boldsymbol{x})}{\partial x_1} dx_2, \quad x_1 \in (0, l_1). \tag{3.70}$$

For a fictitious homogeneous specimen with the same geometry, it is

$$J_{\text{homog}} = D^* \frac{l_2}{l_1}. \tag{3.71}$$

Then the effective diffusion coefficient of chloride in the heterogeneous specimen is

$$D_{\text{eff}} = \frac{l_1}{l_2} \int_{x_1 \times (0, l_2)} D(\boldsymbol{x}) \frac{\partial C(\boldsymbol{x})}{\partial x_1} dx_2, \quad x_1 \in (0, l_1). \tag{3.72}$$

Since the effective diffusivity D_{eff} depends on the chloride diffusivity $D(\boldsymbol{x})$ and the chloride concentration gradient $\partial C(\boldsymbol{x})/\partial x_1$, and Eq. 3.67 is linear, D_{eff} is independent of the chloride concentration field to which the specimen is subjected, that is, the use of boundary conditions $C(0, x_2) = 0$ and $C(l_1, x_2) = 1$, $x_2 \in (0, l_2)$, is not restrictive [80].

Alternatively, it can be calculated by averaging the expression in Eq. 3.72 over a subset $(l_1 - \zeta, l_1) \times (0, l_2)$, $0 < \zeta < l_1$, of H or over the entire domain H, that is, from

$$D_{\text{eff}} = \frac{l_1}{\zeta l_2} \int_{(l_1 - \zeta, l_1) \times (0, l_2)} D(\boldsymbol{x}) \frac{\partial C(\boldsymbol{x})}{\partial x_1} d\boldsymbol{x} \tag{3.73}$$

or

$$D_{\text{eff}} = \frac{1}{l_2} \int_H D(\boldsymbol{x}) \frac{\partial C(\boldsymbol{x})}{\partial x_1} d\boldsymbol{x}. \tag{3.74}$$

Estimate of D_{eff} given by Grigoriu and Papoulia [80] is based on Eq. 3.72, which requires $\partial C/\partial x_1$ only on a line $x_1 \times (0, l_2)$. Suppose that the values of C at a collection of equally spaced points $(l_1 - \zeta, x_{2,k})$ have been calculated, where $x_{2,k} = (k + 1/2)\triangle x_2$, $k = 0, 1, \ldots, n_2 - 1$, $\triangle x_2 = l_2/n_2$, $n_2 \geq 1$ is an integer, and $0 < \zeta \ll l_1$ is a constant. Then the effective diffusion coefficient can be approximated by

$$D_{\text{eff}} \simeq \frac{l_1}{l_2} \triangle x_2 \sum_{k=0}^{n_2-1} D\left(l_1 - \zeta, x_{2,k}\right) \frac{1 - C\left(l_1 - \zeta, x_{2,k}\right)}{\zeta}. \tag{3.75}$$

Since the values of C is needed only on a line $(l_1 - \zeta, x_{2,k})$ to estimate the effective diffusion coefficient, it is not worthy to use a global method to calculate the values of C. Instead they can be calculated by the RWM given in Section 3.3.4.

Suppose that D_δ is an approximation to D, and let C_δ be the solution of Eq. 3.67 with D_δ in place of D. It can be shown that C_δ approximates C satisfactorily if D_δ satisfies some conditions and the approximate effective diffusion coefficient $D_{\text{eff},\delta}$ obtained with (D_δ, C_δ) in place of (D, C) converges to D_{eff} [80].

Let $\boldsymbol{X}_\delta$ be a series of $\mathbb{R}^2$-valued Itô processes defined by

$$d\boldsymbol{X}_\delta(\tau) = \boldsymbol{a}_\delta(\boldsymbol{X}_\delta(\tau))d\tau + \boldsymbol{b}_\delta(\boldsymbol{X}_\delta(\tau))d\boldsymbol{B}(\tau) \tag{3.76}$$

and

$$\tilde{\boldsymbol{X}}_\delta = \left[\tilde{X}_{\delta,1} = X_{\delta,1}, \tilde{X}_{\delta,2} = r(X_{\delta,2})\right] \tag{3.77}$$

be the $\mathbb{R}^2$-valued Itô process obtained from $\boldsymbol{X}_\delta$ by reflection at the Neumann boundaries $(0, l_1) \times \{0\}$ and $(0, l_1) \times \{l_2\}$, where $r(\varepsilon)$ is the periodic function with period $2l_2$ coinciding with $|\varepsilon|$ for $\varepsilon \in [-l_2, l_2]$. The drift and diffusion coefficients are supposed to have the form

$$a_{\delta,1}(\boldsymbol{x}) = \frac{\partial D_\delta(\tilde{\boldsymbol{x}})}{\partial \tilde{x}_1}, \quad a_{\delta,2}(\boldsymbol{x}) = r'(x_2)\frac{\partial D_\delta(\tilde{\boldsymbol{x}})}{\partial \tilde{x}_2}, \tag{3.78}$$

$$\boldsymbol{b}_\delta(\boldsymbol{x}) = \sqrt{2D_\delta(\tilde{\boldsymbol{x}})}\boldsymbol{i}, \tag{3.79}$$

where $\boldsymbol{x} \in (0, l_1) \times \mathbb{R}$ and $\tilde{\boldsymbol{x}} = (\tilde{x}_1 = x_1, \tilde{x}_2 = r(x_2)) \in H$.

The approximate chloride concentration is numerically equal to the expectation

$$C_\delta(\boldsymbol{x}) = E\left\{C_\delta(\tilde{\boldsymbol{X}}_\delta(T_\delta))\right\}, \quad \boldsymbol{x} \in H, \tag{3.80}$$

where $\tilde{\boldsymbol{X}}_\delta(0) = \boldsymbol{x} \in H$ and

$$T_\delta = \inf\left\{\tau \geq 0 : \tilde{\boldsymbol{X}}_\delta(\tau) \notin H\right\} \tag{3.81}$$

is a stopping time, that is, the time at which the process $\tilde{\boldsymbol{X}}_\delta$ exits H for the first time. The detailed proof of Eq. 3.80 is given by Grigoriu and Papoulia [80].

C_δ in Eq. 3.80 can be estimated by the Monte Carlo algorithm given in Section 3.3.4. First, n_s independent samples of $\boldsymbol{X}_\delta$, which starts at $\boldsymbol{X}_\delta(0, \omega) = \boldsymbol{x} \in H$, are generated in the time intervals $[0, T_\delta(\omega)]$, $\omega = 1, \ldots, n_s$. The corresponding samples $\tilde{\boldsymbol{X}}_\delta(\tau, \omega)$ of $\tilde{\boldsymbol{X}}_\delta$ are obtained by reflection (Eq. 3.77) with $\boldsymbol{X}_\delta(\tau, \omega)$ in place of $\boldsymbol{X}_\delta$. The samples $\tilde{\boldsymbol{X}}_\delta(\tau, \omega)$ do not leave H during the time interval $[0, T_\delta(\omega))$ and reach one of the Dirichlet boundaries of H at time $T_\delta(\omega)$. Second, $C_\delta(\boldsymbol{x})$ in Eq. 3.80 is estimated by

$$\hat{C}_\delta(\boldsymbol{x}) = \frac{1}{n_s}\sum_{\omega=1}^{n_s} C_\delta\left\{\tilde{\boldsymbol{X}}_\delta(T_\delta(\omega), \omega)\right\}, \tag{3.82}$$

which returns the fraction of samples of $\tilde{\boldsymbol{X}}_\delta$ exiting H through $\{l_1\} \times (0, l_2)$, since C_δ is 0 and 1 on the Dirichlet boundaries $\{0\} \times (0, l_2)$ and $\{l_1\} \times (0, l_2)$, respectively. The estimator associated with the estimate in Eq. 3.80 is unbiased and converges in probability to $C_\delta(\boldsymbol{x})$ as $n_s \to \infty$ for each $\delta > 0$ [80].

3.6.2 Examples

Two examples analyzing a material specimen with a deterministic diffusivity field and another one with a random diffusivity field are presented below to illustrate the estimation of effective diffusion coefficient by the RWM. The estimates of effective diffusion coefficients and chloride concentrations are based on Eqs. 3.75 and 3.80, respectively.

3.6.2.1 Deterministic Heterogeneous Material

Suppose that a material specimen $H = (0, l_1) \times (0, l_2)$, $l_1 = l_2 = 1$, has a deterministic diffusivity field defined by

$$D(\boldsymbol{x}) = 2 + \sin(2\pi x_1)\cos(2\pi x_2), \quad \boldsymbol{x} \in H. \tag{3.83}$$

D_{eff} has been obtained as 2.0 by using the MATLAB's *PDE Toolbox* in order to compare the estimates of D_{eff} based on the RWM. The parameters that affect the accuracy of $\hat{D}_{\text{eff}}$ are the number of points used to estimate D_{eff}, n_2, the distance between those points and the boundary $x_1 = l_1$, ζ, the time step used to generate samples of $\tilde{\boldsymbol{X}}$, $\triangle\tau$, and the number of samples of $\tilde{\boldsymbol{X}}$, n_s. A series of simulations has been performed for different values of parameters to examine their effects on the accuracy of $\hat{D}_{\text{eff}}$. Two of the samples of $\tilde{\boldsymbol{X}}$ are plotted in

Figs. 3.16 and 3.17. The $\hat{D}_{\text{eff}}$ calculated for different values of ζ, n_2, $\triangle\tau$ and n_s, and the corresponding relative errors calculated as

$$\epsilon_{\text{rel}} = \frac{|\hat{D}_{\text{eff}} - D_{\text{eff}}|}{D_{\text{eff}}} \times 100, \tag{3.84}$$

are given in Table 3.2.

Table 3.2: Effective Diffusion Coefficient by the RWM

ζ	n_2	$\triangle\tau$	n_s	$\hat{D}_{\text{eff}}$	Error (%)
0.1	2	10^{-3}	1000	2.4900	+24.5
0.1	5	10^{-3}	1000	2.4489	+22.4
0.1	10	10^{-3}	1000	2.4212	+21.1
0.1	10	10^{-4}	1000	2.1286	+6.4
0.1	10	10^{-5}	1000	1.9260	-3.7
0.05	10	10^{-5}	1000	2.0328	+1.6
0.05	10	10^{-6}	1000	1.9935	-0.3
0.05	10	10^{-6}	500	1.9729	-1.4
0.05	10	10^{-6}	100	1.7172	-14.1

In general, the values of ζ, n_2, $\triangle\tau$ and n_s are decided according to the limitations imposed by the available computational power. n_2 and n should be chosen as large as possible since the accuracy of $\hat{D}_{\text{eff}}$ improves as n_2 and n increases. After $\hat{C}$ at a given point is calculated for a sequence of decreasing time steps, time step can be selected as the largest time step for which $\hat{C}$ stabilizes. Similarly, $\hat{D}_{\text{eff}}$ should be calculated for several small values of ζ in order to decide the value of ζ making $\hat{D}_{\text{eff}}$ stable.

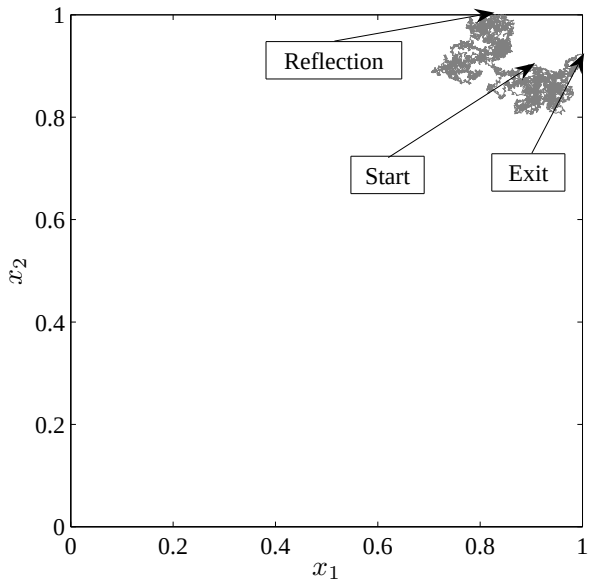

Figure 3.16: A Sample of $\tilde{\boldsymbol{X}}$

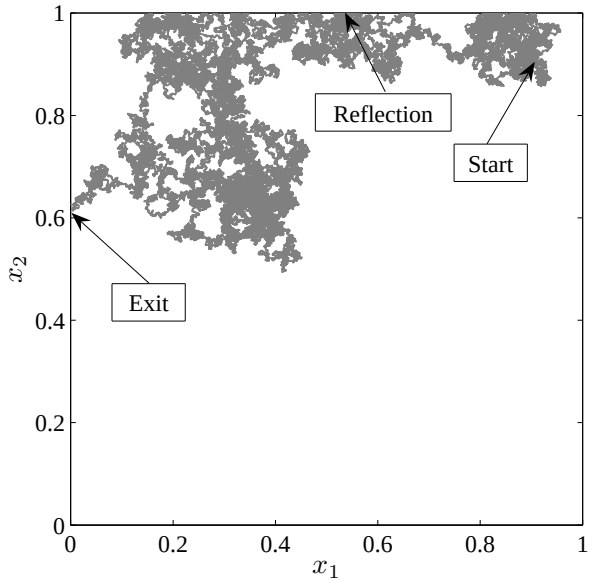

Figure 3.17: Another Sample of $\tilde{\boldsymbol{X}}$

3.6.2.2 Random Heterogeneous Material

Suppose that a material specimen $H = (0, l_1) \times (0, l_2)$, $l_1 = 10$, $l_2 = 5$, has a random diffusivity field D defined by Eq. 3.56, *i.e.*, $D(\boldsymbol{x}) = 0.1 + 0.9Z(\boldsymbol{x})$, $\boldsymbol{x} \in H$, where Z is a beta translation field taking values in $[0, 1]$ with shape parameters equal to 2.

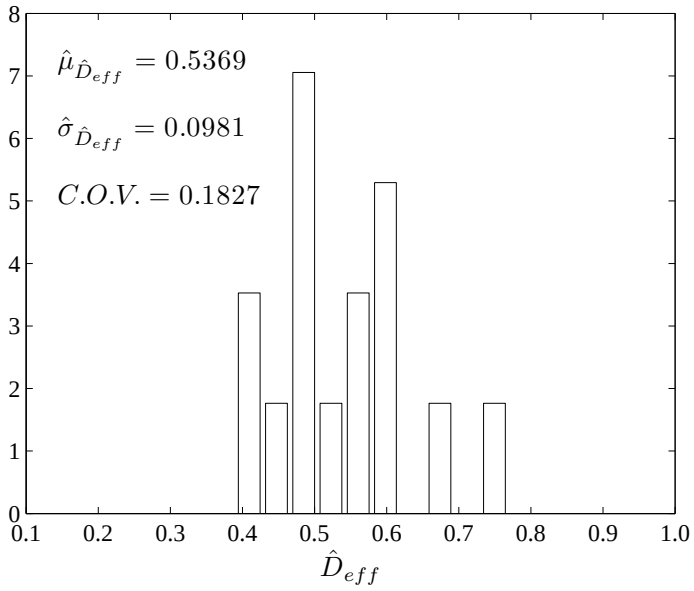

Figure 3.18: Histogram of $\hat{D}_{\text{eff}}$ by the MATLAB's *PDE Toolbox*

Estimates of D_{eff} have been calculated for 15 samples of diffusivity field D with $n_2 = 10$ and $\zeta = 0.1$. First, $\hat{D}_{\text{eff}}(\omega)$, $\omega = 1, \ldots, 15$, has been calculated by using the MATLAB's *PDE Toolbox*. Resulting estimates of mean, standard deviation and coefficient of variation of $\hat{D}_{\text{eff}}$ are 0.5369, 0.0981 and 0.1827, respectively. Then $\hat{D}_{\text{eff}}$, $\omega = 1, \ldots, 15$ has been calculated by using the method based on the RWM. Resulting estimates of mean, standard deviation and coefficient of variation of $\hat{D}_{\text{eff}}$ based on $n_s = 1000$ samples of $\tilde{\boldsymbol{X}}_\delta$ and a time step of $\triangle\tau = 10^{-6}$ are 0.5526, 0.1068 and 0.1934, respectively.

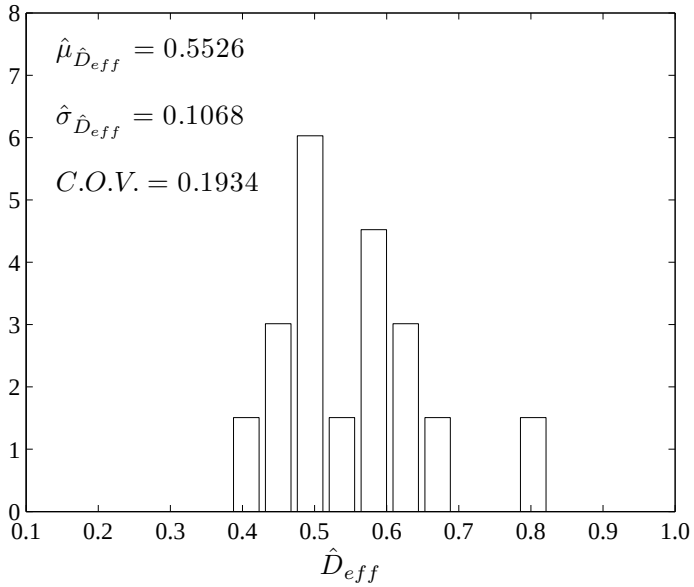

Figure 3.19: Histogram of $\hat{D}_{\text{eff}}$ by the Local Method

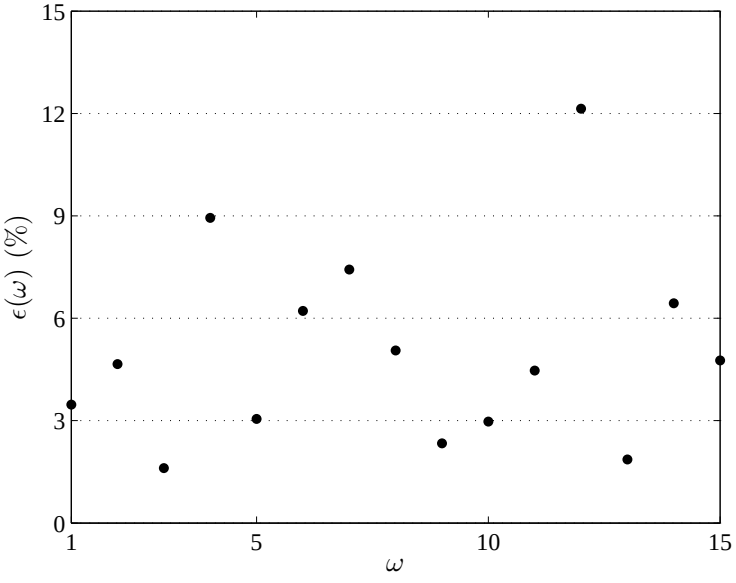

Figure 3.20: Relative error in $\hat{D}_{\text{eff}}$

Relative error in $\hat{D}_{\text{eff}}$ is calculated as

$$\epsilon_{\text{rel}}(\omega) = \frac{|\hat{D}_{\text{eff,RWM}}(\cdot,\omega) - \hat{D}_{\text{eff}}(\cdot,\omega)|}{\hat{D}_{\text{eff}}(\cdot,\omega)} \times 100, \quad \omega = 1,\ldots,15, \tag{3.85}$$

where $\hat{D}_{\text{eff,RWM}}$ and $\hat{D}_{\text{eff}}$ are the effective diffusion coefficients obtained by the RWM and the MATLAB's *PDE Toolbox*, respectively. Relative error for each sample of diffusivity field is shown in Figure 3.20. The maximum relative error is 12.1%.

3.7 Conclusion

A mathematical model for chloride diffusion in concrete is presented in the form of a partial differential equation. Numerical methods, both global and local, for solving this equation are reviewed. Since this research is interested in the solution of this partial differential equation only at particular points, a local method has been chosen as a solution method.

The local method, which is based on an extension of a random walk method, uses samples of an Itô process for obtaining a solution. Two examples, one of which explains how to analyze a material specimen with a random diffusivity field, are presented to illustrate the features of the local method. It has been observed that the computer algorithm employing the local method is simple to develop, stable and can be easily modified for parallel computing. The accuracy can be improved by increasing the number of samples of Itô process and/or decreasing the time step used for generating samples of Itô process.

A simple example for comparing the Euler's and Milstein's schemes is presented. As expected, better results have been obtained by using the Milstein's

scheme, since the order of convergence of the Milstein's scheme is higher than that of the Euler's scheme. However, the samples of Itô processes in the other examples have been generated by using the Euler's scheme in order to reduce the computational cost. Considering the fact that small values of time step have been chosen for generating samples of Itô processes, the use of Euler's scheme has not introduced a significant error.

A method based on the local method for calculating the effective diffusion coefficient of a material specimen is also presented. The method is applicable to random heterogeneous media with arbitrary number of phases and geometry. The analyses of two material specimens, one with a deterministic diffusivity field and the other with a random diffusivity field, are presented. It has been identified that the number of samples of Itô process, the time step used to generate samples of Itô process, the number of points used to estimate the effective diffusion coefficient and the distance between those points and the boundary of specimen are the parameters affecting the accuracy of the estimates.

CHAPTER 4

VIRTUAL SPECIMENS

4.1 Introduction

Particle packing is of interest to various research fields studying granular materials, the constituents of which are particles of any shape and size ranging from micrometers to centimeters. Powders, a special class of granular materials, refer to the granular materials with particle size in the order of micrometers. Numerous computer algorithms that simulate particle packing have been developed in order to be able to assess the packing characteristics of granular materials , particularly powders, without carrying out extensive experiments. The algorithms have become more sophisticated with the increasing computational power.

A common simulation approach is to use a sequential random-generator procedure. Basically, it is a static simulation method that sequentially places particles within a container by generating random coordinates for centroids of particles, rejects the coordinates and generates a new set of coordinates if particle overlapping occurs. The disadvantage of this approach is that, in general, computation time increases significantly with packing density. Moreover, it might not be possible to obtain high packing densities in some cases. In order to obtain dense packs, a dynamic simulation, in which particles are moved and rotated, is performed following the static simulation. Generally, the concept of discrete element method is applied in dynamic simulation. Particles are treated individually in discrete element method, that is, they are allowed to exhibit fi-

nite displacements and rotations separately. Another approach to obtain dense packs is to use a growth algorithm, where a number of points are randomly positioned within a container and particles are allowed to grow around those points while moving in the container. It is similar to an algorithm that generates a *Voronoi tessellation*. It is difficult to control particle size distributions in growth algorithms. There have been numerous researches on particle packing simulation methods, some of which are reviewed below.

Stroeven and Stroeven [156, 158] developed a software package, the Software Package for the Assessment of Compositional Evolution (SPACE), to assess the characteristics of random-packing in granular media. The simulation algorithm consists of two sequential stages. First, a structured or random 3D dilute distribution of particles is generated within a container according to a predefined shape and size distribution, and each particle is assigned random linear and rotational velocity vectors. Second, particles are moved and rotated at each time step according to a Newtonian motion model. Velocity vectors are updated when a contact occurs between particles. The size of the container is gradually reduced in time, so that dense packs are obtained. This iterative procedure is stopped when certain conditions, *e.g.*, required volume fraction of particles, are reached.

Fu and Dekelbab [55] proposed a computer simulation method, which consists of kinematics and dynamics simulations, for random packing of 3D particles. In the kinematics simulation stage, a box is filled with particles to a predetermined height. The particles, planar coordinates of which are random, are dropped sequentially from the top of the box. A dropping particle is allowed to rotate around the particles existing in the box until it is stabilized. A state of

loose random packing is obtained at the end of the kinematics simulation stage. In the dynamics simulation stage, a denser state of packing is obtained by moving the particles in the box. An equation of motion, which involves forces on particle due to gravity, contact and friction, is solved at every time step for each particle. In case of packing a large amount of particles, it is suggested to divide the entire matrix of particles into a few layers and pack each layer independently since the number of equations to be solved increases as the number of particles increases.

Buckmaster *et al.* [94, 95, 181] developed an algorithm to simulate random packing of heterogeneous propellants which consist of ammonium perchlorate particles imbedded randomly in a matrix called fuel binder. A number of points, each of which is assigned a random velocity, are randomly placed in a cube that is an element of a periodic array of cubes. Each point has a state vector consisting of its location and velocity. The points are partitioned into classes, each of which is assigned a different growing rate to produce spheres with different sizes. As time proceeds, a sphere grows around each point at a rate assigned to the class to which that point belongs. The spheres not only grow but also move in the cube and therefore collide. A collision algorithm, based on conservation of momentum, updates the velocity vectors of colliding spheres. Exit of a sphere through a face of the cube and collision of spheres are defined as the event times at which state vectors are updated. Also, the same algorithm can be used with ellipses instead of spheres. It was shown that packing fractions common in heterogenous propellants can be obtained by using the developed algorithm.

The algorithms reviewed above seem to be capable of simulating real inter-

actions between particles by use of discrete element method, but particles are represented by spheres which is a simplification to make computations easier and the duration of computations shorter since spheres are described by a single parameter, *i.e.*, radius. Deriving collision and overlap algorithms for particles of arbitrary shapes and computations by using those particles require much more effort. Gethin *et al.* [70, 133] combined finite element and discrete element methods not to generate packs but to study the deformations in a particulate system consisting of particles with arbitrary shapes. Despite the fact that particle shape has an important effect on the packing characteristics, researches on random packing of particles of arbitrary shapes have been limited.

Smith and Midha [151] remarked that the methods which use spherical particles with smooth surfaces for simulating powders overestimate powder packing densities since the spherical particles with smooth surfaces can be packed closer than the ones with asperities can be done. They developed a method for estimating powder packing densities by using a particle generation algorithm called random sphere construction, which models a particle as a combination of a central sphere and smaller spheres, called corner spheres, randomly located on its surface. Corner spheres, which represent asperities on the surface of the particles, increase the distances between particles, so that a more accurate estimate of powder packing density is obtained. Short-range random particle movements are performed during particle placement.

Jia *et al.* [89] used a digital approach to develop a particle packing software, called DigiPac, which can handle particles of arbitrary shapes. Particles, represented by coherent collections of pixels in a digitized packing space, are either scanned from real particles or generated within the software. At each time

step, particles move in a random direction, where each possible direction has an equal probability to be selected. The movement is one grid cell at a time, on a square lattice. Upward movements are accepted with a so-called rebounding probability, so that gravity effect is simulated. In addition to translation, particles are allowed to rotate. The advantages of the digital approach are: (i) particles of any shape and containers of any geometry can be represented, (ii) collision/overlap detection is simple, (iii) number of pixels, *i.e.*, storage space, does not depend on the complexity of the particle shape, and (iv) it can be performed on ordinary computers. The developed software was validated through a number of case studies [57].

The available packing softwares using the digital approach are inadequate for generating virtual concrete specimens because of the following reasons:

(i) Digital approach discretizes the domain of interest into pixels. However, the solution method presented in the previous chapter does not require discretization of domain.

(ii) Concrete is considered as a three-phase material consisting of aggregate, cement paste and interfacial transition zones. Concrete specimens range from centimeters to meters. Aggregate particles have a size range from micrometers to milimeters. The thickness of transition zones between aggregate particles and cement paste is in the order of micrometers. Hence, pixels with sides of order 1 μm are needed to construct digital concrete models. The resulting models are likely to be computationally infeasible. For example, 2.5×10^{11} pixels are required for a square specimen of size 50 cm.

The objective of the study presented in this chapter is to develop a particle

packing algorithm that generates 2D virtual concrete specimens, while the generation of 3D specimens is left as a further research. Concrete specimens have been modeled as virtual aggregate particles placed randomly within given containers, where space left from virtual aggregate particles has been assumed as cement paste. A stochastic model has been constructed to generate virtual aggregate particles, where the resulting representative elements are polygons, and a random sequential addition algorithm has been derived to pack randomly generated virtual aggregate particles. For this purpose, a MATLAB code has been developed to generate and to place virtual aggregate particles within a given container.

In Section 4.2 and Section 4.3, the algorithms developed to generate and to place a virtual aggregate particle are given, respectively. Constructing a virtual specimen by using the algorithms presented in Section 4.2 and Section 4.3, and input parameters of the MATLAB code are explained in Section 4.4. In Section 4.5, virtual concrete specimens generated by the developed algorithm is presented.

4.2 Particle Generation

A probabilistic model is developed for representing concrete aggregates in 2D. The model is used to implement a Monte Carlo algorithm for generating virtual concrete aggregates. First, a mathematical model of concrete aggregates is given. Second, an algorithm for generating virtual concrete aggregates is presented.

4.2.1 Mathematical Model

Concrete aggregate, referred to as particle within the rest of this chapter, is modeled by adding noise on an ellipse that has axes with random lengths. Consider an interval $I = (i_1, i_{n_i+1}]$, $0 < i_1 < i_{n_i+1} < \infty$, and partition I into subintervals $I_k = (i_k, i_{k+1}]$, $i_1 < i_2 < \ldots < i_k < \ldots < i_{n_i+1}$, $k = 1, \ldots, n_i$, where n_i is the number of subintervals. Let R_1 denote the length of the semi-major axis of an ellipse. Suppose that conditional on $R_1 \in I_k$, R_1 is uniformly distributed on I_k.

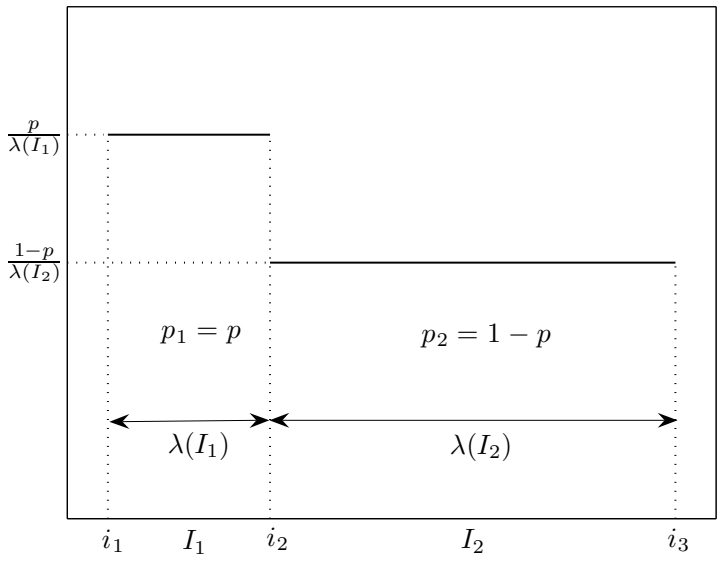

Figure 4.1: Probability Density Function of R_1 for $n_i = 2$

Then the probability density function of R_1 (Figure 4.1) is

$$f_{R_1}(r_1) = \sum_{k=1}^{n_i} 1(r_1 \in I_k) \frac{p_k}{\lambda(I_k)}, \tag{4.1}$$

where $\lambda(I_k)$ is the length of I_k, that is, $\lambda(I_k) = i_{k+1} - i_k$, and

$$p_k = P(R_1 \in I_k), \quad \sum_{k=1}^{n_i} p_k = 1. \tag{4.2}$$

Let I_Σ and R_2 denote an interval $(i_{\Sigma,1}, i_{\Sigma,2}], 0 < i_{\Sigma,1} < i_{\Sigma,2} \leq 1$, and the length of the semi-minor axis of the ellipse, respectively. Suppose that Σ is a random variable with a uniform distribution on I_Σ and independent of R_1, and R_2 has the form given by

$$R_2 = \Sigma R_1, \tag{4.3}$$

so that R_2 is dependent on R_1.

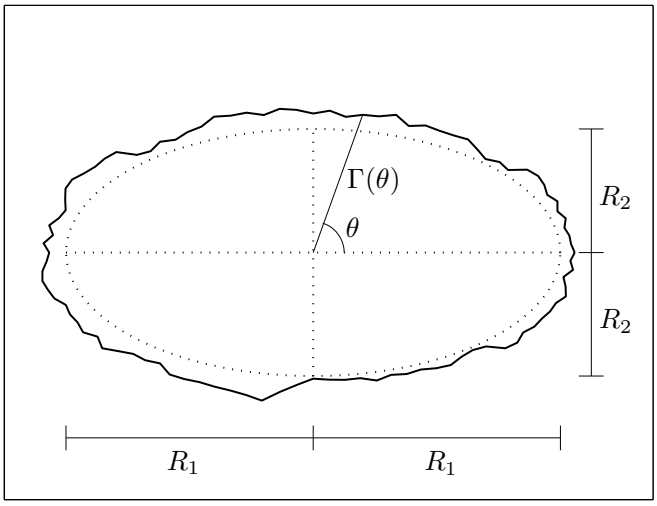

Figure 4.2: Schematic View of a Particle

Let F_Z denote the beta distribution function with shape parameters α_1 and α_2, and $Y(\theta)$, $\theta \in [0, 2\pi]$, be a Gaussian field with zero mean and unit variance, independent of R_1 and R_2. Then the random field

$$Z(\theta) = F_Z^{-1} \circ \Phi(Y(\theta)) \tag{4.4}$$

is called a *beta translation field* taking values in [0,1], where Φ is the standard Gaussian distribution function. The correlation function of Z is completely de-

fined by its marginal distribution and the covariance function of the underlying Gaussian field Y.

Since the ellipse and the noise have been defined, the equation of the particle can be given as

$$\Gamma(\theta) = R_1 \cos(\theta) + R_2 \sin(\theta) + g(R_1)Z(\theta), \quad \theta \in [0, 2\pi], \tag{4.5}$$

where Γ is the distance from a point on the boundary of the particle to the centroid of the ellipse, θ is the angle (counter-clockwise) with respect to the major axis of the ellipse and g is a function of R_1 which gives a positive scaling factor and will be defined in the following section.

In digital environment, particles are stored in discretized form, so that Eq. 4.5 is replaced with

$$\Gamma_q = R_1 \cos(\theta_q) + R_2 \sin(\theta_q) + g(R_1)Z_q, \tag{4.6}$$

where $\theta_q = (q-1)\triangle\theta$, $\triangle\theta = 2\pi/n$, $q = 1, \ldots, n+1$, and Z_q is a coordinate of a $(n+1)$-dimensional random vector

$$\boldsymbol{Z} = \left[\begin{array}{c} \boldsymbol{Z}^{(1)} \\ \hline \boldsymbol{Z}^{(2)} \end{array}\right] = \left[\begin{array}{c} Z_2 \\ \vdots \\ Z_n \\ \hline Z_1 \\ Z_{n+1} \end{array}\right] = \left[\begin{array}{c} Z(\theta_2) \\ \vdots \\ Z(\theta_n) \\ \hline Z(\theta_1) \\ Z(\theta_{n+1}) \end{array}\right] = \left[\begin{array}{c} F_Z^{-1} \circ \Phi(Y(\theta_2)) \\ \vdots \\ F_Z^{-1} \circ \Phi(Y(\theta_n)) \\ \hline F_Z^{-1} \circ \Phi(Y(\theta_1)) \\ F_Z^{-1} \circ \Phi(Y(\theta_{n+1})) \end{array}\right], \tag{4.7}$$

where $Y(\theta_q) = Y_q$ is a coordinate of a $(n+1)$-dimensional Gaussian vector

$$\boldsymbol{Y} = \left[\begin{array}{c} \boldsymbol{Y}^{(1)} \\ \hline \boldsymbol{Y}^{(2)} \end{array}\right] = \left[\begin{array}{c} Y_2 \\ \vdots \\ Y_n \\ \hline Y_1 \\ Y_{n+1} \end{array}\right] \sim N\left(\begin{array}{c} \boldsymbol{0} \end{array} , \begin{bmatrix} \boldsymbol{c}^{(1,1)} & \boldsymbol{c}^{(1,2)} \\ \boldsymbol{c}^{(2,1)} & \boldsymbol{c}^{(2,2)} \end{bmatrix} \right). \tag{4.8}$$

Partitions of covariance matrix $\boldsymbol{c}$ of $\boldsymbol{Y}$ are defined by

$$c_{i,j}^{(1,1)} = \rho^{|i-j|} \quad i,j = 1,\ldots,n-1, \tag{4.9a}$$

$$c_{i,1}^{(1,2)} = \rho^{i} \quad i = 1,\ldots,n-1, \tag{4.9b}$$

$$c_{i,2}^{(1,2)} = \rho^{n-i} \quad i = 1,\ldots,n-1, \tag{4.9c}$$

$$\boldsymbol{c}^{(2,1)} = \left(\boldsymbol{c}^{(1,2)}\right)^T, \tag{4.9d}$$

$$c_{i,j}^{(2,2)} = 1 \quad i = j = 1,2, \tag{4.9e}$$

$$c_{i,j}^{(2,2)} = \rho^{n} \quad i \neq j, \tag{4.9f}$$

where $\rho \in (0,1)$. The conditional vector $\tilde{\boldsymbol{Y}} = \boldsymbol{Y}^{(1)} \mid (\boldsymbol{Y}^{(2)} = \boldsymbol{y})$ is a $(n-1)$-dimensional vector with mean and covariance matrices

$$\tilde{\boldsymbol{\mu}} = \boldsymbol{c}^{(1,2)}(\boldsymbol{c}^{(2,2)})^{-1}\boldsymbol{y}, \tag{4.10}$$

$$\tilde{\boldsymbol{c}} = \boldsymbol{c}^{(1,1)} - \boldsymbol{c}^{(1,2)}(\boldsymbol{c}^{(2,2)})^{-1}\boldsymbol{c}^{(2,1)}, \tag{4.11}$$

respectively, where

$$\boldsymbol{y} = N(0,1)\begin{bmatrix} 1 \\ 1 \end{bmatrix}. \tag{4.12}$$

Then $\tilde{\boldsymbol{Y}}$ can be given in the form

$$\tilde{\boldsymbol{Y}} = \tilde{\boldsymbol{\mu}} + \boldsymbol{\beta}\boldsymbol{G}, \tag{4.13}$$

where $\boldsymbol{\beta}$ is the Cholesky decomposition of $\tilde{\boldsymbol{c}}$, i.e., $\boldsymbol{\beta}\boldsymbol{\beta}^T = \tilde{\boldsymbol{c}}$, and $\boldsymbol{G}$ is a standard Gaussian vector with independent and identically distributed coordinates.

4.2.2 Particle Generation Algorithm

Particle diameter is the maximum distance between any two points on the boundary of particle. A particle is considered as a particle of type-k if its diameter is in the interval $I_k^* = (d_{L,k}, d_{U,k}]$, $0 < d_{L,k} < d_{U,k} < \infty$, where $d_{L,k}$ and $d_{U,k}$ are the lower and upper particle diameter bounds for type-k particles, respectively (Figure 4.3).

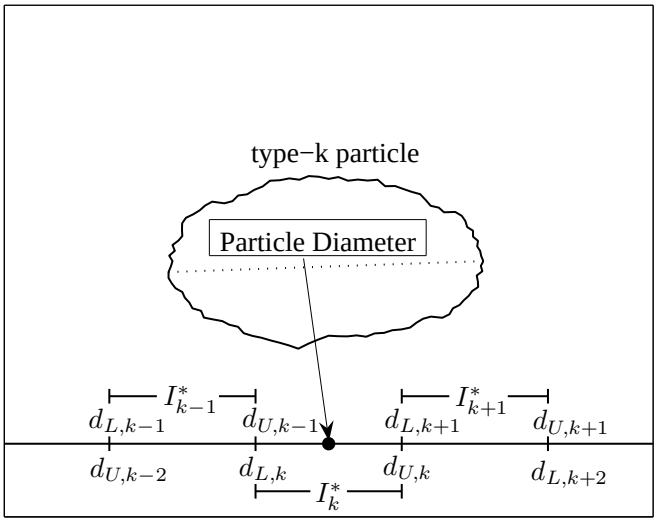

Figure 4.3: Particle of Type-k

Suppose that $\boldsymbol{c}$ (Eq. 4.9) is known for a given ρ, so that $\tilde{\boldsymbol{c}}$ (Eq. 4.11) and $\boldsymbol{\beta}$ are known, I_Σ is given and a particle of type-k will be generated. The algorithm to be followed is outlined below and shown as a flowchart in Figure 4.5.

- The subinterval I_k on which R_1 is assumed to be uniformly distributed is $(d_{L,k}/2, d_{U,k}/2]$. Then a semi-major axis $R_1(\omega) \in I_k$ is generated by using MATLAB's *rand* command, which returns a pseudo-random, scalar value

drawn from a uniform distribution on (0,1), as

$$R_1(\omega) = \frac{d_{L,k}}{2} + \text{rand}(1)\left(\frac{d_{U,k} - d_{L,k}}{2}\right). \tag{4.14}$$

- An axis ratio $\Sigma(\omega) \in I_\Sigma = (i_{\Sigma,1}, i_{\Sigma,2}]$ is generated by using MATLAB's *rand* command as

$$\Sigma(\omega) = i_{\Sigma,1} + \text{rand}(1)(i_{\Sigma,2} - i_{\Sigma,1}), \tag{4.15}$$

so that an ellipse with the semi-major axis of $R_1(\omega)$ and the semi-minor axis of $R_2(\omega) = \Sigma(\omega)R_1(\omega)$ is obtained.

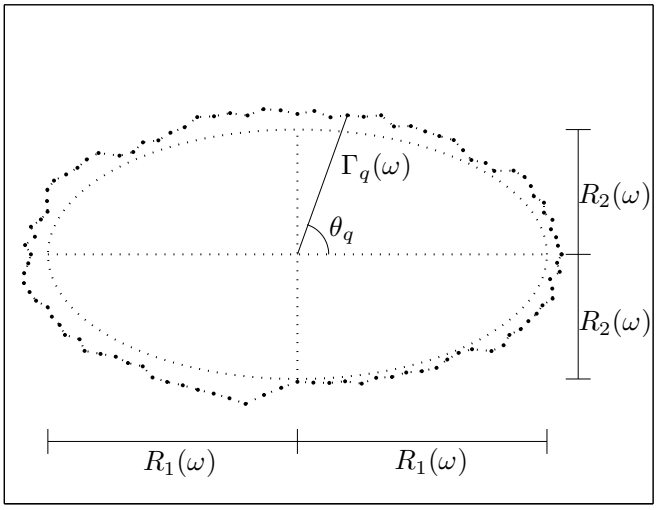

Figure 4.4: Virtual Discretized Particle

- $\boldsymbol{y}(\omega)$ is generated by using MATLAB's *randn* command (Eq. 4.12), which returns a pseudo-random, scalar value drawn from a normal distribution with zero mean and unit variance.
- The mean vector $\tilde{\boldsymbol{\mu}}(\omega)$ of $\tilde{\boldsymbol{Y}}(\omega)$ is calculated by using Eq. 4.10.
- $\boldsymbol{G}(\omega)$ is generated by using MATLAB's *randn* command.

- $\hat{\boldsymbol{Y}}(\omega)$ is calculated by using Eq. 4.13.
- $\boldsymbol{Y}(\omega)$ is constructed by using Eq. 4.8.
- $\boldsymbol{Z}(\omega)$ is obtained by memoryless transformation Eq. 4.7.
- Scaling factor is calculated by

$$g(R_1(\omega)) = \frac{d_{U,k}}{2} - R_1(\omega) \geq 0. \tag{4.16}$$

- Final shape of the particle (Figure 4.4) is obtained by using Eq. 4.6.

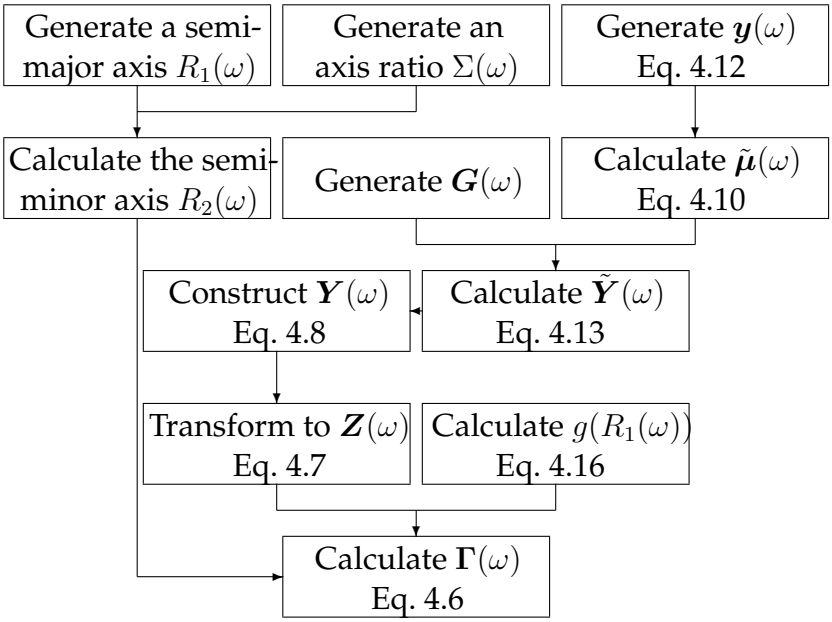

Figure 4.5: Generation of a Virtual Particle

4.3 Particle Placement

Particle placement is presented below by explaining, first, the algorithm of placing a single particle, second, the overlap detection algorithm used in par-

ticle placing algorithm. Let H denote a bounded rectangle whose lower-left corner coincides with the origin of $\mathbb{R}^2$, that is, $H = (0, l_1) \times (0, l_2)$, $l_1 > 0$, $l_2 > 0$. Suppose that the random point field N_h is a *homogenous Poisson field*. Conditional on $N_h(l_1, l_2) = n_h \geq n_p$, where n_p is the number of particles to be placed in H, the points of the Poisson field N_h are uniformly and independently distributed in H (Section 3.2, [152]), that is,

$$V_{m,1} \sim U(0, l_1) \quad \text{and} \quad V_{m,2} \sim U(0, l_2), \quad m = 1, \ldots, n_h \geq n_p, \tag{4.17}$$

where $V_{m,1}$ and $V_{m,2}$ denote the coordinates of point m.

Let Λ_j be the initial orientation angle of particle j, $j = 1, \ldots, n_p$. Λ_j is assumed to be uniformly distributed on $[0, 2\pi]$ and independent of the coordinates of point at which particle j will be placed.

4.3.1 Particle Placement Algorithm

Suppose that $j - 1$ particles have already been placed in H and particle j will be placed. The algorithm to be followed is outlined below and shown as a flowchart in Figure 4.9.

- Initial orientation angle of particle j, $\Lambda_j(\omega)$, is generated by using MATLAB's *rand* command as

$$\Lambda_j(\omega) = 2\pi \times \text{rand}(1). \tag{4.18}$$

- Point m, $m \geq j$, with coordinates $(V_{m,1}(\omega), V_{m,2}(\omega))$ is generated by using

MATLAB's *rand* command as

$$V_{m,1}(\omega) = l_1 \times \text{rand}(1), \tag{4.19a}$$

$$V_{m,2}(\omega) = l_2 \times \text{rand}(1). \tag{4.19b}$$

- Particle j is placed at point m in such a way that the centroid of ellipse is positioned at the coordinates $V_{m,1}(\omega)$ and $V_{m,2}(\omega)$, then, it is rotated clockwise by an amount of $\Lambda_j(\omega)$ (Figure 4.6).

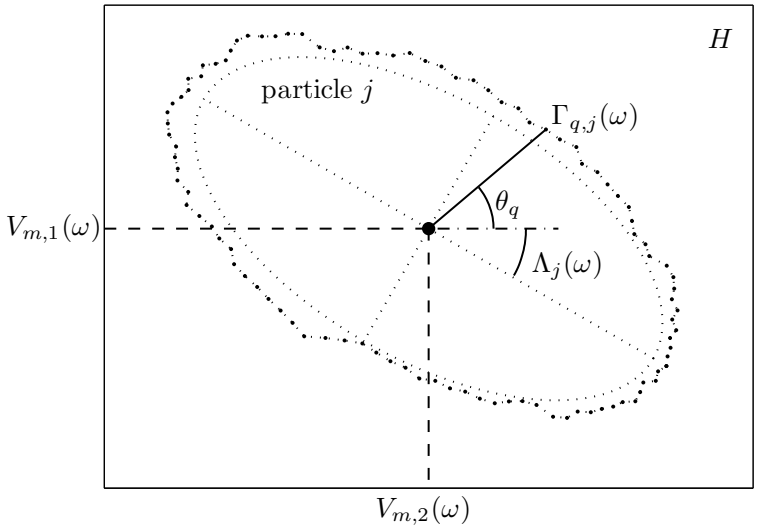

Figure 4.6: Placing Particle j

- It is checked whether particle j is in H or not.
- If particle j is not in H, it is rotated clockwise incrementally until it does not extend out of H. If no orientation angle is found to place particle j in H, a new point is generated and the same procedure is followed.
- After particle j is placed in H, it is checked whether particle j overlaps with another particle. If it does, particle j is rotated clockwise incrementally until it does not overlap with any other particle. If no orientation

angle is found to place particle j without overlapping, a new point is generated and the same procedure is followed.

If there exist points rejected during particle placement, the resulting random point field can no longer be called a homogenous Poisson field. The random field formed by the remaining points in H, denoted by N_p, is called a *Poisson hard-core field* or the *Matern hard-core model* [106, 152]. This type of a random field is generated by applying dependent thinning to the primary Poisson field N_h [152].

4.3.2 Overlap Detection Algorithm

Since the particles have random shapes, an algorithm has been developed to check overlapping. The algorithm that checks whether particle j overlaps with particle i, $i = 1, \ldots, j-1$, when the centroid of underlying ellipse of particle j is positioned at $(V_{m,1}(\omega), V_{m,2}(\omega))$, is outlined below.

- Distance between particles i and j is calculated by

$$\varphi_{i,j} = \sqrt{(V_{i,1}(\omega) - V_{m,1}(\omega))^2 + (V_{i,2}(\omega) - V_{m,2}(\omega))^2}, \tag{4.20}$$

  where $(V_{i,1}(\omega), V_{i,2}(\omega))$ are the coordinates at which the centroid of underlying ellipse of particle i is positioned.

- Let $\Gamma_{q,i}(\omega)$ be distance from point q on the boundary of particle i to the centroid of its underlying ellipse (Eq. 3.6). If the condition

$$\varphi_{i,j} \leq \max_{1 \leq q \leq n} (\Gamma_{q,i}(\omega)) + \max_{1 \leq q \leq n} (\Gamma_{q,j}(\omega)) \tag{4.21}$$

is not satisfied, there is no need to proceed since particles i and j cannot overlap.

- First, it is checked whether all points depicting particle i is outside the region enclosed by particle j or not (Figure 4.7). For this purpose, a local polar coordinate system is located at $(V_{m,1}(\omega), V_{m,2}(\omega))$. Let $(\varrho_{i,q}^{(m)}, \varsigma_{i,q}^{(m)})$, $q = 1, \ldots, n$, be the polar coordinates of points depicting particle i and $\varrho_{j,q}^{(m)}$ be the radius of the point on the boundary of particle j corresponding to the angle $\varsigma_{i,q}^{(m)}$ with respect to the local polar coordinate system just defined. If

$$\varrho_{i,q}^{(m)} > \varrho_{j,q}^{(m)}, \quad \forall\, q = 1, \ldots, n, \tag{4.22}$$

  is satisfied, then all points depicting particle i is outside the region enclosed by particle j.

- Second, it is checked whether all points depicting particle j is outside the region enclosed by particle i or not (Figure 4.8). For this purpose, a local polar coordinate system is located at $(V_{i,1}(\omega), V_{i,2}(\omega))$. Let $(\varrho_{j,q}^{(i)}, \varsigma_{j,q}^{(i)})$, $q = 1, \ldots, n$, be the polar coordinates of points depicting particle j and $\varrho_{i,q}^{(i)}$ be the radius of the point on the boundary of particle i corresponding to the angle $\varsigma_{j,q}^{(i)}$ with respect to the local polar coordinate system just defined. If

$$\varrho_{j,q}^{(i)} > \varrho_{i,q}^{(i)}, \quad \forall\, q = 1, \ldots, n, \tag{4.23}$$

  is satisfied, then all points depicting particle j is outside the region enclosed by particle i.

- If both Eqs. 4.22 and 4.23 are satisfied, then particles i and j do not overlap, so particle j is placed.

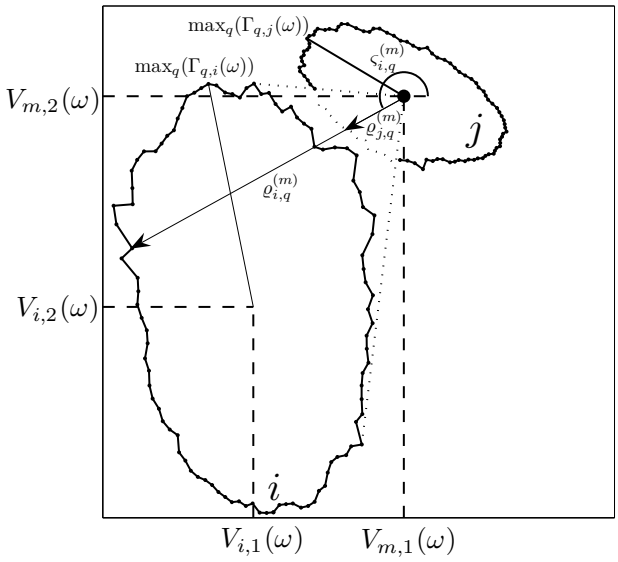

Figure 4.7: Local Polar Coordinate System Located at $(V_{m,1}(\omega), V_{m,2}(\omega))$

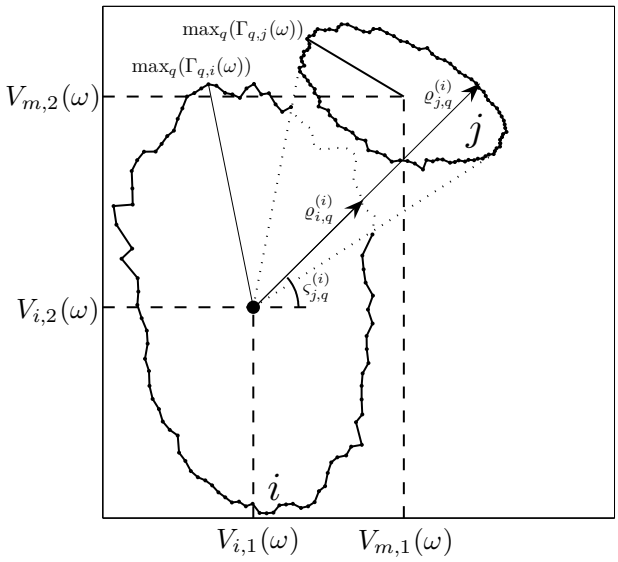

Figure 4.8: Local Polar Coordinate System Located at $(V_{i,1}(\omega), V_{i,2}(\omega))$

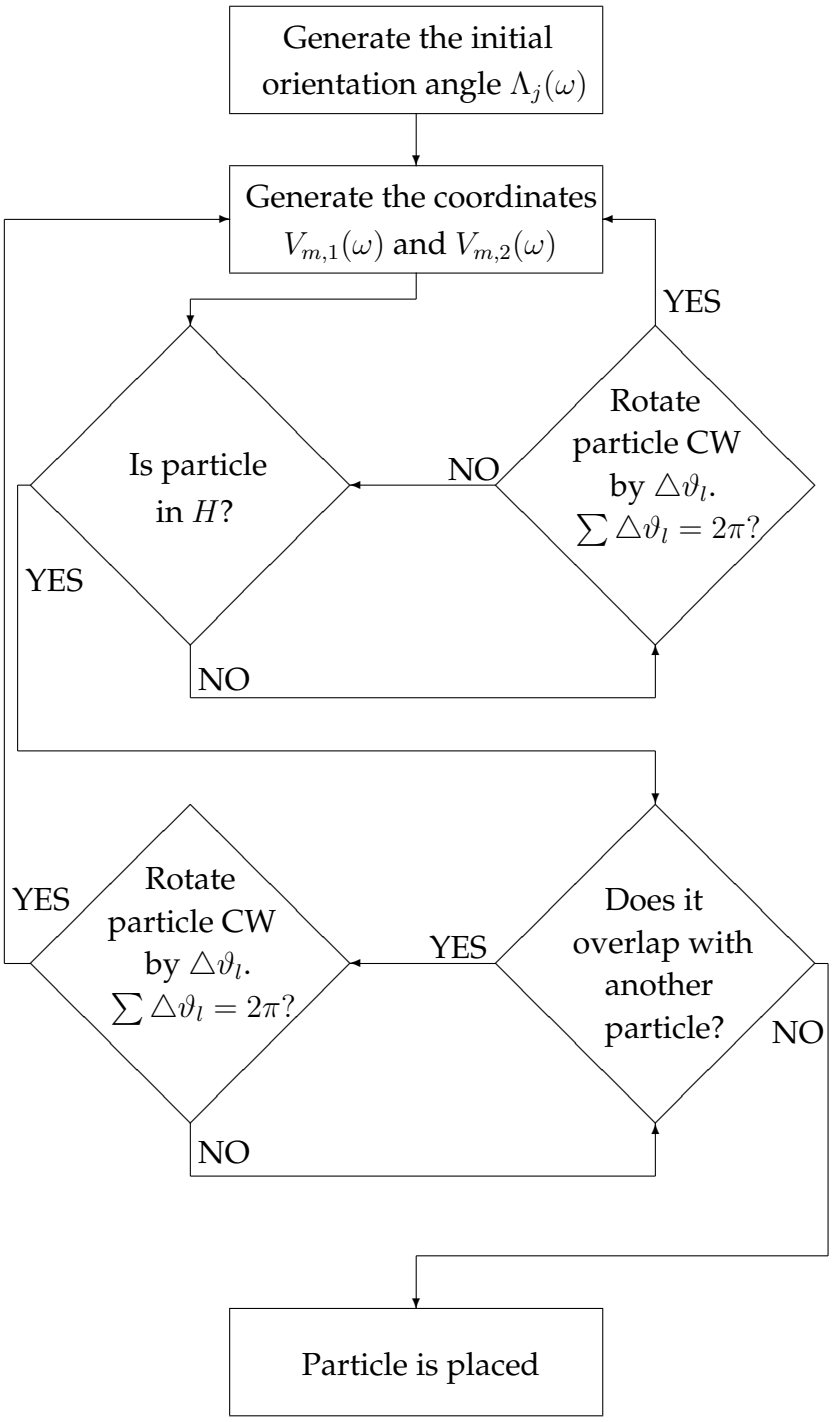

Figure 4.9: Placement of a Particle

4.4 Construction of Specimen

Having built the algorithms of particle generation and placement, construction of a specimen for a given input is straightforward. Input parameters are:

- particle size distribution, that is,
  - number of particle types, n_i.
  - lower and upper particle diameter bounds for each type, $I_k^* = (d_{L,k}, d_{U,k}]$, $k = 1, \ldots, n_i$, where $d_{U,k} = d_{L,k+1}$ for $k = 1, \ldots, n_i - 1$.
  - and proportion (by area) of each particle type, p_k, $\sum_{k=1}^{n_i} p_k = 1$,
- area fraction of particles, A_{agg},
- dimensions of specimen, l_1 and l_2,
- shape parameters of beta translation field, α_1 and α_2,
- ρ used in calculation of $\boldsymbol{c}$,
- and interval $I_\Sigma = (i_{\Sigma,1}, i_{\Sigma,2}]$ on which Σ is uniformly distributed.

Prior to construction of specimen,

- required total area of type-k particles, $A_k = p_k A_{\text{agg}} l_1 l_2$, $k = 1, \ldots, n_i$,
- intervals $I_k = (d_{L,k}/2, d_{U,k}/2]$,
- covariance matrices $\boldsymbol{c}$ of $\boldsymbol{Y}$ (Eq. 4.9) and $\tilde{\boldsymbol{c}}$ of $\tilde{\boldsymbol{Y}}$ (Eq. 4.11),
- and $\boldsymbol{\beta}$ (Cholesky decomposition of $\tilde{\boldsymbol{c}}$),

are calculated.

Construction of specimen is accomplished in two sequential stages. First, all particles are generated. Second, these particles are placed within a given rectangular container. The algorithm to be followed is outlined below:

- Particles are generated by using the algorithm given in Section 4.2. They are numbered according to the generation sequence. It does not matter which type of particles are generated first, but it is started with type-n_i in order to be consistent with the placing algorithm, so that the one with lower index has a larger diameter among the two particles of different types.
- Let $\hat{A}_k$ denote the total area of the particles that have been generated as type-k. Initially, number of all particles that needs to be generated is not known, so that after a type-k particle is generated, $\hat{A}_k$ is updated and it is checked whether $\hat{A}_k < A_k$ or not. If $\hat{A}_k < A_k$, next particle will also be generated as type-k, otherwise, it will be type-$(k-1)$, so that a collection of virtual particles in proportions, $\hat{p}_k$, approximately equal to the given p_k's, is obtained at the end of the particle generation stage.
- Particles are sequentially placed within the given container by using the algorithm presented in Section 4.3 in the order of their indexes, that is, the ones with larger diameter are placed first. If the ones with smaller diameter were placed first, there might not be enough space left for the ones with larger diameter after a few particles had been placed.
- While placing particle j, it is checked whether it overlaps with any of the $j-1$ particles that exist within the container. If it is found that particle j overlaps with one of the $j-1$ particles, there is no need to check the others.

- When all particles are placed, a virtual concrete specimen with area fraction of particles, $\hat{A}_{\text{agg}}$, approximately equal to the given A_{agg}, is obtained.

4.5 Examples

Three virtual concrete specimens have been generated to illustrate some of the features of the developed algorithm. First, a specimen has been generated to show that the developed algorithm is able to generate dense packs. Second, a smaller specimen has been generated to examine the size effect on packing characteristics. Third, a pack with coarser particles has been generated to observe the effect of particle size distribution on packing characteristics. The common parameters in all three examples are shape parameters of beta translation field Z, whose probability density function is given in Figure 4.10, $\alpha_1 = 2$ and $\alpha_2 = 7$, $\rho = 0.9$ and $I_\Sigma = (0.3, 0.9)$.

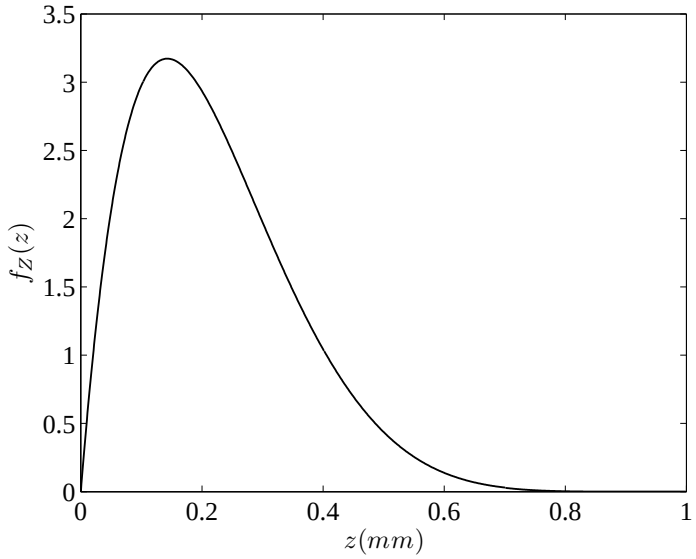

Figure 4.10: Probability Distribution Function of Z

4.5.1 Example 1: High Area Fraction of Particles

Particle size distribution has been characterized with $n_i = 7$ particle types with the corresponding particle diameter bounds, $d_{L,k}$ and $d_{U,k}$, and proportions, p_k, $k = 1, \ldots, 7$. Particle diameter bounds have been determined from the standard sieve sizes [3]. Particle diameter bounds and proportions chosen for this example are shown in Table 4.1. The area fraction of particles A_{agg} has been selected as 0.8, which is a very high value for ordinary concretes [114]. Dimensions of specimen are $l_1 = l_2 = 100$ mm.

Table 4.1: Particle Size Distribution (Specimen 1)

Type-k	$d_{L,k}$ (mm)	$d_{U,k}$ (mm)	p_k (by area)	$\hat{p}_k$ (by area)	Rel. Err. (%)
1	0.15	0.30	0.02	0.0199	-0.72
2	0.30	0.60	0.08	0.0794	-0.70
3	0.60	1.18	0.10	0.0993	-0.68
4	1.18	2.36	0.15	0.1490	-0.69
5	2.36	4.75	0.12	0.1191	-0.73
6	4.75	9.53	0.35	0.3483	-0.47
7	9.53	12.70	0.18	0.1849	+2.75

For the given input, 13659 particles have been generated in proportions, $\hat{p}_k$, shown in the fifth column with errors in the sixth column of Table 4.1. The resulting area fraction of particles is 0.8059. The generated virtual concrete specimen is plotted in Figure 4.11. Even though the developed algorithm does not have a dynamic simulation stage, the algorithm has been able to generate a specimen with a high area fraction of particles by rotating the particles.

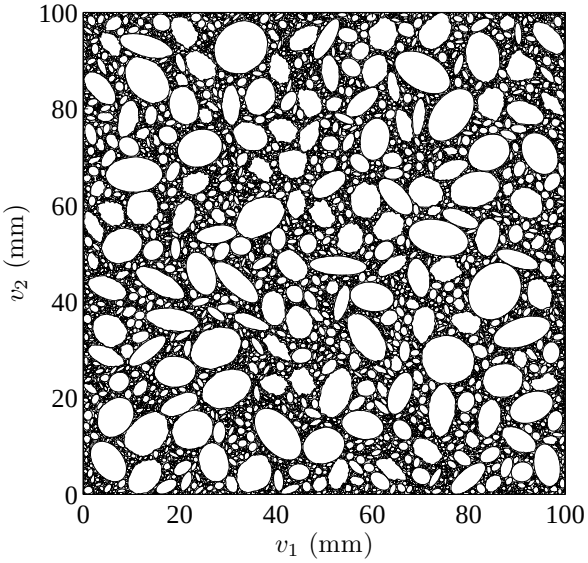

Figure 4.11: Virtual Concrete Specimen 1

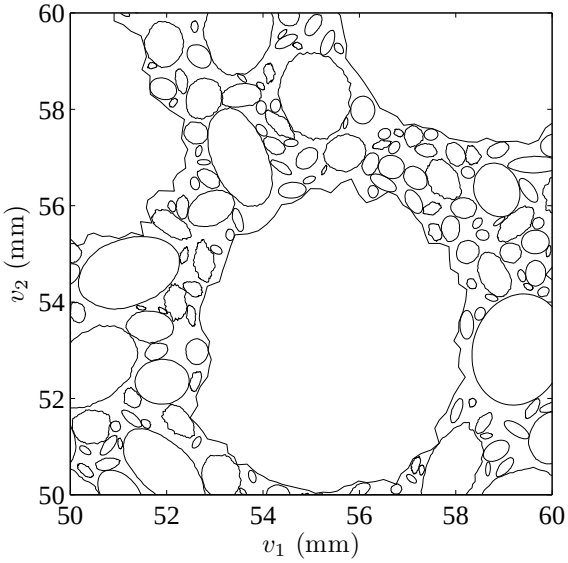

Figure 4.12: A Closer View of Particles

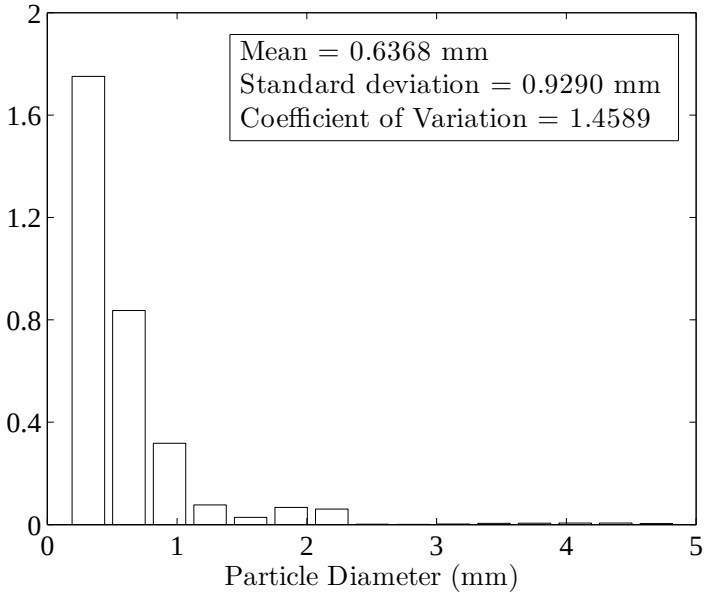

Figure 4.13: Histogram of Particle Diameters (Specimen 1)

4.5.2 Example 2: Size Effect

A smaller specimen, $l_1 = l_2 = 50$ mm, has been generated to examine the effects of the dimensions of specimen on the area fraction and proportions of generated particles. The rest of the input is the same as Example 1.

For this smaller specimen, 3412 particles have been generated in proportions shown in the fifth column with errors in the sixth column of Table 4.2. The resulting area fraction of particles is 0.8139. Relative error in the area fraction of particles is 1.73%, while it is 0.73% in Example 1, where a larger specimen has been generated. It has been observed that relative errors in the area fraction of particles and the proportions of particles increase as the dimensions of specimen decrease.

Table 4.2: Particle Size Distribution (Specimen 2)

Type-k	$d_{L,k}$ (mm)	$d_{U,k}$ (mm)	p_k (by area)	$\hat{p}_k$ (by area)	Rel. Err. (%)
1	0.15	0.30	0.02	0.0197	-1.68
2	0.30	0.60	0.08	0.0787	-1.68
3	0.60	1.18	0.10	0.0985	-1.54
4	1.18	2.36	0.15	0.1477	-1.52
5	2.36	4.75	0.12	0.1198	-0.16
6	4.75	9.53	0.35	0.3579	+2.27
7	9.53	12.70	0.18	0.1778	-1.25

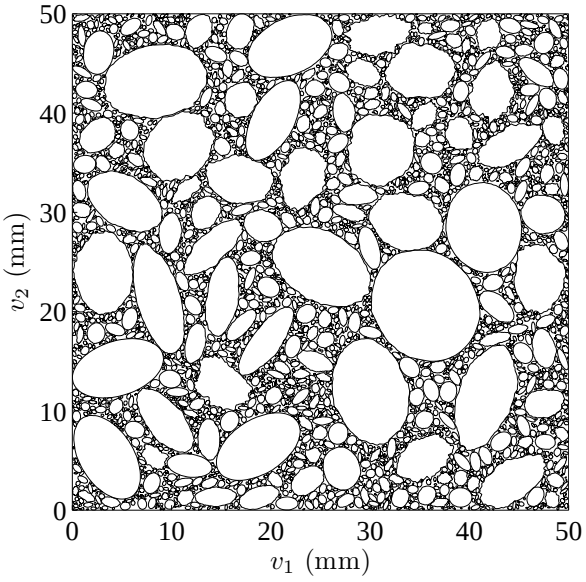

Figure 4.14: Virtual Concrete Specimen 2

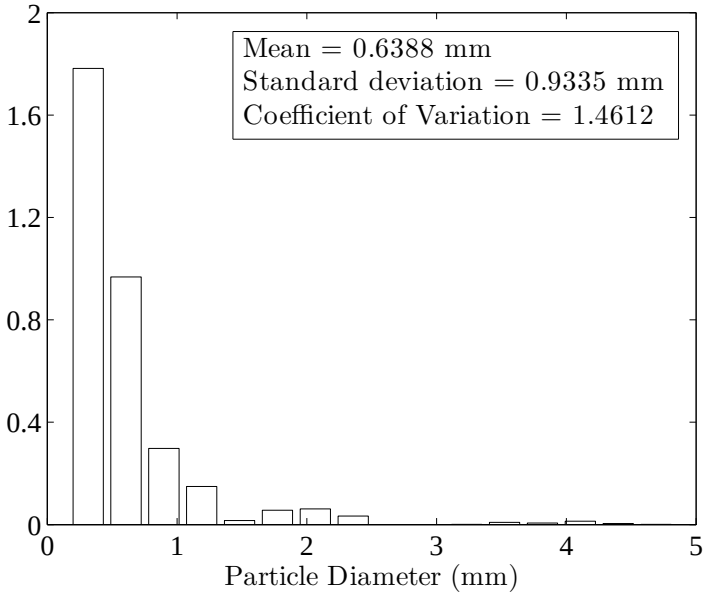

Figure 4.15: Histogram of Particle Diameters (Specimen 2)

4.5.3 Example 3: Effects of Particle Size Distribution

A specimen with $l_1 = l_2 = 50$ mm has been generated to examine the effect of particle size distribution on the area fraction of particles. Particle size distribution shown in Table 4.3 has been used. The area fraction of particles has been chosen as 0.6.

1740 particles have been generated in proportions shown in the fifth column with errors in the sixth column of Table 4.3. The resulting area fraction of particles is 0.6268, where relative error is 4.46%. It has been observed that relative errors in area fraction of particles and proportions of particles increase as fraction of coarser particles increases, particularly in a relatively small specimen.

Table 4.3: Particle Size Distribution (Specimen 3)

Type-k	$d_{L,k}$ (mm)	$d_{U,k}$ (mm)	p_k (by area)	$\hat{p}_k$ (by area)	Rel. Err. (%)
1	0.30	0.60	0.10	0.0958	-4.16
2	0.60	1.18	0.10	0.0958	-4.16
3	1.18	2.36	0.12	0.1150	-4.19
4	2.36	4.75	0.06	0.0586	-2.26
5	4.75	9.53	0.26	0.2611	+0.43
6	9.53	12.70	0.30	0.3024	+0.79
7	12.70	19.05	0.06	0.0712	+18.74

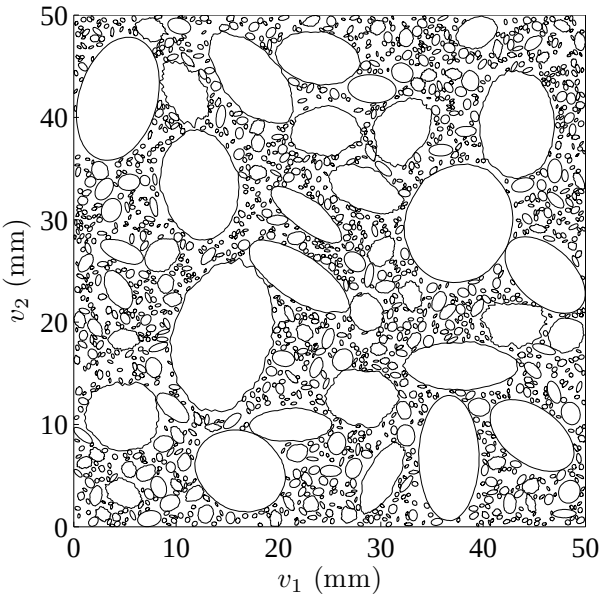

Figure 4.16: Virtual Concrete Specimen 3

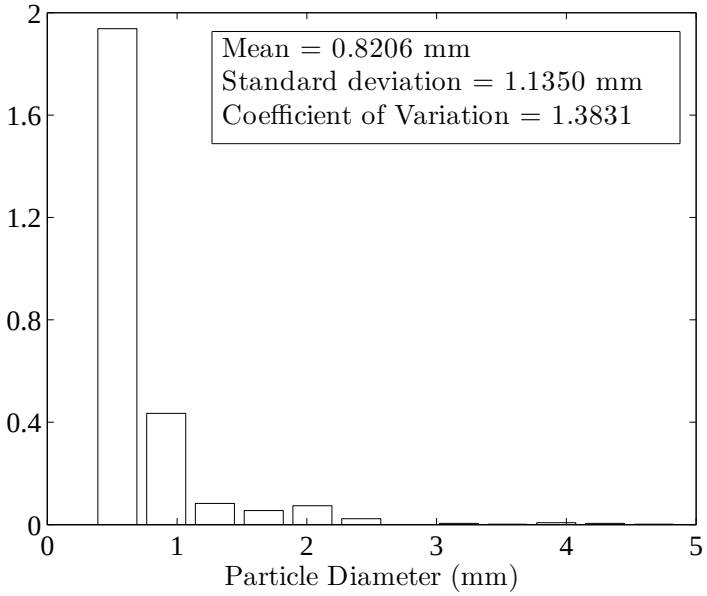

Figure 4.17: Histogram of Particle Diameters (Specimen 3)

4.6 Conclusion

A probabilistic model has been developed for representing concrete aggregate particles in 2D. The aggregate particles are ellipses with random geometry and size whose boundaries are altered by adding beta translation fields. A Monte Carlo algorithm has been implemented to generate virtual concrete aggregate particles in given proportions using this model.

A packing algorithm has been developed for generating 2D virtual concrete specimens. The algorithm sequentially places the virtual concrete aggregate particles within a given container such that the centroids of particles are positioned at random coordinates. The packing algorithm does not have a dynamic simulation stage. A dynamic simulation stage would require a collision algo-

rithm which detects the collisions between the particles and updates the velocity of the colliding particles according to a presumed collision mechanism. If particles had a simple and regular shape such as a sphere, it would be relatively easy to perform a dynamic simulation. However, constructing a collision algorithm for particles of arbitrary shapes and performing a dynamic simulation using these particles require significant computational effort.

Three examples are presented to illustrate the features of the particle generation and placement algorithms. It has been shown that the developed packing algorithm is capable of generating virtual concrete specimens with high area fraction of particles for ordinary concretes. It has been observed that the particle size distribution and the area fraction of particles in the generated specimen depends on specimen size. If the specimen size is relatively small with respect to the average aggregate size, then the particle size distribution in the resulting virtual concrete specimens can differ significantly from the target distribution.

It has been shown that the developed model enables generating 2D virtual concrete specimens consistent with observations. The generated virtual specimens will be used to estimate the transport characteristics of a given concrete specimen by using the local method.

CHAPTER 5

EFFECTIVE DIFFUSION COEFFICIENT

5.1 Introduction

Reinforced concrete is a widely used structural material due to its relatively low cost and high strength. Strength-based criteria are insufficient for the design of reinforced concrete structures since these structures deteriorate in time. In recent years, research focused on the mechanism of deterioration of reinforced concrete structures to develop durability-based design criteria. Current building codes specify durability-based design criteria as well as strength-based design criteria [110].

Reinforced concrete structures are likely to be subjected to various adverse conditions, *e.g.*, chemical attacks and freeze-thaw cycles. Of the various deterioration mechanisms of reinforced concrete structures, chloride-induced corrosion of steel reinforcement bars is of great importance since numerous reinforced concrete structures are exposed to chloride sources, *e.g.*, de-icing salts or marine environment [129].

Diffusion, convection, migration and permeation are chloride transport mechanisms in reinforced concrete structures (Section 2.3). For example, in case of a concrete exposed to drying-wetting cycles, *e.g.*, tidal conditions, chloride ingress occurs by a coupled mechanism of convection and diffusion. On the other hand, it is the diffusion that dominates the chloride transport through a fully saturated concrete, *e.g.*, fully submerged into seawater, unless there exists a high pressure head. Diffusion is of interest to this research, since it is the

most dominant chloride transport mechanism. A critical parameter for evaluating the resistance of concrete against chloride diffusion is the effective diffusion coefficient, which provides information on the rate of chloride ingress through concrete specimens.

The parameters affecting the diffusivity of chloride in concrete are discussed in Section 2.4. Section 5.2, Section 5.3 and Section 5.4 reviews the most common methods for obtaining the effective diffusion coefficient of chloride in cement paste, mortar or concrete. The application of the proposed method is illustrated within the rest of the chapter.

5.2 Experimental Techniques

Significant experimental work has been peformed to measure the resistance of concrete against chloride diffusion. Various experimental techniques, *e.g.*, diffusion-based methods and electrical methods, have been developed for this purpose. The most common ones are reviewed briefly below.

5.2.1 Diffusion-Based Methods

Diffusion-based experiments can be carried out under either steady-state or non-steady-state conditions. The idea in the steady-state diffusion experiments is to achieve a steady-state flow by applying a constant chloride concentration gradient across a material specimen [13, 28, 49, 71, 74, 85, 101, 119, 126]. A material specimen, in the shape of a thin disc, is mounted in between two reservoirs,

an upstream reservoir of high chloride concentration and an initially chloride-free downstream reservoir of low chloride concentration. Chloride ions diffuse from the upstream reservoir through the specimen to the downstream reservoir. The steady-state chloride flux is measured by monitoring the chloride concentration change in the downstream reservoir. Then the effective diffusion coefficient D_{eff} is obtained from Fick's first law [42] as follows:

$$D_{\text{eff}} = -J_{\text{down}} \frac{l_1}{\triangle C}, \tag{5.1}$$

where J_{down} is the chloride flux measured at the downstream face of the specimen, $\triangle C$ is the chloride concentration difference between the upstream and downstream reservoirs, and l_1 is the thickness of the specimen. Arsenault *et al.* [12] observed no significant effect of the specimen thickness on the measurements of chloride diffusion coefficient in mortar specimens, except for the duration to reach steady-state conditions. MacDonald and Northwood [101] observed a small decrease in the measurements of chloride diffusion coefficient in cement paste specimens with the increasing specimen thickness. The effective diffusion coefficient is independent of the chloride binding effect (see Section 2.3.2), because all chemical reactions involving chloride should be completed to achieve a steady-state flow [175]. However, the chloride binding mechanism affects the duration to reach steady-state conditions. Generally, it takes months, or even years, to achieve steady-state conditions.

In the case of the non-steady-state diffusion experiments, the chloride concentration profile across a material specimen is measured along time [31, 53, 88], and then the apparent diffusion coefficient D_{app}, which includes the chloride binding effect implicitly, is calculated from Fick's second law [42]:

$$\frac{\partial C(x,t)}{\partial t} = -D_{\text{app}} \frac{\partial^2 C(x,t)}{\partial x^2} \tag{5.2}$$

with the initial and boundary conditions

$$C(x,0) = 0, \quad x > 0, \tag{5.3a}$$

$$C(0,t) = C_s, \quad t > 0, \tag{5.3b}$$

$$C(x,t) = 0, \quad x \uparrow \infty, \quad t = \text{a large number}, \tag{5.3c}$$

where $C(x,t)$ is the chloride concentration at a distance x from the upstream surface of the specimen at time t, and C_s is the chloride concentration at the upstream surface of the specimen. The widely used solution to Eq. 5.2, which is valid with the semi-infinite medium assumption [42], is

$$\frac{C(x,t)}{C_s} = 1 - \text{erf}\left(\frac{x}{2\sqrt{D_{\text{app}}t}}\right), \tag{5.4}$$

where erf is the Gaussian error function given as

$$\text{erf}(y) = \frac{2}{\pi}\int_0^y e^{-t^2}dy, \quad y = \frac{x}{2\sqrt{D_{\text{app}}t}}. \tag{5.5}$$

The most prominent disadvantage of the diffusion-based experiments is that both the steady-state and non-steady-state experiments are time-consuming, especially for high performance concretes. There are two well-known standardized diffusion-based experimental techniques, (i) AASHTO T259 Test, and (ii) NordTest (NT-Build 443).

5.2.1.1 AASHTO T259 Test

The AASHTO T259 test [162], also referred to as the *90-day salt ponding test*, is a widely used experimental method for measuring the resistance of concrete to chloride ingress. Test specimen is a 75 mm thick concrete slab having a 300 mm by 300 mm surface. After 14 days of moist curing, the specimen is stored in

a drying room at 50% relative humidity for 28 days. Then a 3% NaCl solution is ponded on the top surface of the specimen for 90 days. The bottom surface is left exposed to drying environment and the sides are sealed. After 90 days of ponding, the specimen is removed from the drying environment, and the chloride concentrations at different depths are measured. The apparent diffusion coefficient is then obtained by fitting Eq. 5.4 to the measured chloride concentration profile [189].

There occurs an sorption effect when a specimen is first exposed to the chloride solution, since it has been kept in the drying room for 28 days. As a result of the sorption effect, the chloride solution is drawn into the capillary pores of the specimen. In addition to initial sorption effect, wicking takes place since the bottom surface of the specimen is exposed to the drying environment. Wicking is the movement of water into the specimen carrying chloride ions within itself due to the vapor transmission from the wet surface to the surface exposed to the drying environment. Therefore the chloride concentration profile provided by the AASHTO T259 test is not a result of diffusion only [153].

5.2.1.2 NordTest (NT-Build 443)

The NordTest [5] is the first standardized test among the bulk diffusion type of experiments. Contrary to the AASHTO T259 test, test specimen is saturated with limewater for 28 days, which prevents the sorption effect observed in the AASHTO T259 test, and the faces of the specimen, except the one exposed to the chloride solution, are sealed. It is kept fully submerged into a 2.8 M NaCl solution for at least 35 days. After the chloride concentrations at different depths are measured, the apparent diffusion coefficient is determined by fitting Eq. 5.4

to the measured chloride concentration profile. A similar experimental method has been proposed by ASTM C1556-04 [2].

5.2.2 Electrical Methods

Since the diffusion-based experiments are time-consuming, electrical methods, which reduce the duration of experiments significantly, have been developed for measuring the resistance of concrete against chloride ingress. When a concrete specimen is subjected to an electrical field, the movement of ions diffusing through the specimen is affected such that (i) the ions are directed towards electrodes, and (ii) they are accelerated proportional to their mobility and the magnitude of the applied electrical field [9]. Electrical methods can be divided into three as conduction experiments, steady-state and non-steady-state migration experiments. A well-known electrical method is rapid chloride permeability test (ASTM C1202 [1] or AASHTO T277 [163]). Despite its disadvantages, it is an important method regarding to its role in the development of migration experiments.

5.2.2.1 Rapid Chloride Permeability Test (RCPT)

The idea of RCPT was first proposed by Whiting [182]. Contrary to its name, it is not the permeability being measured but the ionic movement. RCPT uses a water-saturated concrete specimen having a thickness of 50 mm and a diameter of 100 mm. The specimen mounted in between two reservoirs, one of which contains a 3.0% NaCl solution and the other does 0.3 M NaOH solution, is subjected to a 60 V DC voltage [1, 163]. The chloride ion penetrability of the specimen is

evaluated according to the total charge passed through the specimen within 6 hours, where the higher the amount of total coulombs measured, the higher the "permeability" of the specimen (Table 5.1).

Table 5.1: RCPT Ratings [1]

Charge Passed (coulombs)	Chloride Ion Penetrability
> 4000	High
$2000 - 4000$	Moderate
$1000 - 2000$	Low
$100 - 2000$	Very Low
< 100	Negligible

Although it is a standardized experimental method, numerous researchers [8, 197] have criticized RCPT on the basis of the following issues:

- the amount of current passed through a concrete specimen is affected by all ions existing in its pore solution, not just by the chloride ions,
- the measurements are made before a steady-state flow is achieved,
- and the applied voltage is so high that it leads to an increase in temperature, which affects the rate of ionic movement.

5.2.2.2 Steady-State Migration Experiments

The discussions on RCPT led to the development of new electrical methods for measuring the resistance of concrete against chloride ingress [8, 49, 154, 197]. Steady-state migration experiment, inspired from RCPT, is based on the Nernst-

Planck equation [35], which describes the movement of ions in a solution subjected to an electrical field:

$$-J_j(x) = \underbrace{D_j \frac{dC_j(x)}{dx}}_{\text{Diffusion}} + \underbrace{D_j C_j(x) \frac{z_j F}{RT_a} \frac{d\Psi(x)}{dx}}_{\text{Migration}} + \underbrace{C_j(x) v_j(x)}_{\text{Convection}}, \tag{5.6}$$

where J_j is the flux of species j, D_j is the diffusion coefficient of species j, $C_j(x)$ is the concentration of species j at location x, z_j is the valence of species j, F is the Faraday's constant, R is the universal gas constant, T_a is the absolute temperature, Ψ is the applied electrical potential and $v_j(x)$ is the convection velocity of species j at location x. The flux of species j defined by Eq. 5.6 depends on diffusion, migration and convection of species j.

A standardized steady-state migration experiment is the Nordic standard NT BUILD 355 [4], the experimental setup of which consists of two electrolyte reservoirs separated by a concrete disc with a diameter of 100 mm and a thickness ranging from 15 mm to 50 mm. The thickness of a specimen is supposed to be larger than the maximum aggregate particle size in order to avoid an interfacial transition zone forming a path all the way through the specimen. A steady-state flow can be achieved in a few days by applying an electrical potential across the anodic and cathodic electrodes placed in the reservoirs. The diffusion and convection terms in Eq. 5.6 are generally considered as negligible compared to the migration term. Then D_{eff} can be calculated by using the simplified version of Eq. 5.6 such that

$$D_{\text{eff}} = J_{\text{down}} \frac{RT_a}{z_{\text{Cl}^-} F C_s} \frac{l_1}{\triangle \Psi}, \tag{5.7}$$

where J_{down} is the chloride flux measured at the downstream face of the specimen, C_s is the chloride concentration at the upstream surface of the specimen, l_1 is the thickness of the specimen, z_{Cl^-} is the valence of chloride ions and $\triangle \Psi$ is

the absolute value of the electrical potential difference between the electrodes. In the literature, D_{eff} obtained from migration experiments is also called the steady-state migration coefficient D_{ssm}. Truc *et al.* [175] pointed out possible errors in the resulting D_{eff} due to the use of chloride concentration change in the downstream reservoir for obtaining J_{down}, such as the error due to the evolution of chlorine gas, and suggested to measure the drop in the chloride concentration in the upstream reservoir.

The voltage applied in a migration experiment determines the duration of the experiment. The applied voltage should be low enough to avoid the evolution of gas at the electrodes and the heating of the specimen, while high enough to reduce the duration of the experiment considerably. A voltage range of 10-12 V is used commonly [12, 32, 33, 43, 49, 82, 107, 175, 197].

An alternative method for calculating the effective diffusion coefficient of chloride in a concrete specimen is to use the Nernst-Einstein equation [35]:

$$D_j = \frac{RT_a\kappa_j}{z_j^2F^2C_j}, \tag{5.8}$$

where κ_j is the specific conductivity of species j and the rest is the same as defined in Eq. 5.6. If the specific conductivity and concentration of species j are known, the diffusion coefficient of species j can be calculated. The specific conductivity of species j is

$$\kappa_j = t_j\kappa, \tag{5.9}$$

where κ is the conductivity of concrete and

$$t_j = \frac{Q_j}{Q}\frac{I_j^e}{I^e} \tag{5.10}$$

is the transference number of species j, where Q_j and I_j^e are the electric charge and current carried by species j, respectively, and Q and I^e are the total elec-

tric charge and current, respectively [8, 100]. Even though it is not correct, Lu [100] suggested to assume the transference number of chloride as 1. Then the effective diffusion coefficient of chloride in a concrete specimen can be calculated by equating C_j to the chloride concentration in the solution used to fill the specimen.

Zhang and Gjørv [197, 198] derived an alternative equation, based on the Einstein equation, for calculating the effective diffusion coefficient as

$$D_{\text{eff}} = \beta_0 \frac{300 k_B T_a}{z_{\text{Cl}^-} e_0 \triangle \Psi} \frac{l_1 V_{\text{res,up}}}{C_0 A_0} \frac{dC}{dt}, \tag{5.11}$$

where β_0 is the correction factor for ionic interaction (see Section 2.4.3), k_B is the Boltzman constant, e_0 is the charge of proton (or electron), $V_{\text{res,up}}$ is the volume of upstream reservoir, C_0 is the chloride concentration in the upstream reservoir, A_0 is the cross-sectional area of test specimen, dC/dt is the steady-state migration rate of chloride ions and the rest is the same as defined in Eqs. 5.6 and 5.7.

5.2.2.3 Rapid Migration Test (CTH Rapid Test)

Tang and Nilsson [168] proposed a different type of migration experiment using a test specimen with a thickness of 50 mm and a diameter of 100 mm, subjected to a voltage of 30 V. The difference from the usual migration experiment is that the specimen is removed and split after 8 hours, and the depth of chloride penetration is determined in one half of the specimen, using a colorimetric technique, *e.g.*, silver nitrate ($AgNO_3$) solution spray method, instead of monitoring the chloride concentration in the downstream reservoir. Then the effective diffusion coefficient is determined by using an equation derived from

the Nernst-Einstein equation (Eq. 5.8):

$$D_{\text{eff}} = \frac{RT_a}{z_{\text{Cl}^-}F\Psi}\frac{x_f}{t}, \tag{5.12}$$

where x_f is the inflection point of the chloride concentration profile, t is time and the rest is the same as defined in Eqs. 5.6 and 5.7. When a silver nitrate solution is sprayed on a concrete containing chloride ions, a white precipitate of silver chloride forms in the zone penetrated by chloride ions, whereas a brown precipitate of silver oxide forms in the absence of chlorides [125]. Otsuki *et al.* [125] determined the optimum solution as 0.1 N silver nitrate solution, resulting in a soluble chloride concentration of 0.15% by weight of cement at the color change border. The CTH Rapid Test has overcome the issues of RCPT about not examining chloride profile and causing errors due to a temperature increase resulting from high voltage. The Nordic standard NT BUILD 492 [6] is based on the CTH Rapid Test with some modifications.

5.2.2.4 Non-Steady-State Migration Experiments

In a non-steady-state migration experiment, it is a challenging task to determine the breakthrough time for chloride ions penetrating over through the specimen. Despite this difficulty, few researchers [82, 168] obtained good results from non-steady-state migration experiments. Halamickova *et al.* [82] applied a voltage of 12 V to mortar specimens having a thickness of 50 mm and a diameter of 100 mm. The upstream and downstream reservoirs were filled with 3% KCl solution and 0.3M KOH solution, respectively. The chloride diffusion coefficients, referred to as the non-steady-state migration coefficient D_{nssm}, were calculated from

$$-\frac{\partial J(x,t)}{\partial x} = \frac{\partial C(x,t)}{\partial t} = D_{\text{nssm}}\left(\frac{\partial^2 C}{\partial x^2} - \frac{zF\triangle\Psi}{RT_a l_1}\frac{\partial C}{\partial x}\right), \tag{5.13}$$

which has a solution given as

$$\frac{C(x,t)}{C_s} = \frac{1}{2}\left[e^{\xi_M x}\text{erf}\left(\frac{x+\xi_M D_{\text{nssm}} t}{2\sqrt{Dt}}\right) + \text{erf}\left(\frac{x-\xi_M D_{\text{nssm}} t}{2\sqrt{Dt}}\right)\right], \quad (5.14)$$

where $\xi_M = (zF\triangle\Psi)/(RT_a l_1)$ and the initial and boundary conditions are the same as Eq. 5.3.

The calculation of the D_{nssm} is based on the time delay t_D, defined as the time at which the initial increase in the chloride concentration in the downstream reservoir is detected. The ratio of $C(l_1, t_D)$ to C_s is a small number at the first reliable detection. Halamickova *et al.* [82] used a value of 0.005 for this ratio. The change in the chloride concentration in the upstream reservoir does not affect the value of t_D but the rate of the change in the chloride concentration at the downstream face after t_D. Hence, the chloride concentration in the upstream reservoir should be kept constant in order to be able to calculate the chloride diffusion coefficient from the slope of the chloride concentration profile after t_D.

Samson *et al.* [144] proposed an alternative multi-ionic approach to calculate the diffusion coefficient of each species in concrete from the results of a non-steady-state migration experiment. It is suggested to use two disc-shaped specimens, which have a diameter of 100 mm and a thickness ranging from 25 mm for mortar to 50 mm for concrete, per mixture. The specimens are vacuum saturated in a 0.3 M NaOH solution prior to testing. Both reservoirs are filled with a NaOH solution prepared at a pH of 13.5 in order to minimize the microstructural changes during the experiment. The upstream reservoir also contains NaCl or Na_2SO_4. An electrical potential of 500 V/m is applied across the specimen. The current passing through the specimen and the chloride concentration in the downstream reservoir are recorded for 120 hours. Then the experimental data are analyzed with the coupled extended Nernst-Planck/Poisson

set of equations:

$$\frac{\partial C_j(x,t)}{\partial t} - D_j \frac{\partial}{\partial x}\left[\frac{\partial C_j(x,t)}{\partial x} + C_j(x,t)\left(\frac{z_j F}{RT_a}\frac{d\Psi}{dx} + \frac{d\ln\gamma_j}{dx}\right)\right] = 0 \quad (5.15)$$

$$\tau_{\mathrm{t}}\frac{d^2\Psi}{dx^2} + \frac{F}{\varepsilon_{\mathrm{d}}}\sum_{j=1}^{N} z_j C_j(x,t) = 0 \quad (5.16)$$

where $C_j(x,t)$ is the chloride concentration of species j at position x and time t, $D_j = \tau_{\mathrm{t}} D_j^{\mu}$ is the diffusion coefficient of species j in the specimen, τ_{t} is the tortuosity of the specimen, D_j^{μ} is the diffusion coefficient of species j in the free water, γ_j is the chemical activity coefficient, ε_{d} is the dielectric permittivity of the specimen and the rest is the same as defined in Eqs. 5.7 and 5.8. Since the set of equations defined by Eq. 5.15 cannot constitute a complete set of equations, another relation (Eq. 5.16) that accounts for the electrical potential locally induced by the movement of all ions is used to have a complete set of equations. Eqs. 5.15 and 5.16 need to be solved simultaneously to analyze the experimental data since the equations are coupled. They are solved for different values of tortuosity τ_{t}. Then for each value of τ_{t}, the error between the measurements and the model is calculated as

$$\epsilon = \sqrt{\sum_{k=1}^{M}\left(I_{e,k}^{\mathrm{mes}} - I_{e,k}^{\mathrm{num}}\right)^2}, \quad (5.17)$$

where M is the number of measurements, $I_{e,k}^{\mathrm{mes}}$ and $I_{e,k}^{\mathrm{num}}$ are the measured and predicted currents passing through the system, respectively. The best estimate of the diffusion coefficient of each species in the specimen is determined from the tortuosity value yielding the smallest error. For simplicity, Eqs. 5.15 and 5.16 are given for one-dimensional space, but the method is applicable to multi-dimensional spaces. The detailed discussions on modeling ion diffusion mechanisms by solving the coupled extended Nernst-Planck/Poisson set of equations can be found elsewhere [91, 96, 113, 139, 140, 142, 143, 176].

5.2.2.5 Resistivity/Conductiviy Experiments

Concrete conducts electric current as an electrolyte, in other words, electricity is conducted through concrete by the ions present in its pore solution [28]. Since solid phases are highly resistive, their contribution to the conductivity is neglected. The idea in the resistivity/conductivity experiments is to measure the electrical resistance of concrete, and then to relate it to the chloride diffusivity in concrete. Resistivity, the inverse of conductivity, is the electrical resistance of a medium, normalized to a unit area and length. In a saturated porous medium, where the solid phase is an insulator, the relationship between conductivity and diffusivity is given by

$$\frac{D_{\text{eff}}}{D_0} = \frac{\kappa_{\text{eff}}}{\kappa_0}, \tag{5.18}$$

where D_{eff} and κ_{eff} are the effective diffusion coefficient of chloride in the porous medium and the effective conductivity of the porous medium, respectively, D_0 and κ_0 are the chloride diffusivity in the pore solution and the conductivity of the pore solution, respectively [154]. A resistivity/conductivity experiment can be carried out by using either alternating current [112] or direct current [154]. The resistivity/conductivity of the specimen is calculated from the measured values of electric current.

Even though the resistivity/conductivity experiments are fast and avoid the heating of specimens, there exist difficulties in determining the conductivity of pore solution, which is done by either removing the pore solution from the specimen or saturating the specimen with a solution of known conductivity before the experiment [153].

Díaz *et al.* [51] used a method based on impedance spectroscopy (IS), where

impedance measurements are made by using both two-electrode and four-electrode arrangements, and chloride concentration is measured by using a chloride-selective electrode. The resistivity of a specimen is obtained by fitting the measured impedance data to an equivalent electrical model. The advantages of IS technique are [51, 150]: (i) it is non-destructive, (iii) it allows in-situ testing, and (ii) it returns real time data on the variation of diffusion coefficient with time.

Rapid chloride permeability test (RCPT) is a type of conductivity test. It is considered at the beginning of the review of electrical methods (Section 5.2.2.1) since it led to the development of latter electrical methods.

5.2.3 Pressure Penetration Method

An alternative method of accelerating the chloride ingress through a mortar/concrete specimen is to expose one of the faces of the specimen to a chloride solution under an applied pressure [153]. Then chloride is driven into the specimen under both convection and diffusion, described by the equation

$$\frac{\partial C(x,t)}{\partial t} = D_{\text{app}} \frac{\partial^2 C(x,t)}{\partial x^2} - \bar{v} \frac{\partial C(x,t)}{\partial x}, \quad \bar{v} = -\frac{k}{\phi} \frac{\partial h_p}{\partial x}, \tag{5.19}$$

where $\bar{v}$ is the average linear rate of flow, k is the hydraulic permeability, ϕ is the porosity, h_p is the applied pressure head [54]. The solution to Eq. 5.19 is given as

$$\frac{C(x,t)}{C_s} = \frac{1}{2}\left[\exp\left(\frac{\bar{v}x}{D_{\text{app}}}\right) \text{erf}\left(\frac{x+\bar{v}t}{2\sqrt{D_{\text{app}}t}}\right) + \text{erf}\left(\frac{x-\bar{v}t}{2\sqrt{D_{\text{app}}t}}\right)\right], \tag{5.20}$$

where the initial and boundary conditions are the same as Eq. 5.3.

5.2.4 A Brief Comment on Experimental Techniques

It is important to note that the equations to obtain transport coefficients from diffusion and migration experiments are one-dimensional, except multi-ionic approach by Samson *et al.* [144]. This is inevitable since the data obtained from such experiments are one-dimensional.

Chloride diffusion coefficients reported in the literature (see Appendix A) may differ, sometimes widely, mainly due to the differences in the hypotheses behind the methods. For instance, the driving force in diffusion-based experiments is the chloride concentration gradient, while it is the electrical potential in migration experiments, therefore they are not directly comparable in general. There have been numerous attempts, some of which mentioned herein, to establish a relationship between the results obtained from different types of experiments.

McGrath and Hooton [108], and Andrade and Whiting [11] compared the results obtained from 90-day salt ponding test and RCPT. The relationship between the integral chloride content (by mass of concrete), the area under the chloride profile obtained from a 90-day salt ponding test, and the RCPT number measured by McGrath and Hooton [108] is shown in Figure 5.1, in which scattering of data can be observed. The coefficient of determination r^2 for a linear fit of the data was calculated as 0.34 [108]. McGrath and Hooton [108] modified the ponding test by eliminating the partially saturated condition of the specimens to make diffusion the dominant process. They identified the relationship between the penetration depth at 0.1% chloride concentration and the RCPT number as the best correlation (Figure 5.2), where the r^2 was calculated as 0.83 [108].

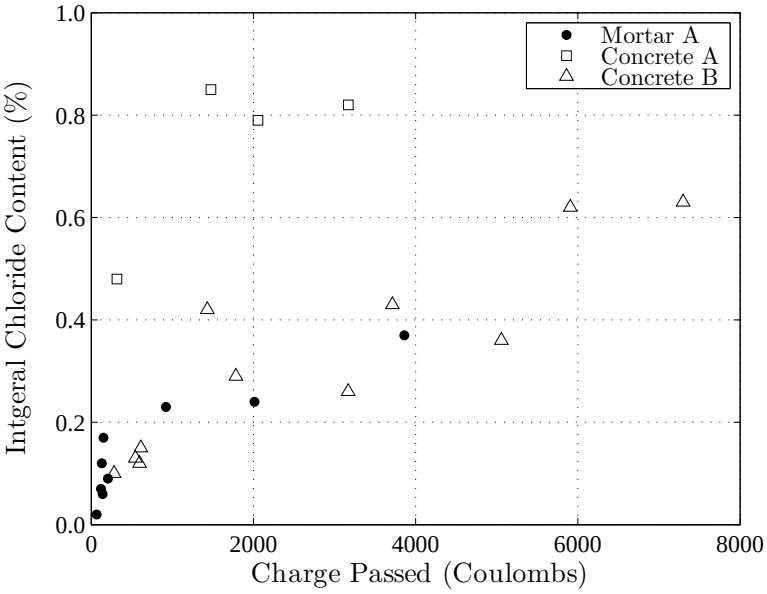

Figure 5.1: AASHTO T259 vs. RCPT [108]

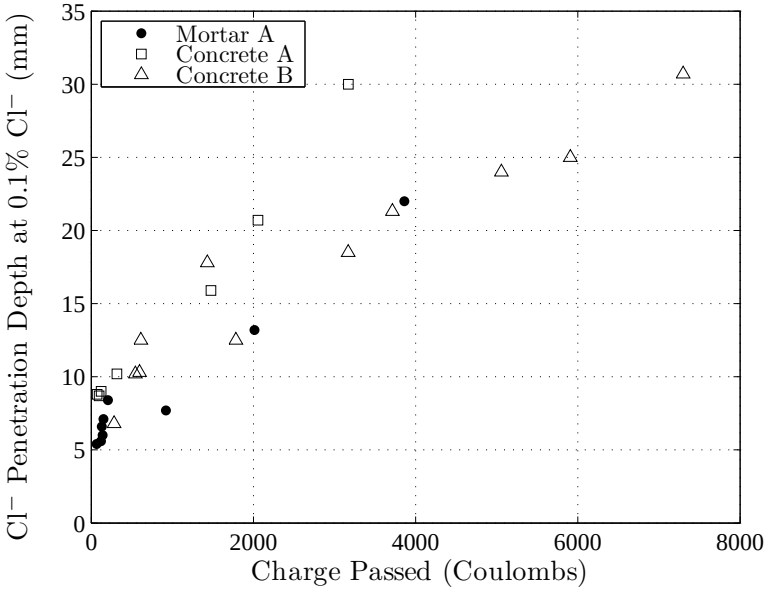

Figure 5.2: Modified Ponding Test (AASHTO T259) vs. RCPT [108]

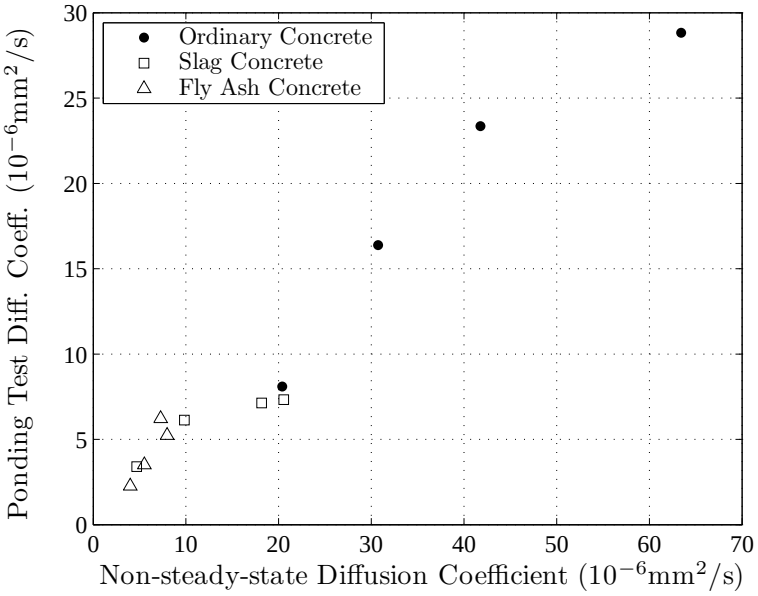

Figure 5.3: Non-steady-state Migration Test vs. 90-Day Ponding Test [189]

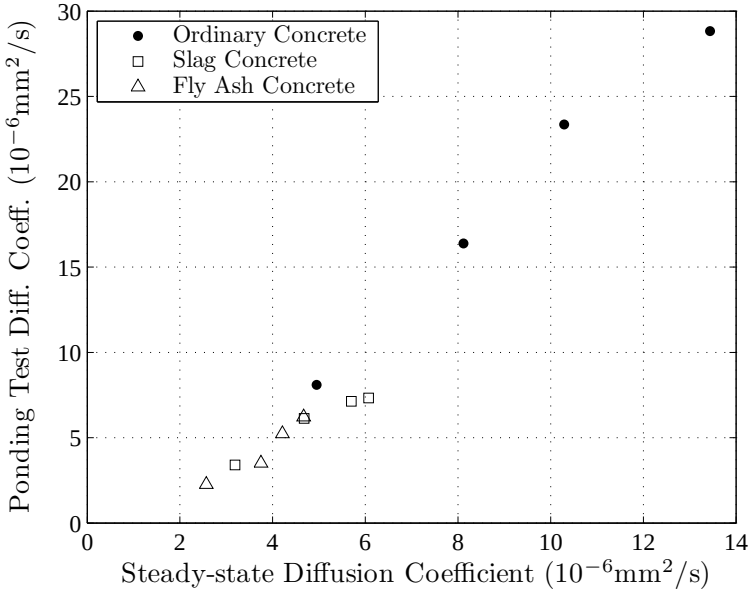

Figure 5.4: Steady-state Migration Test vs. 90-Day Ponding Test [189]

Yang [189] compared the chloride diffusion coefficients obtained from 90-day salt ponding tests and migration experiments for various concrete mixtures. The coefficients obtained from the non-steady-state and steady-state migration experiments are plotted against the ones obtained from the 90-day salt ponding tests in Figure 5.3 and Figure 5.4, respectively, in which a linear relationship can be observed. The coefficient of determination r^2 for a linear fit of the non-steady-state data was calculated as 0.952, while it was computed as 0.973 for the steady-state data [189].

Tang [164] derived a relationship between the chloride diffusion coefficients obtained from steady-state and non-steady-state migration experiments. The coefficients obtained from steady-state and non-steady-state cases were in good agreement for concrete specimens with low w/c ratios ($w/c \leq 0.4$), while large differences were observed for concrete specimens with high w/c ratios ($w/c \geq 0.5$) [164]. In another study, Tang [165, 166] analyzed the concentration dependence of diffusion and migration processes, and studied the relationship between the chloride diffusion coefficients obtained from diffusion and migration experiments. Delagrave *et al.* [45] conducted a similar study on the diffusion coefficients obtained from diffusion and migration experiments.

Tang and Sørensen [170] carried out a research on the relationship between the chloride diffusion coefficients obtained from NT BUILD 443 test (immersion test), NT BUILD 355 test (non-steady-state migration test) and CTH Rapid Test. It can be seen from Figure 5.5 that the measured diffusion coefficients from the CTH Rapid Test and NT BUILD 443 are comparable, while the ones from NT BUILD 355 test are one to two orders of magnitude lower than those obtained from the others.

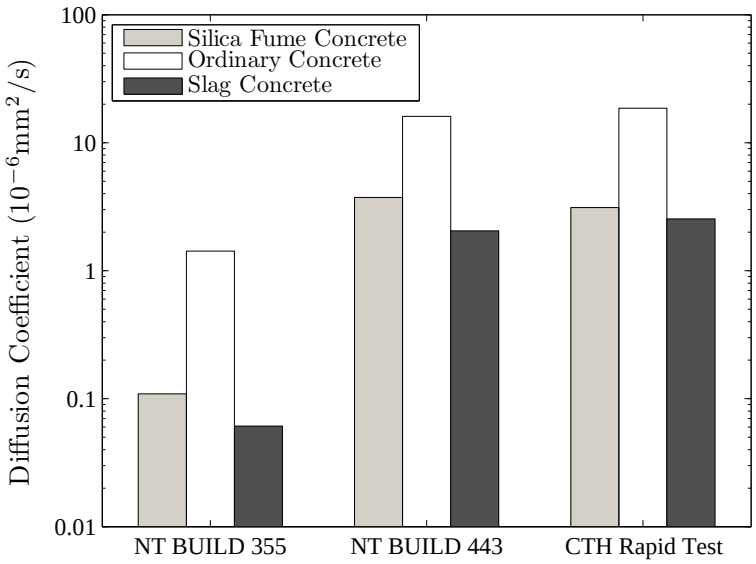

Figure 5.5: Diffusion Coefficients from Different Test Methods [170]

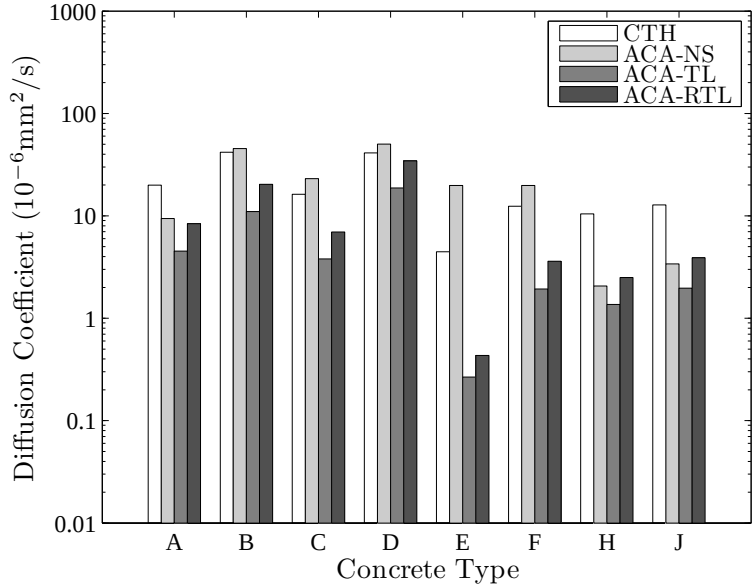

Figure 5.6: Diffusion Coefficients by Different Methods of Calculation [10]

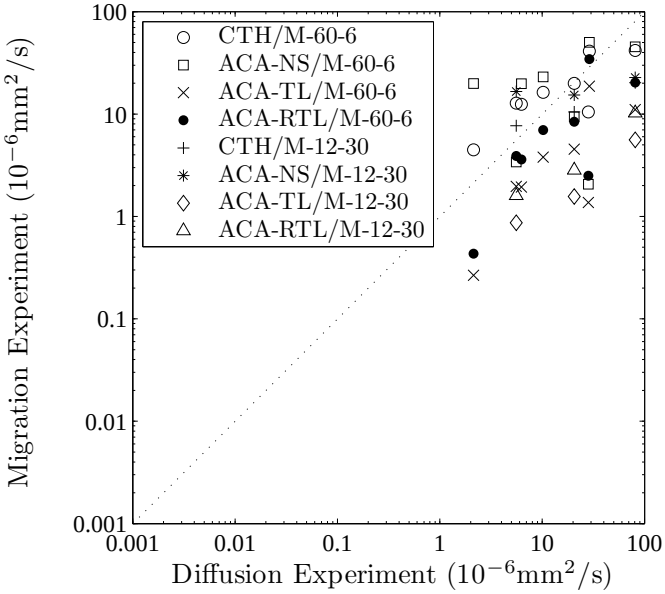

Figure 5.7: Migration Experiments vs. Diffusion Experiments [10]

Castellote *et al.* [33] discussed the possible reasons of the difference between the chloride diffusion coefficients obtained from diffusion and migration experiments. In another study, Castellote *et al.* [32] suggested the use of an applied voltage of 12 V in a steady-state migration experiment on a cement paste specimen with a w/c ratio of 0.4 in order to obtain an effective diffusion coefficient similar to a coefficient that can be obtained from a natural diffusion experiment.

Andrade *et al.* [10] compared the apparent diffusion coefficients obtained through four different methods of calculation from migration experiments at 60 V during 6 hours. The scatter between the values obtained through different methods of calculation can be observed in Figure 5.6, however the diffusion coefficients for the same concrete are generally in the same range of magnitude, except the concrete type E, which is the most impermeable one. Also, Andrade *et al.* [10] compared the diffusion coefficients obtained through four different methods of calculation from migration experiments at 60 V during 6 hours and

at 12 V during 30 hours with the coefficients obtained from natural diffusion experiments. It can be deduced from Figure 5.7 that, (i) for the most impermeable concrete, scatter among the coefficients obtained through the various methods of calculation from the migration experiment is relatively high, but the coefficients are distributed in an interval around the corresponding coefficient obtained from the diffusion experiment, and (ii) the coefficients obtained through the various methods of calculation from the migration experiment become smaller than the corresponding coefficient obtained from the diffusion experiment, as the permeability of concrete increases [10]. Castelotte *et al.* [34] established relationships between the coefficients obtained from natural diffusion experiments under different conditions and between the coefficients obtained from natural diffusion experiments and migration experiments.

Although the chloride diffusion coefficients obtained from the experimental methods reviewed above cannot be considered as material constants, experimental data obtained through the same type of experiments may provide a useful comparison tool to evaluate the effects of certain parameters on the chloride diffusivity in various types of concrete [117]. Each method has advantages and disadvantages. Diffusion-based methods are capable of exhibiting pure diffusion behavior, but they are time-consuming. On the other hand, migration experiments, in which the ionic movement is accelerated by applying an electrical potential, last significantly shorter than diffusion experiments. However, the most common methods calculating the effective diffusion coefficient of chloride through a migration experiment (Eqs. 5.7, 5.8, 5.11 and 5.12) neglect the fact that it is not only the chloride ions affected by the applied electrical potential, but also the other ions existing in pore solution. Samson *et al.* [144] developed a multi-ionic approach, which considers all ions in pore solution, to overcome

this issue, but it is a complicated method since the coupled extended Nernst-Planck/Poisson set of equations (Eqs. 5.15 and 5.16) need to be solved simultaneously. Conductivity experiments also last shorter than diffusion experiments, but they also neglect the ions in pore solution other than chloride ions, and difficulties may arise in determining the conductivity of pore solution.

Since diffusion is of interest to this research, diffusion experiments are considered as more reliable than the others within the context of this research. Since natural diffusion experiments are time-consuming, the objective of this study is to propose a numerical method for estimating the effective diffusion coefficient of chloride in a given mortar/concrete specimen.

5.3 Numerical Techniques

Garboczi and Bentz [62] simulated the chloride diffusivity in saturated cement pastes by converting digital cement pastes into random conductor networks. Once a digital image of a hydrated cement paste is generated by the NIST model [60] (see Section 2.2.3.3), a network of nodes, each of which is placed at the center of each pixel, is constructed. Then conductors connecting the nodes to each other are set up. After the network of nodes and conductors is generated, the effective conductivity of the network is calculated by using either the Fogelholm algorithm or the conjugate relaxation algorithm [62]. The effective diffusion coefficient of chloride in the simulated cement paste is then calculated by using the Nernst-Einstein relation (Eq. 5.18). Based on the results obtained from the developed model, Garboczi and Bentz [62] proposed a formula for calculating the chloride diffusivity in a cement paste normalized to the

diffusivity of chloride in free water as

$$\frac{D}{D_0} = 0.001 + 0.07\phi^2 + 1.8(\phi - \phi_c)^2 H(\phi - \phi_c), \tag{5.21}$$

where ϕ is the capillary porosity of the cement paste, ϕ_c is the capillary porosity percolation threshold and H is the Heaviside function, *i.e.*, $H(x) = 0$ for $x \leq 0$, and $H(x) = 1$ for $x > 0$.

Garboczi *et al.* [22, 63, 65, 68, 145] developed a multi-scale microstructural numerical model to study the diffusivity of chloride in concrete. The model is applicable to the conventional saturated concretes and considers chloride diffusion under steady-state conditions. It has three steps as follows:

(i) Nondiffusive spherical aggregate particles are placed randomly in a computational volume having periodic boundary conditions, according to the aggregate particle size distribution of interest. The thickness of interfacial transition zone (ITZ) is taken equivalent to the median cement particle diameter. Volume fractions of ITZ and bulk cement paste are calculated by systematic point sampling.

(ii) A computational volume for cement hydration, the dimensions of which are determined in such a way that the volume ratio of ITZ to bulk cement paste matches the ratio obtained in the first step, is constructed. Spherical cement particles are placed randomly, according to the cement particle size distribution and w/c ratio of interest. After the hydration of cement particles is simulated up to a presumed degree of hydration by the NIST model [60], capillary porosity of the simulated cement paste is measured as a function of distance from the aggregate surface. Then the normalized chloride diffusivity as a function of distance from the aggregate surface is

obtained from Eq. 5.21. It is assumed that Eq. 5.21 holds also in ITZ. The normalized diffusivity values are averaged into two subsets, ITZ and bulk cement paste having values D_{ITZ}/D_0 and D_{bulk}/D_0, respectively. The ratio $D_{\text{ITZ}}/D_{\text{bulk}}$ is an input to the next step.

(iii) The effective diffusion coefficient of chloride is estimated by executing random walks throughout the computational volume generated in the first step. The computational volume consists of three phases as aggregate particles, bulk cement paste and ITZ having diffusivity values of 0, 1 and $D_{\text{ITZ}}/D_{\text{bulk}}$, respectively. A fixed step size is presumed for random walks. Time elapsed in a step of a random walk depends on the diffusivity of the phase in which the random walk is. A random walk steps from one phase to another one with a probability based on the ratio of their diffusivities. A projected step falling into an aggregate particle is not allowed, but the clock is advanced. After a presumed number of steps, the normalized effective diffusion coefficient of chloride is calculated as

$$\frac{D_{\text{eff}}}{D_{\text{bulk}}} = \frac{1}{\Delta x^2}\left(\frac{1}{n_s}\sum_{i=1}^{n_s}\frac{\bar{R}_i^{\,2}}{t_i}\right)\left(1 - V_{\text{agg}}\right), \tag{5.22}$$

where Δx is the step size, n_s is the number of random walks, $\bar{R}_i$ is the distance between the start and end points of the i-th random walk, t_i is the elapsed time for the i-th random walk and V_{agg} is the volume fraction of aggregate. The D_{eff} is then obtained by multiplying $D_{\text{eff}}/D_{\text{bulk}}$ by D_{bulk}/D_0 obtained from the cement hydration model and D_0, which is taken as $2 \cdot 10^{-9}$ m^2/s by Bentz *et al.* [22].

After executing three independent runs for a single set of parameters, Garboczi *et al.* [22] observed that the coefficient of variation was less than 1.5%, and decided that only one run would be enough to obtain representative results for

each set. Since the random walks executed in the last step of the multi-scale model call for a huge amount of computational power, the method requires using a cluster of computers [65]. Even though Garboczi *et al.* [22, 63, 65, 68, 145] obtained some satisfactory results using the multi-scale model, the model does not simulate the actual chloride diffusion phenomenon. Bentz *et al.* [22] performed a set of simulations to study the effects of water-to-cement ratio w/c, degree of hydration α, aggregate volume fraction V_{agg}, coarse aggregate particles size distribution CA, fine aggregate particle size distribution FA, ITZ thickness l_{ITZ} and air content- on the chloride diffusivity. The results for w/c ratios of 0.3, 0.45 and 0.6, are shown in Tables 5.2, 5.3 and 5.4, respectively. "A" and "B" denote extreme low and high settings for coarse aggregate particle size distribution, respectively. Similarly, "a" and "b" denote extreme low and high settings for fine aggregate particle size distribution, respectively. Based on the simulation results, w/c ratio, α and V_{agg} have been identified as the significant variables affecting the chloride diffusivity in the multi-scale model.

Table 5.2: Simulation Results by Multi-Scale Model (w/c =0.3) [22]

α	V_{agg}	CA	FA	l_{ITZ} (μm)	Air Cont. (%)	D_{eff} (10^{-6} mm^2/s)
0.5	0.600	A	a	10	0	2.10
0.5	0.600	B	a	30	10	4.00
0.5	0.750	A	b	30	10	1.75
0.5	0.750	B	b	10	0	1.20
0.7	0.600	A	b	30	0	0.84
0.7	0.600	B	b	10	10	0.44
0.7	0.750	A	a	10	9	0.21
0.7	0.750	B	a	30	0	0.69

Table 5.3: Simulation Results by Multi-Scale Model (w/c =0.45) [22]

α	V_{agg}	CA	FA	l_{ITZ} (μm)	Air Cont. (%)	D_{eff} (10^{-6} mm^2/s)
0.6	0.675	mid	mid	20	5	9.4
0.6	0.525	B	b	10	0	16.3
0.6	0.825	B	b	10	0	5.34
0.4	0.675	B	b	10	0	39.5
0.8	0.675	B	b	10	0	1.76

Table 5.4: Simulation Results by Multi-Scale Model (w/c =0.6) [22]

α	V_{agg}	CA	FA	l_{ITZ} (μm)	Air Cont. (%)	D_{eff} (10^{-6} mm^2/s)
0.5	0.600	A	b	10	10	58.1
0.5	0.600	B	b	30	0	77.7
0.5	0.750	A	a	30	0	41.0
0.5	0.750	B	a	10	9	28.7
0.7	0.600	A	a	30	10	28.4
0.7	0.600	B	a	10	0	36.3
0.7	0.750	A	b	10	0	20.1
0.7	0.750	B	b	30	10	12.9

Kato and Uomoto [90] proposed a model for estimating the effective diffusion coefficient of chloride in saturated concrete, considering the spatial properties of cement paste and ITZ. The pore structures of cement paste and ITZ are simulated by arranging the solid phases randomly. Cement particles and aggregate particles are represented by circles and squares, respectively. Instead of particle size distributions, average sizes are used for both cement and aggregate particles. The thickness of ITZ is calculated by considering both the wall-effect

and the bleeding. In order to estimate the effective diffusion coefficient of chloride in concrete, the chloride diffusion coefficients in each phase are calculated.

- First, the effective diffusion coefficient of chloride in porous media is calculated. The chloride diffusion coefficient in the pores is set to the chloride diffusion coefficient in a dilute solution, and the chloride diffusion is simulated according to Fick's second law (Eq. 5.2). Then the effective diffusion coefficient of chloride in porous media is obtained from Eq. 5.4.
- Second, the effective diffusion coefficient of chloride in cement paste is calculated. The effective diffusion coefficient of pores comes from the first step, and the chloride diffusion coefficient in the cement particles are set to 0. Then the effective diffusion coefficient of chloride in cement paste is obtained from Fick's second law (Eq. 5.2) and Eq. 5.4, similar to the procedure in the first step.
- Third, the effective diffusion coefficient of chloride in concrete is calculated by following the same solution procedure with the chloride diffusion coefficients obtained in the previous steps.

The authors [90] compared the results obtained from their model with experimental results (Figure 5.9), showing that the effective diffusion coefficients from their model underestimates the experimental results, but the tendency of the relationship between the w/c ratio and the effective diffusion coefficient is similar to the one observed in the experimental results. It is worthy to note that the model simulates the chloride diffusion according to Fick's second law, but ignores the chloride binding effect.

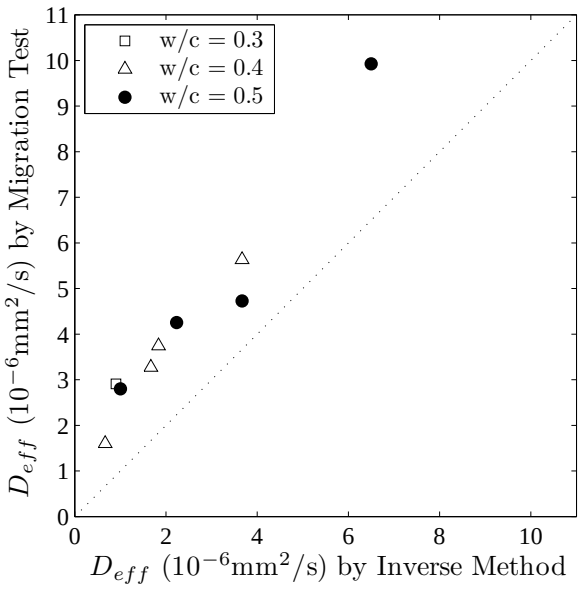

Figure 5.8: Comparison of Results by Yamada *et al.* [188]

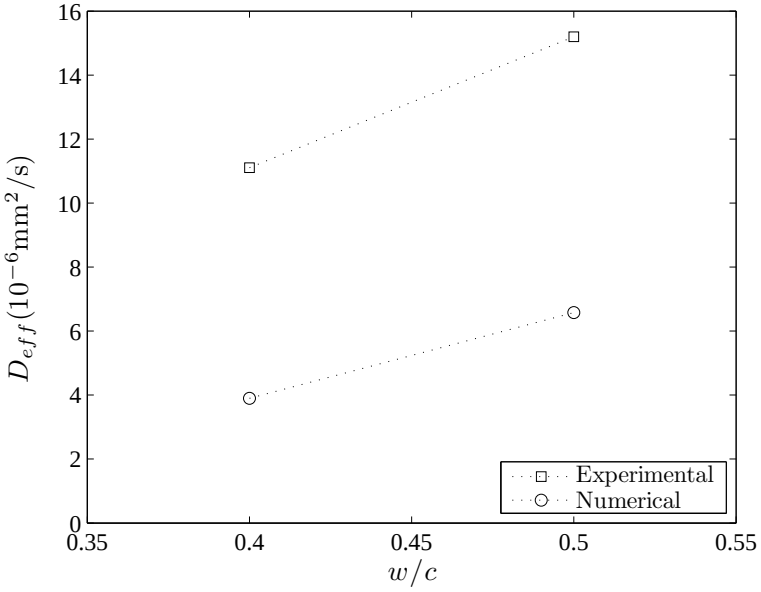

Figure 5.9: Comparison of Results by Kato and Uomoto [90]

Yamada *et al.* [188] proposed an inverse method for calculating the effective diffusion coefficient of chloride in concrete and the parameters of non-linear chloride binding isotherm, modeled as a Freundlich isotherm (see Section 2.3.2), from chloride concentration profiles measured by electron probe micro analysis (EPMA). The analysis is based on the numerical solution of Eq. 5.2 with $D_{\text{eff}}/(\phi(1 + \partial C_b/\partial C_f))$ in place of D_{app} by using the Cranck-Nicolson implicit finite-difference method, where ϕ is the porosity of concrete determined experimentally, C_b and C_f is the bound and free chloride concentrations expressed in per unit volume of pore solution, respectively. Initial condition is determined from EPMA measurements and boundary condition is set to the chloride concentration in the solution in which the concrete specimen is immersed. The effective diffusion coefficient D_{eff} and the parameters of non-linear chloride binding isotherm, c_α and c_β, are determined by minimizing an objective function that measures the agreement between the EPMA results and the numerical results. Comparisons of numerical results with the ones from migration tests are shown in Figure 5.8

5.4 Analytical and Empirical Techniques

Garboczi and Bentz [64, 65, 145] derived analytical formulas, using differential effective medium theory, to avoid executing random walks for estimating the effective diffusion coefficient of chloride in a computational volume, representing concrete, in the multi-scale model developed by Garboczi *et al.* [63, 65, 68, 145] (see Section 5.3). To map an ITZ, in which chloride diffusion coefficient varies spatially, into a zone having a constant chloride diffusion co-

efficient, the dilute limit of concrete, which occurs when the volume fraction of aggregate is so small that the effect of each aggregate particle can be treated independently, was analyzed by using a spherical aggregate particle surrounded by a number of shells enough to represent the chloride diffusivity gradient in the ITZ, where each shell was assigned with a constant chloride diffusion coefficient. The results of the dilute limit analysis was used for calculating the chloride diffusion coefficient in any concrete with an arbitrary volume fraction of aggregate by using a weighted average between two extreme cases, a constant D_{ITZ} and a constant $D_{\text{ITZ}}/D_{\text{bulk}}$. The weights were determined from the results of random walk simulations.

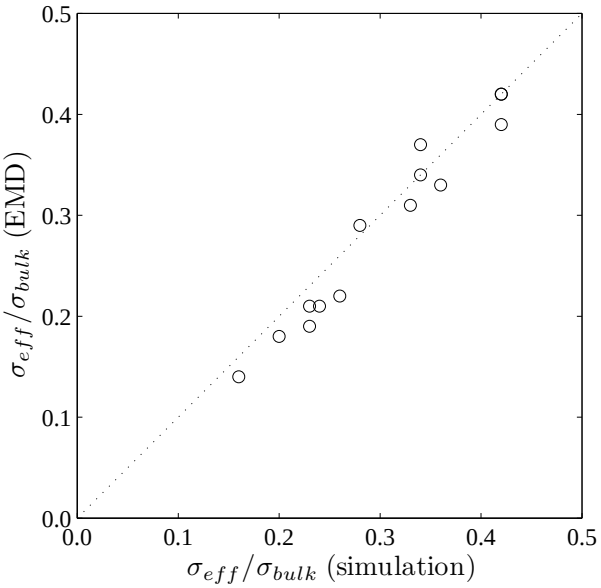

Figure 5.10: Comparison of Results with Simulations [67]

The model developed by Garboczi and Bentz [64, 65, 145] requires an adjustable parameter, but Garboczi and Berryman [67] derived a new differential effective medium theory in order to overcome this handicap. It was accomplished by mapping each aggregate particle and its accompanying ITZ into a

single effective particle, and then analyzing this effective particle using the previous theory. The results of effective medium theory agreed with the results of random walk simulations in general sense (Figures 5.10 and 5.11), but the theory ignores some important effects such as the percolation of ITZs.

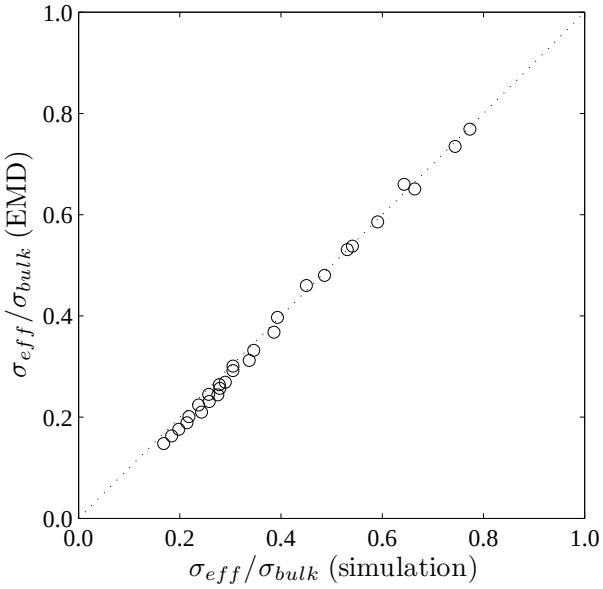

Figure 5.11: Comparison of Results with Simulations [67]

Xi and Bažant [187] modeled the effect of aggregate on the effective diffusion coefficient of chloride in concrete by using a composite model developed by Christensen [39]. For nonporous aggregate particles, the model calculates the effective diffusion coefficient as

$$D_{\text{eff}} = D_{\text{cp}} \frac{2(1 - V_{\text{agg}})}{(2 + V_{\text{agg}})}, \tag{5.23}$$

where D_{cp} and V_{agg} are the chloride diffusion coefficient in the cement paste fraction of concrete and the volume fraction of aggregate, respectively. However, Caré [31] showed that Eq. 5.23 disagrees with the experimental results for mortar specimens since it is a simple model considering mortar as a two-phase

medium. Thus Caré [31] revised the formulation as

$$D_{\text{eff}} = D_{\text{ncp}} \left[0.11 V_{\text{ITZ}} + (1 - V_{\text{agg}})\right] \frac{2}{2 + V_{\text{agg}}}, \tag{5.24}$$

where D_{ncp} is the chloride diffusion coefficient in the corresponding neat cement paste and V_{ITZ} is the volume fraction of ITZ. The multiplier 0.11 was obtained from experimental data. According to Caré [31], it can be determined if the chloride diffusion coefficients for a reference mortar and the corresponding neat cement paste are known, and then the effective diffusion coefficient of chloride in any mortar with the same cement paste but different aggregate content can be estimated.

Yang and Su [193] studied the dilution, tortuosity and ITZ effects of aggregate on the chloride diffusivity in mortar specimens, and proposed an equation for calculating the effective diffusion coefficient of chloride. Modeling the ITZ as a uniform layer around spherical fine aggregate particles and not allowing the aggregate with ITZ to overlap, the authors expressed the effective diffusion coefficient as

$$D_{\text{eff}} = D_{\text{ncp}} \left(1 - V_{\text{agg}}\right)^{3/2} + D_{\text{ncp}} \left(\beta - 1\right) V_{\text{ITZ}}, \quad \beta = \frac{D_{\text{ITZ}}}{D_{\text{cp}}}, \tag{5.25}$$

where D_{ncp} is the chloride diffusion coefficient in the neat cement paste, V_{agg} is the volume fraction of aggregate, V_{ITZ} is the volume fraction of ITZ, D_{cp} and D_{ITZ} are the chloride diffusion coefficients in the bulk cement paste and ITZ, respectively. The first and second terms on the right side of Eq. 5.25 represent the combined effect of dilution and tortuosity, and the effect of ITZ on the effective diffusion coefficient of chloride, respectively. In developing Eq. 5.25, it was assumed that the chloride diffusivity in the ITZ is constant and the flow in the ITZ is locally parallel to the aggregate surface. The effective diffusion coefficient of

chloride in mortar as a function of the volume fraction of aggregate can be determined by conducting steady-state migration experiments on mortar specimens with various aggregate contents. Then the chloride diffusion coefficient in the ITZ for different values of ITZ thickness is calculated by using the experimental results and the regression analyses with Eq. 5.25.

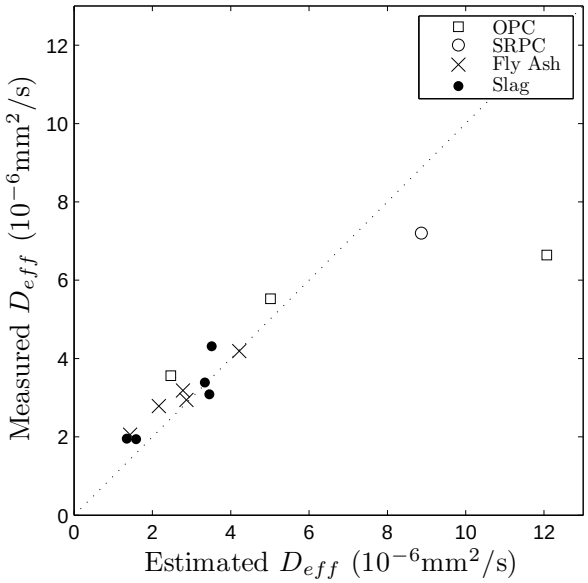

Figure 5.12: Comparison of Diffusion Coefficients in Mortar [121]

Oh and Jang [121] proposed an analytical model for estimating the effective diffusion coefficient of chloride in concrete considering the relationship between the chloride diffusivity and the microstructure of concrete. An analytical solution, in terms of diffusivities normalized to the diffusivity of chloride in pore solution, to the general effective media equation was derived for estimating the effective diffusion coefficient of chloride in cement paste by using the Nernst-Einstein relation (Eq. 5.18). A reasonable agreement was found between the experimental data available in the literature and the results obtained from the derived equation. Then an equation based on composite sphere assemblage

model, proposed by Hashin [83], was derived for estimating the effective diffusion coefficient of chloride in concrete, where the thickness of ITZ was assumed to be the same for all particles. The model depends on two main variables, capillary porosity and volume fraction of aggregate. The main parameters of the model are the normalized chloride diffusivity in solid phases, the percolation exponent, the ratio of diffusivity in ITZ to the diffusivity in bulk cement paste and the thickness of ITZ relative to the average radius of aggregate particles. The results obtained from the model were in reasonable agreement with the results of the non-steady-state migration experiments carried out for validating the model (Figures 5.12 and 5.13).

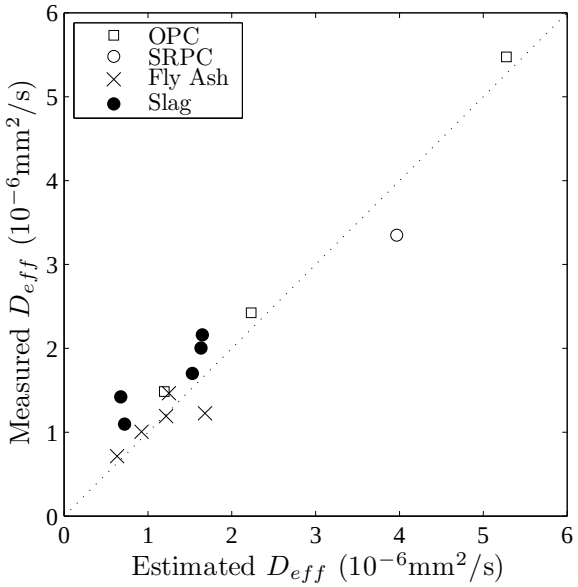

Figure 5.13: Comparison of Diffusion Coefficients in Concrete [121]

5.5 Effective Diffusion Coefficient

A numerical method for estimating the effective diffusion coefficient of chloride in a deterministic/random heterogeneous medium is discussed extensively in Chapter 3. Hereinafter, the application of the proposed method to virtual concrete specimens is presented.

Let $H = (0, l_1) \times (0, l_2) \in \mathbb{R}^2$, be a bounded subset containing a virtual concrete specimen of interest. The chloride concentration $C(\boldsymbol{x})$ satisfies

$$\sum_{p=1}^{2} \frac{\partial D(\boldsymbol{x})}{\partial x_p} \frac{\partial C(\boldsymbol{x})}{\partial x_p} + D(\boldsymbol{x}) \Delta C(\boldsymbol{x}) = 0, \quad \boldsymbol{x} \in H, \tag{3.67}$$

where $D(\boldsymbol{x})$ is the chloride diffusion coefficient at $\boldsymbol{x}$ and Δ is the Laplace operator, with the Dirichlet boundary conditions

$$C(0, x_2) = 0 \quad \text{and} \quad C(l_1, x_2) = 1, \quad x_2 \in (0, l_2), \tag{3.68}$$

and the Neumann boundary conditions

$$\frac{\partial C(\boldsymbol{x})}{\partial x_2} = 0, \quad \boldsymbol{x} \in (0, l_1) \times \{0\} \quad \text{and} \quad \boldsymbol{x} \in (0, l_1) \times \{l_2\}. \tag{3.69}$$

Concrete is viewed as a three-phase material: aggregate, bulk cement paste and interfacial transition zone (ITZ). Through the analyses of virtual concrete specimens, the chloride diffusion coefficient in these phases is defined as follows:

- The aggregate is assumed to be nonporous, *i.e.*, $D = 0$ in the aggregate particles.
- The bulk cement paste is assumed to have a constant chloride diffusion coefficient D_{cp}.

- The chloride diffusion coefficient in the ITZ is assumed to be described by

$$D(u) = c_1 u + c_2 u^2 + c_3 e^{-u}, \quad 0 < u \leq l_{\text{ITZ}}, \tag{5.26}$$

where u is the distance from the aggregate surface, l_{ITZ} is the ITZ thickness, and c_1, c_2 and c_3 are constants satisfying a presumed ratio of $D(0)/D(l_{\text{ITZ}})$, referred to as α_D, $\partial D(l_{\text{ITZ}})/\partial u = 0$ and $D(l_{\text{ITZ}}) = D_{\text{cp}}$.

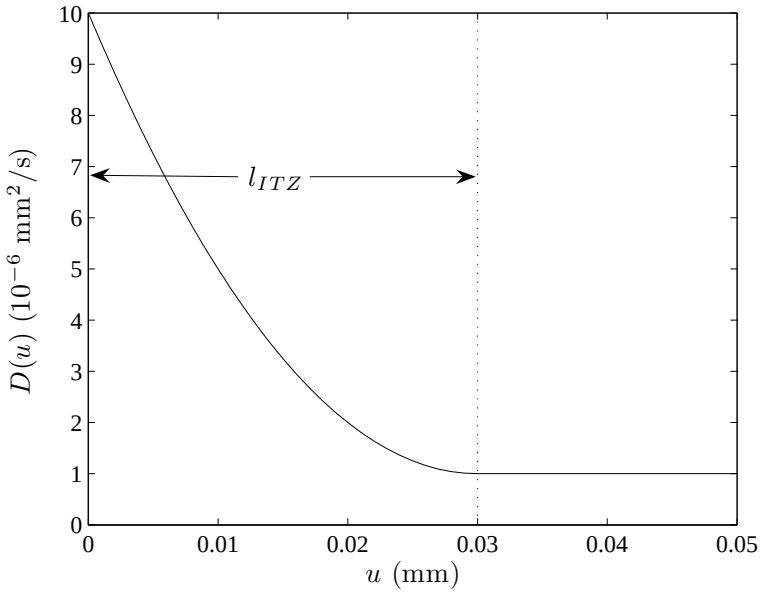

Figure 5.14: $D(u)$ for $l_{\text{ITZ}} = 30$ μm, $\alpha_d = 10$ and $D_{\text{cp}} = 1 \cdot 10^{-6}$ mm^2/s

5.5.1 Single Particle System

This example demonstrates the effect of a single particle and its accompanying ITZ on the effective diffusion coefficient of chloride in a virtual specimen with $l_1 = 5$ mm and $l_2 = 10$ mm, *i.e.*, $H = (0, 5) \times (0, 10)$, and $D_{\text{cp}} = 1 \cdot 10^{-6}$ mm^2/s. Suppose that a single circular nonporous aggregate particle having a diameter of 2.5 mm is placed at the center of H (Figure 5.15).

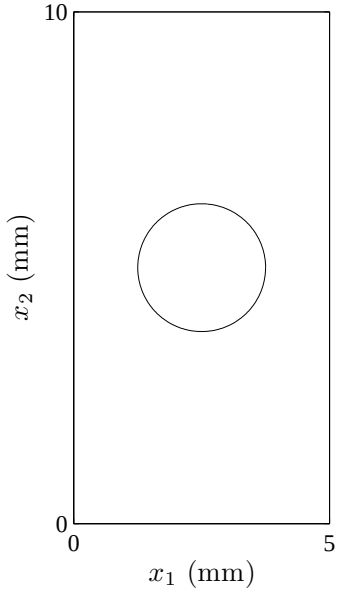

Figure 5.15: A Single Particle System

The objective is to calculate the effective diffusion coefficient

$$D_{\text{eff}} = \frac{1}{l_2} \int_H D(\boldsymbol{x}) \frac{\partial C(\boldsymbol{x})}{\partial x_1} d\boldsymbol{x}, \quad \boldsymbol{x} \in H, \tag{3.74}$$

for different values of the ITZ thickness l_{ITZ} and the ratio $\alpha_D = D(0)/D(l_{\text{ITZ}})$. Based on the calculations for different values of l_{ITZ} and α_D by using the *MATLAB's PDE Toolbox*, it can be observed in Figure 5.16 that placing a particle constituting 10% of the specimen by area results in:

- $D_{\text{eff}}/D_{\text{cp}} = 0.84$ if there is no ITZ, that is, replacing 10% of the porous medium with a nonporous medium reduces the effective diffusion coefficient since there is less room for chloride to diffuse through. In other words, the amount of chloride passing through the specimen decreases with increasing amount of nonporous medium, if there is no ITZ.
- $D_{\text{eff}}/D_{\text{cp}} = 1.01$ if $l_{\text{ITZ}} = 50$ μm and $\alpha_D = 100$, and $D_{\text{eff}}/D_{\text{cp}} = 1.02$ if $l_{\text{ITZ}} = 100$ μm and $\alpha_D = 50$, that is, even though the specimen with a sin-

gle particle contains 10% less amount of porous medium than the homogeneous specimen does, the amount of chloride passing through the heterogeneous specimen is almost the same as the amount passing through the homogeneous specimen if $l_{\text{ITZ}} = 50$ μm and $\alpha_D = 100$, or $l_{\text{ITZ}} = 100$ μm and $\alpha_D = 50$, since chloride travels faster in the ITZ.

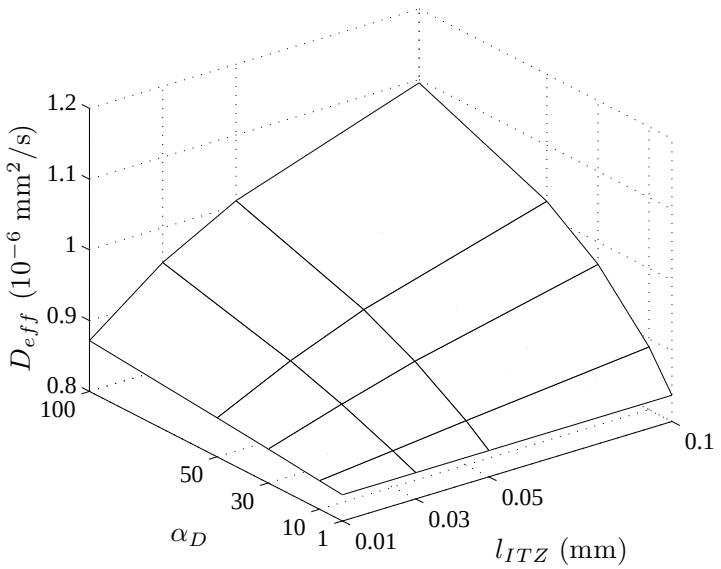

Figure 5.16: Variation of the D_{eff} with l_{ITZ} and α_D

- $D_{\text{eff}}/D_{\text{cp}} = 1.10$ if $l_{\text{ITZ}} = 100$ μm and $\alpha_D = 100$, that is, as the ITZ gets thicker or more porous, the amount of chloride passing through the specimen increases, and exceeds the amount passing through the homogeneous specimen at some combinations of l_{ITZ} and α_D.

5.5.2 Determination of Specimen Size

Since computation time for calculating the effective diffusion coefficient of chloride in a virtual specimen increases with its size, the size of the virtual spec-

imen needs to be sufficiently small to reduce the computation time, but sufficiently large to obtain an accurate result. A two-stage procedure is proposed to determine the specimen size. First, the dimension parallel to the chloride flow, l_1, is determined. Second, the dimension perpendicular to the chloride flow, l_2, is identified. Virtual specimens are labeled as SP$-l_1 \times l_2 - \omega_s$, $\omega_s = 1, \ldots, n_{sp}$, where n_{sp} is the number of virtual specimen samples.

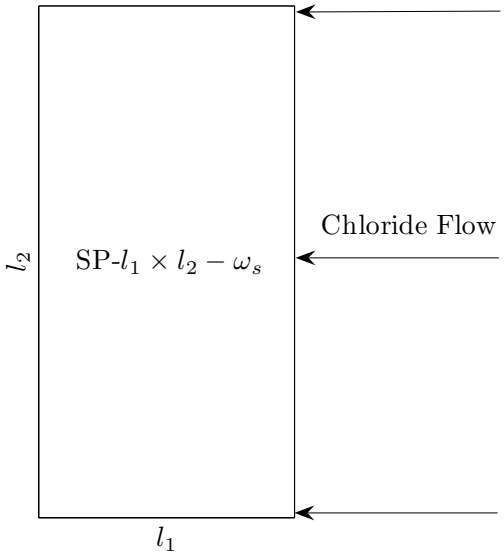

Figure 5.17: Labeling of Virtual Specimens

Since aggregate particles in mortar are finer than those in concrete, relatively small virtual specimens are sufficient to examine mortar. Since computation time is less for smaller specimens, all numerical results are limited to mortar specimens. Virtual mortar specimens are constructed in 2D using volume fraction statistics obtained from 3D specimens. This is an approximation and has been used to reduce calculations. Three 2D virtual mortar specimens have been generated as explained below.

- One of the mortar specimens tested by Caré [31] has been chosen as a ba-

sis for generating virtual specimens used in specimen size determination. The sand particle size distribution in the mortar specimen of Caré [31] is shown in Figure 5.18. The volume fraction of aggregate is 50% [31].

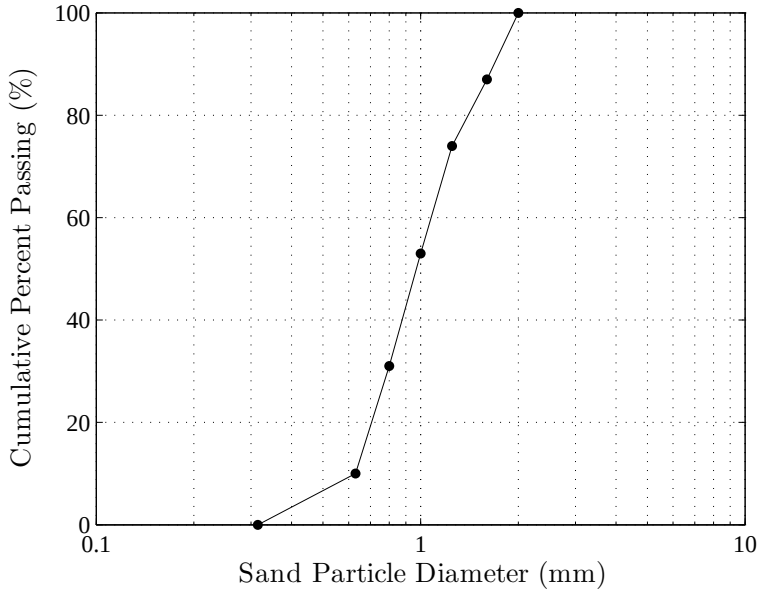

Figure 5.18: Sand Particle Size Distribution [31]

Table 5.5: Particle Size Distribution in Virtual Specimens

Type-k	$d_{L,k}$ (mm)	$d_{U,k}$ (mm)	p_k (by area)	$\hat{p}_k$ (by area)
1	0.315	0.630	0.10	0.10
2	0.630	0.800	0.21	0.21
3	0.800	1.000	0.22	0.22
4	1.000	1.250	0.21	0.21
5	1.250	1.600	0.13	0.13
6	1.600	2.000	0.13	0.13

- According to the sand particle size distribution shown in Figure 5.18, the particle types and the corresponding proportions p_k, $k = 1, \ldots, 6$, for vir-

tual specimens have been determined as shown in Table 5.5, where $d_{L,k}$ and $d_{U,k}$ are the minimum and maximum particle size for type-k particles, respectively. The target area fraction of aggregate in virtual specimens is 50%.

- A rectangular virtual mortar specimen, $l_1 = 200$ mm by $l_2 = 100$ mm has been generated, and labeled as SP$-200\times100-1$. The resulting proportions $\hat{p}_k$, $k = 1, \ldots, 6$, are shown in Table 5.5, and the resulting area fraction of 23955 particles, $\hat{A}_{\text{agg}}$, is 0.5001.

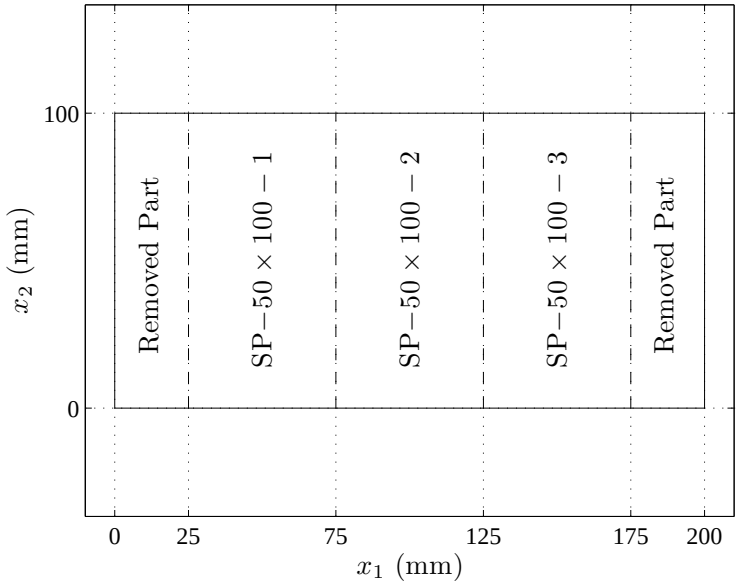

Figure 5.19: Cutting SP$-200 \times 100 - 1$ into Three Test Specimens

- The 25 mm thick ends of SP$-200 \times 100 - 1$ have been removed, and the remaining specimen $(25, 175) \times (0, 100)$ has been cut into three rectangular specimens, 50 mm by 100 mm (Figure 5.19). The new specimens have been labeled as SP$-50 \times 100 - \omega_s$, $\omega_s = 1, 2, 3$. They have 6075, 6095 and 6096 particles, where $\hat{A}_{\text{agg}}$'s are 0.5014, 0.5021 and 0.5007, respectively. One of the specimens, SP$-50 \times 100 - 1$, is shown in Figure 5.20.

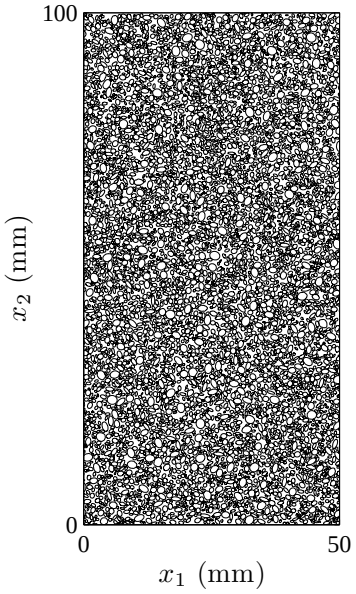

Figure 5.20: Specimen SP$-50 \times 100 - 1$

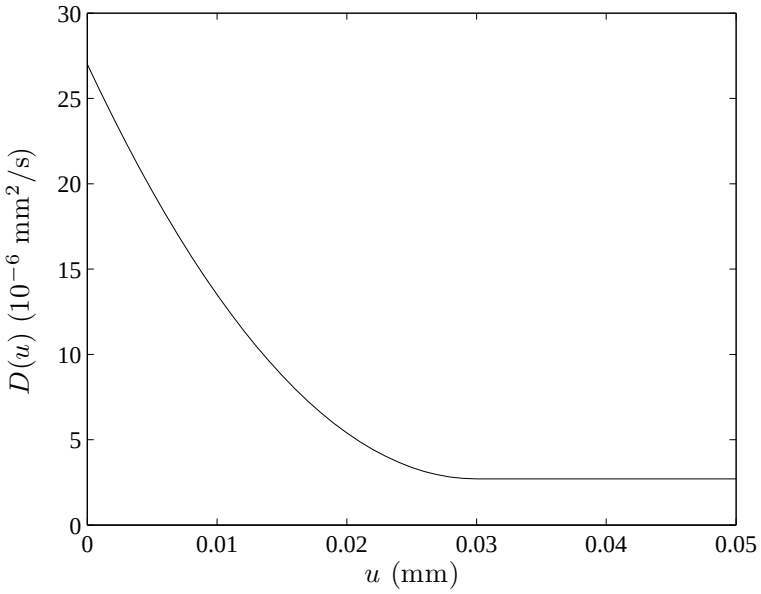

Figure 5.21: Chloride Diffusion Coefficient in the ITZ

The chloride diffusion coefficient in the bulk cement paste D_{cp}, the ITZ thickness l_{ITZ} and the ratio $\alpha_D = D(0)/D(l_{\text{ITZ}})$ have been chosen as $2.7 \cdot 10^{-6}$ mm^2/s, 30 μm and 10, respectively, for the specimens used in this section (Figure 5.21). Then c_1, c_2 and c_3 in Eq. 5.26 have been calculated as -0.0016, 0.027 and $2.7 \cdot 10^{-5}$, respectively. l_{ITZ} is assumed to be the same for all particles and uniform around each particle.

The calculation of the effective diffusion coefficient of chloride in a specimen is based on

$$D_{\text{eff}} = \frac{l_1}{l_2} \int_{x_1 \times (0,l_2)} D(\boldsymbol{x}) \frac{\partial C(\boldsymbol{x})}{\partial x_1} dx_2, \quad x_1 \in (0, l_1). \tag{3.72}$$

D_{eff} can be approximated by Eq. 3.75, which in this case is in the form

$$\hat{D}_{\text{eff}} = \frac{l_1}{l_2} \sum_{k=1}^{n_2} \triangle x_{2,k} D\left(l_1 - \zeta, x_{2,k}\right) \frac{1 - C\left(l_1 - \zeta, x_{2,k}\right)}{\zeta}, \tag{5.27}$$

where ζ is the distance between the line, on which numerical integration is done, and the upstream boundary $\{l_1\} \times (0, l_2)$, n_2 is the number of integration points on the line $\{l_1 - \zeta\} \times (0, l_2)$, $\triangle x_{2,k}$ is the increment assigned to the k-th integration point, $D(l_1 - \zeta, x_{2,k})$ and $C(l_1 - \zeta, x_{2,k})$ are the chloride diffusion coefficient and the chloride concentration at the k-th integration point.

Since the values of $D(l_1 - \zeta, x_{2,k})$ are known, the only unknowns in Eq. 5.27 are $C(l_1 - \zeta, x_{2,k})$. They can be estimated by using the random walk method (RWM) presented in Chapter 3. The algorithm is summarized briefly below.

- n_s independent samples of an $\mathbb{R}^2$-valued Itô process $\boldsymbol{X}(\tau)$, defined by

  $$d\boldsymbol{X}(\tau) = \boldsymbol{a}(\boldsymbol{X}(\tau))d\tau + \boldsymbol{b}(\boldsymbol{X}(\tau))d\boldsymbol{B}(\tau), \quad \tau \geq 0, \tag{3.23a}$$

  where $\boldsymbol{a}$ and $\boldsymbol{b}$ are the drift and diffusion coefficients, and $\boldsymbol{B}$ is a Brownian motion, are generated for each point, where $\boldsymbol{X}(0, \omega_{i,k}) = [l_1 - \zeta, x_{2,k}]$, $k = 1, \ldots, n_2$, $i = 1, \ldots, n_s$.

- Samples of $\tilde{\boldsymbol{X}} = [\tilde{X}_1 = X_1, \tilde{X}_2 = r(X_2)]$, are obtained from the samples of $\boldsymbol{X}$ by reflection at the Neumann boundaries $(0, l_1) \times \{0\}$ and $(0, l_1) \times \{l_2\}$, where $r(\varepsilon)$ is the periodic function with period $2l_2$ coinciding with $|\varepsilon|$ for $\varepsilon \in [-l_2, l_2]$. The drift and diffusion coefficients are given by Eqs. 3.78 and 3.79, respectively, which in this case are in the form

$$a_1(\boldsymbol{x}) = \frac{\partial D(\tilde{\boldsymbol{x}})}{\partial \tilde{x}_1}, \quad a_2(\boldsymbol{x}) = r'(x_2)\frac{\partial D(\tilde{\boldsymbol{x}})}{\partial \tilde{x}_2}, \tag{5.28}$$

$$\boldsymbol{b}(\boldsymbol{x}) = \sqrt{2D(\tilde{\boldsymbol{x}})}\boldsymbol{i}, \tag{5.29}$$

  respectively, where $\boldsymbol{x} \in (0, l_1) \times \mathbb{R}$, $\tilde{\boldsymbol{x}} = (\tilde{x}_1 = x_1, \tilde{x}_2 = r(x_2)) \in H$ and $\boldsymbol{i}$ is the 2 by 2 identity matrix.

- Chloride concentration at an integration point $x_{2,k}$ is numerically equal to the expectation of $C(\tilde{\boldsymbol{X}}(T))$ (Eq. 3.80). The expectation can be estimated by Eq. 3.82, which in this case is in the form

$$\hat{C}(l_1 - \zeta, x_{2,k}) = \frac{1}{n_s}\sum_{i=1}^{n_s} C\left\{\tilde{\boldsymbol{X}}(T(\omega_{i,k}), \omega_{i,k})\right\}, \quad k = 1, \ldots, n_2, \tag{5.30}$$

  where $T = \inf\{\tau \geq 0 : \tilde{\boldsymbol{X}}(\tau) \notin H\}$ is a stopping time, that is, the time at which $\tilde{\boldsymbol{X}}$ reaches one of the Dirichlet boundaries of $H = (0, l_1) \times (0, l_2) \in \mathbb{R}^2$ for the first time.

For analyses of SP$-50\times100-1$, SP$-50\times100-2$ and SP$-50\times100-3$, ζ, n_2 and n_s have been chosen as 0.5 mm, 100 and 1000, respectively. Samples of $\tilde{\boldsymbol{X}}$ have been generated by using Euler's scheme (Eq. 3.37). The time step $\triangle\tau$ needs to be sufficiently small to exhibit chloride diffusion in the ITZ, which has a thickness of 30 μm. A $\triangle\tau$ of 1.5 seconds when $\tilde{\boldsymbol{X}}(\tau, \omega)$ is in the ITZ and 15 seconds when it is in the bulk cement paste have been decided by generating a few samples of $\tilde{\boldsymbol{X}}$ with various values of $\triangle\tau$. Estimates of mean and standard deviation of step size of resulting samples of $\tilde{\boldsymbol{X}}$ are approximately 8 μm and 6 μm, respectively.

$\triangle\tau$ has been decreased as an aggregate surface has been approached in order to avoid stepping into the aggregate particle. Five stopping times have been set as

$$T_j = \inf\left\{\tau \geq 0 : \tilde{\boldsymbol{X}}(\tau) \notin (10\cdot(j-1), 50)\times(0,100)\right\}, \quad j = 1,\ldots,5, \tag{5.31}$$

to obtain estimates of D_{eff} for different values of l_1, *i.e.*, $l_{1,j} = 50 - 10\cdot(j-1)$. For each value of j, estimate of D_{eff} can be obtained by introducing $l_{1,j}$ and $\hat{C}(l_{1,j} - \zeta, x_{2,k})$, $k = 1,\ldots,n_2$, obtained from Eq. 5.30, into Eq. 5.27.

Table 5.6: $\hat{D}_{\text{eff}}$ (10^{-6} mm^2/s) vs. Specimen Size $(0, l_1)\times(0,100)$

l_1 (mm)	10	20	30	40	50
SP$-50\times100-1$	5.27	5.29	5.40	5.62	5.60
SP$-50\times100-2$	4.44	4.18	4.16	4.16	4.34
SP$-50\times100-3$	4.31	4.27	4.29	4.36	4.41

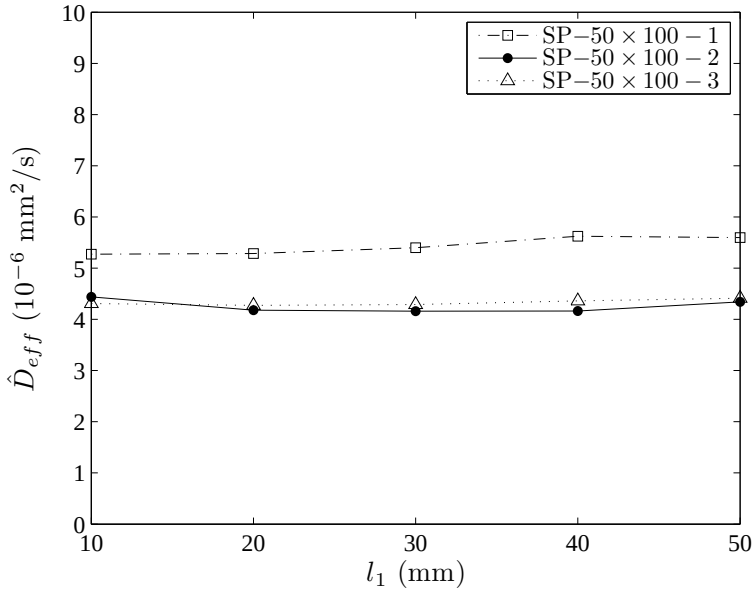

Figure 5.22: $\hat{D}_{\text{eff}}$ vs. Specimen Size $(0, l_1)\times(0,100)$

The resulting estimates of D_{eff} for different values of l_1 are shown in Table 5.6 and plotted in Figure 5.22. The results show that reducing the dimension in

the direction parallel to chloride flow, l_1, from 50 mm to 10 mm does not have any significant effect on the resulting estimate of D_{eff}, which is consistent with the results reported by Arsenault *et al.* [12].

The difference between the $\hat{D}_{\text{eff}}$ obtained from SP$-50 \times 100 - 1$ and the other specimens, SP$-50 \times 100 - 2$ and SP$-50 \times 100 - 3$, has been analyzed, and it has been found out that $n_2 = 100$ points, which are almost uniformly distributed on the line $\{l_1 - \zeta\} \times (0, l_2)$, is not a fine enough mesh, for $l_2 = 100$ mm, to represent the chloride diffusivity profile on the line $\{l_1 - \zeta\} \times (0, l_2)$. Therefore, an algorithm, which improves the accuracy of $\hat{D}_{\text{eff}}$, has been developed to determine the number and location of integration points.

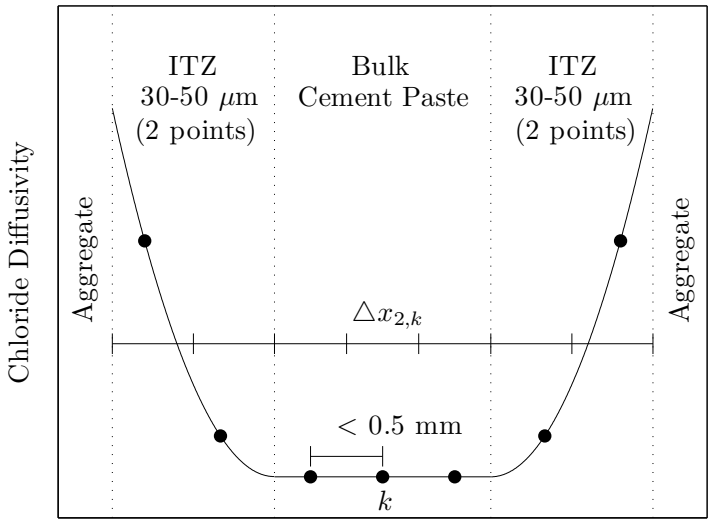

Figure 5.23: Schematical Representation of Integration Points

- The line $\{l_1 - \zeta\} \times (0, l_2)$ is partitioned into segments according to the phases -aggregate, ITZ and bulk cement paste- in which they are. A schematical representation of integration points falling in between two aggregate particles is shown in Figure 5.23.

- A segment in bulk cement paste contains enough number of points to satisfy the condition that the distance between two consecutive points on the same segment is less than 0.5 mm.
- A segment in ITZ contains two points, that is, the spacing of points in ITZ is much smaller than the spacing of points in bulk cement paste, therefore the gradient of chloride diffusivity in ITZ can be captured.
- Segments in aggregate does not contain any point.
- The increment $\triangle x_{2,k}$ assigned to the k-th integration point, $k = 1, \ldots, n_2$, is a subset of the segment on which the k-th integration point is.

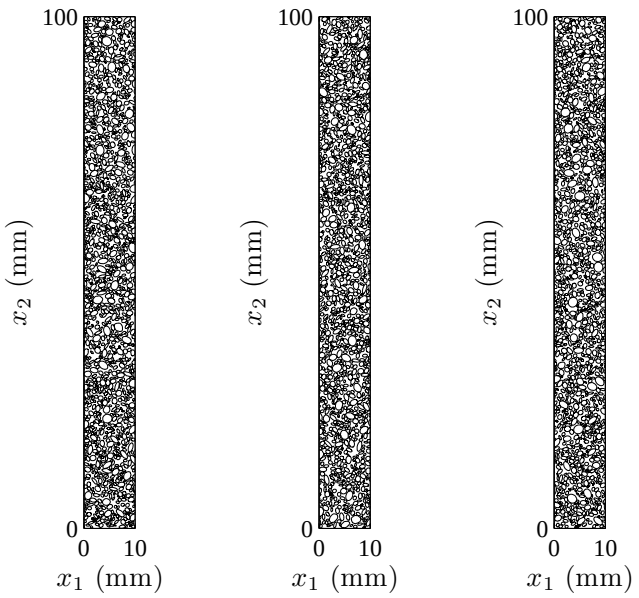

Figure 5.24: SP$-10 \times 100 - 1$, SP$-10 \times 100 - 2$ and SP$-10 \times 100 - 3$

The rightmost 10 mm thick parts of SP$-50 \times 100 - 1$, SP$-50 \times 100 - 2$ and SP$-50 \times 100 - 3$ have been cut, and labeled as SP$-10 \times 100 - 1$, SP$-10 \times 100 - 2$ and SP$-10 \times 100 - 3$ (Figure 5.24). The new specimens have 1291, 1288 and 1294 particles, where the resulting area fractions of particles are 0.5042, 0.5014 and

0.5003, respectively. The number of integration points on the line $\{l_1-\zeta\}\times(0,l_2)$, $l_1 = 10$ mm, $l_2 = 100$ mm, $\zeta = 0.5$ mm, have been determined as 383, 460 and 461, respectively, using the improved algorithm. Five stopping times have been set as

$$T_j = \inf\left\{\tau \geq 0 : \tilde{\boldsymbol{X}}(\tau) \notin (2\cdot(j-1), 10)\times(0,100)\right\}, \quad j = 1,\ldots,5, \tag{5.32}$$

to obtain estimates of D_{eff} for different values of l_1, *i.e.*, $l_{1,j} = 10 - 2\cdot(j-1)$. For each value of j, the estimate of D_{eff} can be obtained by introducing $l_{1,j}$ and $\hat{C}(l_{1,j}-\zeta, x_{2,k})$, $k = 1,\ldots,n_2$, obtained from Eq. 5.30, into Eq. 5.27.

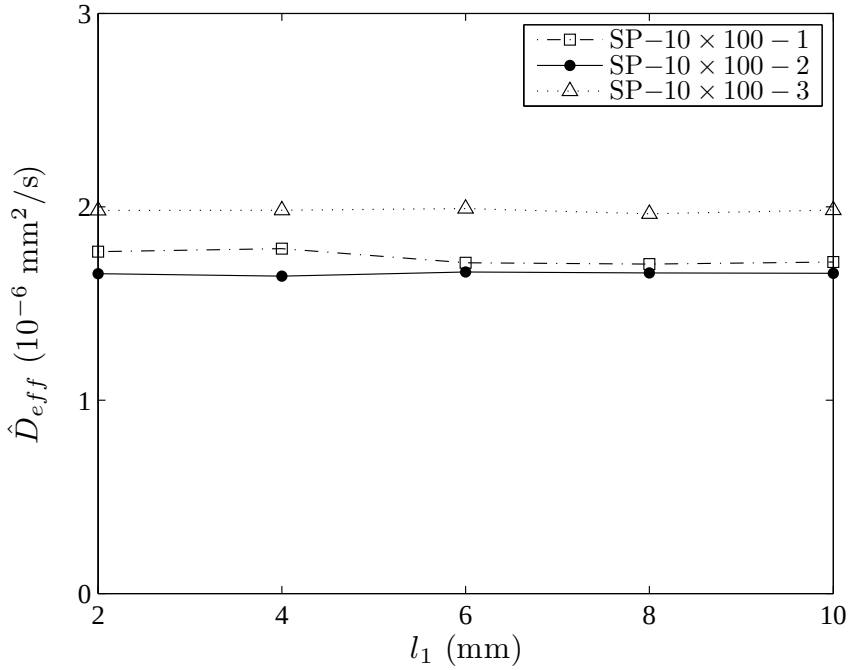

Figure 5.25: $\hat{D}_{\text{eff}}$ vs. Specimen Size $(0,l_1)\times(0,100)$

Based on $n_s = 1000$ samples of $\tilde{\boldsymbol{X}}$ for each integration point placed by the improved algorithm, the resulting estimates of D_{eff} for different values of l_1 are plotted in Figure 5.25 and shown in Table 5.7.

Table 5.7: $\hat{D}_{\text{eff}}$ (10^{-6} mm^2/s) vs. Specimen Size $(0, l_1) \times (0, 100)$

l_1 (mm)	2	4	6	8	10
SP$-10 \times 100 - 1$	1.76	1.78	1.71	1.70	1.71
SP$-10 \times 100 - 2$	1.65	1.64	1.66	1.66	1.66
SP$-10 \times 100 - 3$	1.98	1.98	1.99	1.96	1.98

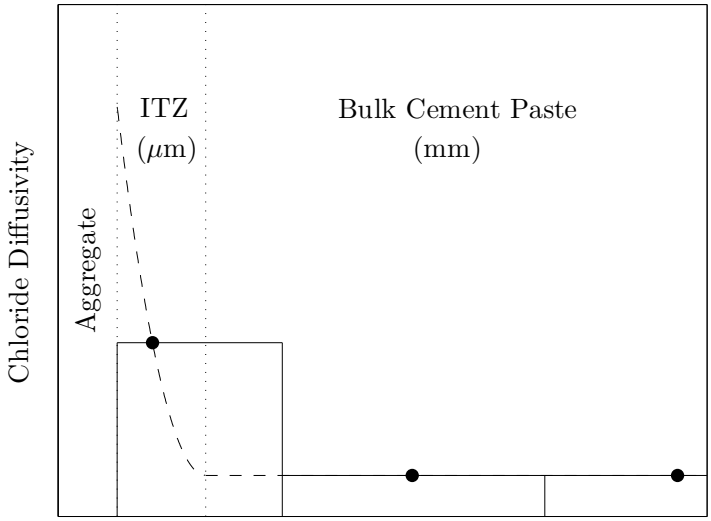

Figure 5.26: Schematical Representation of Uniform Integration Points

Different meshes of integration points have caused large differences between the resulting estimates of D_{eff}, as can be observed in Table 5.6 and Table 5.7. The results in Table 5.6 have been obtained from integration points distributed almost uniformly along the line $\{l_1 - \zeta\} \times (0, l_2)$. This type of mesh has two shortcomings: (i) if an integration point falls in ITZ and the increment assigned to that point covers a part of bulk cement paste as shown in Figure 5.26, then relatively low chloride diffusivity in bulk cement paste is represented by the higher chloride diffusivity in ITZ, which might result in an overestimation of

D_{eff}, and (ii) no integration point is present in between two aggregate particles, if the particles are in between two consecutive integration points. Therefore, an algorithm that differentiates bulk cement paste and ITZ, and then places integration points according to the phases -bulk cement paste and ITZ- is crucial. The results in Table 5.7 have been obtained by using such an algorithm, thus they are more accurate than the ones in Table 5.6.

For further analysis of the effect of l_1 on the estimate of D_{eff}, the rightmost 2 mm thick parts of SP$-10\times100-1$, SP$-10\times100-2$ and SP$-10\times100-3$ have been cut, and labeled as SP$-2\times100-1$, SP$-2\times100-2$ and SP$-2\times100-3$. The new specimens have 317, 337 and 326 particles, where the resulting area fractions of particles are 0.5025, 0.5049 and 0.5023, respectively. The number of integration points on the line $\{l_1-\zeta\}\times(0,l_2)$, $l_1=2$ mm, $l_2=100$ mm, $\zeta=0.1$ mm, have been determined as 436, 482 and 449, respectively. Five stopping times have been set as

$$T_j=\inf\left\{\tau\geq 0:\tilde{\boldsymbol{X}}(\tau)\notin(0.4\cdot(j-1),2)\times(0,100)\right\},\quad j=1,\ldots,5, \tag{5.33}$$

to obtain estimates of D_{eff} for different values of l_1, *i.e.*, $l_{1,j}=2-0.4\cdot(j-1)$. For each value of j, estimate of D_{eff} can be obtained by introducing $l_{1,j}$ and $\hat{C}(l_{1,j}-\zeta,x_{2,k})$, $k=1,\ldots,n_2$, obtained from Eq. 5.30, into Eq. 5.27.

Table 5.8: $\hat{D}_{\text{eff}}$ (10^{-6} mm^2/s) vs. Specimen Size $(0,l_1)\times(0,100)$

l_1 (mm)	0.4	0.8	1.2	1.6	2.0
SP$-2\times100-1$	1.91	1.79	1.75	1.71	1.72
SP$-2\times100-2$	2.09	1.94	1.92	1.90	1.90
SP$-2\times100-3$	1.93	1.83	1.79	1.75	1.69

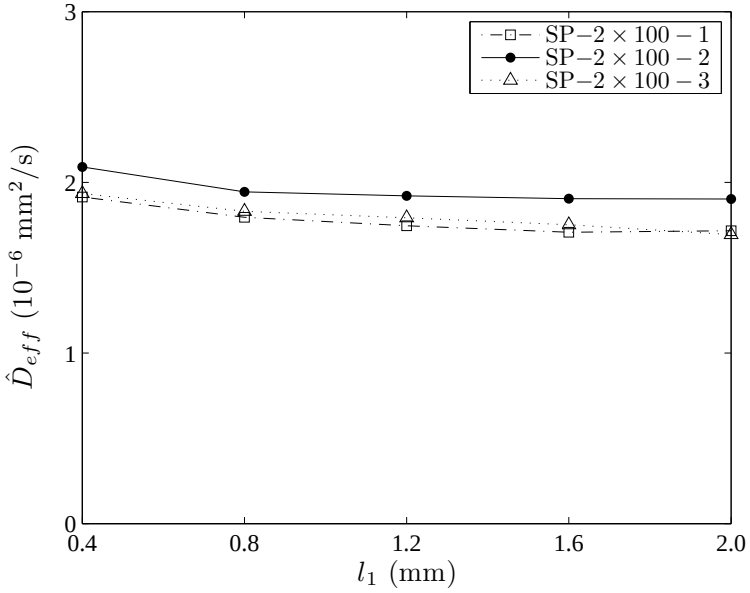

Figure 5.27: $\hat{D}_{\text{eff}}$ vs. Specimen Size $(0, l_1) \times (0, 100)$

Based on $n_s = 1000$ samples of $\tilde{\boldsymbol{X}}$ for each integration point, the resulting estimates of D_{eff} are shown in Table 5.8 and plotted in Figure 5.27. The resulting estimates of D_{eff} for different values of l_1 ranging from 0.4 mm to 50 mm show that l_1 should be equal to or greater than maximum aggregate particle size, which is 2 mm in this case. A value of 5 mm has been chosen for l_1 in the analyses presented in the next section.

In order to examine the effect of the dimension of specimen perpendicular to the chloride flow, l_2, $\hat{D}_{\text{eff}}$ (Eq. 5.27) has been calculated for different values of l_2, *i.e.*, $l_{2,i}$, $i = 1, \ldots, n_2$, based on the analyses of SP$-10 \times 100 - 1$, SP$-10 \times 100 - 2$ and SP$-10 \times 100 - 3$, as

$$\hat{D}_{\text{eff},i} = \frac{l_1}{l_{2,i}} \sum_{j=1}^{i} \triangle x_{2,j} D\left(l_1 - \zeta, x_{2,j}\right) \frac{1 - C\left(l_1 - \zeta, x_{2,j}\right)}{\zeta}, \tag{5.34}$$

where $\{l_1 - \zeta\} \times (0, l_{2,i})$ is a subset of $\{l_1 - \zeta\} \times (0, l_2)$, $l_1 = 10$ mm, $l_2 = 100$ mm, $\zeta = 0.5$ mm, and contains integration points from 1 to $i = 1, \ldots, n_2$.

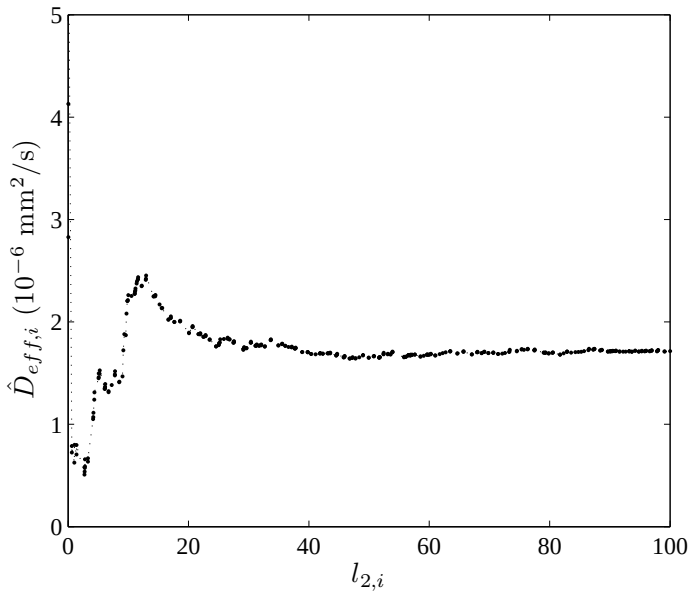

Figure 5.28: $\hat{D}_{\text{eff},i}$ vs. $l_{2,i}$, $i = 1, \ldots, n_2$ (Specimen SP$-10 \times 100 - 1$)

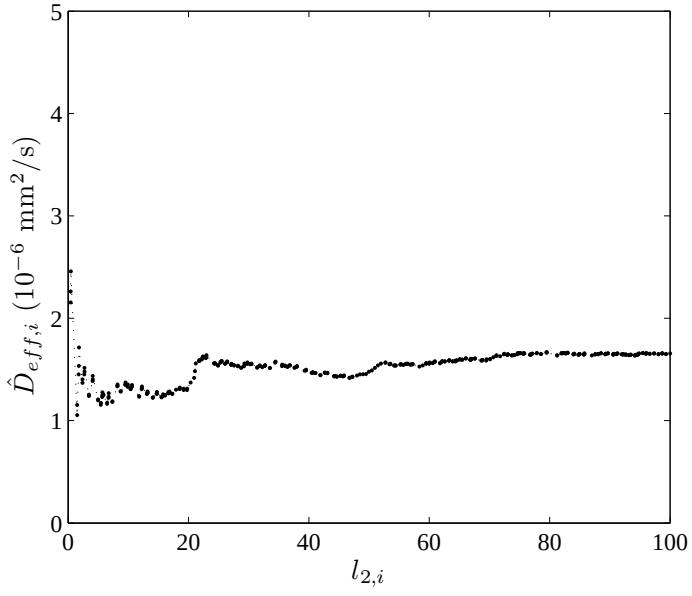

Figure 5.29: $\hat{D}_{\text{eff},i}$ vs. $l_{2,i}$, $i = 1, \ldots, n_2$ (Specimen SP$-10 \times 100 - 2$)

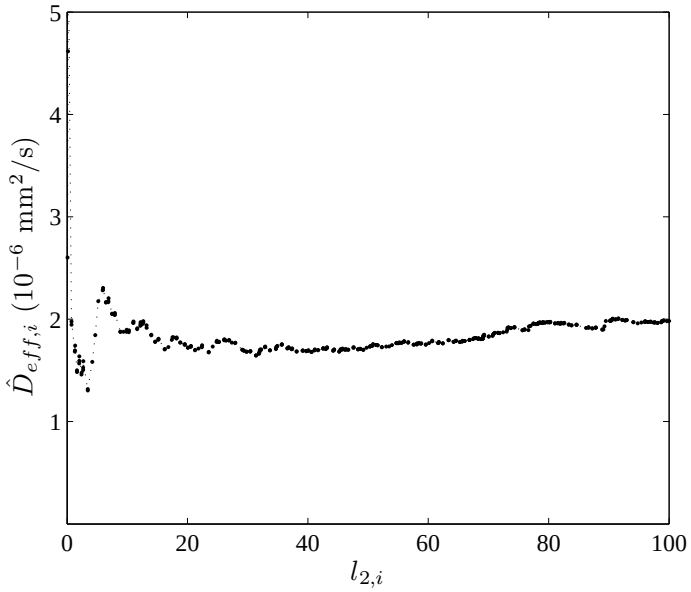

Figure 5.30: $\hat{D}_{\text{eff},i}$ vs. $l_{2,i}$, $i = 1, \ldots, n_2$ (Specimen SP$-10 \times 100 - 3$)

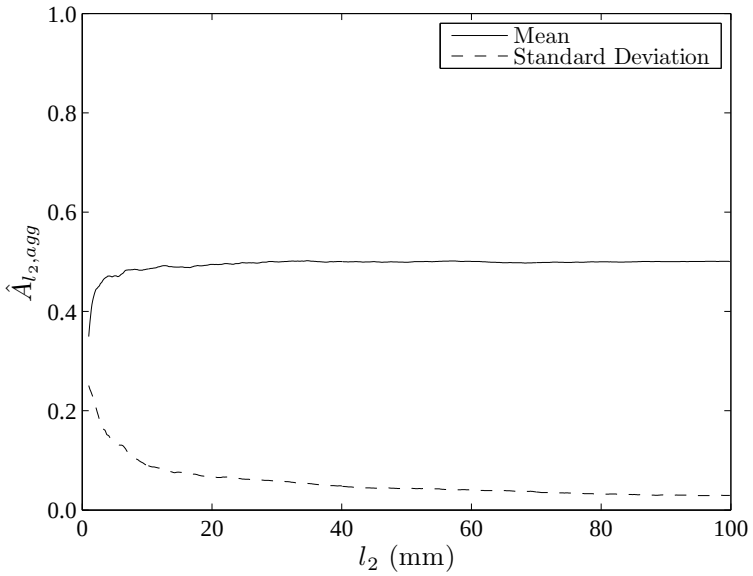

Figure 5.31: Estimates of Mean and Standard Deviation of $A_{l_2,\,\text{agg}}$

The resulting values of $\hat{D}_{\text{eff},i}$, $i = 1, \ldots, n_2$, are shown in Figures 5.28, 5.29 and 5.30, respectively. A critical parameter for determining the value of l_2 is the fraction of the line $\{l_1 - \zeta\} \times (0, l_2)$ falling into aggregate, denoted as $A_{l_2,\,\text{agg}}$. Estimates of mean and standard deviation of $A_{l_2,\,\text{agg}}$ as a function of l_2 have been calculated by using 150 samples from SP$-200 \times 100 - 1$, *i.e.*, $\{x_1\} \times (0, 100)$, $x_1 = 26, \ldots, 175$ (Figure 5.31).

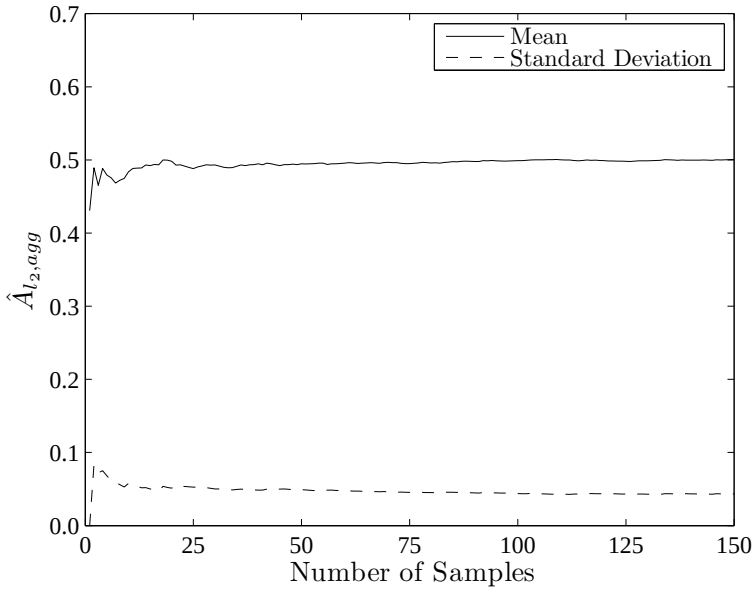

Figure 5.32: Estimates of Statistics of $A_{l_2,\,\text{agg}}$ for $l_2 = 50$ mm

Based on the results shown in Figure 5.28 through Figure 5.31, l_2 has been determined as 50 mm for the analyses presented in Section 5.5.3. According to the estimates of mean and standard deviation of $A_{l_2,\,\text{agg}}$ as a function of sample size for $l_2 = 50$ mm (Figure 5.32), the number of specimen samples n_{sp} has been determined as 20.

5.5.3 Analyses and Results

For estimating the effective diffusion coefficient of chloride in a specimen, chloride diffusivity field within the specimen is required as an input. However, chloride diffusivity fields in interfacial transition zones are not known. Therefore, a real mortar specimen has been analyzed with various chloride diffusivity fields, then the effective diffusion coefficient of chloride in another one has been estimated using one of those diffusivity fields.

A mortar specimen tested by Caré [31] has been chosen for analysis. The sand particle size distribution of the chosen specimen is shown in Figure 5.18 [31]. The specimen was first immersed in a concentrated alkaline solution of KOH (4.65 g/l) + NaOH (1 g/l) and vacuum-saturated. Then, for a non-steady-state diffusion test, it was immersed in a salt solution of KOH (4.65 g/l) + NaOH (1 g/l) + NaCl (30 g/l) for approximately 40 days.

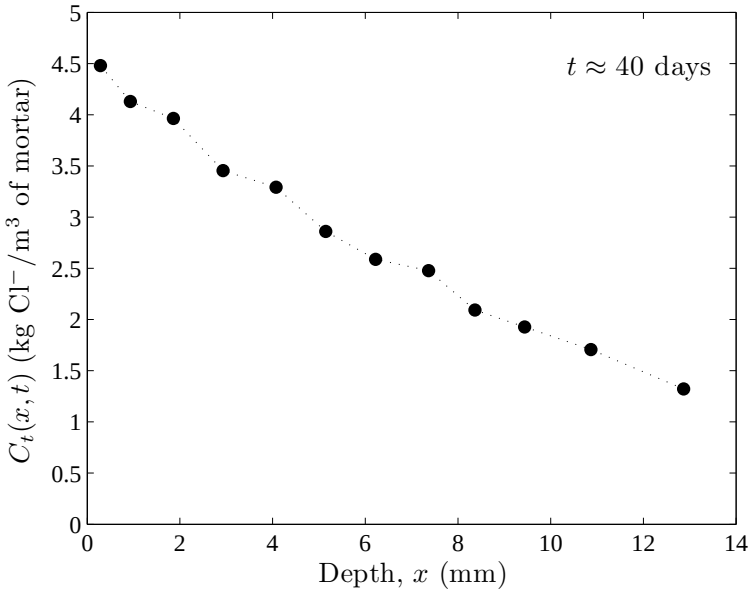

Figure 5.33: Total Chloride Profile at $t \approx 40$ days [31]

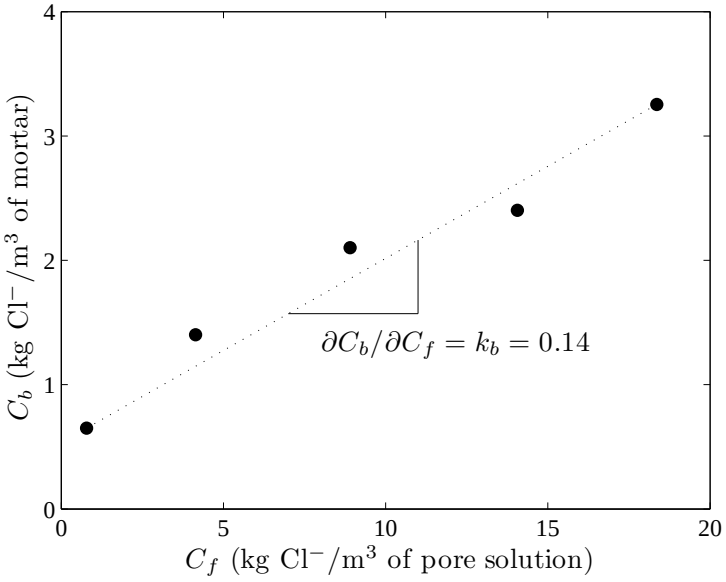

Figure 5.34: Chloride Binding Isotherm [31]

The effective diffusion coefficient of chloride in the specimen was calculated from the measured total chloride profile and chloride binding isotherm, shown in Figures 5.33 and 5.34, respectively [31]. The reason for choosing Caré's specimen is that the effective diffusion coefficient of chloride in the corresponding cement paste specimen was also measured. The effective diffusion coefficients of chloride in the mortar specimen and in the corresponding cement paste specimen, obtained by Caré [31], are shown in Table 5.9.

Table 5.9: Experimental Results by Caré [31]

Specimen	w/c	V_{agg} (%)	D_{eff} (10^{-6} mm^2/s)
Cement Paste	0.45	0	5.65
Mortar	0.45	50	7.40

The particle types and the corresponding proportions p_k, $k = 1, \ldots, 6$, determined according to the sand particle size distribution shown in Figure 5.18, are

shown in Table 5.5, where $d_{L,k}$ and $d_{U,k}$ are the minimum and maximum particle size for type-k particles, respectively. Virtual specimen size, $l_1 \times l_2$ (Figure 5.17), and number of specimen samples, n_{sp}, have been determined as 5 mm $\times$ 50 mm and 20, respectively, as explained in Section 5.5.2. In order to generate specimens of 5 mm by 50 mm, first, specimens of 100 mm by 50 mm have been generated according to the particle size distribution shown in Table 5.5, second, 20 specimens of 5 mm by 50 mm have been cut from the 100 mm by 50 mm specimens. Three of the resulting specimens are shown in Figure 5.35. The number of particles within the specimens range from 323 to 360. The resulting estimates of mean, standard deviation and coefficient of variation of area fraction of aggregate A_{agg} are 0.5023, 0.0114 and 2.26%, respectively. Particle size distributions in virtual specimens SP$-5 \times 50 - \omega_s$, $\omega_s = 1, \ldots, 20$, are shown in Figure 5.36 together with the target particle size distribution.

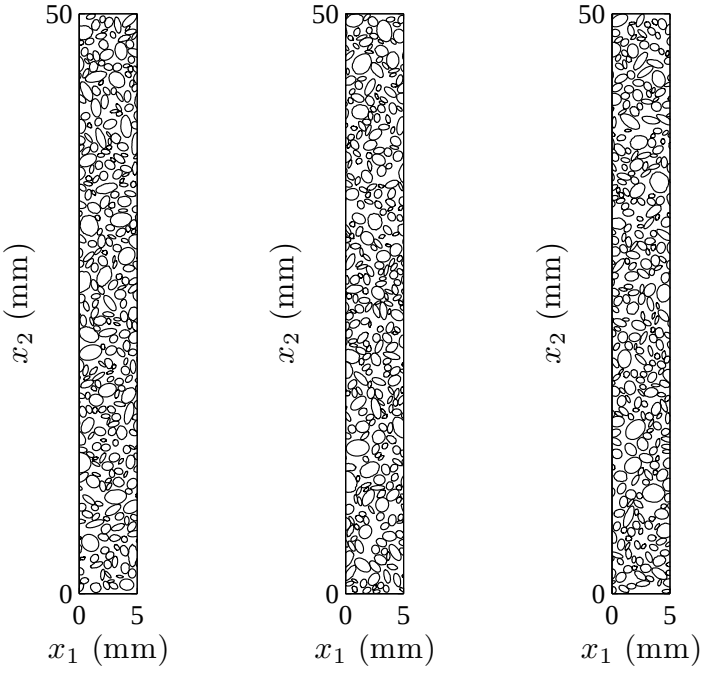

Figure 5.35: SP$-5 \times 50 - 1$, SP$-5 \times 50 - 10$ and SP$-5 \times 50 - 20$

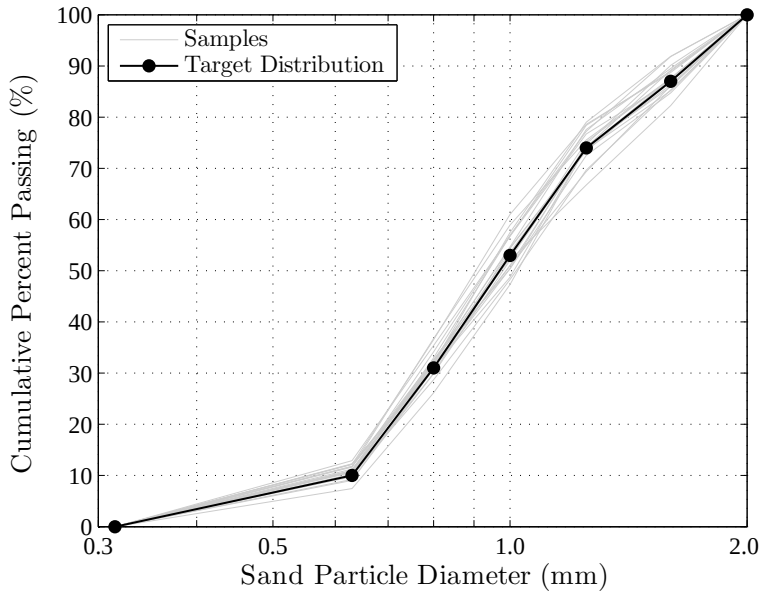

Figure 5.36: Particle Size Distributions in SP$-5 \times 50 - \omega_s$, $\omega_s = 1, \ldots, 20$

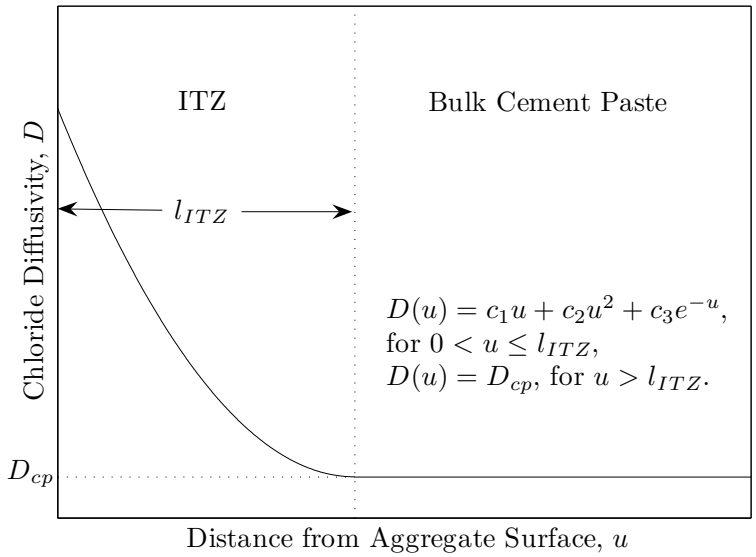

Figure 5.37: Chloride Diffusivity in the Near Vicinity of Aggregate

Table 5.10: Parameters of Chloride Diffusivity Fields

Case	l_{ITZ} (μm)	D_{cp} (10^{-6} mm^2/s)	α_D	α_A
I	0	5.65	1	1
II	30	5.65	35	12.3
III	30	5.65	40	14.0
IV	30	4.00	60	20.6
V	50	5.65	25	9.0

Simulations have been performed for five different cases shown in Table 5.10, where l_{ITZ} is the ITZ thickness, D_{cp} is the effective diffusion coefficient of chloride in the bulk cement paste, $\alpha_D = D(0)/D(l_{\text{ITZ}})$ and α_A is the ratio of chloride diffusion coefficient in the ITZ to the one in the bulk cement paste, if chloride diffusivity field in the ITZ is replaced with a constant diffusivity field, such that

$$\alpha_A = \frac{\int_0^{l_{\text{ITZ}}} D(u)du/l_{\text{ITZ}}}{D_{\text{cp}}}. \tag{5.35}$$

Case I represents a case as if the presence of aggregate does not have any affect on the microstructure of cement paste, *i.e.*, there is no ITZ between cement paste and aggregate. Then the resulting estimate of effective diffusion coefficient reflects the effect of increased tortuosity and dilution due to the presence of aggregate.

The other cases consider various combinations of l_{ITZ} and α_D, or α_A (Figure 5.38). The combinations have been decided in such a way that the resulting estimate of effective diffusion coefficients end up in the neighborhood of the coefficient measured by Caré [31]. l_{ITZ} has been set equal to the estimate of ITZ thickness reported by Caré [31], *i.e.*, 30 μm (Table 5.10), in *Case II*, *Case III* and

Case IV. l_{ITZ} is assumed to be the same for all particles and uniform around each particle in all cases.

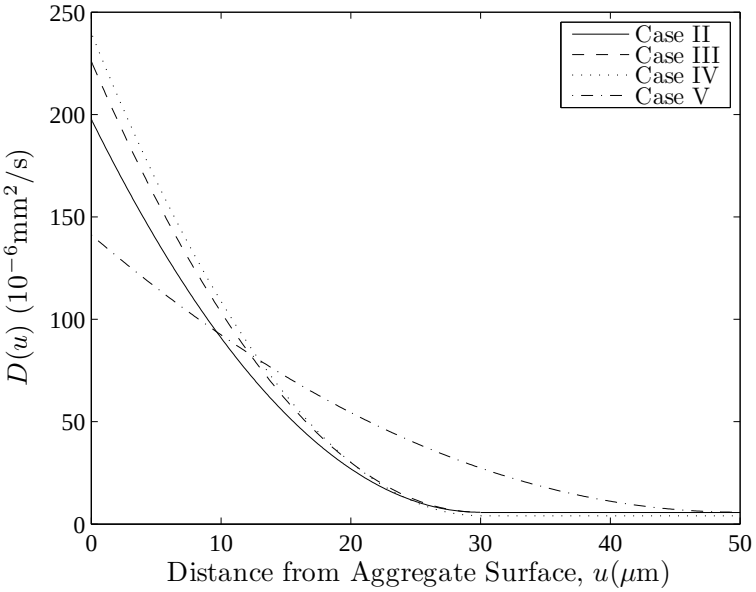

Figure 5.38: Chloride Diffusivity Profiles in the ITZ

Case II and *Case III* assumes that the bulk cement paste in the mortar specimen has the same properties as the cement paste specimen of Caré [31] does, *i.e.*, D_{cp} has been set equal to the effective diffusion coefficient in the cement paste specimen, *i.e.*, $5.65 \cdot 10^{-6}$ mm^2/s (Table 5.10). The values of α_D in *Case II* and *Case III* have been set to 35 and 40, resulting in values of α_A of 12.3 and 14, respectively (Table 5.10), which would result in coefficients bounding the effective diffusion coefficient in the mortar specimen measured by Caré [31].

Case IV considers a redistribution of w/c ratio between bulk cement paste and ITZ. The specimens of Caré [31] have an overall w/c ratio of 0.45 (Table 5.9). However, it is likely that ITZ has a w/c ratio higher than 0.45 due to its relatively high porosity, while bulk cement paste has a ratio lower than 0.45. *Case IV* assumes that D_{cp} is equal to $4.00 \cdot 10^{-6}$ mm^2/s, which corresponds to a

w/c ratio of 0.42-0.43 approximately. Since the value of D_{cp} is smaller than those in *Case II* and *Case III*, the chloride diffusivity in the ITZ needs to be larger than those in *Case II* and *Case III* in order to obtain an estimate close to the effective diffusion coefficient of chloride in the mortar specimen measured by Caré [31]. Therefore α_D has been set equal to 60, resulting in an α_A of 20.6 (Table 5.10).

Case V also assumes that the bulk cement paste in the mortar specimen has the same properties as the cement paste specimen of Caré [31] does. However, it considers an ITZ thickness of 50 μm (Table 5.10), unlike *Case II* and *Case III* do. Since the value of l_{ITZ} in *Case V* is larger than those in *Case II* and *Case III*, the chloride diffusivity in the ITZ needs to be less than those in *Case II* and *Case III* in order to obtain an estimate close to the effective diffusion coefficient of chloride in the mortar specimen of Caré [31]. Therefore α_D has been set equal to 25, resulting in an α_A of 9.0 (Table 5.10).

In an analysis of a case, the procedure followed for analyzing each specimen SP$-5 \times 50 - \omega_s$, $\omega_s = 1, \ldots, 20$, is explained below.

- The number and location of integration points, $n_2(\omega_s)$ and $x_{2,k}(\omega_s)$, $k = 1, \ldots, n_2(\omega_s)$, respectively, are determined using the algorithm explained in Section 5.5.2.
- The chloride concentrations at the integration points $C(l_1 - \zeta, x_{2,k}(\omega_s), \omega_s)$, $k = 1, \ldots, n_2(\omega_s)$, are estimated by using Eq. 5.30, where the number of samples of Itô process $\tilde{\boldsymbol{X}}$ (Eq. 3.23a), n_s, and ζ have been chosen as 1000 and 0.1 mm, respectively. Estimates of mean and standard deviation of step size of resulting samples of $\tilde{\boldsymbol{X}}$ are shown in Table 5.11.
- The effective diffusion coefficient of chloride in the specimen is estimated by introducing $\hat{C}(l_1 - \zeta, x_{2,k}(\omega_s), \omega_s)$ into Eq. 5.27.

Table 5.11: Statistics of Step Size of Samples of $\tilde{\boldsymbol{X}}$

Case	Estimate of Mean (μm)	Estimate of Std. Dev. (μm)
I	18	10
II	12	11
III	14	12
IV	13	12
V	13	11

The resulting statistics of $\hat{D}_{\text{eff}}$ based on 20 specimen samples, *i.e.*, $\hat{\mu}_{D_{\text{eff}}}$ and $\hat{\sigma}_{D_{\text{eff}}}$, and relative error calculated as

$$\epsilon_{\text{rel}} = \frac{\hat{\mu}_{D_{\text{eff}}} - D_{\text{eff,mortar}}}{D_{\text{eff,mortar}}} \times 100, \tag{5.36}$$

where $D_{\text{eff,mortar}} = 5.65 \cdot 10^{-6}$ mm^2/s (Table 5.9) is the effective diffusion coefficient of chloride in the mortar specimen measured by Caré [31], are shown in Table 5.12.

Table 5.12: Statistics of $\hat{D}_{\text{eff}}$ by the RWM

Case	$\hat{\mu}_{D_{\text{eff}}}$ (10^{-6} mm^2/s)	$\hat{\sigma}_{D_{\text{eff}}}$ (10^{-6} mm^2/s)	ϵ_{rel} (%)
I	1.90	0.14	-74.3
II	7.00	0.82	-5.4
III	7.76	0.93	+4.8
IV	7.46	0.95	+0.8
V	8.03	0.78	+8.4

Estimates of mean and standard deviation of the effective diffusion coefficient as a function of number of specimen samples, n_{sp}, are plotted in Figures 5.39, 5.41, 5.43, 5.45 and 5.47. It can be observed that an n_{sp} of 20 is sufficient

to obtain stabilized results. Also, histograms of $\hat{D}_{\text{eff}}$ are plotted in Figures 5.40, 5.42, 5.44, 5.46 and 5.48.

Case I results in a $\hat{\mu}_{D_{\text{eff}}}$ of $1.90 \cdot 10^{-6}$ mm^2/s and a $\hat{\sigma}_{D_{\text{eff}}}$ of $0.14 \cdot 10^{-6}$ mm^2/s, where the resulting relative error in the $\hat{\mu}_{D_{\text{eff}}}$ is -74.3% (Table 5.12). Since there are no interfacial transition zones in *Case I*, *i.e.*, only the increased tortuosity and dilution due to the presence of aggregate are in effect, the resulting estimate of the D_{eff} is much smaller than the $D_{\text{eff,mortar}}$.

Case II leads to a $\hat{\mu}_{D_{\text{eff}}}$ of $7.00 \cdot 10^{-6}$ mm^2/s and a $\hat{\sigma}_{D_{\text{eff}}}$ of $0.82 \cdot 10^{-6}$ mm^2/s, where the resulting relative error in the $\hat{\mu}_{D_{\text{eff}}}$ is -5.4% (Table 5.12). Significant reduction in the relative error compared to that in *Case I*, from -74.3% to -5.4%, shows the effect of ITZ on the effective diffusion coefficient.

Case III, in which l_{ITZ} and D_{cp} are the same as those in *Case II*, yields a $\hat{\mu}_{D_{\text{eff}}}$ of $7.76 \cdot 10^{-6}$ mm^2/s and a $\hat{\sigma}_{D_{\text{eff}}}$ of $0.93 \cdot 10^{-6}$ mm^2/s, where the resulting relative error in the $\hat{\mu}_{D_{\text{eff}}}$ is +4.8% (Table 5.12). The difference between *Case II* and *Case III* is the chloride diffusivity profiles in the ITZ (Figure 5.38). Then the chloride diffusivity profile in the ITZ of the mortar specimen of Caré [31] is in between the chloride diffusivity profiles considered by *Case II* and *Case III* (Figure 5.38), that is, α_D is between 35 and 40, or α_A is between 12.3 and 14.0, provided that the chloride diffusion coefficient in the bulk cement paste is equal to the effective diffusion coefficient of chloride in the cement paste specimen of Caré [31].

Case IV leads to a $\hat{\mu}_{D_{\text{eff}}}$ of $7.46 \cdot 10^{-6}$ mm^2/s and a $\hat{\sigma}_{D_{\text{eff}}}$ of $0.95 \cdot 10^{-6}$ mm^2/s, where the resulting relative error in the $\hat{\mu}_{D_{\text{eff}}}$ is 0.8% (Table 5.12). Since the relative error is small, there is no need to analyze another case to bound the experimental coefficient in the mortar specimen. *Case IV* can be thought as a more

realistic case than the others, since it is likely that a redistribution of w/c ratio would take place due to the relatively high porosity in the ITZ.

Case V, in which l_{ITZ} is larger than those in *Case II* and *Case III*, but D_{cp} is the same as those in *Case II* and *Case III*, results in a $\hat{\mu}_{D_{\text{eff}}}$ of $8.03 \cdot 10^{-6}$ mm^2/s and a $\hat{\sigma}_{D_{\text{eff}}}$ of $0.78 \cdot 10^{-6}$ mm^2/s, where the resulting relative error in the $\hat{\mu}_{D_{\text{eff}}}$ is +8.4% (Table 5.12). *Case V* has been included to examine the effect of l_{ITZ} on the effective diffusion coefficient.

Based on the results obtained by the RWM, it is concluded that ITZ is an important phase affecting the effective diffusion coefficient of chloride significantly. *Case I* shows that a 74.3% reduction would occur in the D_{eff} if there were no ITZ, due to the increased tortuosity and dilution. The presence of ITZ affects the D_{eff} in the opposite direction, and yields a D_{eff} larger than that in the cement paste specimen in these particular cases, *Case II* through *Case V*.

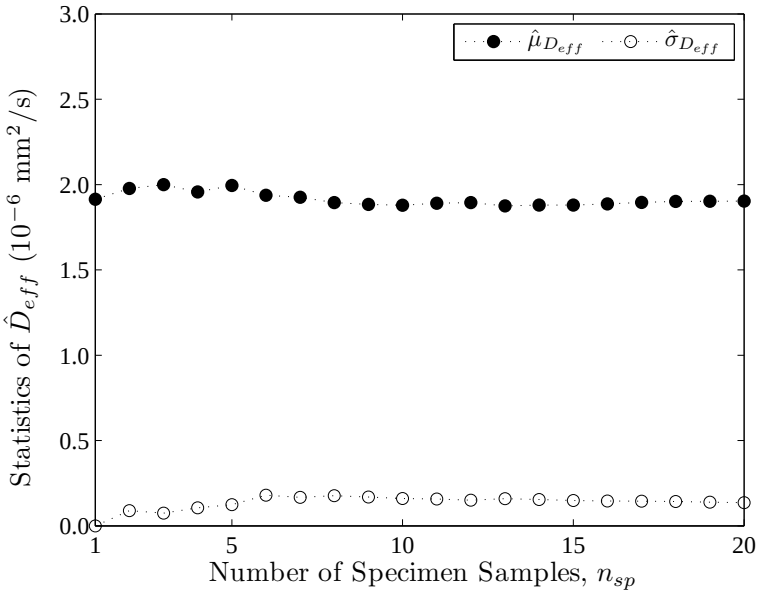

Figure 5.39: Statistics of $\hat{D}_{\text{eff}}$ for Case I

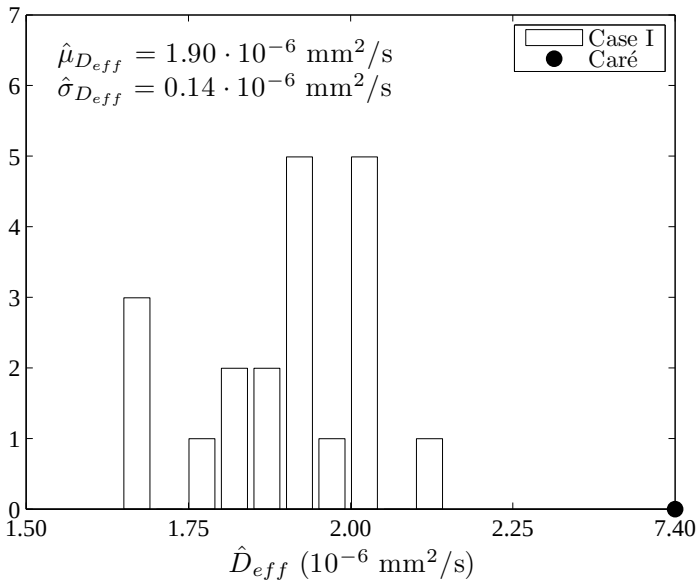

Figure 5.40: Histogram of $\hat{D}_{\text{eff}}$ for Case I

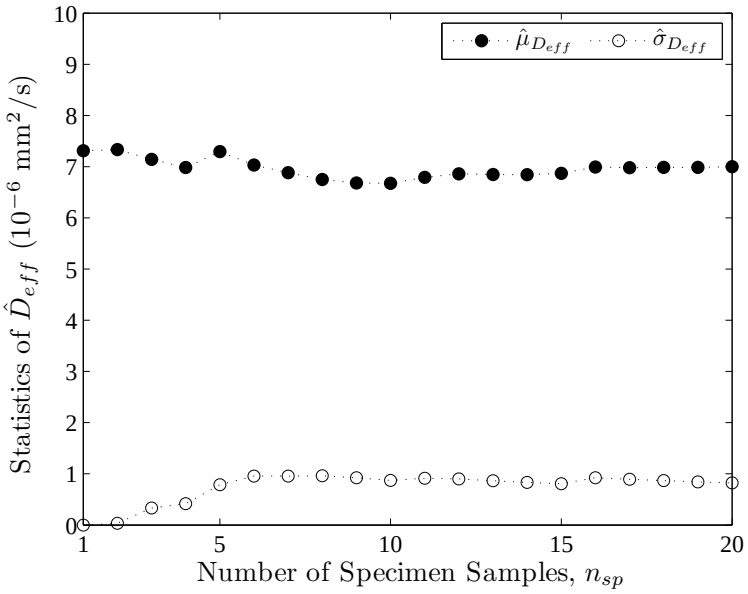

Figure 5.41: Statistics of $\hat{D}_{\text{eff}}$ for Case II

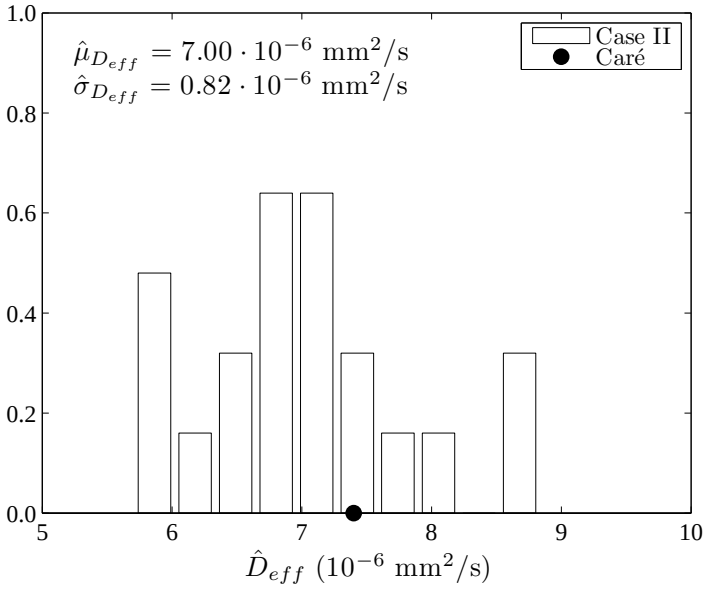

Figure 5.42: Histogram of $\hat{D}_{\text{eff}}$ for Case II

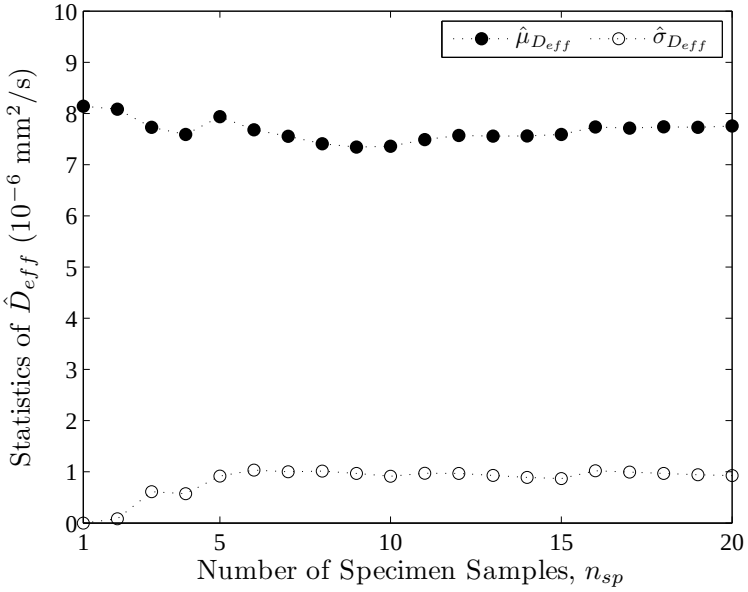

Figure 5.43: Statistics of $\hat{D}_{\text{eff}}$ for Case III

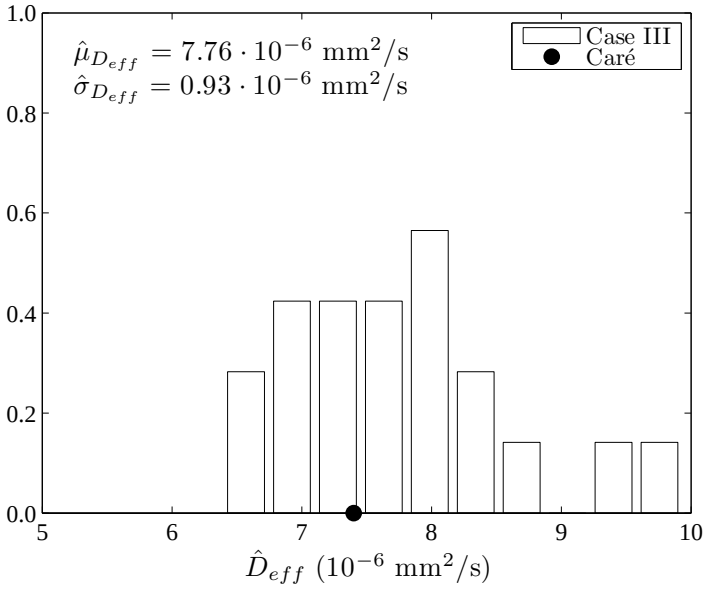

Figure 5.44: Histogram of $\hat{D}_{\text{eff}}$ for Case III

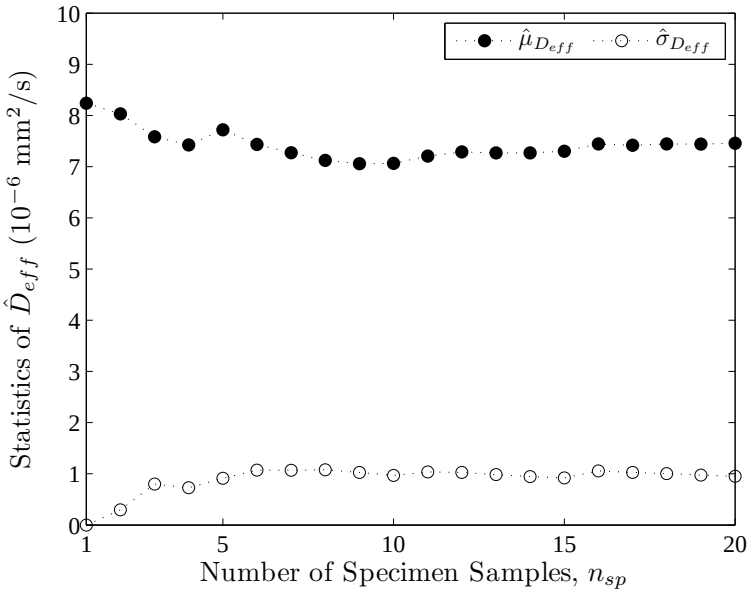

Figure 5.45: Statistics of $\hat{D}_{\text{eff}}$ for Case IV

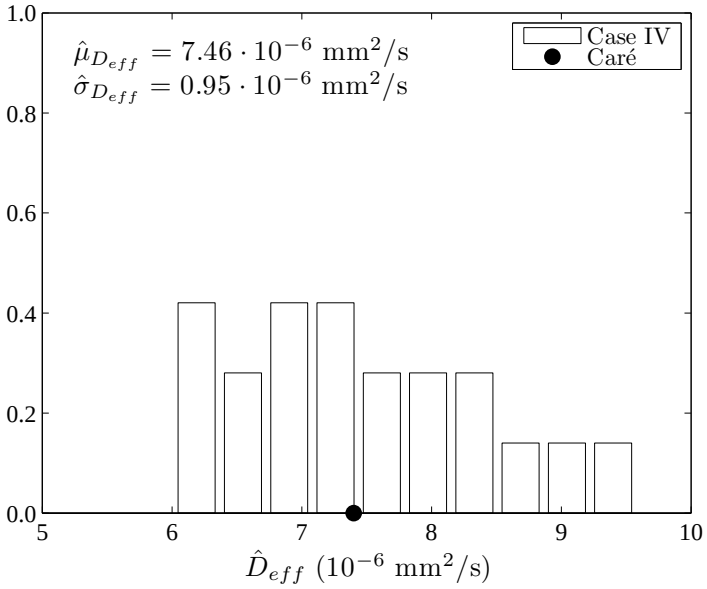

Figure 5.46: Histogram of $\hat{D}_{\text{eff}}$ for Case IV

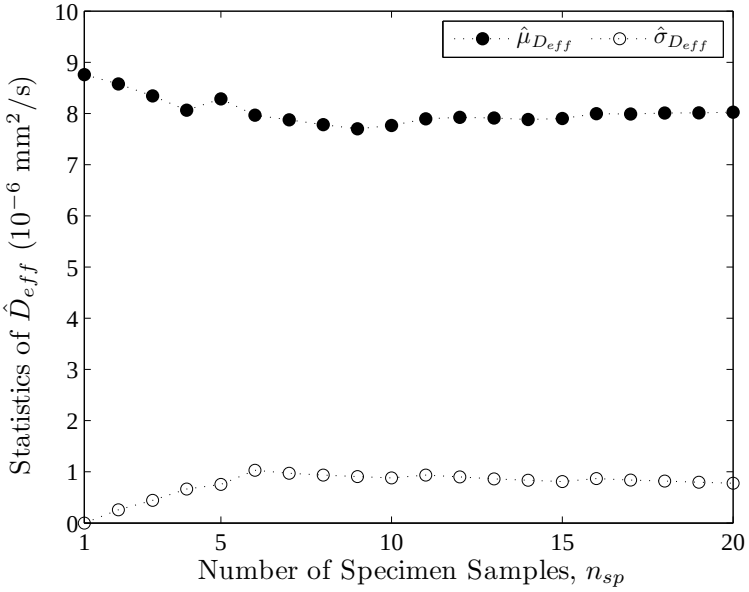

Figure 5.47: Statistics of $\hat{D}_{\text{eff}}$ for Case V

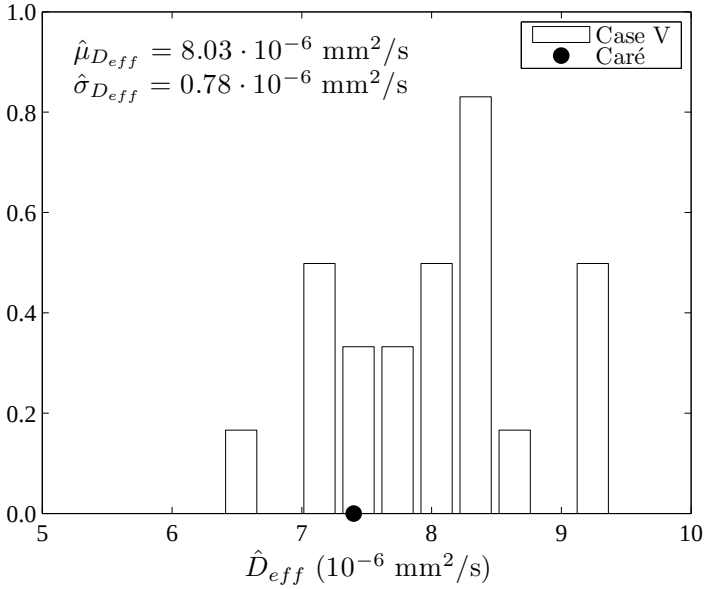

Figure 5.48: Histogram of $\hat{D}_{\text{eff}}$ for Case V

5.5.4 Comparison with Other Methods

For comparison, some of the methods reviewed in Sections 5.3 and 5.4, the ones developed by Garboczi and Bentz [63], Garboczi and Berryman [67], Xi and Bažant [187], and Yang and Su [193], have been used to estimate the effective diffusion coefficient of chloride.

For analysis by the numerical method of Garboczi and Bentz [63], $n_{sp} = 20$ computational cubic volumes having a size length of 10 mm have been generated. Spheres, representing sand particles, have been generated according to the particle size distribution given in Table 5.5, and then they have been placed randomly in cubic volumes, which have periodic boundary conditions. One of the computational cubic volumes is shown in Figure 5.49.

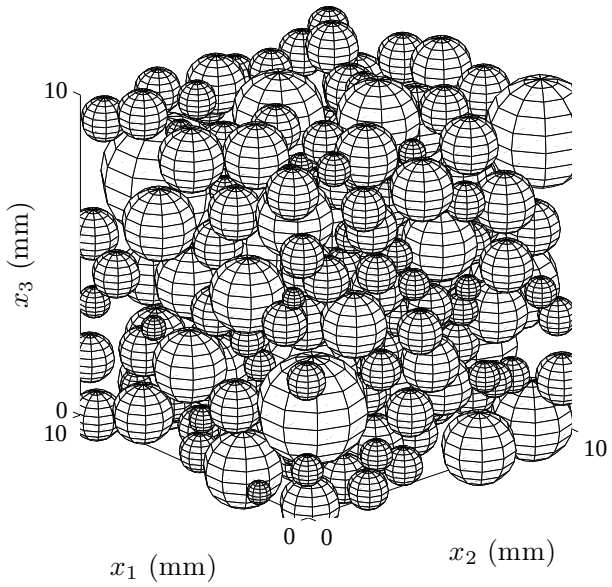

Figure 5.49: A Computational Cubic Volume

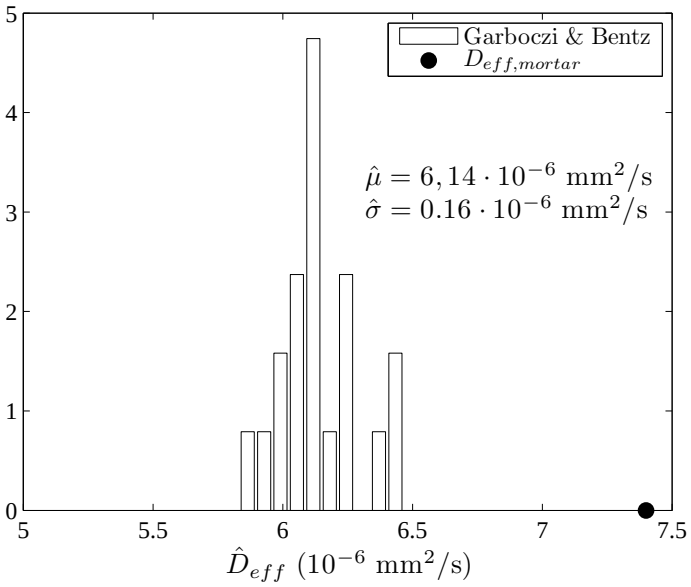

Figure 5.50: Histogram of $\hat{D}_{\text{eff}}$ by the Method of Garboczi and Bentz [63]

The model defines the chloride diffusivity in the vicinity of aggregate particles as a step function. For analyses, chloride diffusivity fields in cubic volumes have been defined with the parameters used in *Case III* (Section 5.5.3), that is, the ITZ thickness l_{ITZ} and the ratio of the chloride diffusion coefficient in the ITZ to the one in the bulk cement paste, α_A, are 30 μm and 14.0, respectively. $n_s = 1000$ random walks, which start from randomly selected points and perform 200,000 steps, have been executed within each cubic volume, and the effective diffusion coefficient of chloride in each cubic volume has been estimated by using Eq. 5.22. The resulting estimates of mean and standard deviation of D_{eff} are $6.14 \cdot 10^{-6}$ mm^2/s and $0.16 \cdot 10^{-6}$ mm^2/s (Figure 5.50), respectively, where the resulting error in the $\hat{D}_{\text{eff}}$ relative to the one obtained in *Case III* by using the RWM is -20.9% (Table 5.13).

The effective diffusion coefficients for all cases studied in Section 5.5.3 have been calculated also by using the effective medium theory developed by Garboczi and Berryman [67]. The resulting estimates of the D_{eff} are shown in Table 5.13. Other than *Case I*, the resulting error in the $\hat{D}_{\text{eff}}$ relative to the one obtained in the corresponding case by using the RWM is more than 30% (Table 5.13).

According to the model developed by Xi and Bažant [187], the effective diffusion coefficient of chloride in the mortar specimen measured by Caré [31] can be approximated by Eq. 5.23. If the chloride diffusion coefficient in the cement paste and the volume fraction of aggregate are introduced into Eq. 5.23 as $5.65 \cdot 10^{-6}$ mm^2/s and 0.5, respectively, Eq. 5.23 calculates the D_{eff} in the mortar specimen as $2.26 \cdot 10^{-6}$ mm^2/s, with an error of +18.7% relative to the one obtained in *Case I* by using the RWM (Table 5.13). It is important to note that Eq. 5.23 does not consider the effect of ITZ on the effective diffusion coefficient.

The effective diffusion coefficient calculated from Eq. 5.25, developed by Yang and Su [193], for *Case I* through *Case IV* are shown in Table 5.13. The chloride diffusion coefficient in the neat cement paste, the volume fraction of aggregate and the volume fraction of ITZ in Eq. 5.25 are $5.65 \cdot 10^{-6}$ mm^2/s, 0.5 and 0.103, respectively [31], and β in Eq. 5.25 is equal to α_A (Eq. 5.35), the value of which is given in Table 5.10 for each case. For *Case I*, the $\hat{D}_{\text{eff}}$ obtained from Eq. 5.25 is in good agreement with the one obtained by using the RWM. On the other hand, the results for *Case IV* are significantly different. The resulting errors in the $\hat{D}_{\text{eff}}$ relative to the ones obtained in *Case II* and *Case III* by using the RWM are +22.5% and +23.3% (Table 5.13), respectively.

Table 5.13: Comparison of $\hat{D}_{\text{eff}}$ by the RWM with Other Methods

Method	$\hat{D}_{\text{eff}}$ (10^{-6} mm^2/s)	Case	$\hat{D}_{\text{eff}}$ (RWM) (10^{-6} mm^2/s)	ϵ_{rel} (%)
Garboczi & Bentz [63]	6.14	III	7.76	-20.9
Garboczi & Berryman [67]	1.70	I	1.90	-10.7
Garboczi & Berryman [67]	4.48	II	7.00	-36.0
Garboczi & Berryman [67]	4.97	III	7.76	-35.9
Garboczi & Berryman [67]	4.91	IV	7.46	-34.2
Xi & Bažant [187]	2.26	I	1.90	+18.7
Yang & Su [193]	2.00	I	1.90	+4.9
Yang & Su [193]	8.57	II	7.00	+22.5
Yang & Su [193]	9.56	III	7.76	+23.3
Yang & Su [193]	13.40	IV	7.46	+79.8

It can be observed in Figure 5.51 that the effective diffusion coefficients obtained by various methods agree well when there is no ITZ, *i.e.*, in *Case I*. In

the other cases, the coefficients obtained by the method of Yang and Su [193] is larger than the ones by the RWM, whereas the coefficients obtained by the method of Garboczi and Berryman [67] is smaller than the ones by the RWM.

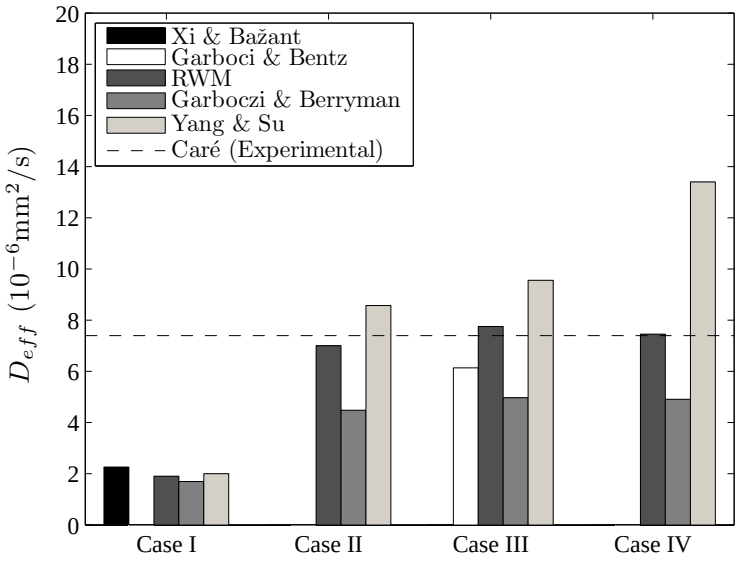

Figure 5.51: Comparison of $\hat{D}_{\text{eff}}$ by Various Methods

5.5.5 Estimating Effective Diffusion Coefficient

Caré [31] tested another mortar specimen prepared with the same cement paste, but finer sand particles, compared to the mortar specimen analyzed in Section 5.5.3. The effective diffusion coefficient of chloride in this specimen was measured as $9.50 \cdot 10^{-6}$ mm^2/s (Table 5.14). The objective is to estimate the effective diffusion coefficient in this specimen by using the RWM method with the chloride diffusivity field defined by *Case IV* (Section 5.5.3).

According to the sand particle size distribution shown in Figure 5.52, the particle types and the corresponding proportions p_k, $k = 1, \ldots, 5$, have been

determined as shown in Table 5.15, where $d_{L,k}$ and $d_{U,k}$ are the minimum and maximum particle size for type-k particles, respectively. Area fraction of particles, A_{agg}, is 0.5 [31]. Specimens of 100 mm by 50 mm have been generated according to the particle size distribution shown in Table 5.15. The resulting proportions $\hat{p}_k$, $k = 1, \ldots, 5$, in SP$-100 \times 50 - 1$ are shown in Table 5.15, where the resulting area fraction of 12955 particles, $\hat{A}_{\text{agg}}$, is 0.5002.

Table 5.14: Experimental Results by Caré [31]

Specimen	w/c	V_{agg} (%)	D_{eff} (10^{-6} mm^2/s)
Cement Paste	0.45	0	5.65
Mortar (F)	0.45	50	9.50

Table 5.15: Particle Size Distribution in Virtual Specimens

Type-k	$d_{L,k}$ (mm)	$d_{U,k}$ (mm)	p_k (by area)	$\hat{p}_k$ (by area)
1	0.315	0.400	0.09	0.09
2	0.400	0.510	0.10	0.10
3	0.510	0.630	0.09	0.09
4	0.630	0.800	0.65	0.6499
5	0.800	1.000	0.07	0.0701

Then 20 specimens of 5 mm by 50 mm have been cut from the 100 mm by 50 mm specimens. Three of the resulting specimens are shown in Figure 5.53. The number of particles within the specimens range from 698 to 739. The resulting estimates of mean, standard deviation and coefficient of variation of area fraction of aggregate A_{agg} are 0.5005, 0.0050 and 1.00%, respectively. Particle size distributions in virtual specimens SP$-5 \times 50 - \omega_s$, $\omega_s = 21, \ldots, 40$, are shown in Figure 5.52 together with the target particle size distribution.

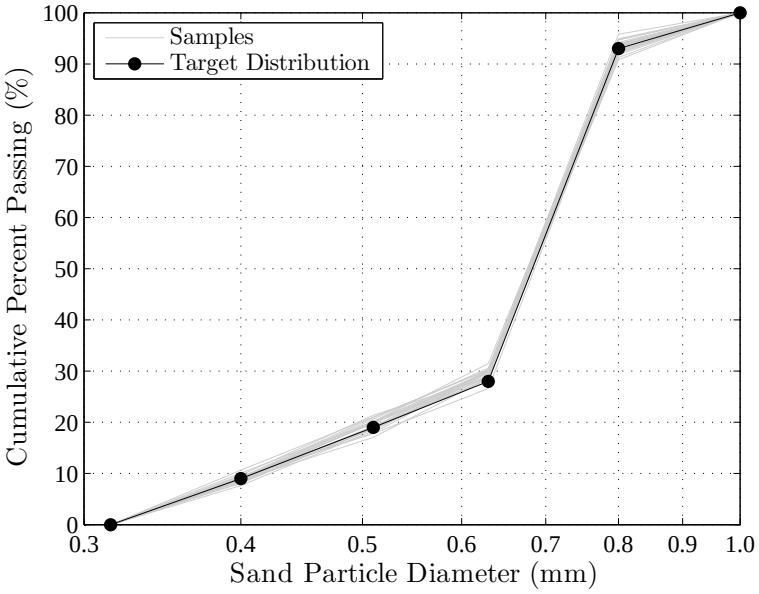

Figure 5.52: Particle Size Distributions in SP$-5 \times 50 - \omega_s, \omega_s = 21, \ldots, 40$

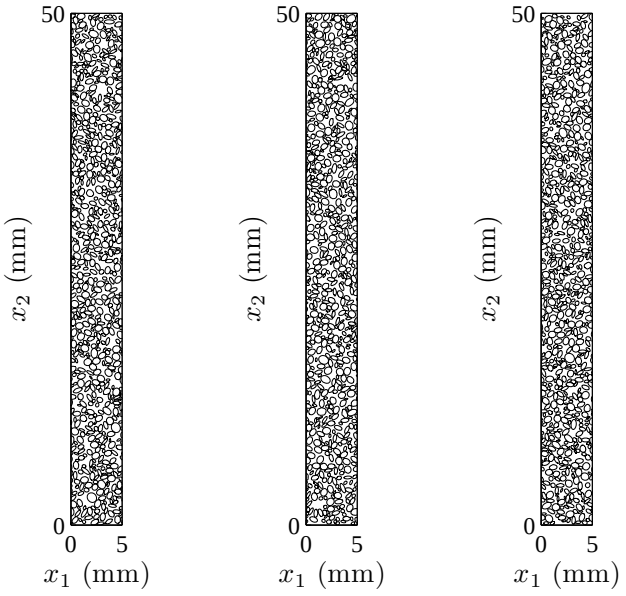

Figure 5.53: SP$-5 \times 50 - 21$, SP$-5 \times 50 - 30$ and SP$-5 \times 50 - 40$

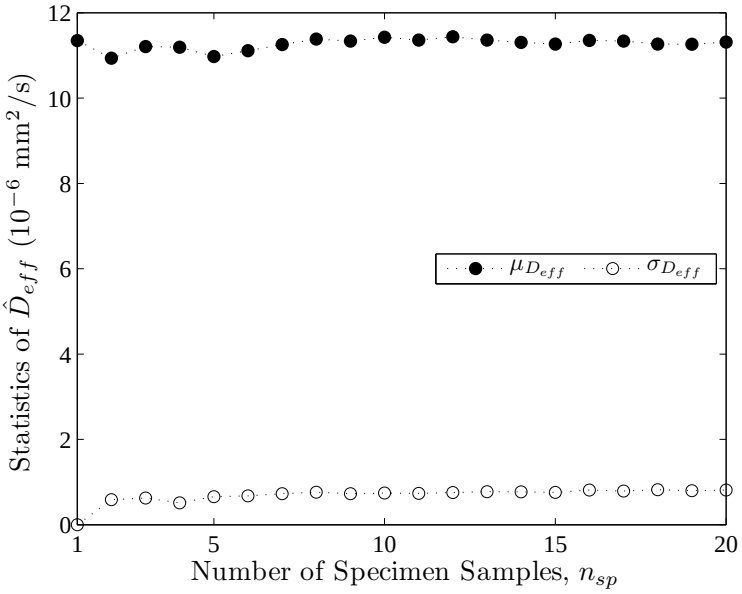

Figure 5.54: Statistics of $\hat{D}_{\text{eff}}$ for Mortar (F)

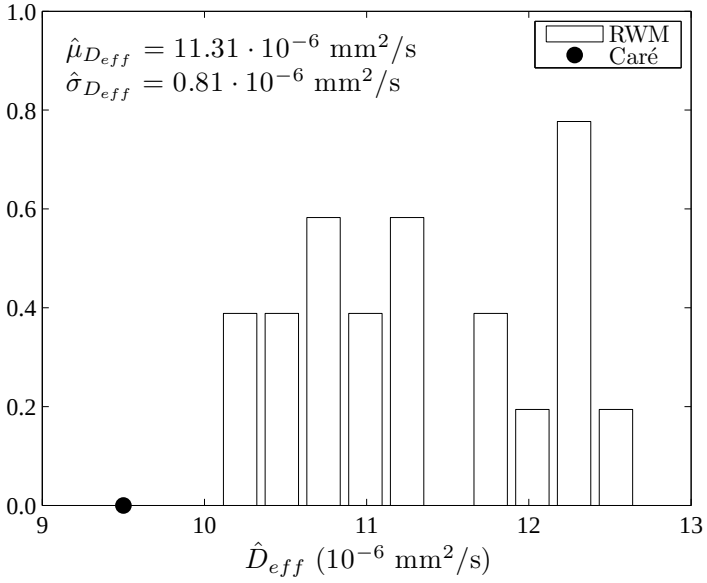

Figure 5.55: Histogram of $\hat{D}_{\text{eff}}$ for Mortar (F)

The procedure followed for analyzing each specimen SP$-5 \times 50 - \omega_s$, $\omega_s = 21, \ldots, 40$, is explained in Section 5.5.3. Estimates of mean and standard deviation of step size of resulting samples of $\tilde{\boldsymbol{X}}$ are 12 μm and 11 μm, respectively. Estimates of mean and standard deviation of the effective diffusion coefficient as a function of number of specimen samples, n_{sp}, and histogram of $\hat{D}_{\text{eff}}$ are plotted in Figures 5.54 and 5.55, respectively. The resulting estimates of mean and standard deviation of D_{eff} are $11.26 \cdot 10^{-6}$ mm^2/s and $0.76 \cdot 10^{-6}$ mm^2/s (Figure 5.55), respectively.

Comparing the results for the mortar (M) analyzed in Section 5.5.3 and the mortar (F) analyzed in this section, it can be observed that using finer sand particles, while keeping aggregate fraction constant, results in a higher effective diffusion coefficient, provided that ITZ has the same transport properties, because finer particles results in a larger amount of ITZ, in which diffusivity is relatively high.

The resulting estimate of the D_{eff} in mortar (F) is 19.1% higher than the corresponding experimental result of Caré [31]. The error shows that the chloride diffusivity field within the mortar (F) is different from the field within the mortar (M). However, the estimate is still in satisfactory agreement with the experimental result.

5.6 Estimating Chloride Concentration

The total chloride profile and the chloride binding isotherm, measured by Caré [31], for the mortar specimen analyzed in Section 5.5.3 are shown in Fig-

ures 5.33 and 5.34, respectively. The free chloride profile can be obtained as follows:

$$\begin{aligned} C_t(x,t) &= C_b(x,t) + \phi C_f(x,t) = k_b C_f(x,t) + \phi C_f(x,t) \\ \Rightarrow C_f(x,t) &= \frac{C_t(x,t)}{k_b + \phi}, \end{aligned} \tag{5.37}$$

where $C_t(x,t)$ is the total chloride concentration (kg/m^3 of mortar), $C_b(x,t)$ is the bound chloride concentration (kg/m^3 of mortar), $C_f(x,t)$ is the free chloride concentration (kg/m^3 of pore solution) at depth x and time t, ϕ is the porosity and k_b is the linear chloride binding isotherm (Figure 5.34). ϕ and k_b are 0.122 and 0.1431, respectively [31]. The calculated free chloride profile is shown in Figure 5.56. The time of measurement is given as approximately 40 days [31].

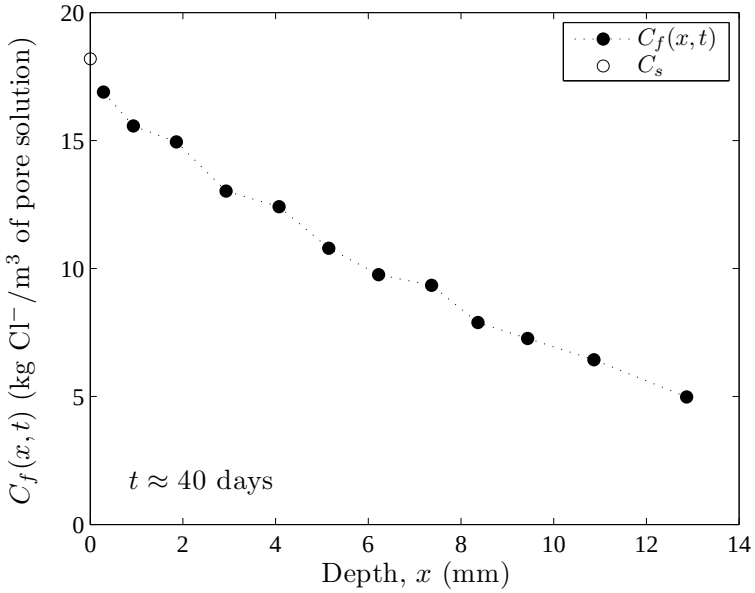

Figure 5.56: Free Chloride Profile

The objective is to calculate the free chloride concentration at a few points at 40 days. Let $H = (0, l_1) \times (0, l_2) \in \mathbb{R}^2$, be a bounded subset containing a virtual mortar specimen of interest and $D(\boldsymbol{x}) > 0$, $\boldsymbol{x} \in H$, be the chloride diffusivity

field. The free chloride concentration $C_f(\boldsymbol{x}, t)$, $\boldsymbol{x} \in H$, $t \geq 0$, satisfies

$$\frac{\partial C_f(\boldsymbol{x}, t)}{\partial t} = \sum_{p=1}^{2} \frac{\partial D^*(\boldsymbol{x})}{\partial x_p} \frac{\partial C_f(\boldsymbol{x}, t)}{\partial x_p} + D^*(\boldsymbol{x}) \Delta C_f(\boldsymbol{x}, t), \tag{2.10}$$

where Δ is the Laplace operator and

$$D^*(\boldsymbol{x}) = \frac{D(\boldsymbol{x})}{k_b + \phi}. \tag{2.11}$$

The initial condition is

$$C_f(\boldsymbol{x}, 0) = 0, \quad \boldsymbol{x} \in H, \tag{5.38}$$

and the boundary conditions are

$$C_f(\boldsymbol{x}, t) = C_s, \quad \boldsymbol{x} \in \{0\} \times (0, l_2), \quad t > 0, \tag{5.39a}$$

$$C_f(\boldsymbol{x}, t) = 0, \quad \boldsymbol{x} \in \{l_1\} \times (0, l_2), \quad t > 0, \tag{5.39b}$$

$$C_f(\boldsymbol{x}, t) = 0, \quad \boldsymbol{x} \in (0, l_1) \times \{0\}, \quad t > 0, \tag{5.39c}$$

$$C_f(\boldsymbol{x}, t) = 0, \quad \boldsymbol{x} \in (0, l_1) \times \{l_2\}, \quad t > 0, \tag{5.39d}$$

where C_s is the surface chloride concentration.

$C_f(\boldsymbol{x}, t)$, $\boldsymbol{x} \in H$, $t > 0$, can be calculated using the random walk method (RWM) given in Chapter 3. Let $\tilde{\boldsymbol{X}} = (\boldsymbol{X}, X_3)$, $\tilde{\boldsymbol{X}}(0) = (\boldsymbol{x}, t)$, be an $\mathbb{R}^3$-valued Itô process defined by the stochastic differential equation

$$d\boldsymbol{X}(\tau) = \boldsymbol{a}(\boldsymbol{X}(\tau))d\tau + \boldsymbol{b}(\boldsymbol{X}(\tau))d\boldsymbol{B}(\tau), \quad \tau \geq 0, \tag{3.23a}$$

$$dX_{d+1}(\tau) = -d\tau, \tag{3.23b}$$

where $\boldsymbol{a}$ and $\boldsymbol{b}$ are the drift and diffusion coefficients, respectively, *i.e.*,

$$a_k(\boldsymbol{x}) = \frac{\partial D^*(\boldsymbol{x})}{\partial x_k}, \quad k = 1, 2, \tag{3.21}$$

$$\boldsymbol{b}(\boldsymbol{x}) = \sqrt{2D^*(\boldsymbol{x})}\boldsymbol{i}. \tag{3.22}$$

Then $C_f(\boldsymbol{x}, t)$ is given by Eq. 3.34, which in this case reduces to

$$C_f(\boldsymbol{x}, t) = E\left[C_f(\tilde{\boldsymbol{X}}(\tilde{T})\right] = E\left[C_f(\tilde{\boldsymbol{X}}(t-\tilde{T}))\,\middle|\,\tilde{T} < t\right] P\left(\tilde{T} < t\right), \quad (5.41)$$

where

$$\tilde{T} = \inf\{\tau > 0 : \tilde{\boldsymbol{X}}(\tau) \notin H \times (0, t)\} \quad (3.30)$$

is a stopping-time, that is, the time at which $\tilde{\boldsymbol{X}}$ exits $H \times (0, t)$ for the first time. It is not possible to solve Eq. 5.41 analytically, but $C_f(\boldsymbol{x}, t)$ can be estimated by Eq. 3.36, which in this case reduces to

$$\hat{C}_f(\boldsymbol{x}, t) = \frac{n'_s}{n_s}\left[\frac{1}{n'_s}\sum_{\omega=1}^{n'_s} C_f(\tilde{\boldsymbol{X}}(\tilde{T}(\omega), \omega))\right], \quad (5.42)$$

where n_s is the number of independent samples of $\tilde{\boldsymbol{X}}$, n'_s is the number of samples of $\tilde{\boldsymbol{X}}$ that exit $H \times (0, t)$ through the boundary of H, *i.e.*, ∂H.

The procedure for estimating the free chloride concentration at a point $\boldsymbol{x} \in H$ and time $t > 0$ is explained below.

- The mortar specimen tested by Caré [31] was a disc-shaped specimen having a 50 mm height and a 70 mm diameter with an aggregate volume fraction of 0.5. Then 2D virtual specimens of $l_1 = 50$ mm and $l_2 = 70$ mm have been generated according to the sand particle size distribution given in Table 5.5. One of the virtual specimens, SP$-50 \times 70 - 1$, is shown in Figure 5.57. The number of particles within the specimens range from 4177 to 4215. The resulting estimates of mean, standard deviation and coefficient of variation of area fraction of aggregate A_{agg} are 0.5007, $2 \cdot 10^{-4}$ and 0.03%, respectively.
- The mortar specimen was immersed in a salt solution of KOH (4.65 g/l) + NaOH (1 g/l) + NaCl (30 g/l) [31]. The atomic weights of sodium (Na)

and chlorine (Cl) are 22.990 g and 35.453 g, respectively. Then the surface chloride concentration C_s is

$$C_s = \left(\frac{35.453}{22.99 + 35.453}\right) \times 30 = 18.2 \text{ g/l}$$
$$= 18.2 \text{ kg/m}^3 \text{ of pore solution.} \quad (5.43)$$

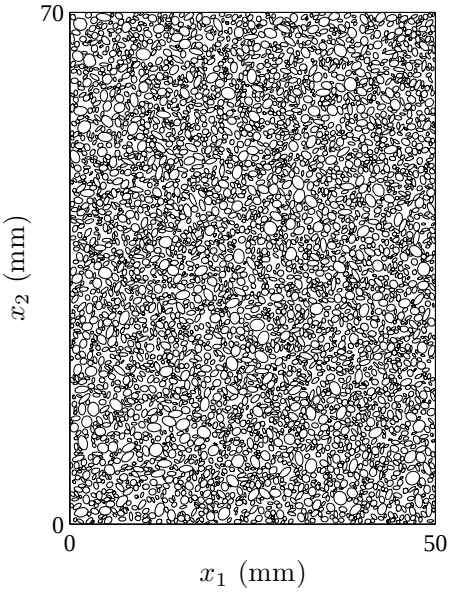

Figure 5.57: Specimen SP$-50 \times 70 - 1$

- Based on n_s samples of $\tilde{\boldsymbol{X}}$ starting from $\boldsymbol{x}$ at time t, $C(\boldsymbol{x}, t)$ is estimated by Eq. 5.42, which in this case reduces to

$$\hat{C}_f(\boldsymbol{x}, t) = \frac{n_s''}{n_s} C_s, \quad (5.44)$$

where n_s'' is the number of samples of $\tilde{\boldsymbol{X}}$ that exit $H \times (0, t)$ through the boundary $\{0\} \times (0, l_2)$.

For estimating the free chloride concentration at a point in a virtual specimen at time $t = 40$ days, $n_s = 1000$ samples of $\tilde{\boldsymbol{X}}$ starting at the point of interest at

$t = 40$ days have been generated. The evolution of n_s''/n_s with n_s for SP$-50 \times 70 - 1$ is shown in Figure 5.58, in which it can be observed that less samples are sufficient to obtain a reliable estimate of $C_f(\boldsymbol{x}, t)$. Estimates of mean and standard deviation of step size of resulting samples of $\tilde{\boldsymbol{X}}$ are 13 μm and 12 μm, respectively.

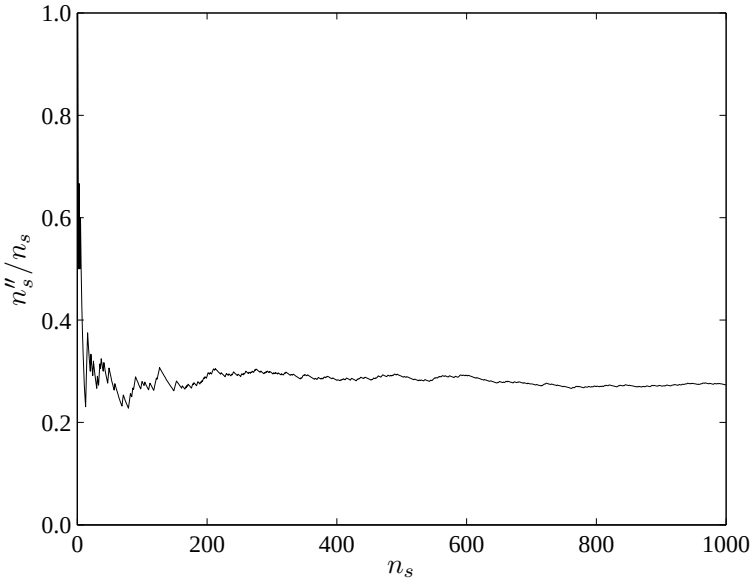

Figure 5.58: Evolution of n_s''/n_s with n_s

For estimating the free chloride concentration at a point at time $t = 40$ days, 10 virtual specimens, SP$-50 \times 70 - \omega_s$, $\omega_s = 1, \ldots, n_{sp}$, where n_{sp} is the number of specimen samples, have been used. The evolution of the resulting estimate of the free chloride concentration at $x_1 = 12$ mm, $x_2 = 35$ mm and $t = 40$ days with n_{sp} is shown in Figure 5.59. The free chloride concentrations at three locations $(x_1, x_2) = (12, 20)$, (12,35) and (12,50), where the locations are in mm, at $t = 40$ days have been estimated using the RWM method. Based on $n_s = 1000$ samples of $\tilde{\boldsymbol{X}}$ and $n_{sp} = 10$ virtual specimens, the resulting estimates of mean and standard deviation of C_f are shown in Table 5.16. The free chloride

concentration at depth 12 mm was measured as 5.37 kg Cl^-/m^3 of pore solution by Caré [31]. Relative errors, calculated as

$$\epsilon_{\text{rel}} = \frac{\hat{\mu}_{C_f} - C_{f,\text{Caré}}}{C_{f,\text{Caré}}} \times 100, \tag{5.45}$$

where $\hat{\mu}_{C_f}$ is an estimate of mean of C_f and $C_{f,\text{Caré}}$ is the free chloride concentration at depth 12 mm measured by Caré [31], are also shown in Table 5.16. The resulting estimates of C_f at depth 12 mm at 40 days differ by less than 12% from the experimental result, which is a satisfactory agreement.

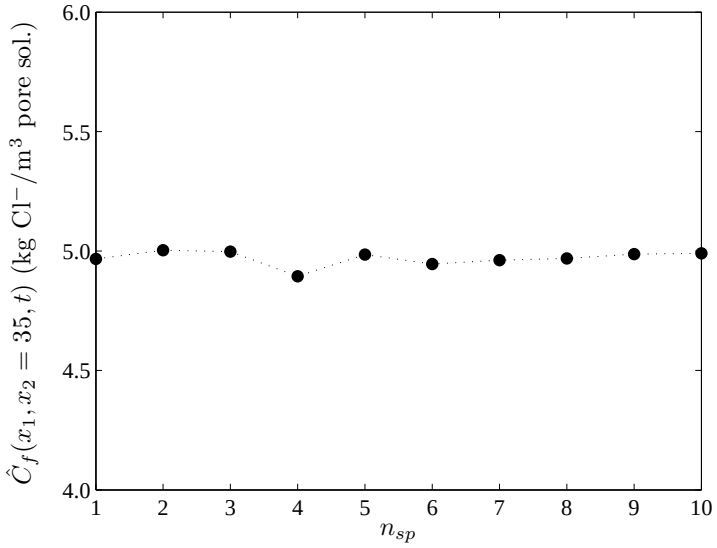

Figure 5.59: Evolution of $\hat{C}_f(x_1 = 12, x_2 = 35, t = 40)$ with n_{sp}

Table 5.16: Statistics of $\hat{C}_f(x_1, x_2, t = 40$ days$)$

x_1 (mm)	x_2 (mm)	$\hat{\mu}_{C_f}$ (kg/m^3 of pore sol.)	$\hat{\sigma}_{C_f}$ (kg/m^3 of pore sol.)	ϵ_{rel} (%)
12	20	4.81	0.18	-10.5
12	35	4.99	0.21	-7.1
12	50	4.76	0.20	-11.4

5.7 Conclusion

Chloride-induced corrosion of steel reinforcement is one of the major causes of deterioration of reinforced concrete structures. Of the various chloride transport mechanisms, diffusion is of interest to this research since it is the most dominant chloride transport mechanism. A critical parameter for evaluating the resistance of concrete against chloride diffusion is the effective diffusion coefficient, which provides information on the rate of chloride diffusion through concrete specimens. The effective diffusion coefficient of chloride can be obtained experimentally (Section 5.2), numerically (Section 5.3) or analytically (Section 5.4).

Diffusion, migration and conductivity experiments are the most common types of experimental methods for obtaining the effective diffusion coefficient of chloride in concrete. The driving force in the diffusion experiments is the chloride concentration gradient, whereas it is the externally applied electrical potential in the migration experiments. In the conductivity experiments, the conductivity measurements are converted to the effective diffusion coefficients. The results obtained through various experimental methods are not directly comparable mainly due to the differences in the hypotheses behind the methods [170]. Since chloride diffusion is of interest to this research, diffusion experiments are considered as more reliable than the others within the context of this research.

A probability-based numerical method was developed for estimating effective diffusion coefficients of concrete specimens and chloride concentration at arbitrary points of these specimens. The method uses virtual concrete specimens consisting of (i) aggregate particles with zero diffusivity, (ii) bulk cement

paste with a constant chloride diffusion coefficient, and (iii) interfacial transition zones around aggregate particles in which the chloride diffusion coefficient increases as the aggregate surface is approached. Virtual specimens are constructed in 2D using volume fraction statistics obtained from 3D specimens. This is an approximation and has been used to reduce calculations. A probabilistic method in [80] for estimating the effective diffusion coefficient of chloride in a virtual concrete specimen was adopted. The effective diffusion coefficient of the virtual concrete specimen is the diffusion coefficient of a virtual homogeneous specimen.

The proposed method for estimating effective diffusion coefficients of concrete specimens and chloride concentration at arbitrary points of these specimens is stable, accurate, simple to code and suitable for parallel computation. Since computation time increases with the size of a specimen, a statistical study was performed to determine the smallest size of the specimen that is still sufficiently large to provide accurate effective diffusivity estimates. Then the parameters of the chloride diffusivity random field model were calibrated to experiments. Using those parameter values, effective diffusion coefficients were calculated for several virtual specimens and chloride concentration was estimated at a few points of virtual specimens. All numerical results are limited to 2D mortar specimens for two reasons. First, computation time is much smaller for 2D specimens than for 3D specimens. Second, effective properties of mortar can be used to construct large virtual concrete specimens.

The results of analyses on a mortar specimen tested by Caré [31] are presented in Section 5.5.3. The results show that ITZ is an important phase affecting the effective diffusion coefficient of chloride significantly. It was found that

the effective diffusion coefficient of chloride in the analyzed mortar specimen would be reduced by 74.3% if there were no ITZ, due to the effects of increased tortuosity of travel paths and dilution of cement paste. The presence of ITZ has an opposite effect on the effective diffusion coefficient, leading to a coefficient larger than the one in the cement paste specimen for the particular cases analyzed in Section 5.5.3. The comparison of the results obtained by the proposed method with the ones by a few methods available in the literature is given in Section 5.5.4.

The calibrated version of the method was used to calculate effective diffusion coefficients in several virtual specimens with the same statistical properties of another mortar specimen tested by Caré [31]. The sand particles in this specimen are finer than those in the specimen used for the calibration. Finer particles led to a higher effective diffusion coefficient for the same aggregate volume fraction and transport properties in the ITZ, since finer particles result in a larger amount of ITZ, in which diffusivity is relatively high. The resulting estimate of the effective diffusion coefficient differs by 19.1% from the experimental result. The method was also used to predict chloride concentration at three points of specimens (Section 5.6). The resulting estimates of the chloride concentration differ by less than 12% from the experimental result. The estimates of the effective diffusion coefficient and the chloride concentration are in satisfactory agreement with the experimental results.

CHAPTER 6

CONCLUSION

6.1 Conclusions

Of the various deterioration mechanisms of reinforced concrete structures, chloride-induced corrosion of steel reinforcement is of great importance since numerous reinforced concrete structures are exposed to chloride sources, *e.g.*, de-icing salts or marine environment [129]. ASCE 2005 Report Card estimates a cost of $9.4 billion a year for 20 years to eliminate deficiencies of 590,750 bridges in the United States, almost half of which are reinforced concrete. A 1998 survey reports that 9% of the reinforced concrete bridges in the United States are structurally deficient, primarily due to corrosion of steel reinforcement [196]. Accurate lifetime predictions are essential for developing efficient strategies to handle the corrosion damage. Since chloride propagation is a transport phenomenon, it is necessary to have an accurate representation of concrete at microscale to obtain adequate lifetime predictions of reinforced concrete structures.

Diffusion, convection, migration and permeation are chloride transport mechanisms in reinforced concrete structures. Chloride ingress into concrete usually occurs by either diffusion or diffusion coupled with another mode of transport. Diffusion is of interest to this research since it is the most dominant mechanism. A critical parameter for evaluating the resistance of concrete to chloride diffusion is the effective diffusion coefficient, which provides information on the rate of chloride diffusion through concrete specimens.

A probability-based numerical method was developed for estimating effective diffusion coefficients of concrete specimens and chloride concentration at arbitrary points of these specimens. The method involves two steps. First, virtual specimens need to be constructed such that they are consistent with statistics of target concrete specimens. A concrete specimen is modeled as a three-phase material consisting of (i) aggregate particles with zero diffusivity, (ii) bulk cement paste with a constant chloride diffusion coefficient, and (iii) interfacial transition zones around aggregate particles in which the chloride diffusion coefficient increases as the aggregate surface is approached. The algorithm constructing virtual concrete specimens places virtual aggregates at random locations. The aggregates are ellipses of random aspect ratios with noisy boundaries defined by beta translation fields. Second, properties of Itô process are used to estimate the effective diffusion coefficients in virtual specimens and the chloride concentration at arbitrary points of specimens. A probabilistic method in [80] for estimating the effective diffusion coefficient of chloride in a virtual concrete specimen was adopted. The effective diffusion coefficient of the virtual concrete specimen is the diffusion coefficient of a virtual homogeneous specimen.

The proposed method for estimating effective diffusion coefficients of concrete specimens and chloride concentration at arbitrary points of these specimens is stable, accurate, simple to code and suitable for parallel computation. The computation time can be lengthy particularly when dealing with large and/or 3D specimens. To reduce calculations, a statistical study was undertaken to identify the smallest size of a specimen that is still sufficiently large to provide accurate effective diffusivity estimates. Then the parameters of the chloride diffusivity random field model were calibrated to experiments. Using those parameter values, effective diffusion coefficients were calculated for sev-

eral virtual specimens and chloride concentration was estimated at a few points of virtual specimens. The resulting estimates are in satisfactory agreement with the experimental results. All numerical results are limited to 2D mortar specimens.

6.2 Future Research

Future research will be related to the extensions of the method proposed in this study. The future research topics are briefly outlined below.

- In this study, 2D mortar specimens were used in order to reduce computation time. The next step is to study concrete specimens. This can be performed either following the approach in this study or considering concrete specimens consisting of mortar, viewed as a homogeneous phase with an effective diffusivity, coarse aggregate and interfacial transition zone around coarse aggregate.
- The method in this study uses 2D virtual specimens, but it can be modified to examine 3D specimens. The random fields proposed for concrete aggregate in [79] can be adopted for generating 3D virtual aggregates. The packing algorithm proposed in this study can be extended to 3D for packing 3D virtual aggregates.
- Interfacial transition zone is an important phase affecting the rate of chloride diffusion through concrete specimens, but chloride diffusivity fields in interfacial transition zones are not known. Therefore more analyses on experimental data are needed to calibrate the parameters defining chlo-

ride diffusivity random field model. Such analyses will possibly lead to more realistic models in later applications.

- The method can be used to estimate corrosion initiation time for a reinforced concrete structure. In such calculations, time-dependence of chloride diffusivity should be considered, since chloride diffusion through reinforced concrete structures is a long term process.

APPENDIX A

CHLORIDE DIFFUSION COEFFICIENTS

It is not possible to put all information in the literature here, but a few chloride diffusion coefficients obtained through diffusion and migration experiments are summarized below.

A.1 Diffusion Experiments

Diffusion-based experiments can be carried out under either steady-state or non-steady-state conditions (Section 5.2.1). Experimental results by Page *et al.* [126], Goto and Roy [74], Dhir and Byars [47], MacDonald and Northwood [101], Jensen *et al.* [88] and Caré [31] are given below.

Table A.1: D_{eff} in Various Cement Pastes by Page *et al.* [126]

Type of Cement	D_{eff} (10^{-6} mm^2/s)
Portland Cement	4.47
Portland Cement/30%PFA	1.47
Portland Cement/65%BFS	0.41
Sulfate-Resistant Portland Cement	10.00

Page *et al.* [126] conducted steady-state diffusion experiments. The specimens were cured under saturated $Ca(OH)_2$ solution at 22°C for 60 ± 3 days. The downstream and upstream reservoirs were filled with saturated $Ca(OH)_2$ solution and 1 M NaCl + saturated $Ca(OH)_2$ solution, respectively. The effective diffusion coefficients at 25°C in various cement paste specimens having a w/c

ratio of 0.5 are shown in Table A.1, where PFA is pulverized fly ash and BFS is ground-granulated blast furnace slag. The coefficients at various temperatures in Portland cement paste specimens having various w/c ratios are plotted in Figure A.1.

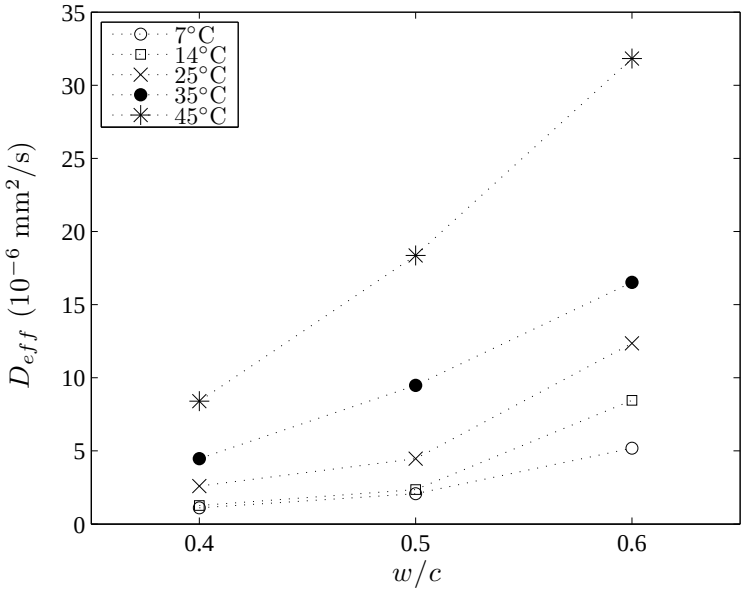

Figure A.1: D_{eff} in Portland Cement Pastes by Page *et al.* [126]

Table A.2: D_{eff} in Portland Cement Pastes by Goto and Roy [74]

Curing T. (°C)	Curing Period (weeks)	Test T. (°C)	D_{eff} (10^{-6} mm^2/s)
27	4	27	6.9
60	4	35	27.0
60	6	35	37.0
60	4	45	37.0
60	6	45	37.0
60	4	60	92.0

Goto and Roy [74] measured the effective diffusion coefficients at various

temperatures in Portland cement paste specimens having a w/c ratio of 0.4. The specimens were cured under saturated $Ca(OH)_2$ solution at various temperatures for 4 or 6 weeks. The downstream and upstream reservoirs were filled with deionized water and a solution of 0.5 M NaCl, respectively. The effective diffusion coefficients obtained from steady-state diffusion experiments are shown in Table A.2 together with the corresponding curing temperature, curing period and experiment temperature.

Table A.3: Curing Conditions Examined by Dhir and Byars [47]

Label	Curing Type	Curing Condition	Curing Duration
A	Water curing	23°	28 days
B	Water curing	23°	180 days
C	Air curing	23° & 55% RH	28 days
D	Air curing	23° & 55% RH	180 days
E	Air curing	5° & 95% RH	1 day
	Air curing	10° & 55% RH	27 days
F	Air curing	5° & 95% RH	1 day
	Air curing	10° & 55% RH	27 days
	Air curing	23° & 55% RH	152 days

Dhir and Byars [47] measured the effective diffusion coefficients of chloride in concrete specimens cured under various conditions shown in Table A.3. The downstream and upstream reservoirs were filled with deionized water and a solution of 5 M NaCl, respectively. The effective diffusion coefficients measured through steady-state diffusion experiments are plotted against w/c ratio in Figure A.2.

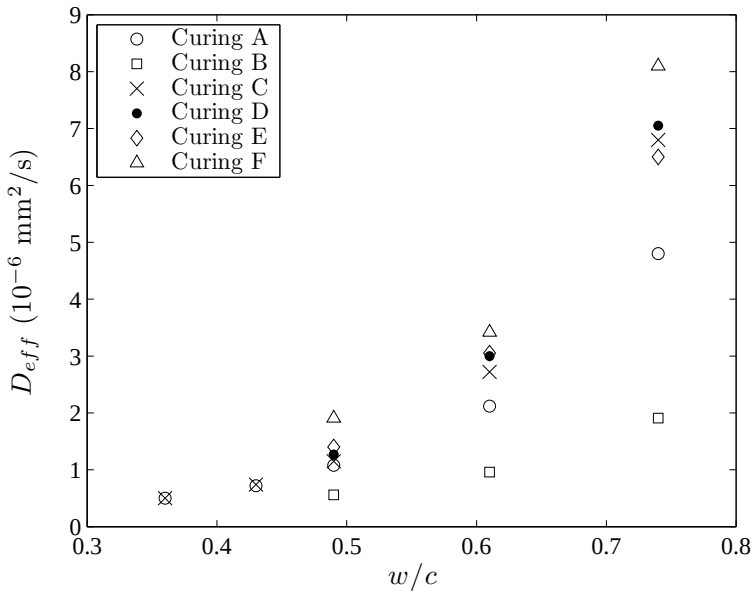

Figure A.2: D_{eff} in Portland Cement Concrete by Dhir and Byars [47]

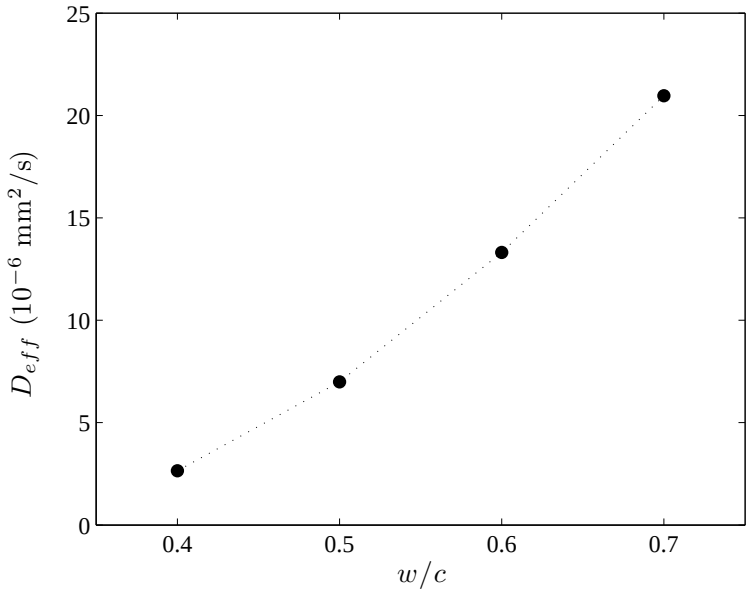

Figure A.3: D_{eff} vs. w/c by MacDonald and Northwood [101]

MacDonald and Northwood [101] measured the effective diffusion coefficients of chloride in Portland cement paste specimens with various w/c ratios (Figure A.3), where the downstream and upstream reservoirs were filled with distilled water and a solution of 1 M NaCl, respectively. Also, the effective diffusion coefficients of chloride in cement paste specimens with a w/c ratio of 0.45 were measured for various chloride concentrations in the upstream reservoir (Figure A.4). The specimens were cured at 25°C and 100% relative humidity for 8 weeks. The measurements were performed under steady-state conditions.

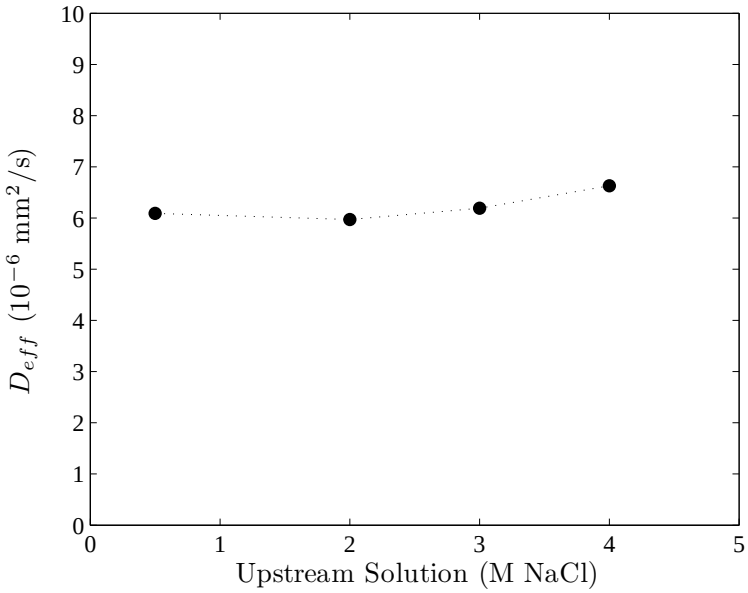

Figure A.4: D_{eff} vs. Upstream Solution [101]

Hornain *et al.* [85] measured the effective diffusion coefficients of chloride in Portland cement paste specimens and mortar specimens with and without limestone fillers, where w/c ratio was 0.55 in all specimens. The specimens were kept at 20°C and 100% relative humidity for 48 hours, then stored in a water bath at 20°C for 60 days. Following this period, they were immersed in a saturated $Ca(OH)_2$ solution for 6 days. The downstream and upstream reservoirs were

filled with a saturated $Ca(OH)_2$ solution and a saturated $Ca(OH)_2$ solution + 35 g/L NaCl, respectively. The mix proportions of the specimens and the coefficients obtained from steady-state diffusion experiments are shown in Table A.4.

Table A.4: D_{eff} in Specimens Tested by Hornain *et al.* [85]

Mixture	Cement (% by weight)	Filler (% by weight)	Sand (% by weight)	D_{eff} (10^{-6} mm^2/s)
P1	100	0	0	11.25
P2	80	20	0	5.36
M1	25	0	75	3.60
M2	20	5	75	2.42

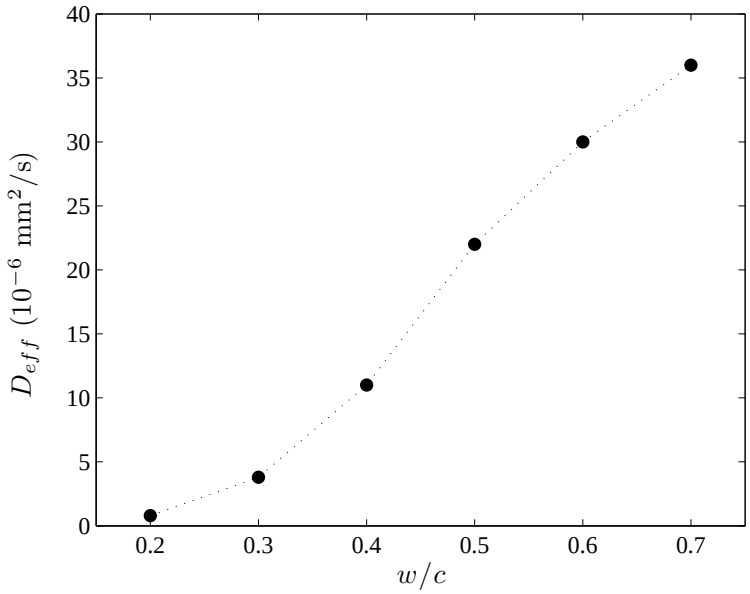

Figure A.5: D_{eff} vs. w/c by Jensen *et al.* [88]

Jensen *et al.* [88] obtained the effective diffusion coefficients in cement paste specimens with various w/c ratios (Figure A.5) and in cement paste specimens

with various silica fume contents by weight (Figure A.6) through non-steady-state diffusion experiments. After approximately 100 days of pre-hardening and water saturation, the specimens were exposed to a 3% NaCl solution for 30 days at 20°C. In calculation of the effective diffusion coefficients from the measured chloride profiles, chloride binding was modeled as Freundlich isotherms (Section 2.3.2).

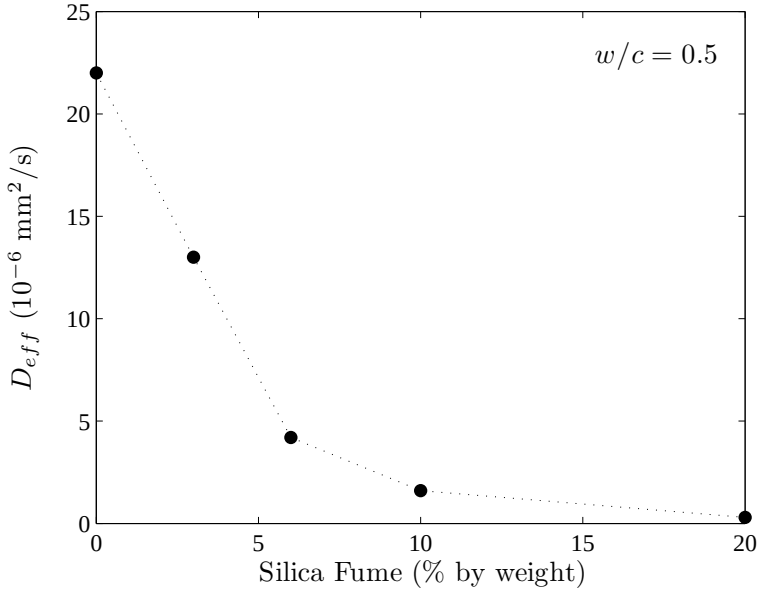

Figure A.6: D_{eff} vs. Silica Fume Content by Jensen *et al.* [88]

Caré [31] measured the effective diffusion coefficients in mortar specimens with a w/c of 0.45 and various aggregate contents through non-steady-state diffusion experiments. The specimens were first immersed in a concentrated alkaline solution of KOH (4.65 g/l) + NaOH (1 g/l) and vacuum-saturated. Then they were immersed in a solution of KOH (4.65 g/l) + NaOH (1 g/l) + NaCl (30 g/l) for 40 days. The coefficients are shown in Table A.5, where V_{agg} is the volume fraction of aggregate, α is the degree of hydration, ϕ is the porosity and aggregate type is the type of sand particle distribution (Figure A.7).

Table A.5: D_{eff} in Mortar by Caré [31]

Aggregate Distribution	V_{agg}	α	ϕ	D_{eff} (10^{-6} mm^2/s)
–	0	0.811	0.226	5.65
C	0.25	0.835	0.151	5.40
C	0.50	0.688	0.110	4.80
M	0.50	0.812	0.122	7.40
F	0.25	0.862	0.179	8.10
F	0.50	0.779	0.130	9.50

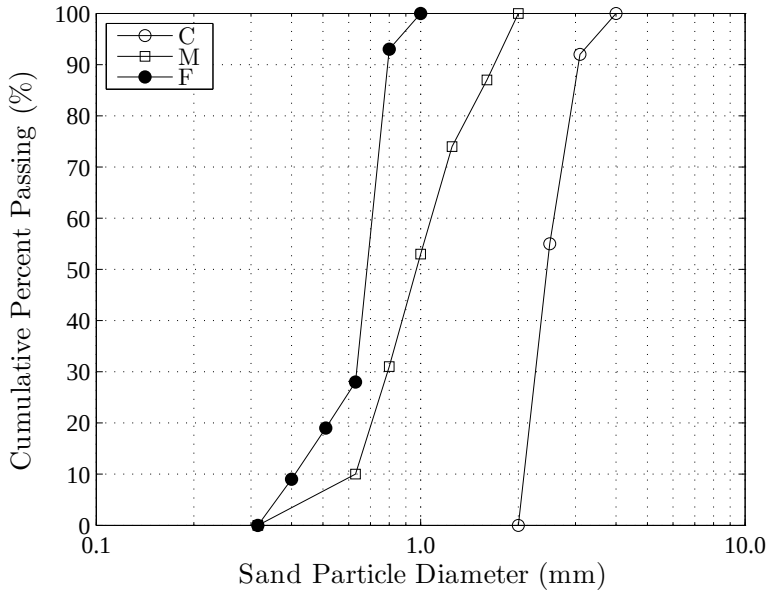

Figure A.7: Sand Particle Distributions Used by Caré [31]

A.2 Migration Experiments

Migration experiments can be carried out under either steady-state or non-steady-state conditions. Various methods of calculating the effective diffusion coefficient from the results of migration experiments are given in Section 5.2.2.

Tang and Nilsson [168] calculated the effective diffusion coefficients in Portland cement paste and mortar specimens using Eq. 5.12 and the results of CTH tests. The specimens were cured under saturated $Ca(OH)_2$ solution at 22°C for 3 months. A solution of 3% NaCl saturated in $Ca(OH)_2$ and a voltage of 30 V were used. For comparison, diffusion experiments were also performed. The results are shown in Table A.6, where $c : s : w$ is cement:sand:water ratio.

Table A.6: D_{eff} in Cement Paste and Mortar by Tang and Nilsson [168]

$c : s : w$ (by weight)	Testing Time (hours)	D_{eff} (10^{-6} mm^2/s) (Eq. 5.12)	D_{eff} (10^{-6} mm^2/s) (Diff. Exp.)
1:0:0.4	8	9.3	2.9
1:0:0.6	8	17.5	9.4
1:0:0.8	8	25.4	21.0
1:0:0.4	24	7.2	2.9
1:0:0.6	24	15.6	9.4
1:2:0.4	8	6.5	1.1
1:2:0.6	8	11.0	2.6
1:2:0.8	8	15.1	6.4
1:2:0.4	4	6.7	1.1
1:2:0.4	24	6.4	1.1
1:2:0.4	48	6.3	1.1

Tang and Nilsson [167] also calculated the effective diffusion coefficients in high strength concrete specimens using Eq. 5.12 and the results of CTH tests. The specimens were sealed in plastic bags and stored in the laboratory until the specified ages shown in Table A.7. A solution of 3% NaCl saturated in $Ca(OH)_2$ were used in the test and a voltage of 30 V were applied for 8 hours. The mix

proportions of the specimens (kg/m^3) and the averages of resulting effective diffusion coefficients at various ages are shown in Table A.7.

Table A.7: D_{eff} (10^{-6} mm^2/s) in HSC by Tang and Nilsson [167]

Mix No.	NSC	HSCSF0	HSCSF6	HSCSF12	HSCSF24
OPC (Slite)	270	522	492.5	466	421
CSF (Norway)	0	0	29.5	56	101
Sand (< 4 mm)	769	0	0	0	0
Sand (< 8 mm)	0	700	700	700	700
Gravel ($8 - 12$ mm)	1153	1050	1050	1050	1050
Water	189	165	165	165	165
Superplasticizer	0	5.22	6.26	6.68	7.20
CSF/OPC	0	0	6%	12%	24%
water/binder	0.7	0.32	0.32	0.32	0.32
admixture/binder	0	1%	1.2%	1.28%	1.38%
D_{eff} at 1 day	45.60	7.39	8.24	6.67	7.96
D_{eff} at 3 days	26.95	6.22	5.14	3.54	1.09
D_{eff} at 7 days	21.10	4.93	2.79	1.60	0.48
D_{eff} at 28 days	14.50	3.22	0.91	0.44	0.19
D_{eff} at 90 days	15.30	1.79	0.49	0.34	0.10
D_{eff} at 180 days	N/A	1.74	0.38	0.22	0.04

Zhang and Gjørv [197] calculated the effective diffusion coefficients in mortar and concrete specimens using Eq. 5.11 and the results of steady-state migration experiments. The experimental setup was the same as that used in the AASHTO T277 test [163]. Before testing, all specimens were subjected to vacuum saturation. Mix proportions of specimens are shown in Table A.8. A so-

lution of 0.3 M NaCl were used in the test and voltages of 6, 9 and 12 V were applied. The averages of resulting effective diffusion coefficients for various applied voltages are shown in Table A.9.

Table A.8: Mix Proportions of Specimens Tested by Zhang and Gjørv [197]

Specimen	w/c	Cement (kg/m^3)	Water (kg/m^3)	Aggregate (kg/m^3)		Air Content (%)
				0-8 mm	8-16 mm	
D7 (Mortar)	0.5	330	165	1894	-	3.9
A2 (Concrete)	0.5	330	165	756	1310	1.2

Table A.9: D_{eff} (10^{-6} mm^2/s) by Zhang and Gjørv [197]

Specimen	Voltage (V)		
	6	9	12
D7-4 (Mortar)	1.94	1.97	1.65
D7-5 (Mortar)	1.26	1.21	1.19
A2-3 (Concrete)	3.63	3.65	3.42
A2-4 (Concrete)	2.86	3.25	3.17

McGrath and Hooton [107] calculated the effective diffusion coefficients in concrete specimens using (i) Eq. 5.7 and the results of steady-state migration experiments, and (ii) Eq. 5.20 and the results of non-steady-state migration experiments. The concrete specimens had a w/c ratio of 0.49, and they were stored under water for a year. The downstream and upstream reservoirs were filled with a solution of 0.3 M NaOH and a solution of 0.5 M NaCl + 0.3 M NaOH, respectively. The calculated coefficients are plotted against nominal voltage in Figure A.8.

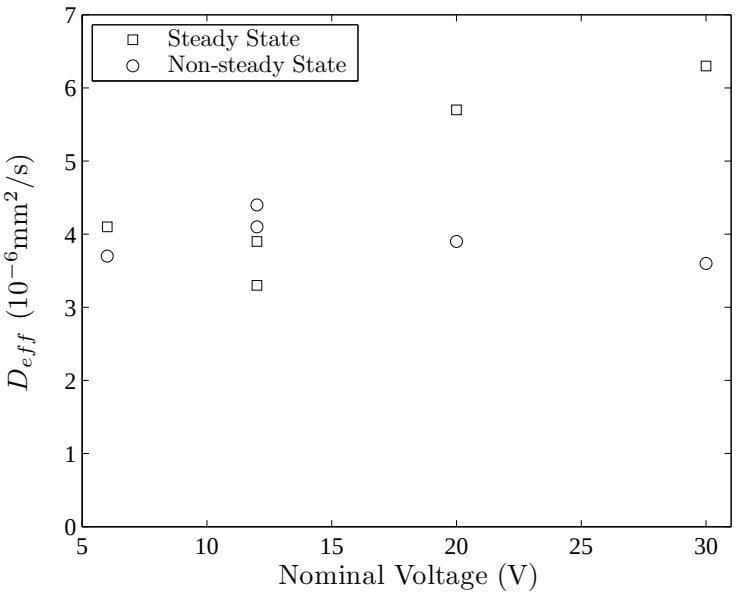

Figure A.8: D_{eff} in Concrete Specimens by McGrath and Hooton [107]

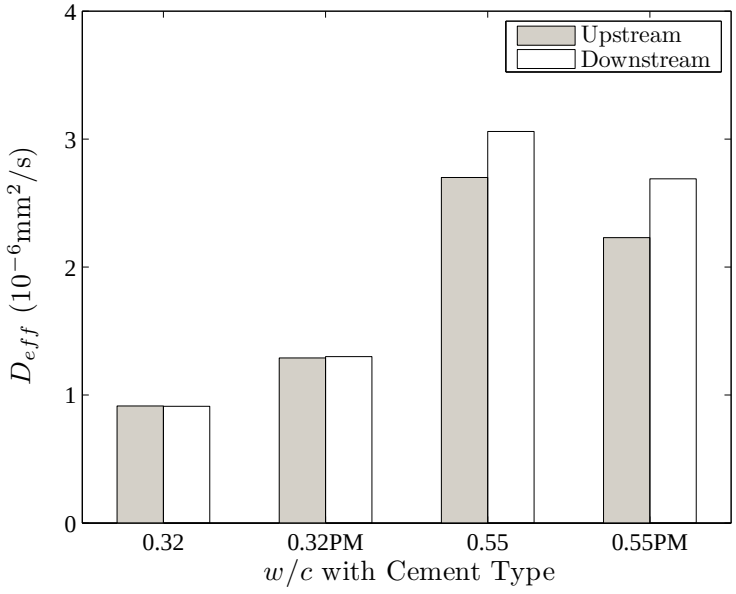

Figure A.9: D_{eff} in Concrete Specimens by Truc *et al.* [175]

Truc *et al.* [175] calculated the effective diffusion coefficients in concrete specimens using Eq. 5.7 and the results of steady-state migration experiments, and compared the results obtained by using the chloride concentration changes in the downstream and upstream reservoirs. Two types of cement and two w/c ratios were studied. The specimens were vacuum-saturated with a basic alkaline solution of NaOH + KOH. They were cured under water for 14 days. The reservoirs were filled with a solution of 0.025 M NaOH + 0.083 M KOH. A solution of 0.564 M NaCl was added in the upstream reservoir. A voltage of 12 V was applied. The resulting coefficients are plotted in Figure A.9.

Table A.10: Mix Proportions of Specimens of Zhang and Gjørv [200]

Mix	w/c	Cement (kg/m^3)	Water (kg/m^3)	Aggregate (kg/m^3)			Wat.-Red. (kg/m^3)
				0-8 mm	8-11 mm	8-16 mm	
A	0.4	397	159	1047	418	418	8.1
B	0.5	380	190	1000	408	408	2.6
C	0.6	326	195	1002	423	423	-

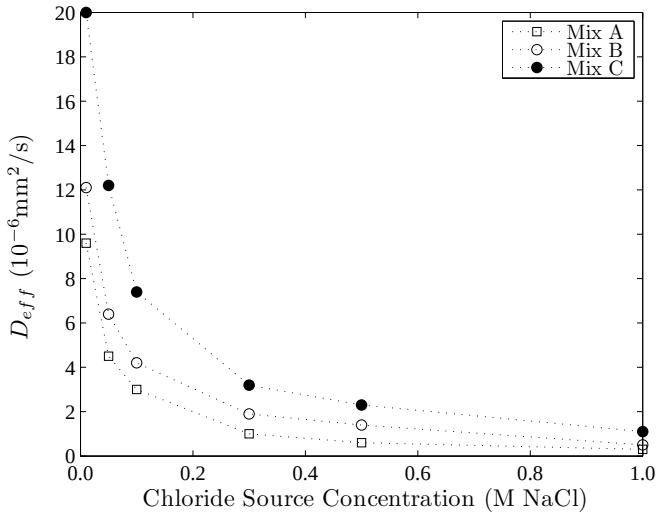

Figure A.10: D_{eff} in Concrete Specimens by Zhang and Gjørv [200]

Zhang and Gjørv [200] calculated the effective diffusion coefficients in concrete specimens using Eq. 5.11 and the results of steady-state migration experiments. The experimental setup was the same as that used in the ASTM C 1202 test [1]. The specimens were cured in water at room temperature for at least 3 months. Mix proportions are shown in Table A.10. A potential difference of 12 V was used. The resulting coefficients are plotted against chloride source concentration in Figure A.10.

Table A.11: D for $w/c = 0.4$ Mortar by Halamickova *et al.* [82]

Sand Volume (%)	Degree of Hydration (%)	Average D (10^{-6} mm^2/s)
0	54-55	1.69
0	59-60	1.09
35	65-70	0.74
45	50-57	2.33
45	65-67	1.62
55	55-61	2.80
55	66-72	0.82

Halamickova *et al.* [82] calculated the effective diffusion coefficients in mortar specimens using Eq. 5.20 and the results of non-steady-state migration experiments. Two w/c ratios, 0.4 and 0.5, and four aggregate volume fractions, 0%, 35%, 45% and 55%, were studied. The specimens were stored in a saturated $Ca(OH)_2$ solution, and vacuum-saturated before testing. The experimental setup was based on the ASTM C 1202 test [1]. A potential difference of 12 V was used. The downstream and upstream reservoirs were filled with 0.3 M KOH and 3% KCl solutions, respectively. The calculated diffusion coefficients are shown in Tables A.11 and A.12.

Table A.12: D for $w/c = 0.5$ Mortar by Halamickova *et al.* [82]

Sand Volume (%)	Degree of Hydration (%)	Average D (10^{-6} mm^2/s)
0	46-48	7.54
0	55-56	2.96
35	70-73	0.96
45	53-55	5.66
45	70-72	1.79
55	55-57	5.30
55	70-73	0.84

Table A.13: Mix Proportions Used by Samson and Marchand [141]

Material	Mix Proportions (kg/m^3)		
	$w/c = 0.45$	$w/c = 0.65$	$w/c = 0.75$
Cement (T10 and T50)	380	280	260
Water	171	182	195
Sand	719	833	915
Coarse Aggregate	1127	1065	956

Samson and Marchand [141] studied the effect of temperature on the chloride diffusivity in concrete by conducting non-steady-state migration experiments and solving the coupled extended Nernst-Planck/Poisson set of equations (Eqs. 5.15 and 5.16). The specimens were cured in a fog chamber (100% relative humidity and 25°C) until the specified age (Table A.14). Test setup was a modified version of ASTM C 1202 test [1]. The downstream and upstream reservoirs were filled with a 0.3 M NaOH solution and a a 0.3 M NaOH + 0.5 M NaCl solution, respectively. An external 20 V potential was applied. The

mix proportions and the calculated chloride diffusion coefficients are shown in Table A.13 and A.14, respectively.

Table A.14: Diffusion Coefficients by Samson and Marchand [141]

w/c	Age (days)	Chloride Diffusion Coefficient (10^{-6} mm^2/s)					
		4°C		23°C		40°C	
		Type 10	Type 50	Type 10	Type 50	Type 10	Type 50
0.45	28	32	71	56	110	80	137
	91	30	45	52	75	67	113
	365	26	45	44	75	71	135
0.65	28	53	77	83	130	129	197
	91	53	73	80	114	145	197
	365	62	66	91	128	157	253
0.75	28	61	107	105	157	161	254
	91	67	94	115	150	188	231
	365	74	103	119	167	194	270

BIBLIOGRAPHY

[1] ASTM C 1202-07. *Standard Test Method for Electrical Indication of Concrete's Ability to Resist Chloride Ion Penetration*. American Society for Testing and Materials (ASTM) International, West Conshohocken, PA, 2007.

[2] ASTM C 1556-04. *Standard Test Method for Determining the Apparent Chloride Diffusion Coefficient of Cementitious Mixtures by Bulk Diffusion*. American Society for Testing and Materials (ASTM) International, West Conshohocken, PA, 2004.

[3] ASTM C 33-03. *Standard Specification for Concrete Aggregates*. American Society for Testing and Materials (ASTM) International, West Conshohocken, PA, 2006.

[4] NT-Build 355. *Concrete, Mortar and Cement Based Repair Materials: Chloride Diffusion Coefficient from Migration Cell Experiments*. Nordtest, Espoo, Finland, 2nd edition, 1997.

[5] NT-Build 443. *Concrete, Hardened: Accelerated Chloride Penetration*. Nordtest, Espoo, Finland, 1995.

[6] NT-Build 492. *Concrete, Mortar and Cement Based Repair Materials: Chloride Migration Coefficient from Non-Steady State Migration Experiments*. Nordtest, Espoo, Finland, 1999.

[7] M.G. Alexander. Role of aggregates in concrete. In J.P. Skalny and S. Mindess, editors, *Materials Science of Concrete V*, pages 119–147, Westerville, Ohio, 1998. The American Ceramic Society.

[8] C. Andrade. Calculation of chloride diffusion coefficients in concrete from ionic migration measurements. *Cement and Concrete Research*, 23(3):724–742, May 1993.

[9] C. Andrade, M. Castellote, D. Cervigón, and C. Alonso. Fundamentals of migration experiments. In L.O. Nillson and J.P. Ollivier, editors, *Chloride Penetration into Concrete: Proceedings of the RILEM International Workshop*, pages 95–104, Cachan, France, 1997. RILEM Publications.

[10] C. Andrade, Alonso-C. Castelotte, M., and C. González. Non-steady-state chloride diffusion coefficients obtained from migration and natural dif-

fusion tests. Part I: Comparison between several methods of calculation. *Materials and Structures*, 33(1):21–28, January 2000.

[11] C. Andrade and D. Whiting. Comparison of aashto t-277 (electrical) and aashto t-259 (90d ponding) results. In L.O. Nillson and J.P. Ollivier, editors, *Chloride Penetration into Concrete: Proceedings of the RILEM International Workshop*, pages 135–149, Cachan, France, 1997. RILEM Publications.

[12] J. Arsenault, J.P. Bigas, and J.P. Ollivier. Determination of chloride diffusion coefficient using two different steady-state methods: Influence of concentration gradient. In L.O. Nillson and J.P. Ollivier, editors, *Chloride Penetration into Concrete: Proceedings of the RILEM International Workshop*, pages 150–160, Cachan, France, 1997. RILEM Publications.

[13] A. Atkinson and A.K. Nickerson. The diffusion of ions through water-saturated cement. *Journal of Materials Science*, 19(9):3068–3078, September 1984.

[14] K. Bathe. *Finite Element Procedures*. Prentice Hall, Englewood Cliffs, NJ, 1996.

[15] A. Bentur and M.D. Cohen. Effect of condensed silica fume on the microstructure of the interfacial zone in portland cement mortars. *Journal of the American Ceramic Society*, 70(10):738–743, October 1987.

[16] D.P. Bentz. A three-dimensional cement hydration and microstructure program. I. Hydration rate, heat of hydration and chemical shrinkage. Technical Report NISTIR No. 5756, U.S. Department of Commerce, Washington, DC, November 1995.

[17] D.P. Bentz. Three-dimensional computer simulation of portland cement hydration and microstructure development. *Journal of the American Ceramic Society*, 80(1):3–21, January 1997.

[18] D.P Bentz. Quantitative comparison of real and CEMHYD3D model microstructures using correlation functions. *Cement and Concrete Research*, 32(2):259–263, February 2006.

[19] D.P. Bentz and E.J. Garboczi. Percolation of phases in a three-dimensional cement paste microstructural model. *Cement and Concrete Research*, 21(2-3):325–344, March-May 1991.

[20] D.P. Bentz and E.J. Garboczi. Computer modelling of interfacial transition zone: Microstructure and properties. In M.G. Alexander, G. Arliguie, G. Ballivy, A. Bentur, and J. Marchand, editors, *Engineering and Transport Properties of the Interfacial Transition Zone in Cementitious Composites*, pages 349–385, Cachan, France, 1999. RILEM Publications.

[21] D.P. Bentz, E.J. Garboczi, C.J. Haecker, and O.M. Jensen. Effects of cement particle size distribution on performance properties of portland cement-based materials. *Cement and Concrete Research*, 29(10):1663–1671, October 1999.

[22] D.P. Bentz, E.J. Garboczi, and E.S. Lagergren. Multi-scale microstructural modeling of concrete diffusivity: Identification of significant variables. *Journal of Cement, Concrete and Aggregates*, 20(1):129–139, June 1998.

[23] D.P. Bentz, E.J. Garboczi, and P.E. Stutzman. Computer modelling of the interfacial zone in concrete. In J.C. Maso, editor, *Interfaces in Cementitious Composites: Proceedings of the International Conference held by RILEM*, pages 107–116, London, 1992. E & FN Spon.

[24] D.P. Bentz, J.T.G. Hwang, C. Hagwood, E.J. Garboczi, K.A. Snyder, N. Buenfeld, and K.L. Scrivener. Interfacial zone percolation in concrete: Effects of interfacial zone thickness and aggregate shape. In S. Diamond, S. Mindess, F.P. Glasser, L.R. Roberts, J.P. Skalny, and L.D. Wakeley, editors, *Microstructure of Cement-Based Systems/Bonding and Interfaces in Cementitious Materials: Symposia held November 28-December 1, 1994, Boston, MA, USA.*, volume 370 of *Materials Research Society Symposium Proceedings*, pages 437–442, Pittsburgh, PA, 1995. Materials Research Society.

[25] D.P. Bentz, O.M. Jensen, A.M. Coats, and F.P. Glasser. Influence of silica fume on diffusivity in cement-based materials: I. Experimental and computer modeling studies on cement pastes. *Cement and Concrete Research*, 30(6):953–962, June 2000.

[26] D.P. Bentz, P.E. Stutzman, and E.J. Garboczi. Experimental and simulation studies of the interacial transition zone. *Cement and Concrete Research*, 22(5):891–902, September 1992.

[27] B. Bourdette, E. Ringot, and J.P. Ollivier. Modelling of the transition zone porosity. *Cement and Concrete Research*, 25(4):741–751, May 1995.

[28] N.R. Buenfeld and J.B. Newman. Examination of three methods for study-

ing ion diffusion in cement pastes, mortars and concrete. *Materials and Structures*, 20(115):3–10, 1987.

[29] G.C. Bye. *Portland Cement: Composition, Production and Properties*. Thomas Telford, London, 2nd edition, 1999.

[30] Y. Cao and R.J. Detwiler. Backscattered electron imaging of cement pastes cured at elevated temperatures. *Cement and Concrete Research*, 25(3):627–638, April 1995.

[31] S. Caré. Influence of aggregates on chloride diffusion coefficient into mortar. *Cement and Concrete Research*, 33(7):1021–1028, July 2003.

[32] M. Castellote, C. Alonso, C. Andrade, G.A. Chadbourn, and C.L. Page. Oxygen and chloride diffusion in cement pastes as a validation of chloride diffusion coefficients obtained by steady-state migration tests. *Cement and Concrete Research*, 31(4):621–625, April 2001.

[33] M. Castellote, C. Andrade, and C. Alonso. Measurement of the steady and non-steady-state chloride diffusion coefficients in a migration test by means of monitoring the conductivity in the anolyte chamber. Comparison with natural diffusion tests. *Cement and Concrete Research*, 31(10):1411–1420, October 2001.

[34] Andrade-C. Castelotte, M. and C. Alonso. Non-steady-state chloride diffusion coefficients obtained from migration and natural diffusion tests. Part II: Different experimental conditions. Joint relations. *Materials and Structures*, 34(6):323–331, July 2001.

[35] R. Cerny and P. Rovnaníková. *Transport Processes in Concrete*. Taylor & Francis, Inc., New York, 2002.

[36] S.C. Chapra and R.P. Canale. *Numerical Methods for Engineers*. McGraw-Hill, 2nd edition, 1988.

[37] S. Chatterji and A.D. Jensen. Formation and development of interfacial zones between aggregates and portland cement pastes in cement-based materials. In J.C. Maso, editor, *Interfaces in Cementitious Composites: Proceedings of the International Conference held by RILEM*, pages 3–12, London, 1992. E & FN Spon.

[38] M. Chemrouk and N. Attari. Durability of concrete with particular ref-

erence to high performance concrete. In R.K. Dhir, M.D. Newlands, and K.A. Paine, editors, *Role of Concrete in Sustainable Construction, Proceedings of the International Symposium dedicated to Professor Surenda Shah, Northwestern University, USA, held on 3-4 September 2003 at the University of Dundee, Scotland, UK*, pages 245–254. American Society of Civil Engineers (Thomas Telford), 2004.

[39] R.M. Christensen. *Mechanics of Composite Materials*. Wiley-Interscience, New York, 1979.

[40] R.A. Cook and K.C. Hover. Mercury porosimetry of hardened cement pastes. *Cement and Concrete Research*, 29(6):933–943, June 1999.

[41] R.D. Cook, D.S. Malkus, M.E. Plesha, and R.J. Witt. *Concepts and Applications of Finite Element Analysis*. John Wiley & Sons, New York, 4th edition, 2002.

[42] J. Crank. *The Mathematics of Diffusion*. Clarendon Press, 2nd edition, 1975.

[43] A. Delagrave, J.P. Bigas, J.P. Ollivier, J. Marchand, and M. Pigeon. Influence of the interfacial zone on the chloride diffusivity of mortars. *Advanced Cement Based Materials*, 5(3-4):86–92, April-May 1997.

[44] A. Delagrave, J. Marchand, J.P. Ollivier, S. Julien, and K. Hazrati. Chloride binding capacity of various hydrated cement paste systems. *Advanced Cement Based Materials*, 6(1):28–35, June 1997.

[45] A. Delagrave, J. Marchand, and E. Samson. Prediction of diffusion coefficients in cement-based materials on the basis of migration experiments. *Cement and Concrete Research*, 26(12):1831–1842, December 1996.

[46] R.J. Detwiler, K.O. Kjellsen, and O.E. Gjø rv. Resistance to chloride intrusion of concrete cured at different temperatures. *ACI Materials Journal*, 88(1):19–24, January-February 1991.

[47] R.K. Dhir and E.A. Byars. PFA concrete: Chloride diffusion rates. *Magazine of Concrete Research*, 45(162):1–9, March 1993.

[48] R.K. Dhir, M.A.K. El-Mohr, and T.D. Dyer. Developing chloride resisting concrete using PFA. *Cement and Concrete Research*, 27(11):1633–1639, November 1997.

[49] R.K. Dhir, M.R. Jones, H.E.H. Ahmed, and A.M.G. Seneviratne. Rapid estimation of chloride diffusion coefficient in concrete. *Magazine of Concrete Research*, 42(152):177–185, September 1990.

[50] R.K. Dhir, M.R. Jones, and A.M.G. Seneviratne. Diffusion of chlorides into concrete influence of PFA quality. *Cement and Concrete Research*, 21(6):1092–1102, November 1991.

[51] B. Díaz, X.R. Nóvoa, and M.C. Pérez. Study of the chloride diffusion in mortar: A new method of determining diffusion coefficients based on impedance measurements. *Cement and Concrete Composites*, 28(3):237–245, March 2006.

[52] A.F. Emery and W.W. Carson. A modification to the monte carlo method - the exodus method. *Journal of Heat Transfer*, 90:328–332, August 1968.

[53] O. Francy and François. Measuring chloride diffusion coefficients from non-steady-state diffusion tests. *Cement and Concrete Research*, 28(7):947–953, July 1998.

[54] R.A. Freeze and J.A. Cherry. *Groundwater*. Prentice-Hall, Englewood Cliffs, NJ, 1979.

[55] G. Fu and W. Dekelbab. 3-d random packing of polydisperse particles and concrete aggregate grading. *Powder Technology*, 133(1-3):147–155, July 2003.

[56] J.M. Gaidis and E.M. Gartner. Hydration mechanisms, ii. In J.P. Skalny and S. Mindess, editors, *Materials Science of Concrete II*, pages 95–125, Westerville, Ohio, 1991. The American Ceramic Society.

[57] M. Gan, N. Gopinathan, X. Jia, and R.A. Williams. Predicting packing characteristics of particles of arbitrary shapes. *KONA*, 22:82–93, 2004.

[58] R. Gao and P. Stroeven. A digital method to simulate the microstructure of the ITZ in concrete. In R.K. Dhir, M.D. Newlands, and K.A. Paine, editors, *Role of Cement Science in Sustainable Development, Proceedings of the International Symposium dedicated to Professor Fred Glasser, University of Abeerdeen, Scotland, held on 3-4 September 2003 at the University of Dundee, Scotland, UK*, pages 123–130. American Society of Civil Engineers (Thomas Telford), 2004.

[59] E.J. Garboczi. Permeability, diffusivity, and microstructural parameters: A critical review. *Cement and Concrete Research*, 20(4):591–601, July 1990.

[60] E.J. Garboczi and D.P. Bentz. Digital simulation of the aggregate-cement paste interfacial zone in concrete. *Journal of Materials Research*, 6(1):196–201, January 1991.

[61] E.J. Garboczi and D.P. Bentz. Fundamental computer simulation models for cement-based materials. In J.P. Skalny and S. Mindess, editors, *Materials Science of Concrete II*, pages 249–277, Westerville, Ohio, 1991. American Ceramic Society.

[62] E.J. Garboczi and D.P. Bentz. Computer simulation of the diffusivity of cement-based materials. *Journal of Materials Science*, 27(8):2083–2092, April 1992.

[63] E.J. Garboczi and D.P. Bentz. Modelling of the microstructure and transport properties of concrete. *Construction and Building Materials*, 10(5):293–300, July 1996.

[64] E.J. Garboczi and D.P. Bentz. Analytical formulas for interfacial transition zone properties. *Advanced Cement Based Materials*, 6(3-4):99–108, November 1997.

[65] E.J. Garboczi and D.P. Bentz. Multiscale analytical/numerical theory of the diffusivity of concrete. *Advanced Cement Based Materials*, 8(2):77–88, July 1998.

[66] E.J. Garboczi and D.P. Bentz. The effect of statistical fluctuation, finite size error, and digital resolution on the phase percolation and transport properties of the NIST cement hydration model. *Cement and Concrete Research*, 31(10):1501–1514, October 2001.

[67] E.J. Garboczi and J.G. Berryman. New effective medium theory for the diffusivity or conductivity of a multi-scale concrete microstructure model. *Concrete Science and Engineering*, 2(6):88–96, June 2000.

[68] E.J. Garboczi, L.M. Schwartz, and D.P. Bentz. Modeling the influence of the interfacial zone on the dc electrical conductivity of mortar. *Advanced Cement Based Materials*, 2(5):169–181, September 1995.

[69] E.M. Gartner and J.M. Gaidis. Hydration mechanisms, i. In J.P. Skalny,

editor, *Materials Science of Concrete I*, pages 95–125, Westerville, Ohio, 1989. The American Ceramic Society.

[70] D. T. Gethin, R. W. Lewis, and R. S. Ransing. A discrete deformable element approach for the compaction of powder systems. *Modelling and Simulation in Materials Science and Engineering*, 11(1):101–114, 2003.

[71] G.K. Glass and N.R. Buenfeld. Theoretical assessment of the steady state diffusion cell test. *Journal of Materials Science*, 33(21):5111–5118, November 1998.

[72] G.K. Glass, G.M. Stevenson, and N.R. Buenfeld. Chloride binding isotherms from the diffusion cell test. *Cement and Concrete Research*, 28(7):939–945, July 1998.

[73] A. Goldman and A. Bentur. Effects of pozzolanic and non-reactive microfillers on the transition zone in high strength concretes. In J.C. Maso, editor, *Interfaces in Cementitious Composites: Proceedings of the International Conference held by RILEM*, pages 53–61, London, 1992. E & FN Spon.

[74] S. Goto and D.M. Roy. Diffusion of ions through hardened cement pastes. *Cement and Concrete Research*, 11(5-6):751–757, September-November 1981.

[75] M. Grigoriu. Estimation of effective conductivity of random heterogeneous media by diffusion processes. *Journal of Applied Physics*, 82(9):4346–4349, November 1997.

[76] M. Grigoriu. Local solution of laplace, heat and other equations by itô processes. *ASCE Journal of Engineering Mechanics*, 123(8):823–829, August 1997.

[77] M. Grigoriu. A monte carlo solution of heat conduction and poisson equations. *Journal of Heat Transfer*, 122(1):40–45, February 2000.

[78] M. Grigoriu. *Stochastic Calculus: Applications in Science and Engineering*. Birkhäuser, Boston, 2002.

[79] M. Grigoriu, E. Garboczi, and C. Kafali. Spherical harmonic-based random fields for aggregates used in concrete. *Powder Technology*, 166(3):123–138, August 2006.

[80] M. Grigoriu and D. Papoulia, K. Effective conductivity by a probability-based local method. *Journal of Applied Physics*, 98(3):1–10, August 2005.

[81] A. Haji-Sheikh and E.M. Sparrow. The solution of heat conduction problems by probability methods. *Journal of Heat Transfer*, 89:121–131, May 1967.

[82] P. Halamickova, R.J. Detwiller, D.P. Bentz, and E.J. Garboczi. Water permeability and chloride ion diffusion in portland cement mortars: Relationship to sand content and critical pore diameter. *Cement and Concrete Research*, 25(4):790–802, May 1995.

[83] Z. Hashin. Thin interphase/imperfect interface in conduction. *Journal of Applied Physics*, 89(4):2261–2267, February 2001.

[84] M.K. Head and N.R. Buenfeld. Confocal imaging of porosity in hardened concrete. *Cement and Concrete Research*, 36(5):896–911, May 2006.

[85] H. Hornain, J. Marchand, V. Duhot, and M. Moranville-Regourd. Diffusion of chloride ions in limestone filler blended cement pastes and mortars. *Cement and Concrete Research*, 25(8):1667–1678, December 1995.

[86] J. Hu and P. Stroeven. Properties of the interfacial transition zone in model concrete. *Interface Science*, 12(4):389–397, October 2004.

[87] O.M. Jensen, A.M. Coats, and F.P. Glasser. Chloride ingress profiles measured by electron probe micro analysis. *Cement and Concrete Research*, 26(11):1695–1705, November 1996.

[88] O.M. Jensen, P.F. Hansen, A.M. Coats, and F.P. Glasser. Chloride ingress in cement paste and mortar. *Cement and Concrete Research*, 29(9):1497–1504, September 1999.

[89] X. Jia and R.A. Williams. A packing algorithm for particles of arbitrary shapes. *Powder Technology*, 120(3):175–186, October 2001.

[90] Y. Kato and T. Uomoto. Modeling of effective diffusion coefficient of substances in concrete considering spatial properties of composite materials. *Journal of Advanced Concrete Technology*, 3(2):241–251, June 2005.

[91] A. Khitab, S. Lorente, and J.P. Ollivier. Predictive model for chloride pen-

etration through concrete. *Magazine of Concrete Research*, 57(9):511–520, November 2005.

[92] C.N. Klahr. A monte carlo method for the solution of elliptic partial differential equations. In A. Ralston and H.S. Wilf, editors, *Mathematical Methods for Digital Computers*, pages 157–164, New York, 1960. John Wiley & Sons.

[93] P.E. Kloeden and E. Platen. *Numerical Solution of Stochastic Differential Equations*. Springer-Verlag, Berlin, New York, 1992.

[94] G.M. Knott, T.L. Jackson, and J. Buckmaster. Random packing of heterogeneous propellants. *American Institute of Aeronautics and Astronautics Journal*, 39(4):678–686, 2001.

[95] S. Kochevets, J. Buckmaster, T.L. Jackson, and A. Hegab. Random packs and their use in modelling heterogeneous solid propellant combustion. *Journal of Propulsion and Power*, 17(4):883–891, 2001.

[96] K. Krabbenhøft and J. Krabbenhøft. Application of the Poisson-Nernst-Planck equations to the migration test. *Cement and Concrete Research*, 38(1):77–88, Janauary 2008.

[97] R. Kumar and B. Bhattacharjee. Study on some factors affecting the results in the use of MIP method in concrete research. *Cement and Concrete Research*, 33(3):417–424, March 2003.

[98] C.K. Larsen. Effect of type of aggregate, temperature and drying/rewetting on chloride binding and pore solution composition. In L.O. Nillson and J.P. Ollivier, editors, *Chloride Penetration into Concrete: Proceedings of the RILEM International Workshop*, pages 27–35, Cachan, France, 1997. RILEM Publications.

[99] Md.A.I. Laskar, R. Kumar, and B. Bhattacharjee. Some aspects of evaluation of concrete through mercury intrusion porosimetry. *Cement and Concrete Research*, 27(1):93–105, January 1997.

[100] X. Lu. Application of the Nernst-Einstein equation to concrete. *Cement and Concrete Research*, 27(2):293–302, February 1997.

[101] K.A. MacDonald and D.O. Northwood. Experimental measurements of chloride ion diffusion rates using a two-compartment diffusion cell:

Effects of material and test variables. *Cement and Concrete Research*, 25(7):1407–1416, October 1995.

[102] J. Marchand and A. Delagrave. Influence of ITZ on ionic diffusion and leaching. In M.G. Alexander, G. Arliguie, G. Ballivy, A. Bentur, and J. Marchand, editors, *Engineering and Transport Properties of the Interfacial Transition Zone in Cementitious Composites*, pages 157–171, Cachan, France, 1999. RILEM Publications.

[103] J. Marchand, B. Gerard, and A. Delagrave. Ion transport mechanisms in cement-based materials. In J.P. Skalny and S. Mindess, editors, *Materials Science of Concrete V*, pages 307–399, Westerville, Ohio, 1998. The American Ceramic Society.

[104] B. Martín-Pérez, S.J. Pantazopoulou, and M.D.A. Thomas. Numerical solution of mass transport equations in concrete structures. *Computers and Structures*, 79(13):1251–1264, May 2001.

[105] B. Martín-Pérez, H. Zibara, R.D. Hooton, and M.D.A. Thomas. A study of the effect of chloride binding on service life predictions. *Cement and Concrete Research*, 30(8):1215–1223, August 2000.

[106] B. Matern. *Spatial Variation: Stochastic Models and Their Application to Some Problems in Forest Surveys and Other Sampling Investigations*. Stockholm, 1960.

[107] P.F. McGrath and R.D. Hooton. Influence of voltage on chloride diffusion coefficients from chloride migration tests. *Cement and Concrete Research*, 26(8):1239–1244, August 1996.

[108] P.F. McGrath and R.D. Hooton. Re-evaluation of the aashto t259 90-day salt ponding test. *Cement and Concrete Research*, 29(8):1239–1248, August 1999.

[109] P.K. Mehta. *Concrete : Structure, Properties, and Materials*. Prentice Hall, Englewood Cliffs, New Jersey, 1986.

[110] P.K. Mehta. Durability of concrete - the zigzag course of progress. In V.M. Malhotra, editor, *Proceedings of Seventh CANMET/ACI International Conference on Durability of Concrete, Montreal, Canada*, pages 1–16, Farmington Hills, MI, 2006. ACI International.

[111] T.U. Mohammed and H. Hamada. Relationship between free chloride and total chloride contents in concrete. *Cement and Concrete Research*, 33(9):1487–1490, September 2003.

[112] W. Morris, E.I. Moreno, and Sagués. Practical evaluation of resistivity of concrete in test cylinders using a Wenner array probe. *Cement and Concrete Research*, 26(12):1779–1787, December 1996.

[113] G.A. Narsilio, R. Li, P. Pivonka, and D.W. Smith. Comparative study of methods used to estimate ionic diffusion coefficients using migration tests. *Cement and Concrete Research*, 37(8):1152–1163, August 2007.

[114] E.G. Nawy. *Reinforced Concrete: A Fundamental Approach*. Prentice Hall, Upper Saddle River, New Jersey, 5th edition, 2003.

[115] A.M. Neville. *Properites of Concrete*. John Wiley & Sons, Inc., New York, 4th edition, 1996.

[116] A.M. Neville and J.J. Brooks. *Concrete Technology*. John Wiley & Sons, Inc., New York, 1987.

[117] V.T. Ngala and C.L. Page. Steady-state diffusion characteristics of cementitious materials. In L.O. Nillson and J.P. Ollivier, editors, *Chloride Penetration into Concrete: Proceedings of the RILEM International Workshop*, pages 77–84, Cachan, France, 1997. RILEM Publications.

[118] V.T. Ngala, C.L. Page, L.J. Parrot, and S.W. Yu. Diffusion in cementitious materials: Ii. Further investigations of chloride and oxygen diffusion in well-cured OPC and OPC/30%PFA pastes. *Cement and Concrete Research*, 25(4):819–826, May 1995.

[119] F. Nugue, S. Lorente, and J.P. Ollivier. Basis for the prediction of chloride ingress into cement-based materials. *Revista de Ciência e Tecnologia de Materiais de Construção Civil*, 1(1):10–21, May 2004.

[120] B.H. Oh and S.Y. Jang. Advanced analysis of chloride diffusion and convection in concrete structures. In R.K. Dhir, M.D. Newlands, and K.A. Paine, editors, *Role of Concrete in Sustainable Construction, Proceedings of the International Symposium dedicated to Professor Surenda Shah, Northwestern University, USA, held on 3-4 September 2003 at the University of Dundee, Scotland, UK*, pages 309–318. American Society of Civil Engineers (Thomas Telford), 2004.

[121] B.H. Oh and S.Y. Jang. Prediction of diffusivity of concrete based on simple analytic equations. *Cement and Concrete Research*, 34(3):463–480, March 2004.

[122] B. Øksendal. *Stochastic Differential Equations*. Springer-Verlag, 6th edition, 2003.

[123] J.P. Ollivier, C.J. Maso, and B. Bourdette. Interfacial transition zone in concrete. *Advanced Cement Based Materials*, 2(1):30–38, January 1995.

[124] D.F. Orchard. *Concrete Technology*, volume II. Applied Science Publishers Ltd., London, England, 4th edition, 1979.

[125] N. Otsuki, S. Nagataki, and K. Nakashita. Evaluation of $AgNO_3$ solution spray method for measurement of chloride penetration into hardened cementitious matrix materials. *ACI Materials Journal*, 89(6):587–592, November-December 1992.

[126] C.L. Page, N.R. Short, and A. El Tarras. Diffusion of chloride ions in hardened cement pastes. *Cement and Concrete Research*, 11(3):395–406, May 1981.

[127] S. Popovics. *Concrete Materials: Properties, Specifications and Testing*. Noyes Publications, Park Ridge, New Jersey, 2nd edition, 1992.

[128] S. Popovics. *Strength and Related Properties of Concrete: A Quantitative Approach*. John Wiley & Sons, New York, 1998.

[129] E. Poulsen and L. Mejlbro. *Diffusion of Chloride in Concrete - Theory and Application*. Modern Concrete Technology 14. Taylor & Francis, 1st edition, 2006.

[130] T.C. Powers. A discussion of cement hydration in relation to the curing of concrete. In *Highway Research Board Proceedings*, volume 27, pages 178–188, Washington, DC, 1947. Highway Research Board.

[131] T.C. Powers, L.E. Copeland, and H.M. Mann. Capillary continuity or discontinuity in cement pastes. *Journal of Portland Cement Association Research and Development Laboratories*, 1(2):38–48, 1959.

[132] W.F. Price, M.R. Jones, S.C. Ting, and R.K. Dhir. Effect of aggregate porosity on chloride ingress into concrete. In R.K. Dhir, M.D. Newlands, and

K.A. Paine, editors, *Role of Concrete in Sustainable Construction, Proceedings of the International Symposium dedicated to Professor Surenda Shah, Northwestern University, USA, held on 3-4 September 2003 at the University of Dundee, Scotland, UK*, pages 287–297. American Society of Civil Engineers (Thomas Telford), 2004.

[133] R. S. Ransing, R. W. Lewis, and D. T. Gethin. Using a deformable discrete-element technique to model the compaction behavior of mixed ductile and brittle particulate systems. *Royal Society of London Transactions Series A*, 362(1822):1867–1884, 2004.

[134] S. Rémond, D.P. Bentz, and P. Pimienta. Effects of the incorporation of Municipal Solid Waste Incineration fly ash in cement pastes and mortars: II. Modeling. *Cement and Concrete Research*, 32(4):565–576, April 2002.

[135] S. Rémond, P. Pimienta, and D.P. Bentz. Effects of the incorporation of Municipal Solid Waste Incineration fly ash in cement pastes and mortars: I. Experimental study. *Cement and Concrete Research*, 32(2):303–311, February 2002.

[136] M.N.O. Sadiku. *Computational Stochastic Mechanics*, chapter 13 Probabilistic Solutions of Poission's Equations, pages 281–299. International Series on Computational Engineering. Computational Mechanics Publications & Elsevier Applied Science, Boston & New York, 1993.

[137] M.N.O. Sadiku, S.O. Ajose, and Z. Fu. Applying the exodus method to solve poisson's equation. *IEEE Transactions on Microwave Theory and Technique*, 42(4):661–666, April 1994.

[138] M.N.O. Sadiku and D.T. Hunt. Solution of problems by the exodus method. *IEEE Transactions on Microwave Theory and Technique*, 40(1):89–95, January 1992.

[139] E. Samson, G. Lemaire, J. Marchand, and J.J. Beaudoin. Modeling chemical activity effects in strong ionic solutions. *Computational Materials Science*, 15(3):285–294, August 1999.

[140] E. Samson and J. Marchand. Numerical solution of the extended nernst-planck model. *Journal of Colloid and Interface Science*, 215(1):1–8, July 1999.

[141] E. Samson and J. Marchand. Modeling the effect of temperature on ionic transport in cementitious materials. *Cement and Concrete Research*, 37(3):455–468, March 2007.

[142] E. Samson, J. Marchand, and J.J. Beaudoin. Describing ion diffusion mechanisms in cement-based materials using the homogenization technique. *Cement and Concrete Research*, 29(8):1341–1345, August 1999.

[143] E. Samson, J. Marchand, J.L. Robert, and J.P. Bournazel. Modeling ion diffusion mechanisms in porous media. *International Journal for Numerical Methods in Engineering*, 46(12):2043–2060, December 1999.

[144] E. Samson, J. Marchand, and K.A. Snyder. Calculation of ionic diffusion coefficients on the basis of migration test results. *Materials and Structures*, 36(257):156–165, April 2003.

[145] L.M. Schwartz, E.J. Garboczi, and D.P. Bentz. Interfacial transport in porous media: Application to dc electrical conductivity of mortars. *Journal of Applied Physics*, 78(10):5898–5908, November 1995.

[146] K.L. Scrivener. The microstructure of concrete. In J.P. Skalny, editor, *Materials Science of Concrete I*, pages 127–161, Westerville, Ohio, 1989. The American Ceramic Society.

[147] K.L. Scrivener. Characterization of the ITZ and its quantification by test methods. In M.G. Alexander, G. Arliguie, G. Ballivy, A. Bentur, and J. Marchand, editors, *Engineering and Transport Properties of the Interfacial Transition Zone in Cementitious Composites*, pages 3–15, Cachan, France, 1999. RILEM Publications.

[148] K.L. Scrivener, A. Bentur, and P.L. Pratt. Quantitative characterization of the transition zone in high strength concretes. *Advances in Cement Research*, 1(4):230–237, October 1988.

[149] K.L. Scrivener, A.K. Crumbie, and P. Laugesen. The interfacial transition zone (ITZ) between cement paste and aggregate in concrete. *Interface Science*, 12(4):411–421, October 2004.

[150] J.D. Shane, T.O. Mason, and H.M. Jennings. Conductivity and microstructure of the interfacial transition zone measurerd by impedance spectroscopy. In M.G. Alexander, G. Arliguie, G. Ballivy, A. Bentur, and J. Marchand, editors, *Engineering and Transport Properties of the Interfacial Transition Zone in Cementitious Composites*, pages 173–203, Cachan, France, 1999. RILEM Publications.

[151] L.N. Smith and P.S. Midha. Computer simulation of morphology and

packing behavior of irregular particles, for predicting apparent powder densities. *Computational Materials Science*, 7(4):377–383, March 1997.

[152] K. Sobczyk and D.J Kirkner. *Stochastic Modelling of Microstructures*. Birkhäuser, Boston, 2001.

[153] K.D. Stanish, R.D. Hooton, and M.D.A. Thomas. Testing the chloride penetration resistance of concrete: A literature review. FHWA Contract DTFH61-97-R-00022, University of Toronto, Toronto, ON, Canada, June 1997.

[154] P.E. Streicher and M.G. Alexander. A chloride conduction test for concrete. *Cement and Concrete Research*, 25(6):1284–1294, August 1995.

[155] M. Stroeven and P. Stroeven. SPACE system for simulation of aggregated matter application to cement hydration. *Cement and Concrete Research*, 29(8):1299–1304, August 1999.

[156] P. Stroeven and M. Stroeven. Assessment of packing characteristics by computer simulation. *Cement and Concrete Research*, 29(8):1201–1206, August 1999.

[157] P. Stroeven and M. Stroeven. Reconstructions by SPACE of the interfacial transition zone. *Cement and Concrete Composites*, 23(2-3):189–200, April-June 2001.

[158] P. Stroeven and M. Stroeven. Dynamic computer simulation of concrete on different levels of the microstructure - part 1. *Image Analysis and Stereology*, 22(1):1–10, March 2003.

[159] P. Stroeven and M. Stroeven. Dynamic computer simulation of concrete on different levels of the microstructure - part 2. *Image Analysis and Stereology*, 22(2):91–95, June 2003.

[160] P.E. Stutzman. Scanning electron microscopy in concrete petrography. In J.P. Skalny, J. Gebauer, and I. Odler, editors, *Materials Science of Concrete Special Volume: Calcium Hydroxide in Concrete*, pages 59–72, Anna Maria Island, Florida, 2001. The American Ceramic Society.

[161] A. Suwito, X. Cai, and Y. Xi. Parallel finite element method for coupled chloride moisture diffusion in concrete. *International Journal of Numerical Analysis and Modeling*, 3(4):481–503, 2006.

[162] AASHTO T259-80. *Standard Method of Test for Resistance of Concrete to Chloride Ion Penetration*. American Association of State Highway and Transportation Officials, Washington, D.C., 1980.

[163] AASHTO T277-89. *Standard Method of Test for Resistance of Concrete to Chloride Ion Penetration*. American Association of State Highway and Transportation Officials, Washington, D.C., 1989.

[164] L. Tang. On chloride diffusion coefficients obtained by using the electrically accelerated methods. In L.O. Nillson and J.P. Ollivier, editors, *Chloride Penetration into Concrete: Proceedings of the RILEM International Workshop*, pages 126–134, Cachan, France, 1997. RILEM Publications.

[165] L. Tang. Concentration dependence of diffusion and migration of chloride ions: Part 1. theoretical considerations. *Cement and Concrete Research*, 29(9):1463–1468, September 1999.

[166] L. Tang. Concentration dependence of diffusion and migration of chloride ions: Part 2. experimental evaluations. *Cement and Concrete Research*, 29(9):1469–1474, September 1999.

[167] L. Tang and L.O. Nilsson. Chloride diffusivity in high strength concrete at different ages. *Nordic Concrete Research*, 11(1):162–171, 1992.

[168] L. Tang and L.O. Nilsson. Rapid determination of the chloride diffusivity in concrete by applying an electrical field. *ACI Materials Journal*, 89(1):49–53, January-February 1992.

[169] L. Tang and L.O. Nilsson. Chloride binding capacity and binding isotherms of opc pastes and mortars. *Cement and Concrete Research*, 23(2):247–253, March 1993.

[170] L. Tang and H.E. Sø rensen. Precision of the nordic test methods for measuring the chloride diffusion/migration coefficients of concrete. *Materials and Structures*, 34(8):479–485, October 2001.

[171] W.A. Tasong, J.C. Cripps, and C.J. Lynsdale. Aggregate-cement chemical interactions. *Cement and Concrete Research*, 28(7):1037–1048, July 1998.

[172] W.A. Tasong, C.J. Lynsdale, and J.C. Cripps. Aggregate-cement paste interface: Part ii. Influence of aggregate physical properties. *Cement and Concrete Research*, 28(10):1453–1465, October 1998.

[173] W.A. Tasong, C.J. Lynsdale, and J.C. Cripps. Aggregate-cement paste interface: Part i. Influence of aggregate geochemistry. *Cement and Concrete Research*, 29(7):1019–1025, July 1999.

[174] J. Tritthart. Chloride binding in cement: Ii. the influence of the hydroxide concentration in the pore solution of hardened cement paste on chloride binding. *Cement and Concrete Research*, 19(5):683–691, September 1989.

[175] O. Truc, J.P. Ollivier, and M. Carcassés. A new way for determining the chloride diffusion coefficient in concrete from steady state migration test. *Cement and Concrete Research*, 30(2):217–226, February 2000.

[176] O. Truc, J.P. Ollivier, and L.O. Nilsson. Numerical simulation of multispecies transport through saturated concrete during a migration test Ms-Diff code. *Cement and Concrete Research*, 30(10):1581–1592, October 2000.

[177] K. van Breugel. *Simulation of Hydration and Formation of Structure in Hardening Cement-Based Materials*. PhD thesis, Delft University of Technology, 1991.

[178] K. van Breugel. Numerical simulation of hydration and microstructural development in hardening cement-based materials (i) theory. *Cement And Concrete Research*, 25(2):319–331, February 1995.

[179] K. van Breugel. Numerical simulation of hydration and microstructural development in hardening cement-based materials (ii) applications. *Cement And Concrete Research*, 25(3):522–530, April 1995.

[180] K. van Breugel and A.L.A. Fraaij. Numerical and experimental studies of percolation phenomena of hardening cement pastes. In R.K. Dhir, M.D. Newlands, and K.A. Paine, editors, *Role of Cement Science in Sustainable Development, Proceedings of the International Symposium dedicated to Professor Fred Glasser, University of Abeerdeen, Scotland, held on 3-4 September 2003 at the University of Dundee, Scotland, UK*, pages 103–112. American Society of Civil Engineers (Thomas Telford), 2004.

[181] X. Wang, J. Buckmaster, and T.L. Jackson. Burning of ammonium-perchlorate ellipses and spheroids in fuel binder. *Journal of Propulsion and Power*, 22(4):764–768, 2006.

[182] D. Whiting. Rapid determination of the chloride permeability of concrete. Report No. FHWA-RD-81/119, Federal Highway Administration, Washington, D.C., August 1981.

[183] D.N. Winslow, M.D. Cohen, D.P. Bentz, K.A. Synder, and E.J. Garboczi. Percolation and pore structure in mortars and concrete. *Cement and Concrete Research*, 24(1):25–37, 1994.

[184] H.S. Wong and N.R. Buenfeld. Euclidean distance mapping for computing microstructural gradients at interfaces in composite materials. *Cement and Concrete Research*, 36(6):1091–1097, June 2006.

[185] H.S. Wong, N.R. Buenfeld, and M.K. Head. Estimating transport properties of mortars using image analysis on backscattered electron images. *Cement and Concrete Research*, 36(8):1556–1566, August 2006.

[186] H.S. Wong, M.K. Head, and N.R. Buenfeld. Pore segmentation of cement-based materials from backscattered electron images. *Cement and Concrete Research*, 36(6):1083–1090, June 2006.

[187] Y. Xi and Z.P. Bažant. Modeling chloride penetration in saturated concrete. *Journal of Materials in Civil Engineering*, 11(1):58–65, February 1999.

[188] K. Yamada, Y. Hosokowa, D. Mori, Y. Yamada, and B. Johannesson. Estimation of effective diffusion coefficients and non-linear binding parameters of chloride by reverse analysis of chloride profiles. In V.M. Malhotra, editor, *Proceedings of Seventh CANMET/ACI International Conference on Durability of Concrete, Montreal, Canada*, pages 39–52, Farmington Hills, MI, 2006. ACI International.

[189] C.C. Yang. A comparison of transport properties for concrete using the ponding test and the accelerated chloride migration test. *Materials and Structures*, 38(277):313–320, April 2005.

[190] C.C. Yang. On the relationship between pore structure and chloride diffusivity from accelerated migration test in cement-based materials. *Cement and Concrete Research*, 36(7):1304–1311, July 2006.

[191] C.C. Yang and S.W. Cho. Approximate migration coefficient of percolated interfacial transition zone by using the accelerated chloride migration test. *Cement and Concrete Research*, 35(2):344–350, February 2005.

[192] C.C. Yang, S.W. Cho, and R. Huang. The relationship between charge passed and the chloride-ion concentration in concrete using steady-state chloride migration test. *Cement and Concrete Research*, 32(2):217–222, February 2002.

[193] C.C. Yang and J.K. Su. Approximate migration coefficient of interfacial transition zone and the effect of aggregate content on the migration coefficient of mortar. *Cement and Concrete Research*, 32(10):1559–1565, October 2002.

[194] G. Ye, K. van Breugel, and A.L.A. Fraaij. Three-dimensional microstructure analysis of numerically simulated cementitious materials. *Cement And Concrete Research*, 33(2):215–222, February 2003.

[195] S.W. Yu and C.L. Page. Diffusion in cementitious materials: I. Comparative study of chloride and oxygen diffusion in hydrated cement pastes. *Cement and Concrete Research*, 21(4):581–588, July 1991.

[196] M. Yunovich and N.G. Thompson. Corrosion of highway bridges: Economic impact and control methodologies. *Concrete International*, 25(1):52–57, January 2003.

[197] T. Zhang and O.E. Gjørv. An electrochemical method for accelerated testing of chloride diffusivity in concrete. *Cement and Concrete Research*, 24(8):1534–1548, 1994.

[198] T. Zhang and O.E. Gjørv. Effect of ionic interaction in migration testing of chloride diffusivity in concrete. *Cement and Concrete Research*, 25(7):1535–1542, October 1995.

[199] T. Zhang and O.E. Gjørv. Diffusion behavior of chloride ions in concrete. In L.O. Nillson and J.P. Ollivier, editors, *Chloride Penetration into Concrete: Proceedings of the RILEM International Workshop*, pages 53–63, Cachan, France, 1997. RILEM Publications.

[200] T. Zhang and O.E. Gjørv. Effect of chloride source concentration on chloride diffusivity in concrete. *ACI Materials Journal*, 102(5):295–298, September 2005.

[201] T. Zhang and O.E. Gjørv. Effect of chloride source concentration on chloride diffusivity in concrete. *ACI Materials Journal*, 102(5):295–298, September-October 2005.